Correlation between Lattice Dynamics and Magnetism in the Multiferroic Manganites

Dissertation zur Erlangung des naturwissenschaftlichen Doktorgrades der Julius-Maximilians-Universität Würzburg

vorgelegt von
Sven Issing
aus Würzburg

Würzburg, 2011

Eingereicht am: .....
bei der Fakultät für Physik und Astronomie

1. Gutachter: Prof. Dr. J. Geurts
2. Gutachter: Prof. Dr. A. Pimenov
der Dissertation

1. Prüfer: Prof. Dr. J. Geurts
2. Prüfer: Prof. Dr. A. Pimenov
3. Prüfer: Prof. Dr. F. Assaad
im Promotionskolloquium

Tag des Promotionskolloquiums: .....

Doktorurkunde ausgehändigt am: .....

Zusammenfassung

Thematik und Zielsetzung

Grundlegendes Verständnis der physikalischen Zusammenhänge innerhalb multifunktionaler Materialien im Hinblick auf spätere potentielle Anwendungen ist eines der Hauptziele der heutigen Forschungsbemühungen in der Festkörperphysik. Im Wesentlichen geht es dabei um das Ausnutzen von intrinsischen Kopplungseffekten, um zusätzliche Funktionalität im Vergleich zur heutigen auf Miniaturisierung von halbleiterbasierten Bauelementen aufbauenden Informationstechnologie zu erreichen.
Die vorgelegte Dissertation zielt in diesem Themengebiet auf die systematische Untersuchung der Kopplungseffekte zwischen Kristallgitterdynamik und Magnetismus in den multiferroischen Manganaten ab. Konkret geht es um das Modelsystem der multiferroischen Selten–Erd–Manganate $RMnO_3$ mit orthorhombischer Pnma–Struktur. Die zu diesem Zweck verwendeten experimentellen Techniken waren Raman und Fourier–Transform Infrarot (FT–IR) Spektroskopie, mit deren Hilfe alle optisch aktiven Kristallgitterschwingungen dieser Systeme spektroskopiert werden konnten. Zur Untersuchung der Kopplungseffekte wurden die spektroskopischen Experimente polarisationssensitiv und unter Variation der Probentemperatur durchgeführt, um insbesondere Renormalisierungseffekte der Gitterschwingungen im Temperaturbereich magnetischer Phasenübergänge nachweisen zu können. In Verbindung mit gitterdynamischen Rechnungen, die auf der Dichtefunktionaltheorie (DFT) basieren, wurden zwei Kopplungseffekte systematisch untersucht: Spin–Phonon Kopplung (SPC) sowie Elektromagnon–Phonon Kopplung (EMPC). Die Ergebnisse sind im Folgenden zusammengefasst.

Ergebnisse: Gitterdynamik der stöchiometrischen und dotierten Selten–Erd Manganate

Grundlage für weitergehende Analysen der Kopplungseffekte ist die systematische Untersuchung der Gitterdynamik der beiden verwendeten einkristallinen Probenserien, also der stöchiometrischen $RMnO_3$ (R = Eu, Gd, Tb) Serie sowie der dotierten $Eu_{1-x}Y_xMnO_3$ ($0 \leq x \leq 0.5$) Serie. Um potentielle Beeinflussung durch Korrelationen der Gitterschwingungen mit den magnetischen Eigenschaften in diesem Fall auszuschließen, wurden die

Experimente bei Raumtemperatur durchgeführt, d.h. weit oberhalb des Temperaturbereichs der magnetisch geordneten Phasen.
Als Vorstufe zu experimentellen Untersuchungen wurden gitterdynamische Rechnungen basierend auf Dichtefunktionaltheorie (DFT) am System $LaMnO_3$ durchgeführt. Auf diese Weise konnten theoretische Daten für die Auslenkungsmuster der jeweiligen Phononenmoden gewonnen werden, die anschließend für eine systematische Auswertung der Kopplungseffekte genutzt wurden.
Der Ausgangspunkt einer Analyse der Gitterdynamik ist die Modenzuordnung aller experimentell beobachteten Raman und infrarot aktiven Phononen. Zu diesem Zweck wurde $GdMnO_3$ herangezogen, auf Grund seiner bis zum optischen Grad aufpolierten b–cut Probenoberfläche und damit verbundenen guten Erfüllung der optischen Auswahlregeln sowie der zumindest für die Raman–Spektren gegebenen Möglichkeit, mit bereits publizierten Messungen an polykristallinen $GdMnO_3$ zu vergleichen [IAL$^+$06]. Zwischen beiden ergab sich eine sehr gute Übereinstimmung bezüglich der Phononenfrequenzen und der Erfüllung der optischen Auswahlregeln. Analog zu den Raman Spektren wurde eine Modenzuordnung mit Hilfe der polarisationssensitiven Reflektivität von b–cut $GdMnO_3$ vorgenommen. Die optischen Auswahlregeln in diesem System erlauben den Zugang zu Phononen mit B_{1u} sowie B_{3u} Symmetrie. Insgesamt ergab sich für die Zahl der Phononen mit B_{1u} und B_{3u} Symmetrie genau die Zahl, die von der Gruppentheorie vorhergesagt wird. Zusätzlich konnten die durch Fits erhaltenen Phononenparameter, wie Resonanzfrequenz, Linienbreite und ionische Plasmafrequenz, qualitativ verglichen werden mit Werten, die von Schmidt et al. [SKR$^+$09] durch Messungen an $TbMnO_3$ gewonnen wurden. Zusammen mit den Raman aktiven Phononen konnte so erstmals eine komplette Analyse der Gitterdynamik von $GdMnO_3$ durchgeführt werden.
Nach der systematischen Modenzuordnung konnte anschließend (i) sowohl der Einfluss eines kompletten Ersatzes der R^{3+} Ionen in der stöchiometrischen $RMnO_3$ (R = Eu, Gd, Tb) Serie (ii) als auch der Einfluss von Dotierung in der $Eu_{1-x}Y_xMnO_3$ ($0 \leq x \leq 0.5$) Serie, in der Eu^{3+} durch Y^{3+} ersetzt wird, untersucht werden. Dies geschah in der Form einer vergleichenden Analyse der Veränderungen der Raman Spektren sowie der Reflektivität beider Probenserien.
Bezüglich der Raman Spektren der $RMnO_3$ Serie konnte folgendes beobachtet werden: Auf der einen Seite wurden für Phononen, die im wesentlichen aus Verschiebungen der O^{2-} Ionen senkrecht zur MnO_2 (ac) Ebene bestehen, deutliche Frequenzverschiebungen hin zu größeren Frequenzen bei einer Reduzierung des R^{3+} Radius beobachtet, was auf die mit der Reduzierung einhergehende Verminderung des Mn–O–Mn Verkippungswinkels zurückgeführt wurde. Auf der anderen Seite zeigte beispielsweise die symmetrische Streckschwingung der MnO_6 Oktaeder innerhalb der MnO_2 (ac) Ebene nahezu keine Abhängigkeit bezüglich einer Veränderung dieses Winkels. Insgesamt konnten alle beobachteten Frequenzverschiebungen der Raman aktiven Phononen in dieser Weise durch die zuvor theoretisch berechneten Auslenkungsmuster der jeweiligen Phononen vollständig erklärt werden. Ferner wurden Mischeffekte der $A_g(1)$ und $A_g(3)$ Moden in

guter Übereinstimmung mit der Literatur [IAL+06] nachgewiesen.
Bei Betrachtung der Reflektivität und somit der infrarot aktiven Phononen wurde zur besseren Übersichtlichkeit eine Klassifizierung entsprechend der Auslenkungsmuster und der Phononenfrequenzen benutzt, um die beobachteten Trends in Abhängigkeit vom vorliegenden R^{3+} Ion zu erklären. Diese können mit Hilfe des Modells eines einfachen harmonischen Oszillators verstanden werden. In diesem Modell sind die zwei für die Phononenfrequenz entscheidenden Faktoren die reduzierte Masse der beteiligten Ionen sowie die Kraftkonstanten der modulierten Bindungen des jeweiligen Phonons. Mit Hilfe dieses Modells konnten unter Verwendung von quantitativen aus der Literatur entnommenen Werten für die Gitterkonstanten und der jeweiligen R^{3+} Ionenmasse alle beobachteten Trends innerhalb der $RMnO_3$ Serie konsistent erklärt werden.
Die dotierte $Eu_{1-x}Y_xMnO_3$ Serie zeigte im Wesentlichen dieselben Trends. Bezüglich der Raman aktiven Moden wurde ein nahezu identisches Verhalten wie bei der $RMnO_3$ Serie – diesmal in Abhängigkeit vom Dotiergrad x – beobachtet, d.h. positive Frequenzverschiebungen und Mischeffekte der $A_g(1)$ und $A_g(3)$ Moden. Die infrarot aktiven Moden zeigten Abweichungen vom Verhalten der $RMnO_3$ Serie und zwar bei den Moden mit starker Beteiligung der Eu^{3+} bzw. Y^{3+} Ionen. Auch diese Effekte konnten mit Hilfe des Modells des einfachen harmonischen Oszillators erklärt werden. Ein weiterer Unterschied zwischen dotiertem $Eu_{1-x}Y_xMnO_3$ und $RMnO_3$ ist die Reduzierung der dipolaren Aktivität der infrarotaktiven Moden mit der niedrigsten Frequenz bei steigender Y^{3+} Dotierung. Da dieser Effekt jedoch auf die niederfrequentesten infrarotaktiven Moden beschränkt ist, konnte auch die dotierte $Eu_{1-x}Y_xMnO_3$ Serie als ebenso geeignet für eine Analyse der Korrelationseffekte zwischen Kristallgitterdynamik und Magnetismus wie die stöchiometrische $RMnO_3$ Serie angesehen werden. Diese Effekte wurden im Anschluss betrachtet.

Ergebnisse: Spin–Phonon Kopplung

Der erste systematisch analysierte Korrelationseffekt war die Spin–Phonon Kopplung (SPC). Diese äußert sich als eine Renormalisierung der Phononfrequenzen beim Übergang in die Temperaturregion der magnetisch geordneten Phasen. Der Ursprung der SPC ist die dynamische Modulation der magnetischen Austauschwechselwirkung durch die entsprechende Phononmode. Daher ist die sich ergebende Frequenzrenormalisierung korreliert mit der zunehmenden Stärke des magnetischen Austauschs bei fallender Temperatur. Obwohl dieser Effekt bereits in $RMnO_3$ Systemen mit relativ großem Selten–Erd–Ionenradius ($R^{3+} = La^{3+} \ldots Sm^{3+}$) nachgewiesen wurde, stand eine systematische Untersuchung der SPC in den multiferroischen Manganaten noch aus.
Die Analyse der Abhängigkeit der Stärke und der Einsatztemperatur der Renormalisierungseffekte von der jeweiligen betrachteten Phononmode zeigte, dass diese im wesentlichen durch den magnetischen Austausch der MnO_6 Oktaeder innerhalb der MnO_2 (ac) Ebene verursacht wird. Dies konnte unter Ausnutzung der Modensymmetrie gezeigt werden, da im Fall der Raman aktiven Phononen die Moden mit hauptsächlicher Modulation

der Mn–O–Mn Bindungen innerhalb dieser Ebene wesentlich stärkere SPC Effekte zeigen als diejenigen mit einer Modulation senkrecht zu dieser Ebene bzw. innerhalb der RO (ac) Ebene. Die Untersuchung der infrarot aktiven Phononen wiederum ließ die Schlussfolgerung zu, dass SPC hauptsächlich bei Phononen mit einer ausgeprägten Modulation der Mn–O–Mn Bindungen beobachtet wird. Moden mit starker Beteiligung der R^{3+} Ionen zeigten keine SPC Effekte. Außerdem konnte belegt werden, dass das Mitschwingen von Mn^{3+} keinen Einfluss auf das Auftreten von SPC hat, da sowohl für Raman als auch für infrarot aktive Phononen Renormalisierungseffekte nachweisbar waren.
Bezüglich der Abhängigkeit der SPC von der Probenzusammensetzung, d.h. die Ausprägung und Einsatztemperatur der Renormalisierungseffekte in Abhängigkeit vom vorliegenden R^{3+} Ion, wurden die beiden Probenserien untersucht und miteinander verglichen:
Im Fall der stöchiometrischen $RMnO_3$ Serie konnte eine Verminderung der Stärke der Renormalisierungseffekte mit abnehmendem R^{3+} Ionenradius von Eu^{3+} über Gd^{3+} zu Tb^{3+} nachgewiesen werden. Dies wurde zurückgeführt auf eine Schwächung des ferromagnetischen Austauschs innerhalb der MnO_2 (ac) Ebene durch eine erhöhte Verkippung der MnO_6 Oktaeder, die wiederum durch den kleineren R^{3+} Ionenradius verursacht wird.
Die dotierte $Eu_{1-x}Y_xMnO_3$ Probenserie zeigte dieselben Trends einer reduzierten SPC mit steigender Y^{3+} Dotierung, die ähnlich zum kompletten Austausch in $RMnO_3$ zu einer Reduzierung des effektiven R^{3+} Ionenradius führt. Es konnte also gefolgert werden, dass die Dotierung von $Eu_{1-x}Y_xMnO_3$, mit der der effektive Ionenradius quasi–kontinuierlich eingestellt werden kann, das Auftreten von SPC Effekten nicht verhindert. Dies wurde als ein weiterer Beleg aufgefasst, dass durch Unordnung bedingte Effekte in $Eu_{1-x}Y_xMnO_3$ vernachlässigbar sind.
Ein Vergleich der SPC Effekte in beiden Probenserien zeigte deutlich die Korrelation von orthorhombischer Gitterverzerrung, d.h. die Ungleichheit der kurzen a– und c–Achse in der Pnma Struktur, die sich durch den Parameter ϵ ausdrücken lässt, mit den durch SPC verursachten Renormalisierungseffekten der Gitterschwingungen. Es konnte also gezeigt werden, dass SPC nicht explizit an die Existenz spezifischer magnetischer Phasen gekoppelt ist, sondern an die Stärke des magnetischen Austauschs zwischen den Mn^{3+} Ionen in der MnO_2 (ac) Ebene. Weiterhin war SPC sowohl für Raman als auch für infrarot aktive Phononen beobachtbar, die die Mn–O–Mn Bindungen in der MnO_2 (ac) Ebene modulieren. Daher konnten bereits publizierte Schlussfolgerungen bezüglich keramischer multiferroischer Manganate widerlegt werden, die SPC Effekte direkt mit deren multiferroischen Eigenschaften verknüpfen [FMA$^+$09, MAF$^+$10].
Ein Korrelationseffekt zwischen Kristallgitterdynamik und Magnetismus in den Manganaten, der explizit mit der Existenz multiferroischer Eigenschaften verbunden ist, wurde ebenfalls in dieser Dissertation behandelt. Diese Resultate werden im Folgenden zusammengefasst.

Ergebnisse: Elektromagnon–Phonon Kopplung

Der zweite in dieser Dissertation betrachtete Korrelationseffekt zwischen Kristallgitterdynamik und Magnetismus war die Elektromagnon–Phonon Kopplung (EMPC). Eine der Ausprägungen dieses Effekts – die Verlagerung spektralen Gewichts von den infrarot aktiven Phononen mit niedriger Frequenz ($\widetilde{\nu} < 300 cm^{-1}$) bei Absenken der Temperatur in Richtung der multiferroischen Phasen hin zum entstehenden Elektromagnon – wurde bereits ausführlich in der Literatur behandelt [PRM$^+$06, TYK$^+$09, SKR$^+$09]. Andere Aspekte von EMPC jedoch, wie z.B. Renormalisierung der Phononenfrequenz beim Eintritt in die Temperaturregion der magnetisch geordneten Phasen, waren bislang nicht systematisch behandelt. Des Weiteren fehlte eine detaillierte Erklärung des Ursprungs dieser Kopplung auf mikroskopischer Ebene. Um dies zu korrigieren, wurden in dieser Arbeit die infrarot aktiven Phononen mit niedriger Frequenz separat untersucht und zwar unter besonderer Beachtung der optischen Auswahlregeln sowie der Verschiebungsmuster der jeweiligen Moden.
Temperaturabhängige Reflektivitätsmessungen an $RMnO_3$ (R = Eu, Gd) zusammen mit bereits veröffentlichten Resultaten von Schmidt el al. [SKR$^+$09] an $TbMnO_3$ zeigten klar den Transfer spektralen Gewichts von der niederfrequentesten polaren Mode mit B_{3u} Symmetrie, d.h. $B_{3u}(1)$, zum entstehenden Elektromagnon innerhalb der stöchiometrischen $RMnO_3$ Serie. Auch ließ sich ein Trend zu stärkerer Ausprägung des spektralen Transfers bei Reduzierung des R^{3+} Ionenradius nachweisen, d.h. die Stärke des Transfers steigt von $EuMnO_3$ monoton bis zu $TbMnO_3$, was als Zunahme der Stärke der EMPC gedeutet wird. Der EMPC–Aspekt spektralen Transfers konnte also durch eigene Messungen bestätigt werden. Darüber hinaus wurden auch weitere Manifestationen untersucht, darunter beispielsweise die Verschiebung der Frequenzen der $B_{3u}(1)$ Moden zu höheren Werten beim Eintritt in die Temperaturregion der magnetisch geordneten Phasen. Diese experimentellen Beobachtungen an $EuMnO_3$ und $GdMnO_3$ stimmten gut mit den Daten von [SKR$^+$09] an $TbMnO_3$ überein. Auch hier bestätigte sich der Trend steigender Ausprägung der EMPC hin zu den $RMnO_3$ Systemen mit multiferroischen Phasen. Diese experimentellen Daten zeigen klar, dass die Renormalisierung der $B_{3u}(1)$ Mode nicht auf SPC zurückgeführt werden kann, da sowohl das Schieben zu höheren Frequenzen als auch die starke Beteiligung des R^{3+} Ions am Verschiebungsmuster dieser Mode einer solchen Interpretation widerspricht.
Nach dem Zusammentragen der wesentlichen experimentellen Ergebnisse, wurde eine Erklärung bezüglich des mikroskopischen Ursprungs dieser Kopplung zwischen Elektromagnon und $B_{3u}(1)$ Mode gegeben. Diese basiert zum einen auf dem Mechanismus für die dipolare Aktivität des hochfrequenten Elektromagnons – das Heisenberg–Austausch Model von Valdés Aguilar [VAMS$^+$09] – und zum anderen auf den Verschiebungsmustern der $B_{3u}(1)$ Mode, die auf Grund der selbst durchgeführten DFT basierten gitterdynamischen Rechnungen vorliegen. Das Einbeziehen beider Faktoren führt schließlich dazu, dass eine gleichförmige Verschiebung der Mn^{3+} Ionen entlang der c–Achse, die ein charakte-

ristischer Teil des Auslenkungsmusters von $B_{3u}(1)$ ist, als für diese Kopplung wesentlich ausgemacht werden kann. Auch im Fall von EMPC bewirkt also die dynamische Modulation des magnetischen Austauschs durch ein Phonon mit einem entsprechend geeigneten Auslenkungsmuster den Korrelationseffekt.
Bezug nehmend auf dieses mikroskopische Modell wurden beide beobachteten Aspekte der EMPC noch einmal beleuchtet und es konnte eine zusätzliche Manifestierung durch genaue Inspektion der Daten von Shuvaev et al. [SML$^+$11] an $GdMnO_3$ nachgewiesen werden. Diese drei Teilaspekte waren: (i) der Transfer spektralen Gewichts, (ii) temperaturabhängige Renormalisierungseffekte der $B_{3u}(1)$ Phononenfrequenz, die eindeutig von der temperaturabhängigen Frequenz des Elektromagnons beeinflusst wird und (iii) eine asymmetrische Linienform der $B_{3u}(1)$ Mode, die in den Transmissionsspektren von [SML$^+$11] an $GdMnO_3$ gesehen werden kann. Diese Asymmetrie der spektralen Linienform konnte mit Hilfe eines Fano–Profils zweier gekoppelter Elementaranregungen in den ϵ_2 Spektren sehr gut reproduziert werden.
Des Weiteren wurden diese Resultate mit den experimentellen Daten der dotierten $Eu_{1-x}Y_xMnO_3$ Serie (x = 0, 0.2, 0.5) verglichen. Bereits bei den zuvor diskutierten Raumtemperaturspektren war eine Verminderung der dipolaren Aktivität von $B_{1u}(1)$ und $B_{3u}(1)$ zu sehen, was auf die Dotierung zurückgeführt werden kann. Zusätzlich führten im Fall von $Eu_{0.8}Y_{0.2}MnO_3$ experimentelle Schwierigkeiten dazu, dass für $Eu_{1-x}Y_xMnO_3$ mit $x > 0$ keine verlässlichen Daten bezüglich der Frequenzverschiebungen von $B_{3u}(1)$ aufgenommen werden konnten. Die restlichen Moden zeigen jedoch das vom zuvor eingeführten Modell erwartete Verhalten. Zusätzlich ist auf Grund von Literaturspektren [TYK$^+$09], die den Transfer von spektralen Gewicht deutlich zeigen, dieser Aspekt von EMPC klar nachgewiesen und damit in Kombination mit den eigenen experimentellen Ergebnissen die analoge Existenz von EMPC im dotierten $Eu_{1-x}Y_xMnO_3$ System erwiesen.

Fazit

Die systematische Untersuchung der temperaturabhängigen Kristallgitterdynamik der multiferroischen Manganate zeigte zwei markante Kopplungseffekte: SPC und EMPC. Die verschiedenen Abhängigkeiten der beiden konnten anhand von Modellen erklärt werden, die auf der dynamischen Modulation des magnetischen Austauschs durch die Gitterschwingungen beruhen. Beide Effekte lassen sich klar voneinander trennen durch explizites Einbeziehen der Verschiebungsmuster, der optischen Auswahlregeln und der Frequenzen der verschiedenen Phononen. Die vorliegende Dissertation kann daher die enge Kopplung von Kristallgitterdynamik und Magnetismus in den multiferroischen Manganaten auf mikroskopischer Ebene systematisch belegen.

Contents

Chapter 1

Introduction

Understanding and applications of multifunctional materials are one of the main goals of scientific efforts in solid state physics today. In most cases the existence of intrinsic coupling effects on mesoscopic or even microscopic scale – ideally within a single material – is the foundation of this multifunctionality. The latter is one of the key properties required for information technology, that goes beyond the current state of the art primarily based on the miniaturisation of integrated semiconductor devices. Slogans for such new technologies are e.g. *"Spintronics"*, i.e. using the spin polarisation of electric current for information technology [WAB$^+$01], or *"Magnonics"*, i.e. the employment of spin waves to carry and process information [KDG10]. Therefore, one of the "hot topics"in solid state physics is the systematic investigation of materials, that incorporate coupling effects between different degrees of freedom such as electronic or magnetic ones.
Among these material classes are the so–called *"Multiferroics"*. These are defined as materials, in which two or more kinds of fundamental ferroic properties coexist. Generally, in a crystalline solid ferroic properties are characterised by the occurrence of a spontaneous symmetry breaking. Prominent examples for such behaviour are ferromagnetism, ferroelectricity or ferroelasticity. Further, antiferromagnetism is also included in this definition. It is immediately clear, that the coexistence of these ferroic properties can be crucial for a lot of different novel applications, e.g. for the storage of information or sensor applications. To illustrate the relevance of multiferroism for the recent investigative efforts in the field of Spintronics and Magnonics, the control of spin waves by an electric field in the multiferroic compound $BiFeO_3$ by Rovillain et al. [RdSG$^+$10] is a good example. Their results show a very elegant way to store information without dissipation in the spin waves of such a multiferroic material utilising the multiferroic behaviour of magnetic and electric degrees of freedom.
The investigative efforts concerning the coupling between ferroelectricity and (anti–)ferromagnetism reach back far beyond the recent "revival", as it is called by M. Fiebig [Fie05]. In these older studies, the coupling of these two ferroic properties is known as the *"Magneto–Electric Effect"*. In order to appreciate the current state of knowledge concerning the multiferroic materials, the historic development of the research activity on these materials will be presented in very short form in the following.

Multiferroism a.k.a. the Magneto–Electric Effect

First predicted theoretically in the year 1894 by P. Curie [Cur94], it took more than fifty years until the Magneto–Electric Effect (ME–Effect) could be experimentally confirmed in Cr_2O_3 in 1960 [Ast60]. This finding triggered a first research boom in the 1970s. In 1974, V.E. Wood et al. listed several potential applications for materials showing the ME–Effect [WA74]. However, at this time only very few such materials could be found. According to N. A. Hill [Hil00], this can be understood by the fact, that conventional ferroelectricity occurs in the presence of empty d–shells within the transition metals, while (anti-)ferromagnetism favours partially filled d–shells. Thus, only materials with unconventional mechanisms for ferroelectricity can show ME–Effects.
In 2003, Kimura et al. [KGS+03] found the "*Giant Magneto–Electric Effect*" in the model system of the rare earth manganite $TbMnO_3$, where the ferroelectric polarisation could be switched by applying an external magnetic field. A revival of the ME–Effect followed and a lot of other materials were found that showed intrinsic ME–Effects, e.g. $HoMnO_3$ [FLF+02] or $Ni_3V_2O_8$ [LHK+05]. A few years before, the generic term *"Multiferroics"* was given by Schmid et al. for these materials [Sch94]. As already discussed, this term also includes materials with other ferroic properties (examples are given above) and further antiferromagnetism, thus broadening the field for potential research activities.
Apart from the coupled static properties, multiferroic materials show new elementary excitations. In the case of ME–Coupling it was predicted, that magnons, as elementary excitations of the magnetic ordering, should gain dipolar activity via the ME–Effect and, thus, should be observable by optical spectroscopy due to their contribution to the dielectric function. These excitations were then called "Seignette magnons". In 2006 their existence was experimentally proven by Pimenov et al. in the Rare–Earth Manganites $GdMnO_3$ and $TbMnO_3$ employing optical spectroscopy in the Terahertz range and termed *Electromagnons* [PMI+06]. Subsequently, an intimate coupling between Electromagnons and low–frequency polar phonons in $GdMnO_3$ could be demonstrated by the application of an external magnetic field [PRM+06] as well as by temperature dependent studies in the doped rare earth manganite series $Eu_{1-x}Y_xMnO_3$ [TYK+09]. This coupling was primarily indentified as a shift of spectral weight between these two excitations.
On the other side, due to the intimate coupling between lattice, electronic and spin degrees of freedom in this model system, there are other coupling effects observable by optical and Raman spectroscopy, with the most prominent being the coupling between high–frequency polar or unpolar phonon modes and the magnetic exchange within the equatorial MnO_2 plane of the perovskite $RMnO_3$ system [GGS+99, LJM+06]. This effect was termed *"Spin–Phonon Coupling"*. The rich field of potential coupling mechanisms led to various – sometimes even contradicting – interpretations of such effects often relating them to multiferroic behaviour – with some being questionable, e.g. [SHV+08] contradicting [RCG+10] or [FMA+09] and [MAF+10] compared to [IPI+10a] and [IPI+10b].
However, no systematic investigation of these coupling effects has been carried out on all experimentally accessible phonon modes. Only a systematic and complete study of the coupling effects between lattice dynamics and magnetism can provide the ground for a

clear and unambiguous analysis of these material properties within the Rare–Earth Manganites. Such an investigation would also give the opportunity to pay special attention to the mode symmetries and their influence on the mentioned coupling effects. Carrying out a systematic and complete study is therefore the motivation and starting point for this thesis.

Scope and organization of this thesis

The scope of this thesis is the systematic investigation of coupling effects of lattice dynamics and magnetism in the model system of the Multiferroic Manganites $RMnO_3$. The employed experimental techniques are optical and Raman Spectroscopy. The model system, that is chosen for this study, are the Multiferroic Manganites $RMnO_3$, that crystallise in the Pnma structure with orthorhombic unit cell. Due to crystalline symmetry, both employed spectroscopical techniques are complementary and together they allow a systematic investigation of all optically active lattice vibrations. The study of the coupling effects is carried out by temperature dependent spectroscopic measurements to probe for renormalisation effects occurring at magnetic phase transitions.
The investigated model system of the Multiferroic Manganites are in fact two series of Rare–Earth Manganites, whose crystalline properties and with it the magnetic behaviour can be tuned via decreasing the Rare–Earth ionic radii R^{3+}. For the measurements carried out within this thesis, the R^{3+} radii were tuned by two different approaches. The starting point for both series was the non–multiferroic $EuMnO_3$. While in one sample series the Eu^{3+} were completely replaced by Gd^{3+} or Tb^{3+}, in the other series a doping approach was followed, i.e. a partial substitution of Eu^{3+} by Y^{3+}. This gives the additional opportunity to compare both approaches concerning the impact on the lattice dynamics and its coupling effects to magnetism.
In consequence to this scope, the thesis is organised as follows: part I deals with all fundamental and theoretical parts important for the understanding of the following discussions. First, the physically relevant basics of the employed spectroscopical techniques, i.e. Raman and Fourier–Transform Infrared (FT–IR) Spectroscopy, will be introduced in section 2. In section 3, this will be followed by a systematic discussion of the static crystalline, magnetic and multiferroic properties of the Rare–Earth Manganites $RMnO_3$. The lattice dynamics will be highlighted in section 4 with special emphasising the optical selection rules and the corresponding specific vibrational properties, that can be selectively probed by employing polarisation dependent Raman and FT–IR Spectroscopy. Further, in this section the mode patterns obtained from Density Functional Theory based ab–initio calculations will be presented. The last section of part I presents the current state of the understanding of the coupling effects between lattice dynamics and magnetism to be experimentally investigated in part II.
Said part II begins with section 6, where the room temperature Raman and FT–IR measurements are utilised for a complete characterisation of the lattice dynamics of both sample series. This way, a complete picture of the crystalline properties of the series is

obtained without coupling effects. It is therefore possible, to compare both R^{3+} tuning approaches concerning their impact on the crystalline quality and the lattice vibrations. This will be followed in section 7 by a systematic investigation of the coupling between polar as well as unpolar lattice vibrations and the magnetic exchange (Spin–Phonon Coupling). A second coupling effect between the low–frequency polar phonons and the Electromagnons (Electromagnon–Phonon Coupling) of the $RMnO_3$ system will be dealt with in section 8. A conclusion and outlook summarises the gained insights into the correlation effects between lattice dynamics and magnetism present in the Multiferroic Manganites in section 9.

Part I

Theory

Chapter 2

Spectroscopical techniques

Spectroscopy as a technique of investigation is a very powerful and non–destructive method allowing deep insights into the physical properties of solid state materials. For this thesis two prominent spectroscopical techniques are used to probe the lattice vibrations of crystalline solid state materials and their coupling to magnetic properties: Raman Spectroscopy and Fourier–Transform Infrared (FT–IR) Spectroscopy. In solid state physics quantised lattice vibrations accessible for optical spectroscopy are called *optical phonons*. The term optical phonons is used to distinguish them from acoustic phonons, which will be not further discussed here. The investigation of phonons can be used to gather information about chemical composition, state of order or disorder within a crystal or their possible coupling to other order parameters (e.g. the magnetic structure).
In solid state crystalline materials optical phonons usually occur in the far infrared region of the spectrum. Roughly speaking, their energy is in the range from $\approx 1meV$ to $255meV$. Table 2.1 gives a list of the conversion factors of the most commonly used physical units in optical spectroscopy. In the following we will deal with two spectroscopical techniques in which the energy is usually denoted in wave number $[\widetilde{\nu}] = cm^{-1}$. It is defined as $\widetilde{\nu} = \nu/c$ where ν is the frequency and c the speed of light. Thus, the spectral range of optical phonons reaches from ≈ 10 to 2000 cm^{-1}.

In the next two sections the fundamental principles of Raman Spectroscopy and FT–IR Spectroscopy will be introduced in this order. The techniques are underscored by theoret-

Table 2.1: Conversion factors for the various scales employed for spectroscopy, extracted from [HW03]

	E [meV]	f [THz]	λ [mm]	$\widetilde{\nu}$ [cm^{-1}]
E [meV]	1	0.24	$1.24/E$	8.07
f [THz]	4.14	1	$0.30/f$	33.4
λ [mm]	$1.24/\lambda$	$0.30/\lambda$	1	$10.0/\lambda$
$\widetilde{\nu}$ [cm^{-1}]	0.12	0.03	$10.0/\widetilde{\nu}$	1

ical considerations as far as it is needed for an understanding of the experimental results within this thesis.

2.1 Raman Spectroscopy

Raman Spectroscopy is based on the analysis of inelastically scattered light, which goes along with the generation or annihilation of a quasi–particle. Examples for such quasi-particles are elementary excitations of the lattice (phonons), the spin structure (magnons), collective oscillations of the free electron density (plasmons) or even electronic excitations [Kuz98]. In this thesis optical phonons are investigated in the Raman experiments, thus only these will be regarded further.

In a Raman experiment the spectral distribution of the scattered light is analysed relative to the position of the elastically scattered light. The interaction of the incident photons with the investigated material leads to the creation or annihilation of optical phonons and, thus, to an energy loss or gain of the scattered photons, respectively. It manifests itself in the appearance of red– (lower energy) or blue–shifted (higher energy) lines with respect to the Laser line in the spectrum of the scattered light. These shifts are called Stokes and Anti–Stokes shift, respectively. Figure 2.1 shows a schematic Raman spectrum comprising both kinds of the aforementioned shifts. The intensity ratio between Stokes and Anti–Stokes shift is essentially determined by the thermal occupation of the phonon states. Thus, without going into details, one can state, that at cryogenic temperatures

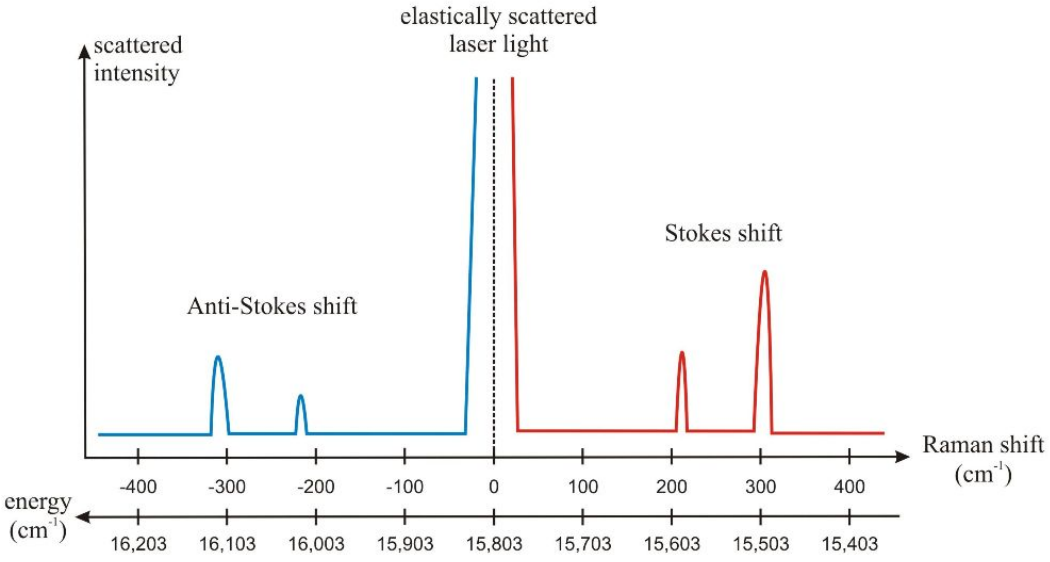

Figure 2.1: Schematic Raman spectrum obtained with the Laser line of a Helium-Neon Laser (wavelength $\lambda = 632.8nm$) as light source. The scattered intensity is plotted versus the relative frequency shift with respect to the elastically scattered Laser line at 0 cm^{-1}. The lower x-axis shows the absolute energy – also in wave number. As indicated in the figure, the intensity of the elastically scattered Laser light is several orders of magnitude larger than the Raman signals.

($T \ll 300K$) the intensity of the Anti–Stokes shifted photons tends to be lower than that of the Stokes–shifted photons (as indicated in figure 2.1) due to the thermal distribution, which reflects the higher probability for a phonon creation than for an annihilation. Within this thesis the Raman spectra are investigated in the temperature range from room temperature down to T = $10K$. In the following, we will therefore restrict ourselves to the Stokes shifted Raman signals.
The information that can be directly extracted from a Raman spectrum are phonon frequency, linewidth and intensity (i.e. the scattering cross section). Depending on the sample system various physical properties can be deduced from these quantities. Some of these were listed at the beginning of this chapter.
As can be seen in figure 2.1, the inelastically scattered Raman signals are rather weak. Thus, the experimental requirements for a Raman setup concerning e.g. stray light rejection or spectral resolution are rather strict. The configurations of the Raman setups used for the experiments of this thesis are described in detail in Appendix A.

Fundamentals of Raman scattering

The base for any Raman process in a crystal is the modulation of the dielectric susceptibility χ by the excited quasi–particles. In contrast to Infrared Spectroscopy – which will be discussed in the next section – the change of the response function χ is important for the observability of a lattice vibration within a Raman experiment and not the dielectric polarisation induced by the vibronic oscillator. The most simple model for an understanding of the principle of the Raman effect – the picture of a two–atom molecule – leads to the following considerations, according to [Kuz98]:
In a general case, when applying an electric field $\boldsymbol{E}(\omega)$ to a molecule, the polarisability $\overline{\alpha}$ would need to be considered. This polarisability $\overline{\alpha}$ would be determined by the concrete scattering configuration. It would, thus, be an admixture of the polarisabilities $\alpha_{\parallel}$ and $\alpha_{\perp}$, i.e. parallel and perpendicular to the molecule's principal axis, respectively. In our case, we will consider an exemplary value of $\overline{\alpha} = \alpha_0$. The mentioned electric field leads to a dipole moment $P_D(\omega) = \alpha_0 E_(\omega)$ which is the source of an electromagnetic wave in the scattering process. Now if the molecule oscillates with frequency Ω, the distance between the atoms changes periodically and the polarisability will be modulated. The total dipole moment reads:

$$\boldsymbol{P}_D(\omega) = (\alpha_0 + \alpha_1 \cos \Omega t)\, \boldsymbol{E}_0 \cos \omega t. \tag{2.1}$$

With the application of trigonometric sum rules this can be expressed as:

$$\boldsymbol{P}_D(\omega) = \alpha_0 \boldsymbol{E}_0 \cos \omega t + \left(\frac{\alpha_1 \boldsymbol{E}_0}{2}\right) \left[\cos\left(\omega + \Omega\right) t + \cos\left(\omega - \Omega\right) t\right]. \tag{2.2}$$

What can be clearly seen is that, beside the oscillation frequency ω of the incident electromagnetic wave, there are additional sidebands with frequencies $\omega \pm \Omega$.

For crystalline solid state materials this simple model needs to be adapted [Kuz98]. Therefore a non–isotropic periodic structure is assumed. The scalar polarisability α is replaced by the second–rank dielectric susceptibility tensor χ_{jl} and the simple movements of atoms within the molecule by the normal coordinates Q_k of the lattice vibrations. That way, χ_{jl} can be expanded with respect to Q_k:

$$\chi_{jl} = (\chi_{jl})_0 + \sum_k \left(\frac{\partial \chi_{jl}}{\partial Q_k}\right)_0 Q_k + \sum_{k,m} \left(\frac{\partial^2 \chi_{jl}}{\partial Q_k \partial Q_m}\right)_0 Q_k Q_m + \dots \tag{2.3}$$

The sums run over all normal coordinates k and m, $\partial\chi_{jl}/\partial Q_k$ is a component of the aforementioned polarisability tensor and is called *Raman tensor*. It is denoted as $\chi_{jl,k}$. The tensor has three indices: j and l are the indices for the coordinates 1 to 3 and k runs over all $3N-3$ optical phonon modes. Thus, $\chi_{jl,k}$ is a tensor of rank three and for each individual mode given by a 3×3 matrix. In analogy to equation (2.1) the Raman tensor can be expressed with respect to the vibration–induced polarisation by restricting the Taylor expansion of equation (2.3) to linear order:

$$\chi_{jl} = (\chi_{jl})_0 + (\chi_{jl,k})_0 Q_k \quad with \quad Q_k = Q_{k0} \cos \Omega_k t. \tag{2.4}$$

What we get now, is an expression for the induced dipole moment within a crystal:

$$P^s_{Dj}(\omega \pm \Omega_k) \propto \chi_{jl,k} E^i_{l0} Q_{k0} \cos(\omega \pm \Omega_k) t. \tag{2.5}$$

This equation gives a qualitative understanding how the Stokes and Anti–Stokes shifted sidebands in the spectrum of the scattered light can occur.
The next step is to choose an explicit scattering geometry, which in this thesis is strongly influenced by symmetry properties of the investigated sample series and the resulting selection rules. For a detailed discussion of the symmetry properties of the investigated samples the reader is referred to section 3.1 for static symmetry aspects and to chapter 4 for symmetry aspects of the lattice vibrations.
For the characterisation of the scattering geometry within a Raman experiment the directions of the incident and scattered light ($\boldsymbol{k}_i$ and $\boldsymbol{k}_s$) as well as their polarisations ($\boldsymbol{e}_i$ and $\boldsymbol{e}_s$) need to be considered either. In Raman Spectroscopy there is a very convenient way to describe these directions in a compact way, according to [YC01], as:

$$\boldsymbol{k}_i \, (\boldsymbol{e}_i, \boldsymbol{e}_s) \, \boldsymbol{k}_s. \tag{2.6}$$

This notation is known as *Porto's notation* and contains all information concerning the geometry of the Raman scattering experiment.
The quantitative calculation of Raman scattering intensities is a very difficult task and in most cases it is sufficient to check, which components of the Raman tensor are nonzero. If we assume that the scattering intensity is proportional to the square of the dipole moment P^s_D, it is – for a given mode k and for specific direction of $\boldsymbol{e}_s$ – given by the absolute square of the projection of the P^s_D on $\boldsymbol{e}_s$ [Kuz98, YC01] as:

$$I_s \propto C \, |\boldsymbol{e}_s \boldsymbol{P}^s_D|^2 = C \left| \sum_j e_{sj} P^s_{Dj}(k) \right|^2 , \tag{2.7}$$

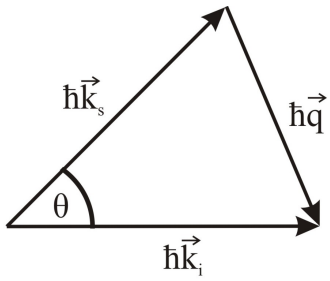

Figure 2.2: Momentum conservation for a Raman process with the generation of a phonon. $\boldsymbol{k}_i$ and $\boldsymbol{k}_s$ are the wave vectors of the incident and scattered photons and $\boldsymbol{q}$ that of the phonon, respectively.

where P^s_{Dj} and e_{sj} are the components of the dipole moment induced by the Raman effect and the components of the polarisation direction of the scattered light, respectively. With equation (2.5) the induced dipole moment in the general case for a non–specific polarisation can be further evaluated, if the polarisation of the incident light $\boldsymbol{e}_i$ is also considered. This is easily done by inserting e_{il} in equation (2.5). Thus, for a general scattering geometry the scattering intensity is:

$$I_s \propto C' \left| \sum_{j,l} e_{sj} \chi_{jl,k} e_{il} \right|^2 E_0^2. \tag{2.8}$$

Quantum–Mechanical considerations

The above discussed classical formulation of the scattering process can be transformed in a quantum–mechanical picture [Kuz98, YC01]. In that case, the scattering geometry is determined by the quasi–momentum conservation as shown in figure 2.2. It is denoted as quasi–momentum, because the wavevector of a phonon is determined unambiguously only within the first Brillouin zone.
The Stokes and Anti–Stokes shifts are explained as an emission or absorption of a phonon by the light wave together with the simultaneous conservation of energy. The two conservation rules (energy and momentum) are expressed as follows within the first Brillouin zone:

$$\hbar\omega_i = \hbar\omega_s \pm \hbar\Omega \tag{2.9}$$

$$\hbar\boldsymbol{k}_i = \hbar\boldsymbol{k}_s \pm \hbar\boldsymbol{q}. \tag{2.10}$$

The indices i and s refer to incident and scattered light, respectively. + corresponds to phonon generation and − to phonon annihilation. Given the values of k_i and k_s ($\approx 2 \cdot 10^4 cm^{-1}$), which correspond to the wavelength of visible light ($\lambda \approx 500nm$), the wavevector of the phonon q has a maximum value for 180° backscattering geometry of

$$q_{max} = k_i + k_s \approx 2k_i. \tag{2.11}$$

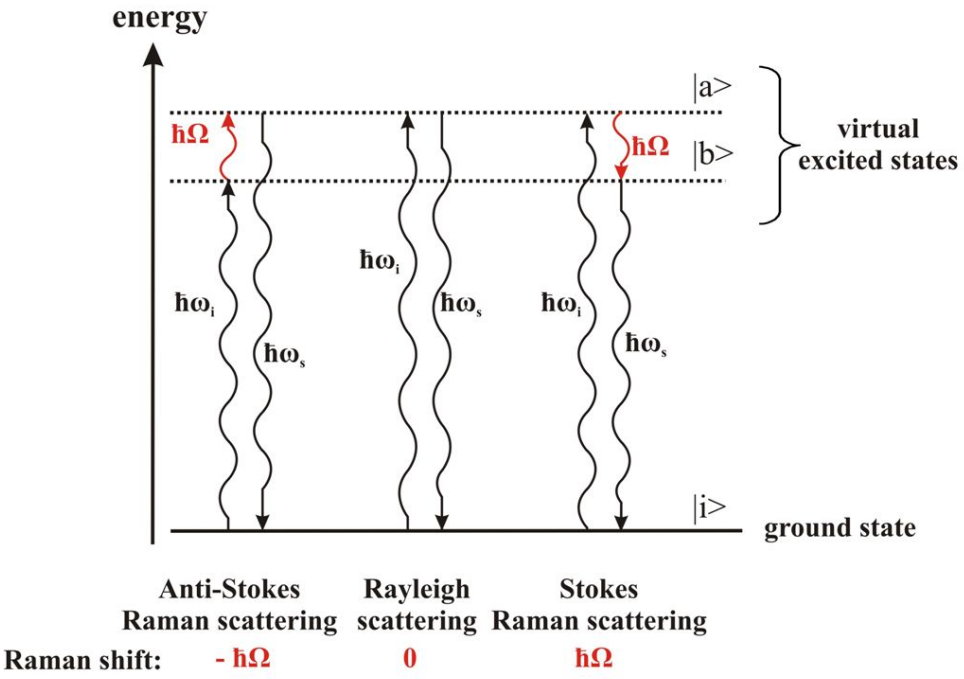

Figure 2.3: Energy level diagram for the various types of Raman scattering processes.

Compared with the maximum k–values of the Brillouin zone of $\approx 2 \cdot 10^7 cm^{-1}$ for a lattice constant a of $\approx$ 5Å, which are a factor $\approx 10^3$ larger, one can deduce that Raman scattering with visible light only occurs for phonons from the centre of the Brillouin zone. This corresponds to $\boldsymbol{q} \approx 0$. Thus, the ambiguity of the quasi–momentum conservation for larger pseudo wavevectors mentioned before is omitted.

How can the Raman scattering process be understood in a quantum–mechanical picture? According to [YC01], three systems need to be considered for describing the microscopic process of inelastic light scattering: (i) incident and scattered photons with energy $\hbar\omega_i$ and $\hbar\omega_s$, respectively, (ii) electrons within the material, and (iii) the phonon with energy $\hbar\Omega$. The possibilities for realising such a scattering process are depicted in figure 2.3.
In the following, we will restrict ourselves to Stokes scattering. The electronic ground state acts as initial and final state $|i\rangle$ as illustrated in figure 2.3. For the quantum–mechanical picture of the Raman process the excitation of a ground state electron in $|i\rangle$ by a photon $\hbar\omega_i$ into the intermediate state $|a\rangle$ is anticipated. What follows, is a transition from $|a\rangle$ to $|b\rangle$, which goes along with the emission of a phonon with energy $\hbar\Omega$. Since energy and momentum conservation holds, the transition to the final state $|i\rangle$ leads to the emission of a photon with the energy $\hbar\omega_s$ ($\omega_s < \omega_i$).
For a formulation of the scattering probability within a quantum–mechanical perturbation approach the interactions of the Raman process outlined above have to be collected for all possible permutations of the time order. A very instructive way to do this, are Feynman diagrams. Figure 2.4 shows one possible realisation of the Stokes Raman scattering process. The diagram should be read starting from the left: an incident photon creates

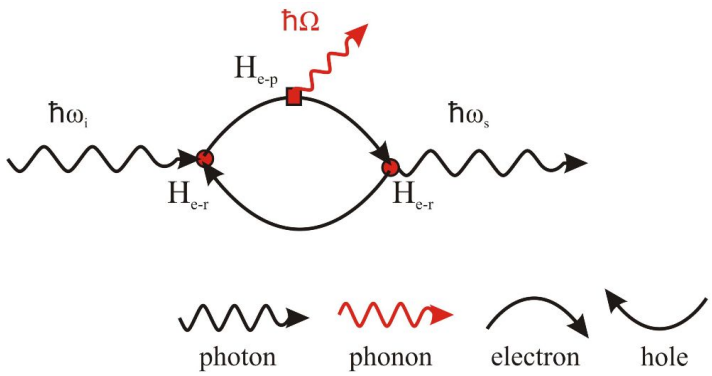

Figure 2.4: Feynman diagram for the Stokes Raman process. There are three possibilities for the permutation of the time order of the three vertices participating in this three–step process. Adapted from [YC01].

an electron–hole pair via the electron–radiation interaction described by the Hamiltonian H_{e-r}. An intermediate state is obtained, where a phonon is emitted by the electron–phonon interaction H_{e-p}, and finally the electron–hole pair recombines (again described by H_{e-r}) with a simultaneous emission of a photon with different energy and momentum. The other possibilities are obtained by permutation of the time order of the three vertices (H_{e-r}, H_{e-p}, and again H_{e-r}) [YC01].
The next step, after drawing these diagrams, is the formulation of the probability of these scattering processes. As we are dealing with a three–step process, perturbation theory of third order is required. This probability is derived from the Feynman diagrams via Fermi's Golden Rule. This is carried out in [YC01] for the process depicted in figure 2.4 leading to this expression for the scattering probability:

$$P_{ph}\left(\omega_s\right) = \frac{2\pi}{\hbar}\left|\sum_{a,b}\frac{\langle i|\, H_{e-r}\left(\omega_s\right)|b\rangle\,\langle b|\, H_{e-p}\,|a\rangle\,\langle a|\, H_{e-r}\left(\omega_i\right)|i\rangle}{\left[\hbar\omega_i - \hbar\Omega - \left(E_b - E_i\right)\right]\left[\hbar\omega_i - \left(E_a - E_i\right)\right]}\right|^2 \delta\left[\hbar\omega_i - \hbar\Omega - \hbar\omega_s\right]. \tag{2.12}$$

The three terms in the numerator denote the three vertices of interaction shown in figure 2.4. The sum runs over all intermediate states $|a\rangle$ and $|b\rangle$. One would expect also three terms in the denominator in analogy to the three terms of the numerator. However, the last energy term of the denominator would simply represent the energy conservation for the whole three–step process. Thus, it is converted to the δ–function $\delta\left(\hbar\omega_i - \hbar\Omega - \hbar\omega_s\right)$. For a general expression all permutations need to be summed up, as discussed before. This gives a lengthy expression without new physical aspects. We will avoid it here for reasons of brevity.

Equation (2.12) suggests that, beside the information about phonon frequency and phonon linewidth, also information about the scattering cross section can be extracted. As shown in figure 2.4, the interaction strength between light and electron (H_{e-r}) as well as the interaction between electron and phonon (H_{e-p}) also contribute to the scattering

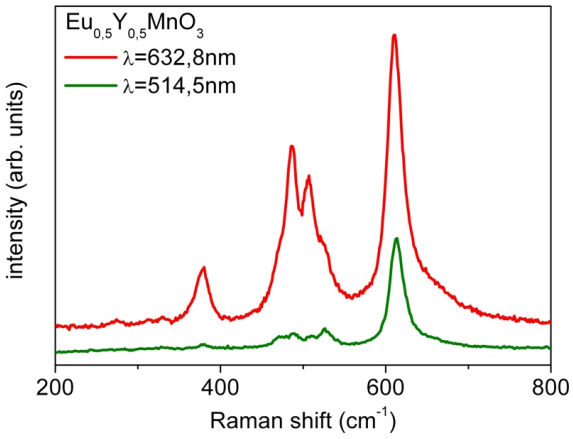

Figure 2.5: Raman spectra of $Eu_{0.5}Y_{0.5}MnO_3$ recorded with identical integration time and Laser power, but with different wavelengths of the exciting Laser light .

strength of the Raman process. Thus, information about these quantities, which can give insights into the electronic structure of the investigated material, could in principle be deduced from the quantitative scattering cross section. However, this task is almost impossible, because of the large number of intermediate states one has to sum up in equation (2.12). Within this thesis solely information about phonon frequency and linewidth are therefore considered.
Nevertheless, there is one aspect of the dependence of the transition probability on the electronic states of the investigated system, which needs a short discussion. In figure 2.3 the excited states are referred as virtual states, which means that they are no Eigenstates of the system. Now what happens, if the excitation energy $\hbar\omega_i$ is tuned, so that one of the excited electronic states $|a\rangle$ or $|b\rangle$ coincides with an Eigenstate? In that case the transition probability in equation (2.12) diverges leading to a resonant enhancement of the Raman scattering reflecting the larger lifetime of the Eigenstate compared to the virtual state [Kuz98].
Nice examples for this behaviour are the Raman spectra shown in figure 2.5. These are recorded with different excitation wavelengths ($\lambda = 514.5\ nm$ and $\lambda = 632.8\ nm$) on an arbitrarily chosen sample within the investigated Manganite series. All other experimental parameters are identical. The spectrum recorded with $\lambda = 632.8\ nm$ shows a resonant enhancement, which is attributed to an electronic Mn d–d transition characteristic for the Manganites [KSN+04].

2.2 Fourier–Transform Infrared Spectroscopy

The second spectroscopical technique employed in this thesis is Fourier–Transform Infrared (FT–IR) Spectroscopy. In clear contrast to Raman Spectroscopy, FT–IR is a non–dispersive or interferometric method. This means, the signal is not dispersed into its

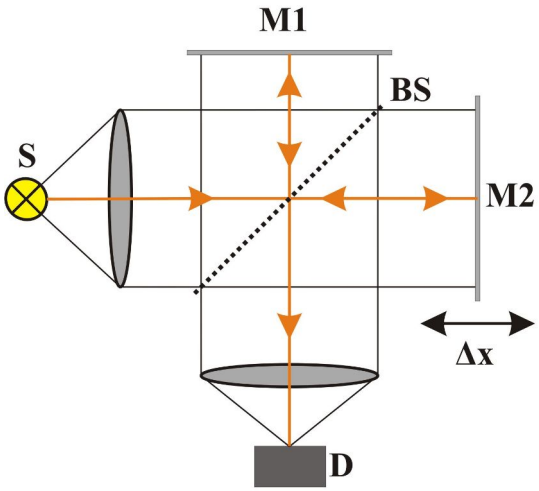

Figure 2.6: Schematic drawing of a Michelson interferometer. **S** is the source of infrared radiation, **BS** the beam splitter, **M1** the stationary mirror, **M2** the mobile mirror, and **D** the radiation detector.

spectral components for detection. On the contrary, the whole spectral range (within a given part of the spectrum) is detected simultaneously and decomposed by the means of a Fourier transformation yielding a frequency–dependent spectrum. The basic principle of FT–IR can be illustrated in the most instructive way by discussing it for the case of the Michelson Interferometer.

The interferometric principle

Figure 2.6 shows a schematic sketch of a Michelson interferometer. Radiation from the source **S** is split into two parts by the beam splitter **BS**. The first part is reflected from the stationary mirror **M1**, while the second part is reflected from the mobile mirror **M2**. After recombination at the **BS** an interference of the two partial beams is obtained, which depends on the position x of **M2**. Usually only the partial beam propagating to the detector **D** is employed for spectroscopic investigations. As stated before, a shift of the mobile mirror **M2** causes a path difference Δx between the two partial beams and, thus, interference fringes in the recombined beam recorded with **D**. The intensity of the radiation with respect to Δx of the two mirrors **M1** and **M2** is called *interferogram* $I(x)$. It contains all spectral information of the radiation source.
The simplest example for an interferogram is that of monochromatic light (e.g. Laser–light). As can be seen in figure 2.7(a) the detected signal has the form

$$I(x) = I_0 \left[1 + cos\left(2\pi\widetilde{\nu}\Delta x\right)\right] \tag{2.13}$$

with I_0 as the maximum intensity of the partial beam at the detector. Equation (2.13) can be understood very easy by analysing the phase shift of the partial beams. For $\Delta x = 0$ the two paths lengths are equal and constructive interference occurs at **D**. Now if

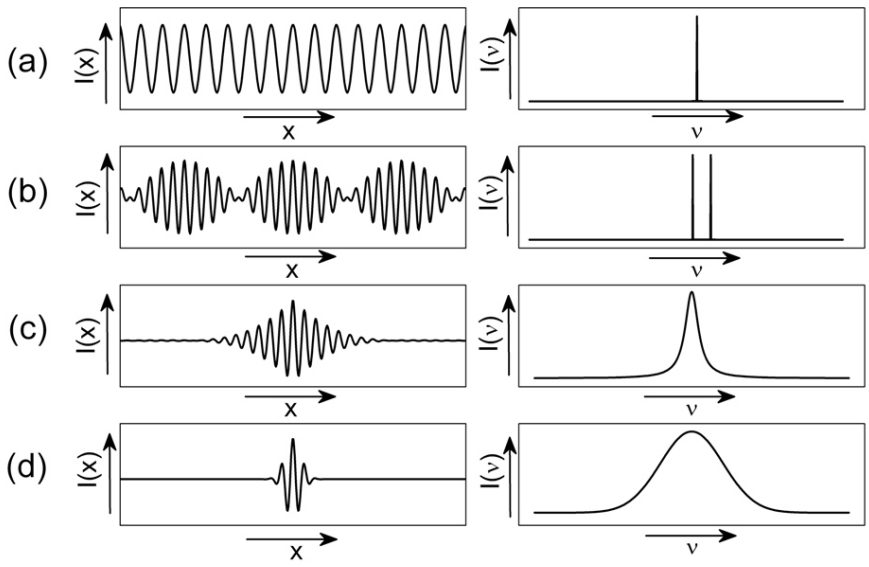

Figure 2.7: Examples for interferograms $I(x)$ and their corresponding spectra $I(\widetilde{\nu})$ obtained by a Fourier transformation of $I(x)$. The examples show (a) monochromatic light, (b) light with two discrete wavelengths, (c) a Lorentzian peak with a relative small linewidth compared to (d) a Gaussian peak with large linewidth.

M2 is shifted by $\lambda/4$, the resulting path difference $\Delta x = \lambda/2$ and the beams interfere in a destructive way. Thus, for a motion with constant velocity of **M2** a cosine–function for $I(x)$ is obtained.
The generalisation to arbitrary signals can be carried out by adding discrete wavelengths, which each contribute a cosine-function to $I(x)$. Figure 2.7(b) shows the example for two discrete wavelengths leading to a beat in $I(x)$. For broadband signals the intensity decays rather fast for varying Δx, examples are shown in figure 2.7(c) and (d). In all discussed cases the spectrum $I(\widetilde{\nu})$ can be obtained by a Fourier Transformation of the interferogram $I(x)$:

$$I\left(\widetilde{\nu}\right) = \int_{-\infty}^{\infty} I\left(x\right) cos\left(2\pi\widetilde{\nu}x\right) dx, \tag{2.14}$$

where we have replaced Δx by dx.
The employed FT–IR setup, which is not as straightforward as the Michelson Interferometer, is shown in detail in Appendix A. Nevertheless it uses the method just introduced to obtain a spectrum $I(\widetilde{\nu})$. In an infrared spectroscopic experiment, a sample is introduced between **BS** and **D**. Depending on their optical thickness it is more convenient to measure the intensity of the reflected (I_R) or the transmitted (I_R) beam or both. The samples, that are investigated within this thesis, are opaque crystals with a macroscopic thickness (d $\geq 1\ mm$). Thus, only reflectivity measurements are carried out. In the next paragraph the basics of the measured physical quantity reflectivity will be discussed, according to [Kit02].

Reflectivity and index of refraction

The reflection of light with a frequency ω is physically treated by introducing a complex reflection coefficient $\widehat{r}(\omega)$. It can be defined as the ratio between the electric field of the incident light, E_0, and the electric field of the reflected light, E_R. As a complex function, it can be written as

$$\widehat{r}(\omega) = \frac{E_R}{E_0} = \sqrt{r(\omega)}e^{i\phi(\omega)} \tag{2.15}$$

where $r(\omega)$ is determined by the amplitude and $\phi(\omega)$ by the phase of the electric field of the light wave. For perpendicular reflection, $\widehat{r}(\omega)$ has the following connection to the complex index of refraction $\widehat{n}(\omega) = n(\omega) + i\kappa(\omega)$:

$$\widehat{r}(\omega) = \frac{\widehat{n} - 1}{\widehat{n} + 1} = \frac{n(\omega) + i\kappa(\omega) - 1}{n(\omega) + i\kappa(\omega) + 1}. \tag{2.16}$$

$n(\omega)$ denotes the real part and $\kappa(\omega)$ the imaginary part of $\widehat{n}(\omega)$. The index of refraction is on the other side linked to the complex dielectric function $\epsilon(\omega) = \epsilon_1 + i\epsilon_2$ by:

$$\widehat{n}(\omega) = \sqrt{\epsilon(\omega)}. \tag{2.17}$$

The real and imaginary part of $\epsilon(\omega)$ in terms of $n(\omega)$ and $\kappa(\omega)$ are therefore:

$$\epsilon_1 = n^2 - \kappa^2 \tag{2.18}$$

$$\epsilon_2 = 2n\kappa. \tag{2.19}$$

With these definitions, the quantity measured within a FT–IR experiment – the reflectivity R – can be expressed as a function of the complex $\widehat{r}(\omega)$. R is defined as the intensity ratio of incident and reflected light:

$$R = \frac{I_R}{I_0} = \frac{E_R^* E_R}{E_0^* E_0} = \widehat{r}^*(\omega)\widehat{r}(\omega) = |r(\omega)|^2. \tag{2.20}$$

The reflectivity contains only information about the real part of $\widehat{r}(\omega)$ and, thus, the amplitude of the light wave. For a complete determination of the dielectric function $\epsilon(\omega)$, $\widehat{r}(\omega)$ and $\phi(\omega)$ are needed. Employing the Kramers–Kronig–Relation, $\phi(\omega)$ can be obtained. This will be discussed in the next paragraph.

Kramers–Kronig–Relation

The Kramers–Kronig–Relation (KKR) is connecting the real and imaginary part of a complex response function (e.g. the dielectric function $\epsilon(\omega)$). It can be employed to deduce one part of such a function, if the other part is measured or reasonably extrapolated over a wide range of frequencies. Thus, the KKR for the complex reflection coefficient $\widehat{r}(\omega)$ can obtained through its connection with $\epsilon(\omega)$ in equation (2.16) and equation (2.17).
For the reflection coefficient it is convenient to rewrite equation (2.15) to $\ln \widehat{r}(\omega) =$

$\ln\sqrt{r(\omega)} + i\phi(\omega)$. According to [Kuz98], the phase $\phi(\omega)$ is connected to the amplitude $r(\omega)$ via

$$\phi(\omega_0) = -\frac{\omega_0}{\pi}\int_0^\infty \frac{\ln\sqrt{r(\omega)} - \ln\sqrt{r(\omega_0)}}{\omega^2 - \omega_0^2} d\omega. \tag{2.21}$$

This means, a measurement of R and its connection to $r(\omega)$ via equation (2.20) can be used to determine the phase $\phi(\omega)$, and, in turn, $\widehat{n}(\omega)$ and $\kappa(\omega)$ or the dielectric function $\epsilon(\omega)$. But, as can also be seen, R has to be measured for all frequencies ω from 0 to ∞, which is of course impossible. One relies therefore on extrapolations for the high and low frequency part of the spectrum.

The complex dielectric function

With the help of the KKR the dielectric function $\epsilon(\omega)$ of the investigated system can thus be obtained. $\epsilon(\omega)$ as a response function is determined by the excitations of the investigated solid. These can be – equivalent to the excitations that act as Raman scatterers – of very different nature depending on the regarded material and frequency range. As in the case of Raman scattering, we will restrict ourselves to optical phonons. However, it should be noted again, that for an exact determination of $\epsilon(\omega)$ reflectivity measurements over a wide range of frequencies are necessary. The measurements within this thesis omit these task by introducing model functions, whose KKR is already known. These are fitted to the experimental data. Thus, the high and low frequency part of the spectra are extrapolated – for details the reader is referred to Appendix B.
In the case of FT–IR the electric field of the radiation interacts directly with the crystal lattice to excite vibrational transitions within the solid. Thus, conservation of energy and momentum is required. For the latter, one can easily conclude that for the spectral range of FIR the wave vector of the optical phonons $q \approx 0$ compared to the maximum k–values of the Brillouin zone. Thus, FT–IR and Raman both probe the optical phonons in the centre of the Brillouin zone.
As stated before, all optical quantities measured in FT–IR can be expressed in terms of the complex $\epsilon(\omega)$ of the material under study. Therefore, for a meaningful interpretation of the spectra the most convenient approach is to model $\epsilon(\omega)$. In our case only the optical phonons will be considered and the frequency ranges below and above those will be reasonably extrapolated. The most simple case of modelling $\epsilon(\omega)$ can be derived from a set of damped harmonic oscillators [Kuz98].
Within this model, a periodically modulated electric field $E(t) = E_0 e^{-i\omega t}$ excites a harmonic oscillator with reduced mass μ, charge e, damping Γ, and Eigenfrequency ω_T. Now if there are n of these harmonic oscillators per unit volume, the macroscopic polarisation P is $P = nex$ and, together with the relation $P = \chi\epsilon_0 E = (\epsilon - 1)\epsilon_0 E$, one can derive an expression for the dielectric model function:

$$\epsilon(\omega) = \epsilon_\infty + \frac{\omega_p^2}{\omega_T^2 - \omega^2 - i\omega\Gamma} \quad with \quad \omega_p = \sqrt{\frac{ne^2}{\epsilon_0\mu}}. \tag{2.22}$$

ϵ_∞ is the contribution from all oscillators located at higher frequencies compared to the frequency range under consideration. It contains, for example, the contribution of the electronic transitions to $\epsilon(\omega)$. For the case of optical phonons ω_p is the ion plasma frequency and is defined as shown in equation (2.22) with e as the effective charge and μ as the reduced mass of the corresponding oscillator. The value of ω_p determines the strength of the response of the system to the electric field and hence the dipolar strength of the corresponding oscillator.
It is also convenient to split this complex function into its real (ϵ_r or ϵ_1) and imaginary part (ϵ_{im} or ϵ_2):

$$\epsilon_r = \epsilon_\infty + \omega_P^2 \frac{\omega_T^2 - \omega^2}{\left(\omega_T^2 - \omega^2\right)^2 + \omega^2\Gamma^2} \tag{2.23}$$

$$\epsilon_{im} = \omega_P^2 \frac{\omega\Gamma}{\left(\omega_T^2 - \omega^2\right)^2 + \omega^2\Gamma^2}. \tag{2.24}$$

Equation (2.22) can be further generalised for a set of infrared active phonon modes. In this case the various contributions to $\epsilon(\omega)$ are summed up yielding

$$\epsilon(\omega) = \epsilon_\infty + \sum_j \frac{\omega_{p,j}^2}{\omega_{T,j}^2 - \omega^2 - i\omega\Gamma_j} \tag{2.25}$$

Figure 2.8 shows schematically the discussed quantities R, ϵ_r, and ϵ_{im} for a single damped harmonic oscillator. The connection between $R(\omega)$, $\widehat{n}(\omega)$, and $\epsilon(\omega)$ can easily explain the characteristics of these functions: The Eigenfrequency ω_T of the oscillator causes the resonance behaviour of the real part of the dielectric function and the peak in ϵ_{im}. In the frequency range above ω_T ϵ_r is negative and approaches zero at the so–called *longitudinal* frequency ω_L. Accordingly ω_L is defined by setting ϵ_r equal zero and one obtains:

$$\omega_L^2 = \omega_T^2 + \frac{\omega_p^2}{\epsilon_\infty}. \tag{2.26}$$

The range between ω_T and ω_L (where $\epsilon_r < 0$) corresponds to an imaginary index of refraction due to equation (2.17) and, thus, light waves cannot penetrate the material. The reflectivity approaches 1 in this spectral range (see upper panel of figure 2.8), which is called *Restrahlenbande*. Equation (2.26) can be used to rewrite the first term of equation (2.24) to yield

$$\epsilon_r = \epsilon_\infty \frac{\omega_L^2 - \omega^2}{\omega_T^2 - \omega^2}. \tag{2.27}$$

What immediately follows from this expression is the Lydane-Sachs-Teller relation

$$\frac{\epsilon(0)}{\epsilon_\infty} = \frac{\omega_L^2}{\omega_T^2}. \tag{2.28}$$

Summing up, a model of damped harmonic oscillators can be used to model the dielectric function $\epsilon(\omega)$. With the help of the KKR and the further expressions discussed before a

model function for the reflectivity is obtained, whose model parameters are in our case the phonon frequency ω_T, the ion plasma frequency ω_p, and the damping Γ. Fitting this model function to the experimental data gives the corresponding information about phonon frequency, dipolar strength, and linewidth, respectively.
For a further discussion of the phonon modes observed with these two spectroscopical techniques one needs to consider their symmetry properties. This is carried out in chapter 4. But before, we will deal with the general properties of the investigated sample systems.

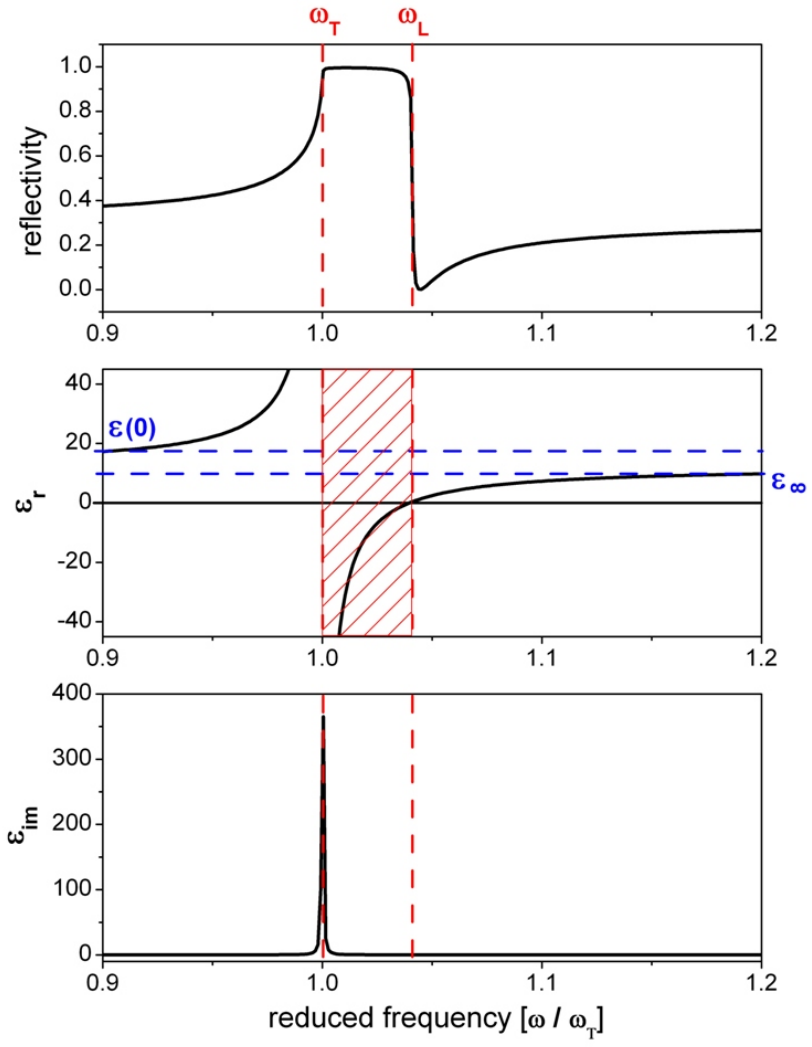

Figure 2.8: Schematic diagram for the reflectivity R, real part of the dielectric function ϵ_r, and imaginary part of the dielectric function ϵ_{im} with a single damped oscillator located at $\omega/\omega_T = 1.0$. ω_T and ω_L denote the Eigenfrequency and longitudinal frequency, whereas $\epsilon(0)$ and ϵ_∞ are the values of the dielectric function for frequencies below and above ω_T.

Chapter 3

The Multiferroic Manganites $RMnO_3$ (R = $Eu_{1-x}Y_x$, Gd, Tb)

The Multiferroic Rare–Earth Manganites $RMnO_3$ belong to the crystal class of the Perovskites with an orthorhombic unit cell. As in this material class crystalline, electronic and spin degrees of freedom are very intimately coupled, an elaborate introduction into all these physical properties within this material class is appropriate.
In section 3.1 we will deal with the crystalline structure of the orthorhombic Perovskites $RMnO_3$ starting from the general point of the ideal cubic Perovskite structure. This will be followed by a discussion about their magnetic properties in section 3.2. Then an introduction into the multiferroic properties of $RMnO_3$ will be given (section 3.3). In the last section 3.4 the possibility to tune the crystalline properties (and with it the other mentioned degrees of freedom) by substituting the Rare-Earth ions via the approaches of complete or partial substitution will be reasoned. For information about the synthetisation of the measured sample systems, see Appendix C.

3.1 The Perovskite structure of $RMnO_3$

The material class of Perovskites is a large family of compounds having a crystal structure related to the mineral Perovskite $CaTiO_3$. Its general chemical formula is ABX_3, where A and B are cations and X is an anion. The Perovskite structure is a very common crystalline structure allowing a wide range of possibilities for realisation with different ions for A, B and X.
In our case, we are dealing with Rare–Earth Manganites, thus the A–site cation is a rare–earth ion R with the valency 3+, the cations on the B–site cation are Mn^{3+}, and the anion is O^{2-}. As Rare–Earth ion almost the whole series of Lanthanides can be employed for synthetisation. The orthorhombic $RMnO_3$ series, therefore, covers the whole range from $LaMnO_3$ to $LuMnO_3$.
The crystalline structure of the Rare–Earth Manganites can be understood best by starting from the ideal Perovskite structure (space group $Pm\overline{3}m$). In this form, the $RMnO_3$ Rare–Earth Manganite Perovskite structure has a cubic unit cell and consists of corner–

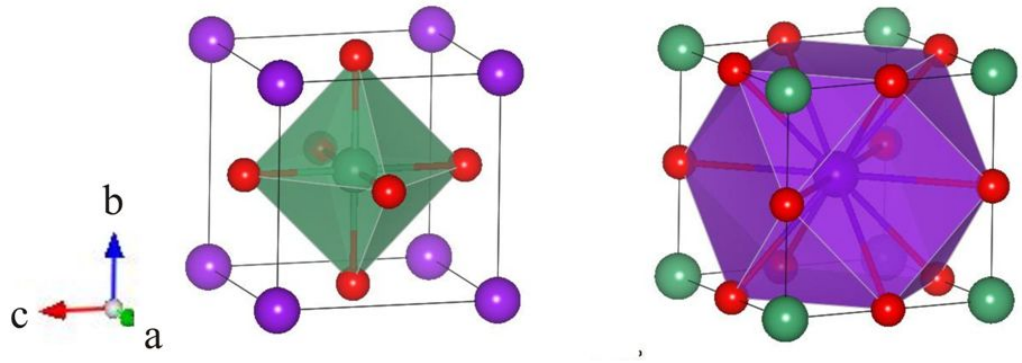

Figure 3.1: Schematic sketch of the building blocks of the Perovskite structure. The Rare–Earth ions R^{3+} are drawn in purple, the Mn^{3+} in green, and O^{2-} in red. The left part shows the octahedral environment of the Mn^{3+}, while the right part illustrates the 12–fold coordination site of R^{3+}. Drawn with [Mom08]

sharing MnO_6 octahedra, while the R–site cation is located on a 12–fold coordination site within the spaces left out by the octahedra [JL06]. Figure 3.1 shows the schematic view of these two building blocks of the Perovskite structure. Also table 3.1 lists the Wyckoff positions and the corresponding relative coordinates within the cubic unit cell. It is important to point out, that the Perovskite structure can be considered as organized in two alternating polar layers: the RO (ac) planes with valency +1 and the MnO_2 (ac) planes with valency −1.

As mentioned, the just discussed structure is an ideal structure. Most Perovskites are distorted and do not show the cubic structure. There are several factors that can lead to a deviation from this structure causing a wide field of possible realisations of crystalline Perovskite phases with lowered symmetry. For $RMnO_3$ compounds two factors are dominant: (i) size effects of the A– and B–site cations and (ii) the Jahn–Teller effect.

Size effects of the R–site cation

The size effects can be traced back to geometrical constraints. It can be easily understood that the lattice constant a of the ideal cubic Perovskite structure is related to the ionic radii (r_R, r_{Mn}, and r_O) via

$$a = \frac{2}{\sqrt{2}} (r_R + r_O) = 2 (r_{Mn} + r_O) . \tag{3.1}$$

In reality these two expressions do not have to be exactly equal. The ratio of these two terms is called Goldschmidt's *tolerance factor* t [JL06]:

$$t = \frac{r_R + r_O}{\sqrt{2} (r_{Mn} + r_O)} . \tag{3.2}$$

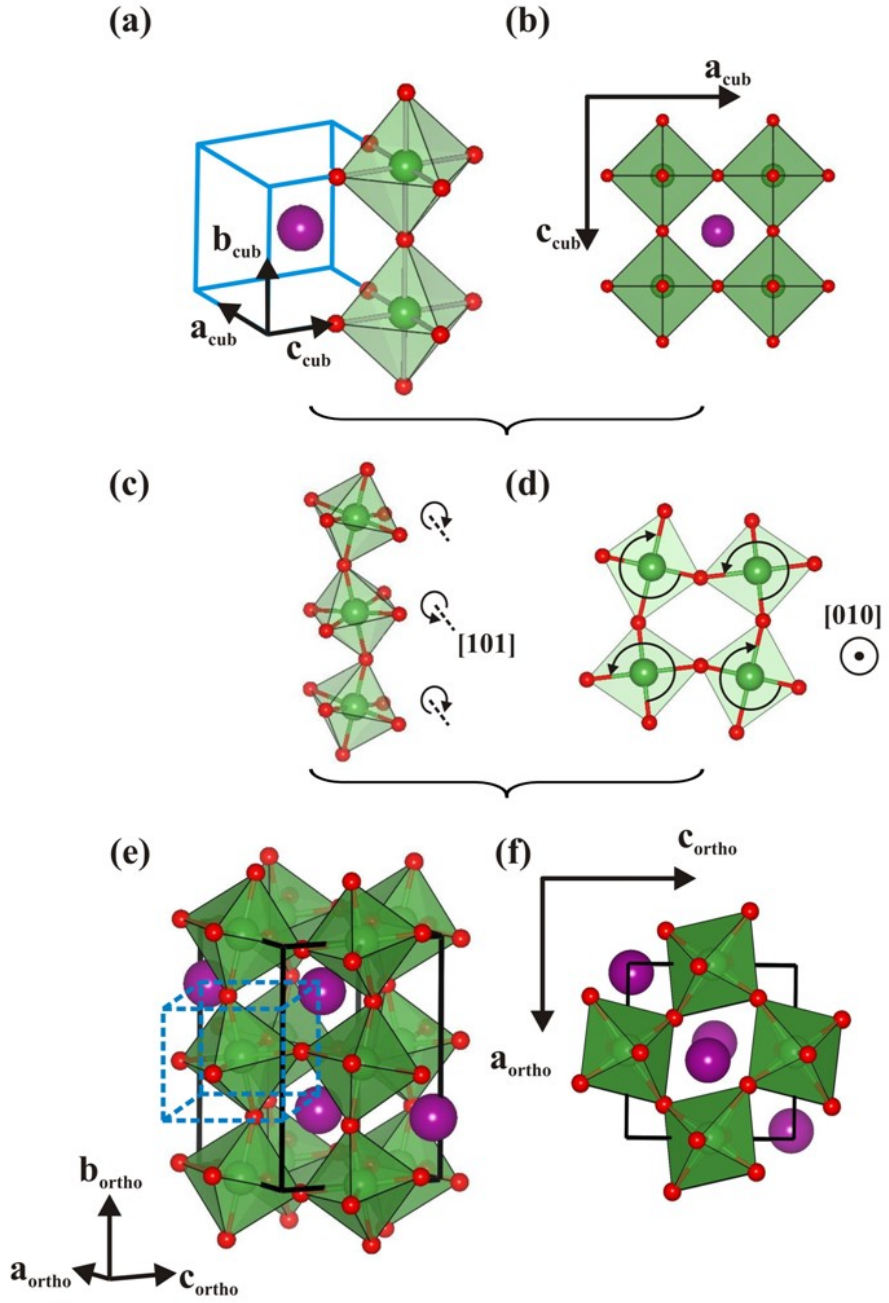

Figure 3.2: Transition from the ideal $Pm\bar{3}m$ structure – projections are shown in the panels (a) and (b) – to the orthorhombic Pnma structure illustrated in the panels (e) and (f). The rotations and tilts causing this lowered symmetry are an (c) out–of–phase tilt about the [101] axis and an (d) in–phase tilt about the [010] axis. The resulting orthorhombic structure is a fourfold cubic unit cell rotated by 45°. In (e) the original cubic unit cell is also indicated. Drawn with [Mom08]

It allows the estimation of the degree of deviation from the ideal geometric structure. An ideal cubic Perovskite has $t = 1.00$. But if the A–site cation is smaller than the ideal value, the tolerance factor t would be < 1. For low enough values of t the cubic symmetry is broken by tilts and rotations of the MnO_6 octahedra in order to fill space. Thus, for tolerance factors $0.8 < t < 0.89$ an orthorhombic structure with space group *Pnma* is obtained [JL06].
The distortion from the ideal cubic Perovskite structure is called $GdFeO_3$–like. It can be obtained from the ideal structure by two rotations of the MnO_6 octahedra: (i) out–of–phase equal tilts about the [101] direction of the cubic Perovskite and (ii) in–phase tilts about the [010] direction [IA01]. The transition from cubic to an orthorhombic unit cell by these two tilts is illustrated in figure 3.2. The resulting orthorhombic structure is a fourfold cubic unit cell rotated by 45°. The factor four originates from the doubling of the b–axis and from the replacement of the cubic a– and c–axis by the corresponding face diagonals of the MnO_2 (ac) plane. This new unit cell contains 20 atoms accordingly.
It is clearly understandable that this distorted orthorhombic structure is highly sensitive to the ionic radius of R^{3+}. A reduction of R^{3+} consequently leads to a decrease of the tolerance factor and, thus, to an increase of the orthorhombic distortion. In this context the reduction of the ionic radii of the Lanthanide series from La to Lu is of special importance. Due to the complicated shape of the 4f–orbitals the shielding effects of the 4f–electrons are rather weak. Thus, the increasing charge of the nucleus across the Lanthanide series causes a pronounced reduction of the ionic radii. This is also known as *Lanthanide contraction* [Gol25]. The orthorhombic distortion therefore increases from $LaMnO_3$ to $DyMnO_3$ which is the last stable orthorhombic Rare–Earth Manganite compound. $HoMnO_3$ – the next compound in the $RMnO_3$ series – crystallises in the hexagonal $P6_3cm$ phase, but can be converted to the orthorhombic phase by applying pressure during the growth procedure [LWSC04].
One can think of two possible approaches for the reduction of the R^{3+} ionic radius: (i) a complete replacement of the Rare–Earth element by another element which has a smaller ionic radius and (ii) a partial substitution of the R^{3+} with another ion with smaller ionic radius. Both approaches are employed for sample series investigated within this thesis, thus we will discuss them in more detail in the last section of this chapter and also in the first chapter of the experimental part (chapter 6). This will be done especially in the light of possible disorder induced effects within the doping approach.

The Jahn–Teller Effect

The other aforementioned mechanism, that lowers the crystalline symmetry, is the *Jahn–Teller Effect*. For an explanation of this effect the symmetry properties of the environment of the Mn^{3+} ions within the $RMnO_3$ compounds need to be considered. This will be done according to an empirical approach outlined in [Blu03] using crystal field theory. In this theory neighbouring orbitals are modelled as point charges. As could already be seen in figure 3.1 the Mn^{3+} are each surrounded by six O^{2-} in an octahedral environment. Latter

cause a crystal field for the Mn^{3+} originating from the electrostatic repulsion, due to the negatively charged electrons in the 2p–orbitals of the O^{2-}. Thus, the fivefold degeneracy of the Mn 3d–orbitals is lifted. From the five degenerate 3d–orbitals the energy of two orbitals – the e_g levels – increases, while for three orbitals – the t_{2g} levels – the energy decreases. This energy split due to the octahedral environment can be understood best by considering the d_{xz} and $d_{x^2-z^2}$ orbitals shown in figure 3.3. The d_{xz} orbitals belong to the class of t_{2g}. Thus, they point between the x– and z–axes. In contrast, the $d_{x^2-z^2}$ orbitals are e_g levels pointing along the x– and z–axes. It is easily understandable that for $d_{x^2-z^2}$ the electrostatic repulsion in an octahedral environment is stronger and, thus, increases the energy with respect to the spherical situation. For d_{xz}, whose overlap with the 2p–orbitals of the O^{2-} is lower, the situation is exactly opposite and, therefore, the energy decreases with respect to the spherical case. Figure 3.4(b) shows the resulting splitting of the 3d–orbitals within an octahedral environment.
This splitting due to the crystal field can be potentially found in all 3d–transition metals within such an octahedral surrounding. Now, the partial occupation of the 3d–orbitals must also be considered. In $RMnO_3$ the manganese is in a threefold positive charge state and, therefore, it has four electrons in its 3d–orbitals. There are two possibilities for occupying these orbitals with electrons: the high–spin and low–spin state [Blu03]. In the first case all 3d–orbitals are singly filled before any of these orbitals becomes doubly occupied. The second case applies when the lower lying t_{2g} orbitals are completely filled before the single occupation of the energetically higher e_g orbitals starts. The precise order is determined by the competition between the crystal field energy Δ_{cf} and the Coulomb energy cost for a double occupation of the 3d–orbitals J_H. Latter is equivalent to the energy scale of Hund's first rule. For $LaMnO_3$ the literature values for the crystal

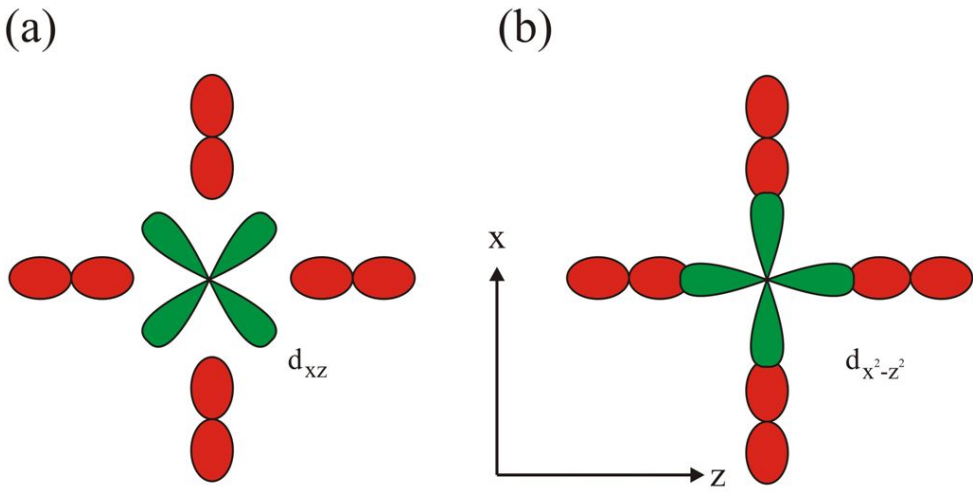

Figure 3.3: Schematical projection of two Mn^{3+} 3d–orbitals in the MnO_2 (ac) plane of the octahedra. In (a) the d_{xz}–orbital of Mn^{3+} is shown, whose energy is lowered due to the reduced overlap with the 2p–orbitals of the surrounding O^{2-} and, thus, a reduced electrostatic repulsion, while in (b) the energy of the $d_{x^2-z^2}$ is raised due to an increased overlap. Adapted from [Blu03].

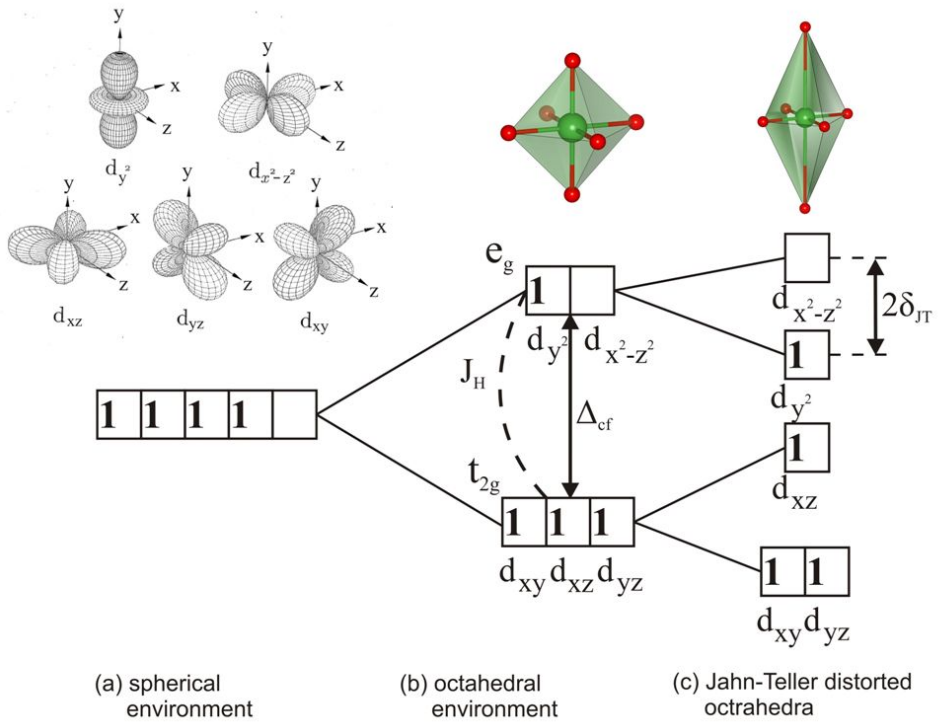

Figure 3.4: Occupation and splitting of the energy levels of the 3d–orbitals of Mn^{3+} shown in the upper left part, (b) due to the lowering of its environmental symmetry from spherical to octahedral and (c) due to the Jahn–Teller Effect. Parts adapted from [Blu03].

field energy are $\Delta_{cf} \approx 1.5eV$ [ADGF+92] and $J_H \approx 2 - 3eV$ [TT99]. The same holds for all $RMnO_3$ compounds. Thus, within this thesis we are in the high–spin state for all investigated systems.

The resulting occupation of the e_g and t_{2g} orbitals in Mn^{3+} is shown figure 3.4(b). This leads to a degenerated ground state, because only one of the e_g–orbitals is occupied. The degeneracy is lifted, as the crystal distorts itself spontaneously and, thus, lowers the crystalline symmetry of the MnO_6 octahedra further by stretching itself along one of the crystalline axes – an effect that is named after its discoverers *Jahn–Teller Effect* [JT37]. Without loss of generality we define this axis of elongation as y–axis and can, therefore, appreciate, that the energy of d_{y^2}, d_{xy}, and d_{yz} (see the upper left part of figure 3.4) is lowered due to the lowering of the orbital overlap along the y–axis and the resulting less pronounced Coulomb repulsion. On the contrary, the energy for the 3d–orbitals with components mainly in the xz–plane – $d_{x^2-z^2}$ and d_{xz} – is raised due to the reduced Mn–O distances within this plane and the resulting higher Coulomb repulsion. The corresponding splitting of the energy levels is shown in figure 3.4(c). It can be clearly seen, that for Mn^{3+} the net energy of the occupied orbitals is lowered.

In the case of the orthorhombic $RMnO_3$ system such a distortion within the MnO_2 (ac) plane as that sketched in figure 3.5 is experimentally observed. This Jahn–Teller distortion is called cooperatively and is distributed throughout the crystal leading to orbital order

in turn [Goo55]. This point is crucial for the following discussions about the magnetic properties of the $RMnO_3$ systems.

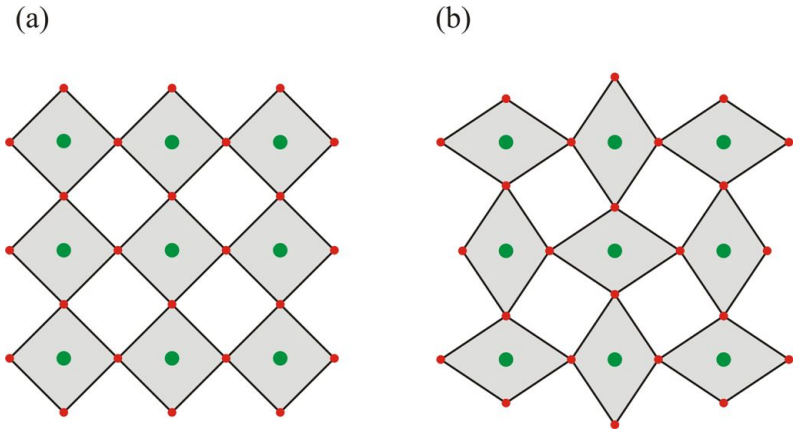

Figure 3.5: Schematic drawing of the consequences of the cooperative Jahn–Teller distortion for the MnO_2 (ac) plane of the $RMnO_3$ compounds. (a) shows the undistorted and (b) the Jahn–Teller distorted plane. The green points symbolize Mn^{3+} ions, the red points O^{2-}. Adapted from [Nal05].

Space Group Symmetry of orthorhombic $RMnO_3$

In this paragraph the resulting symmetry properties concerning the static lattice structure of the orthorhombic $RMnO_3$ will be summed up with the help of group theory. This part is of special importance, because the symmetry of the lattice will be employed in chapter 4 for a normal mode analysis of the lattice vibrations leading to selection rules for spectroscopic experiments.
According to [Hal69], group theory allows predictions about certain symmetry dependent properties of crystalline materials, e.g. the number and optical activity of lattice vibrations. However, predictions about phonon frequencies are not possible within this frame. The symmetry of an infinite crystal can be described by its space group. This is a set of symmetry operations, which leave the crystal invariant, fulfilling the mathematical criteria of a group: closure, associativity, identity and invertibility. For a Bravais lattice, i.e. a lattice with a pattern of spherical symmetry, there are five symmetry operations (translations will be omitted as this discussion is restricted to a single unit cell): the identity operation (E), reflections in a plane (σ), proper rotations of $360°/n$ (C_n), improper rotations, i.e. rotations of $360°/n$ followed by a reflection in a plane perpendicular to the axis of rotation, (S_n) and inversion (i). If the criterion of spherical symmetry is dropped, one has to add two additional symmetry operations: screw axes and glide planes. In total, this results in 230 possible space groups. For these, there are several methods of notation. In this thesis the so–called international symbol notation will be employed.

As discussed before, the most instructive way to deal with the Perovskite structure is to start from the highly symmetric cubic phase with space group $Pm\bar{3}m$ and then consider

Table 3.1: Wyckoff positions and relative coordinates of $RMnO_3$ in the ideal cubic Perovskite structure of space group $Pm\bar{3}m$, adapted from [JL06].

Ion	Wyckoff position	x	y	z
R^{3+}	1a	0	0	0
Mn^{3+}	1b	0.5	0.5	0.5
O^{2-}	3c	0	0.5	0.5
		0.5	0	0.5
		0.5	0.5	0

the additional effects, that lead to a lowering of the symmetry. Thus, in table 3.1 the Wyckoff positions (all points of a space group having equivalent atomic site symmetry) of the different ions within the unit cell are listed together with their relative coordinates. It can be easily understood, that all ions are located at highly symmetric points. For example each atom can be considered as a centre of inversion.
The next step is to include the symmetry lowering effects as the size effects of the R–site cation and the Jahn–Teller Effect. In table 3.2 the Wyckoff positions and relative coordinates of the resulting orthorhombic Pnma structure are given together with additional information about the atomic site symmetry for each ion. These informations show that only the Mn^{3+} remain at a centre of inversion (equivalent to site symmetry C_i), while for the R^{3+} and $O^{2-}(1)$ only a reflection on a mirror plane leaves these sites invariant leading to site symmetry C_s. The C_1 site symmetry for $O^{2-}(2)$ indicates that these ions are at a general position within the crystal, i.e. they have no site symmetry. These properties are also reflected in the relative coordinates within the unit cell, where only the Mn^{3+} are located at distortion–independent positions, while the other ions are shifted depending on the choice of the R–site cation. Thus, a variation of the latter within the $RMnO_3$ sample series leads to a shift R^{3+} ions as well as to tilting and buckling of the MnO_6 octahedra within the unit cell, but not to a change of the symmetry properties of the lattice.

The according change of the relative coordinates leads to an increasing orthorhombic distortion which is also reflected in the lattice constants. It manifests itself as increasing difference of the a– and c–axis as well as a decrease of the unit cell volume in total (mainly by a continuous shrinking of the b–axis). The experimental lattice constants for the investigated systems are listed in table 6.2 and 6.3 and will be discussed in detail in the corresponding experimental section 6.2.
Summing up, in this section the static lattice properties of the $RMnO_3$ system were discussed in the light of several effects, which lower the symmetry from cubic to orthorhombic. The symmetry aspects of the lattice were described with the help of group theory leading to insights into the local site symmetries of the incorporated ions. The next step would be a symmetry analysis of the lattice dynamics and its consequences for spectroscopical investigations, i.e. optical selection rules. This will be done in chapter 4. But first other important static aspects of the $RMnO_3$ system need to be discussed, due to their resulting

Table 3.2: Wyckoff positions, site symmetries and relative coordinates of $RMnO_3$ in the orthorhombic structure of space group Pnma. The variables u, v, m and n depend on the particular structure, i.e. the size of the R^{3+}, whereas a, b and c are general positions within the unit cell. From [Wyc64] adapted to Pnma.

Ion	Wyckoff position	site symmetry	x	y	z
R^{3+}	4c	C_s	$\pm u$	$\pm 1/4$	$\pm v$
			$\pm(u+1/2)$	$\pm 1/4$	$\pm(1/2-v)$
Mn^{3+}	4b	C_i	0	0	1/2
			1/2	0	0
			0	1/2	1/2
			1/2	1/2	0
$O^{2-}(1)$	4c	C_s	$\pm m$	$\pm 1/4$	$\pm n$
			$\pm(m+1/2)$	$\pm 1/4$	$\pm(1/2-n)$
$O^{2-}(2)$	8d	C_1	$\pm a$	$\pm b$	$\pm c$
			$\pm(a+1/2)$	$\pm(1/2-b)$	$\pm(1/2-c)$
			$\pm(-a)$	$\pm(b+1/2)$	$\pm(-c)$
			$\pm(1/2-a)$	$\pm(-b)$	$\pm(c+1/2)$

coupling effects with the lattice dynamics. These coupling effects are the main topic of this thesis. Thus, our next point will be the magnetic properties of $RMnO_3$.

3.2 Magnetic properties

To understand the magnetic properties, the implications determined by the crystalline structure discussed in the last section need to be considered in more detail. As can be seen in figure 3.4, the d–orbitals of the Mn^{3+} ions are neither completely empty nor completely occupied. Thus, one would expect delocalised electrons within a partially filled band scheme and, therefore, metallic behaviour. However, this is not the case due to electronic correlations within the Manganites [Ram08].
In these systems the effect of electronic correlations, i.e. the repulsive electron–electron interaction, cannot be neglected as is done in the one–electron picture of band theory [YC01]. It was argued by Mott and Peierls that, if these interactions are strong enough, electrons will be localised at their parent atoms, because electron transfer from one atom to another would lead to large additional electron repulsion due to their Coulomb interaction with each other [Mot37]. Such a system, which is an insulator due to electron correlation effects, is called a *Mott insulator* [Ram08].

The Hubbard Model

To quantitatively describe this behaviour, a lattice model, which includes kinetic energy as well as correlation effects, is usually employed – the *Hubbard model* [Hub63]. In this model a system is considered, where an electron occupies a single orbital with two possible spin orientations ($\sigma = \uparrow$ or $\downarrow$) at a given lattice site i. The Hamiltonian can be written as follows [Ope05]:

$$\widehat{H} = \underbrace{-t \sum_{\langle ij \rangle, \sigma} \left(c^{+}_{i\sigma} c_{j\sigma} + c^{+}_{j\sigma} c_{i\sigma} \right)}_{\widehat{H}_t} + \underbrace{U \sum_{i} n_{i\uparrow} n_{i\downarrow}}_{\widehat{H}_U} \tag{3.3}$$

The first term of the right side of equation (3.3), $\widehat{H}_t$, describes the kinetic energy in second quantisation. $c^{+}_{i\sigma}$ and $c_{j\sigma}$ are the annihilation and creation operators of an electron on the lattice sites i and j with spin σ, respectively. The sum runs over the nearest neighbours $i < j$ avoiding double counting and the two possible spin orientations. The parameter t is therefore a measure for the amount of energy, the electrons gain by delocalisation.
The second term, $\widehat{H}_U$, describes the Coulomb energy, that has to be brought up to add a second electron to a singly occupied orbital. The so–called Hubbard energy U has to be paid, when the two occupation operators $n_{i\uparrow}$ and $n_{i\downarrow}$ have both the eigenvalue one.
With these two parameters t and U one can define two regimes:
(i) $t/U \gg 1$: The Hamiltonian describes a metallic ground state as the electrons can delocalise and form a conduction band. Thus, consequently we obtain a "tight binding"single electron model in this case.
(ii) $t/U \ll 1$: The term $\widehat{H}_U$ dominates and, thus, an insulating ground state is obtained due to the energy cost, that has to be paid for electron hopping from one lattice site to another.
The Rare–Earth Manganites belong to the latter category, as in these systems partially filled 3d–orbitals occur, but nevertheless an insulating ground state exists. The simple Hubbard model discussed above can be applied straightforwardly to the case of the $RMnO_3$ compounds. For the following discussion, we will include the effects of crystal field splitting ($\Delta_{cf} \approx 1.5eV$), the intra–atomic ferromagnetic coupling due to Hund's first rule ($J_H \approx 2 - 3eV$) as well the Hubbard U ($U \approx 10eV$ [SPacVac96]), but not the Jahn–Teller splitting of the e_g orbitals due to the relatively small value of $\delta_{JT} \approx 0.5eV$. Thus, we can regard the e_g as partially filled doubly–degenerated orbitals, whose spin is ferromagnetically coupled via Hund's rule to the lower lying t_{2g} orbitals [TT99]. The immediate consequence for the magnetic structure is that we are dealing with localised magnetic moments. With these considerations the magnetic structure of the Rare–Earth Manganites can now be discussed.

The A–type antiferromagnetic structure of $RMnO_3$

The mechanism responsible for the magnetic ordering within the $RMnO_3$ system is the *Superexchange*. In the large majority of long range magnetic orderings in crystalline

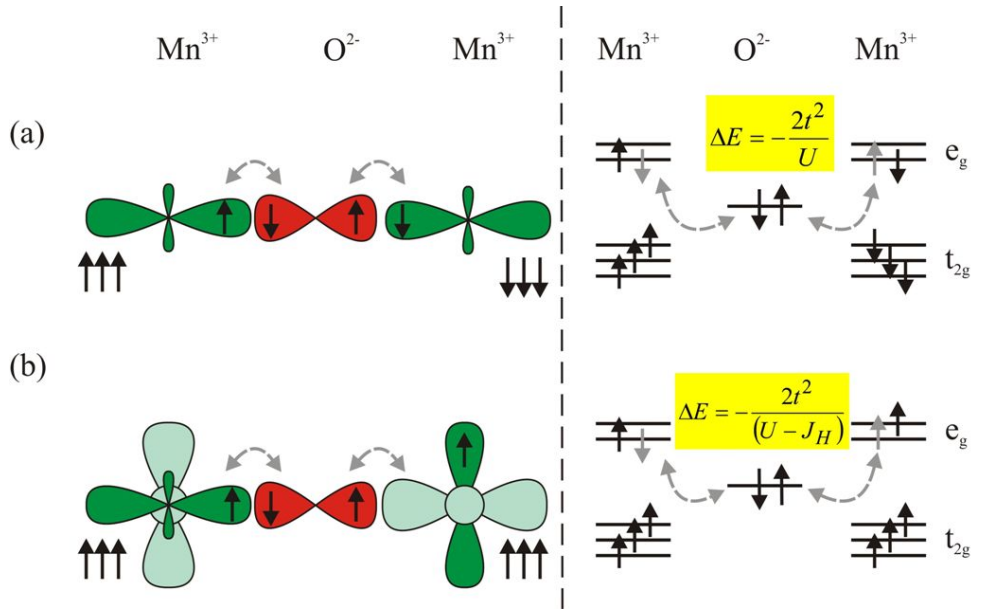

Figure 3.6: Goodenough–Anderson–Kanamori (GKA) Rules applicable to the virtual hopping within the frame of Superexchange in the $RMnO_3$ system. On the left side the orbital overlap and the resulting interaction between the Mn 3d and O 2p spins is shown and on the right side the energy levels participating in this exchange mechanism. Adapted from [Ope05].

solids due to localised magnetic moments, the exchange interaction is of indirect nature. In the case of $RMnO_3$ the essential magnetic exchange path is between adjacent 3d–orbitals of Mn^{3+} mediated by the 2p–orbitals of O^{2-}. For the Rare–Earth ions within the investigated $RMnO_3$ series with non–vanishing magnetic moments (i.e. $R^{3+} = Gd^{3+}$, Tb^{3+}) also a magnetic ordering may occur, due to the magnetism of partially filled 4f–orbitals of R^{3+}. However, their ordering takes place at temperatures $T < 10K$ [KLG+05]. As the experiments within this thesis were all done at higher temperatures, we will not consider the magnetic exchange of the 4f–orbitals of R^{3+} further.

The Superexchange can be understood as virtual hopping processes from the ground state. Depending on the spin orientation of the corresponding 3d–orbitals the resulting excited state can be lowered or raised in energy. This excited state, in turn, is admixed to the ground state and, thus, leads to an effective lowering of the total energy in the order of $\approx t^2/U$. As discussed before, the Superexchange depends strongly on the orbital structure. A detailed theoretical description can be very complicated. Thus, we will restrict ourselves to a more qualitative discussion based upon the Goodenough–Kanamori–Anderson (GKA) Rules [Goo63]. The two GKA Rules applicable to the $RMnO_3$ systems are sketched in figure 3.6.

The first rule, illustrated for the example of two d_{y^2} orbitals in figure 3.6(a), is applicable for two singly occupied or two empty e_g–orbitals. The core spin of the t_{2g} is indicated by the three spins below the e_g orbital and is ferromagnetically coupled to the single e_g spin corresponding to a strong J_H. For the case of two occupied or two empty e_g orbitals the energy gain due to antiparallel alignment of the Mn^{3+} spins is $\Delta E = -2t^2/U$. Thus, an

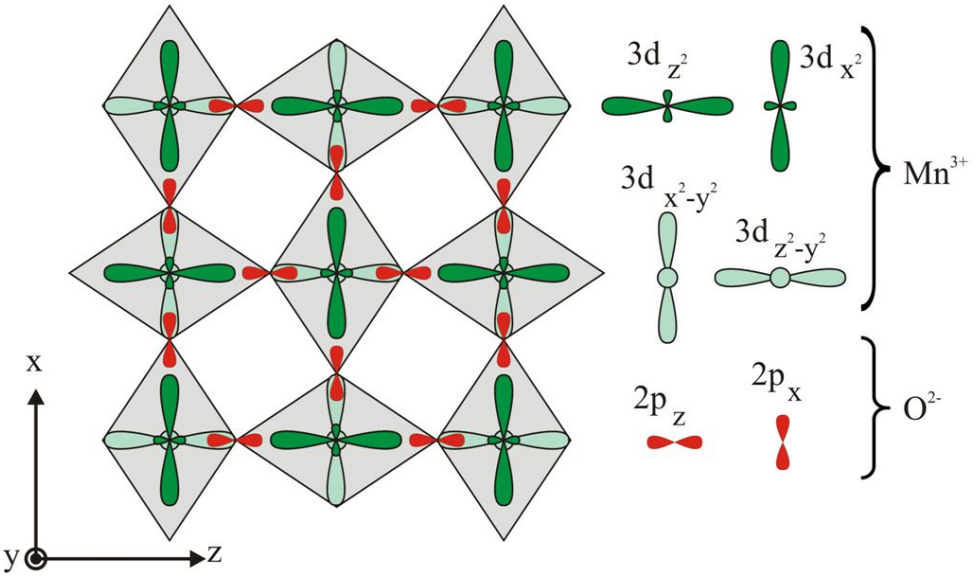

Figure 3.7: Schematic drawing of the orbital overlap between Mn 3d– and O 2p–orbitals within the MnO_2 (ac) plane. The orbital overlap between singly occupied $3d_{x^2}$ or $3d_{z^2}$ and unoccupied $3d_{x^2-z^2}$ or $3d_{y^2-z^2}$, respectively, causes a ferromagnetic coupling between the spins of the Mn^{3+} ions within this plane due to the GKA Rules. The tilting of the e_g orbitals with respect to the cubic Perovskite structure is left out for reasons of simplicity.

antiferromagnetic interaction occurs.

The second situation, depicted in figure 3.6(b), shows the GKA Rule for the overlap of one singly occupied and one empty e_g orbital. The second orthogonal e_g orbital is occupied as indicated. Here the energy gain by a parallel alignment of the Mn^{3+} spins is $\Delta E = -2t^2/(U - J_H)$ and a ferromagnetic interaction is favoured.

These two rules have to be applied to the orbital and crystalline order within the $RMnO_3$ systems. As indicated in figure 3.5(b), an alternate elongation of the MnO_6 octahedra along the x– and z–axis leads to a stacked orbital order due to the cooperative Jahn–Teller Effect within the MnO_2 (ac) plane. The resulting orbital structure is sketched in figure 3.7. The d_{y^2} orbitals are now alternating within this plane (denoted as d_{x^2} and d_{z^2} in the figure) and, thus, the magnetic exchange between these can be neglected. Instead magnetic exchange between the occupied d_{x^2} or d_{z^2} and the empty $d_{x^2-z^2}$ or $d_{y^2-z^2}$ is significant leading to a ferromagnetic ordering within the MnO_2 (ac) plane, according to the second GKA Rule. The situation perpendicular to this plane is much clearer, as there is no stacked orbital order and, thus, the first GKA rule for an overlap between two singly occupied or two empty orbitals applies. The magnetic structure therefore consists of a ferromagnetic coupling within the MnO_2 (ac) plane and an antiferromagnetic coupling perpendicular to this plane. The resulting magnetic structure is the A–type antiferromagnetic ordering shown in figure 3.8.

What is left out in this discussion, are non–isotropic effects of the Superexchange. The most important non–linear correction is due to spin–orbit coupling. This leads to the so–called *Dzyaloshinskii-Moriya interaction* (DMI) [Mor60]. The theoretical treatment of

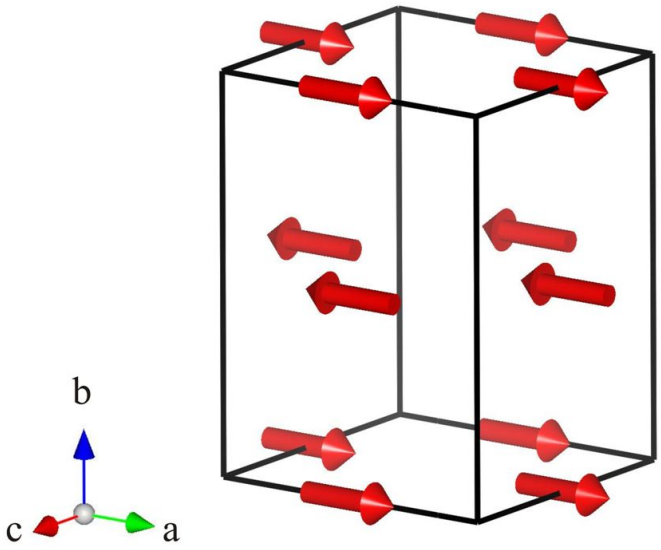

Figure 3.8: A–type antiferromagnetic ordering of the Mn^{3+} spins within the orthorhombic unit cell of $RMnO_3$.

this effect is rather complex and, therefore, only a short motivation of the basic form of the Hamiltonian will be given in Appendix D. The essentials are that there are correction terms favouring a canted spin arrangement within an antiferromagnet. The corresponding Hamiltonian is

$$H_{DMI} = \boldsymbol{D}\left[\boldsymbol{S}_i \times \boldsymbol{S}_j\right], \tag{3.4}$$

where $\boldsymbol{D}$ is the phenomenologically defined Dzyaloshinskii vector. It is straightforward to follow, that this Hamiltonian implies a canted antiferromagnetic spin arrangement. In the case of $RMnO_3$ compounds a small canting along the b–axis (see figure 3.8) occurs and leads to a weak ferromagnetic moment and, thus, to a canted A–type antiferromagnetic (canted A-type AFM) structure.

The incommensurate magnetic structures of $RMnO_3$

The above discussed canted A–type AFM structure occurs for a wide range of $RMnO_3$ with a relatively large R^{3+} ionic radius ($R^{3+} = La^{3+}$, Pr^{3+}, Nd^{3+}, Sm^{3+}, Eu^{3+}). However, for decreasing R^{3+} ionic radii the ordering temperature also decreases indicating a weakening of the strength of the magnetic ordering [KIS+03]. In this paragraph we will discuss the origin of this behaviour in order to gain an understanding of the phase diagram of the $RMnO_3$ series.

In section 3.1 it was already discussed, that a reduction of the R^{3+} ionic radius (e.g. by a complete substitution with a smaller Rare–Earth ion) has consequences on the crystalline structure, i.e. an increased tilting and buckling of the MnO_6 octahedra. This, in turn, has consequences for the magnetic structure due to the localised nature of the magnetic

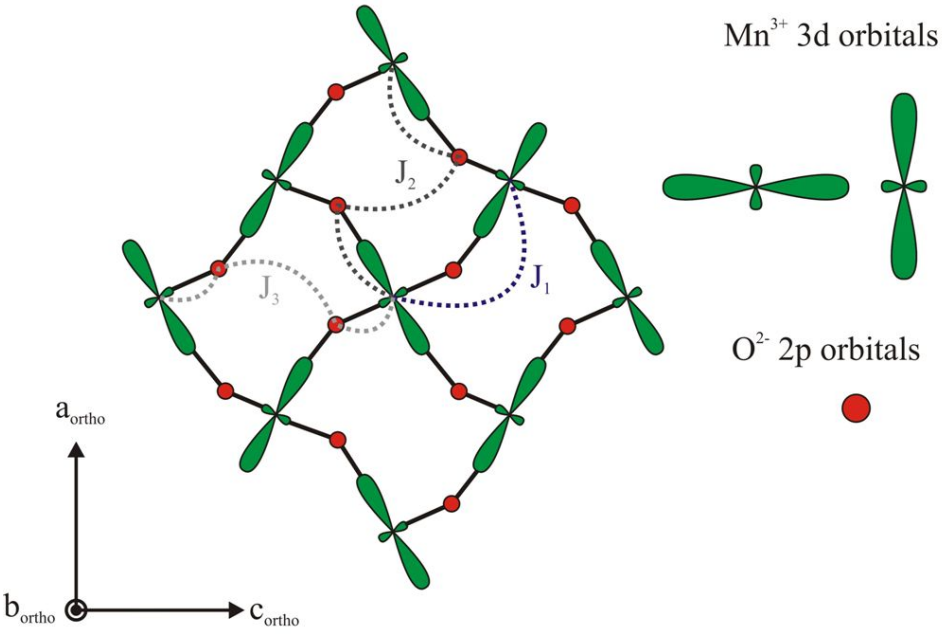

Figure 3.9: Schematic drawing of the orbital ordering and the resulting magnetic exchange paths between nearest neighbouring (NN) and next nearest neighbouring (NNN) e_g orbitals of the Mn^{3+}. The t_{2g} as well as the unoccupied e_g orbitals are omitted for reasons of simplicity. The magnetic exchange paths indicated in the figure are the ferromagnetic Mn–O–Mn exchange J_1, the antiferromagnetic Mn–O–O–Mn exchange J_2 along the a–axis and the weaker antiferromagnetic Mn–O–O–Mn exchange J_3 along the c–axis. Adapted from [KIS+03]

moments.

In figure 3.9 the orthorhombic distortion is included in a sketch of the projection of the occupied Mn^{3+} e_g orbitals and the O^{2-} 2p orbitals on the MnO_2 (ac) plane. The magnetic exchange discussed in the previous paragraph is responsible for the ferromagnetic spin arrangement within the MnO_2 (ac) plane. It is denoted as J_1 and describes the magnetic exchange between nearest neighbour (NN) Mn^{3+}. For the following discussion the magnetic exchange between next nearest neighbours (NNN) has to be considered, either. Due to the stacked orbital order, there are two possible exchange paths in the MnO_2 (ac) plane depending on the orientation of the d_{x^2} or d_{z^2}, respectively. For both cases the magnetic exchange is between two occupied e_g orbitals with the exchange path Mn–O–O–Mn. Thus, it is antiferromagnetic according to the GKA rules.

A closer inspection of the ordered orbitals sketched in figure 3.9 shows, that an increased tilting of the MnO_6 octahedra causes a tendency for a shortening of some O–O distances in the MnO_2 (ac) plane (e.g. the both O^{2-} ions involved in the J_2 exchange). This in turn leads to an increasing importance of the NNN magnetic exchange causing a weakening of the overall ferromagnetism within the MnO_2 (ac) plane. Thus, a decrease of the transition temperature (indicated as Néel temperature T_N) from the paramagnetic to the A–type AFM is expected for a decreasing R^{3+} ionic radius. This trend is clearly visible for T_N of the $RMnO_3$ system shown in figure 3.10.

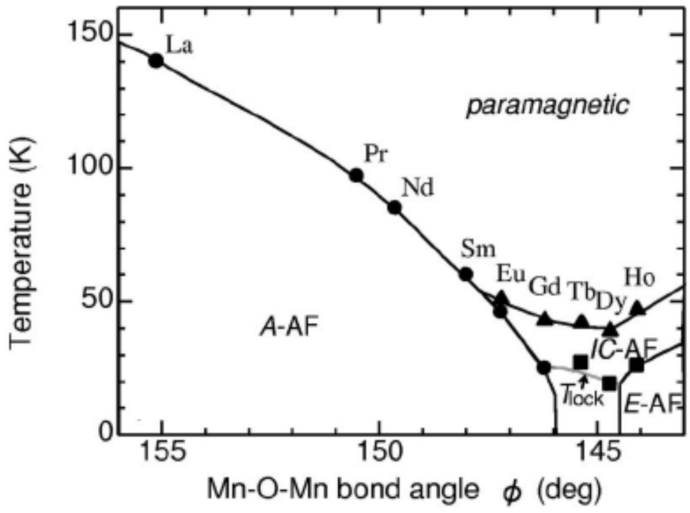

Figure 3.10: Spin ordering temperatures of $RMnO_3$ as a function of the Mn–O–Mn bond angle. A–AF denotes the canted A–type AFM, IC–AF the incommensurate antiferromagnetic phases (e.g. sinusoidal or spiral spin structures), and E–AF the E–type AFM. From [KIS+03]

For a complete understanding of the phase diagram shown in this figure, the magnetic interactions of NN and NNN Mn^{3+} need to be considered on a more systematic base. The most instructive way to do this, according to [Blu03], is a simple model for a layered magnetic structure with a ferromagnetic alignment within the layers. The magnetic exchange between NN layers is denoted as J_1 and that between NNN layers as J_2. The angle between the spins of the two adjacent layers is defined as θ. Within this model we can write the energy of the system as

$$E = -2NS^2 \left(J_1 \cos\theta + J_2 \cos 2\theta\right), \tag{3.5}$$

where N is the number of atoms in each plane and S their corresponding spin. This energy is minimized by the condition $\partial E/\partial\theta = 0$ leading to

$$\left(J_1 + 4J_2 \cos\theta\right) \sin\theta = 0. \tag{3.6}$$

One possible solution for this equation is $\sin\theta = 0$, which corresponds to $\theta = 0$ or $\theta = \pi$, leading to a ferromagnetic or an antiferromagnetic ordering of the layers, respectively. However, there is a third solution

$$\cos\theta = -\frac{J_1}{4J_2}, \tag{3.7}$$

which describes a so–called helical order, where the spins of adjacent layers couple under a definite angle $0 < \theta < \pi$. In this magnetic order the periodicity of lattice and magnetic order do not have to be commensurate. Thus, such a structure has a wave vector, whose values with respect to the reciprocal lattice do not necessarily have to be integer numbers. The situation in the $RMnO_3$ crystal lattice is highly sensitive on lattice properties of this

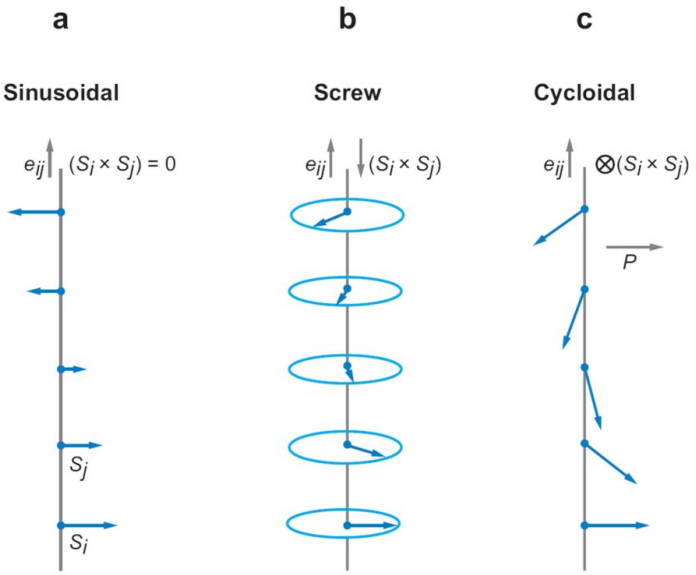

Figure 3.11: Illustrations of some types of possibly incommensurate magnetic structures. a) denotes a sinusoidal, b) a screw (= helical in the text), and c) a cycloidal spin structure. e_{ij} denotes the propagation direction of the spin modulation. The cross product of S_i and S_j is also shown for the three structures. From [Kim07].

structure and, therefore, much more complicated than this simple model. Thus, we will discuss it qualitatively in the light of the just deduced findings for an incommensurate magnetic structure.

Figure 3.11 shows three possible realisations of an incommensurate (IC) magnetic structure. Relevant for the IC–phases of the $RMnO_3$ system are the sinusoidal (a) and cycloidal (c) spin configurations [Kim07]. For $TbMnO_3$, as the most prominent example of a multiferroic $RMnO_3$ system with incommensurate magnetic ordering, a sinusoidal order appears upon cooling down from the paramagnetic phase at room temperature. This phase transition occurs at $T \approx 41K$ [Kim07]. A model proposed for this structure has the Mn magnetic moments aligned along the a–axis with a propagation wave vector of $(k_{Mn}, 0, 0)$ [QTRM$^+$77]. k_{Mn} is temperature–dependent until the second phase transition at $T_C \approx 28K$, where the dependence on T vanishes [KHJ$^+$05]. This temperature is indicated as T_{lock} in figure 3.10. It symbolises the transition to a cycloidal order in which the propagation direction of the rotation of the Mn^{3+} spins is also along the a–axis, but the rotation is transversely modulated as shown in figure 3.11(c). Thus, there are magnetic moments along the b–axis causing a non–collinear character of the cycloidal structure. Furthermore, this spin order is not invariant under a spatial inversion – a fact, that will be very important for the discussion of the multiferroic properties of the $RMnO_3$ systems (see section 3.3).

Summing up, the magnetic phase diagram of $RMnO_3$ systems can be understood as highly sensitive to the crystalline properties, i.e. the tilting and buckling of the MnO_6 octahedra, which can be tuned by the ionic radius of the R^{3+}. The consequences are a

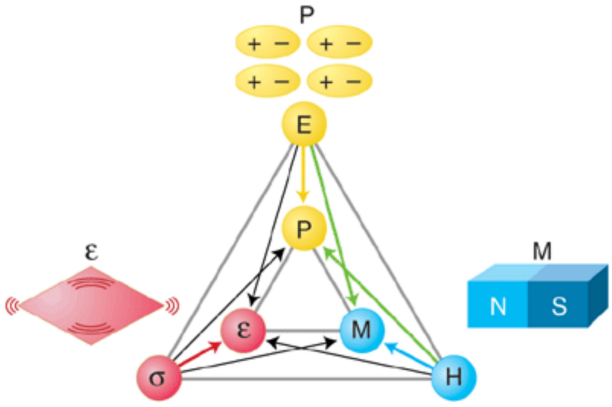

Figure 3.12: Schematics of multiferroic coupling effects. Three possible ferroic properties of a material are shown with their potential couplings indicated by arrows. Depicted are the order parameters electric polarisation P, magnetisation M and strain ϵ, which can order spontaneously in their corresponding ferroic phase. The green arrows highlight the Magneto–Electric Coupling, i.e. the induction of an electric polarisation P by an external magnetic field H or vice versa. [SF05]

decrease of the Néel temperature T_N of the A–type AFM. For R^{3+} with a smaller ionic radius than Eu^{3+} the A–type AFM is replaced by IC magnetic orderings reflecting the increasing importance of the NNN magnetic exchange within the MnO_2 (ac) plane.
It should also be mentioned, that for R^{3+} smaller than Dy^{3+} the E–type AFM occurs with a so–called up–up–down–down spin ordering along the Mn–O–Mn bonds in the MnO_2 (ac) plane [KIS+03]. However, this magnetic ordering is not relevant for this thesis and will be therefore not further discussed.

3.3 Multiferroism in $RMnO_3$

As stated in the introduction, multifunctional materials are one of the most interesting research areas in solid state physics with the Magneto–Electric Multiferroics being one of the so–called "hot topics"[CM07]. Thus, in this section a short overview of the multiferroic properties of the $RMnO_3$ system will be given.
Generally the Magneto–Electric Effect is the induction of electric polarisation by a magnetic field or the induction of a magnetisation by an electric field [Cur94]. This effect has been studied extensively in the 1960s and 1970s [O'D70, FS75], but the interest ceased due to the small coupling strengths. From theoretical considerations it was clear, that only a material in which ferromagnetic and ferroelectric order coexist, could show a considerable Magneto–Electric Effect. This leads to the material class of the (Magneto–Electric) Multiferroics. Originally, this term denoted materials, in which at least two ferroic orders exist in the same phase [Sch94]. Figure 3.12 shows schematically the potential couplings for the three order parameters polarisation P, magnetisation M and stress ϵ. The green arrows in the same figure indicate the Magneto–Electric Coupling as one of those multiferroic couplings.

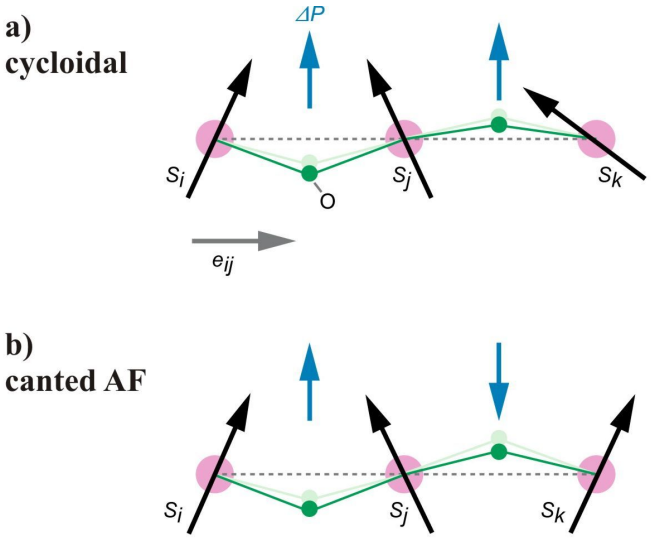

Figure 3.13: Sketch of the local ferroelectric polarisation due to the spin canting in (a) a cycloidal incommensurate spin structure and (b) a canted antiferromagnetic spin structure. The light green spots show the positions of the unshifted O^{2-} ions. The blue arrows symbolise the induced local electric polarisation. Taken from [Kim07].

In 2003 the Magneto–Electric Effect in $TbMnO_3$ was discovered [KGS+03]. Precisely, a ferroelectric polarisation was found, that can be switched by an external magnetic field. This triggered a giant wave of research activity for an understanding of this coupling effect and is also the motivation for the investigations of this thesis. Despite this success it has to be noted that the value of the ferroelectric polarisation is $\approx 500\mu C\ m^{-2}$ and, therefore, much smaller than that in conventional ferroelectrics (e.g. $BaTiO_3$ with P $\approx 300mC\ m^{-2}$ [CBL+04]) thus making the realisation of technological applications rather difficult. The relevant aspect for this thesis, however, is the determination of the Magneto–Electric Coupling by the magnetic structure. This will be discussed shortly in the following.

Due to symmetry arguments, it can be easily understood, that only in a magnetic structure, that breaks inversion symmetry, the Magneto–Electric Effect can occur [Mos06]. For $RMnO_3$ this is only possible for the cycloidal spin structure (see figures 3.8 and 3.11), where a spatial inversion causes a reversal of the direction of rotation of the spins.

This phenomenological treatment allows the search for multiferroic materials based on symmetry considerations. Moreover, a general relation between the electric polarisation and magnetic moments in a multiferroic system with incommensurate magnetic structure could be deduced [MF09]:

$$\boldsymbol{P} \propto \gamma \boldsymbol{e}_{ij} \times (\boldsymbol{S}_i \times \boldsymbol{S}_j)\,, \tag{3.8}$$

where γ is a coupling constant, $\boldsymbol{e}_{ij}$ the propagation vector of the spin cycloid and $(\boldsymbol{S}_i \times \boldsymbol{S}_j)$ the spin chirality, i.e. a vector parallel to the axis of spin rotation.

However, a complete microscopic theory is still missing. Several possible models were proposed in the last years. The most instructive one considers the Magneto–Electric Coupling

as an inverse DMI effect, where the noncollinear arrangement of the spins causes a shift of the O^{2-} ions between the two magnetic moments via magnetostriction [SD06]. In figure 3.13(a) these shifts are depicted together with the resulting local ferroelectric polarisations. One might expect, that this effect could also take place in a commensurate magnetic phase, e.g. a canted AFM structure as shown in figure 3.13(b). In this case the spin angle can be regarded as alternating between positive and negative sign but with the same value, i.e. an alternation of clockwise and counter clockwise spin rotation. Thus, macroscopically the local ferroelectric polarisation is cancelled out in agreement with equation (3.8).
Summing up, the presented considerations concerning the Magneto–Electric Coupling in incommensurate magnetic structures can explain the multiferroic properties of the $RMnO_3$ system, i.e. the appearance of a ferroelectric polarisation in the cycloidal spin phase of this system. Thus, the ferroelectric order is determined by the magnetic structure and can be suppressed or rotated by magnetic fields [KLG+05].
There is one further consequence of this intimate coupling between magnetism and dielectric properties relevant for this thesis: the Magneto–Electric Coupling leads to the occurrence of a corresponding elementary excitation: the so–called *Electromagnon*. This point will be discussed in the light of its coupling to the lattice vibrations in section 5.2.

3.4 Stoichiometric and non–stoichiometric $RMnO_3$

In section 3.1 it was argued that the orthorhombic distortion of the $RMnO_3$ system is determined by size effects of the R–site cation. This, in turn, affects the magnetic

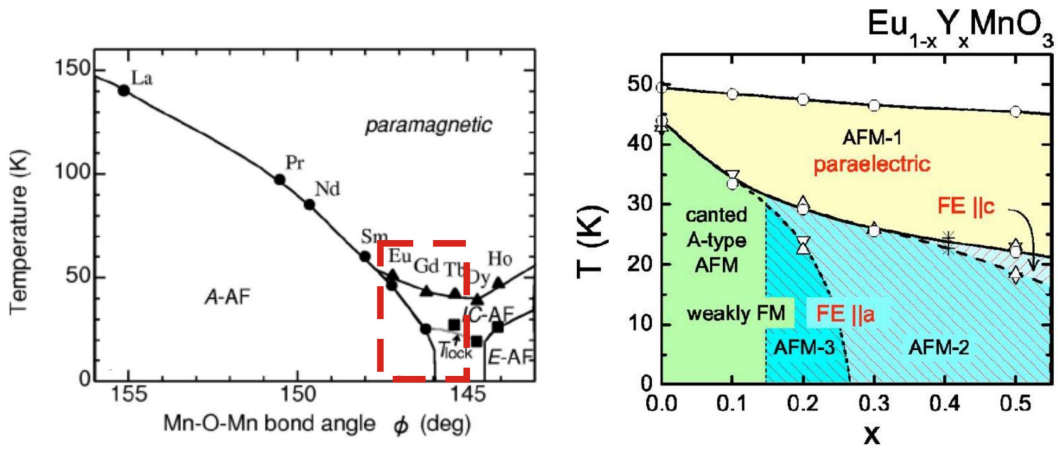

Figure 3.14: Magnetic phase diagrams of stoichiometric $RMnO_3$ (left side) and substituted $Eu_{1-x}Y_xMnO_3$ (right side). The red box in the phase diagram of $RMnO_3$ indicates the region where the two sample systems show comparable magnetic phases. In the phase diagram of $Eu_{1-x}Y_xMnO_3$ AFM–1 denotes a sinusoidally modulated spin structure and AFM–2 a spin cycloidal. The magnetic phase AFM–3 shows a weak ferromagnetic moment along the b–axis and simultaneously multiferroic behaviour. Taken from [KIS+03] and [HSP+07].

structure. A decrease of the effective size of the R–site cation can be achieved in two ways: (i) a complete replacement of R^{3+} with another cation with a smaller ion radius (e.g. substituting Eu^{3+} by Gd^{3+} or Tb^{3+}) or (ii) a partial substitution also by a smaller ion. An example for the latter is the mixed $La_{1-x}Gd_xMnO_3$ series [HLKvN$^+$04]. This substitutional approach gives also the opportunity to clarify the question, whether the multiferroic behaviour in $RMnO_3$ emerges only due to the magnetic moments of the Mn^{3+} or if the magnetic moments due to the partially filled 4f–orbitals of the Rare–Earths R^{3+} are also needed [YMG$^+$07]. This is done by employing the mixed–crystalline series $Eu_{1-x}Y_xMnO_3$, where both Eu^{3+} and Y^{3+} do not show a long range magnetic ordering as Eu^{3+} has a half filled 4f–shell causing a vanishing of the total angular momentum J and Y^{3+} is non–magnetic [HSP$^+$07].

The static lattice, magnetic and dielectric properties of $Eu_{1-x}Y_xMnO_3$ were investigated systematically and the results showed clearly, that multiferroic behaviour exists in this substituted system [IMT$^+$06, HSP$^+$07, YMG$^+$07]. Figure 3.14 shows the magnetic phase diagram of $Eu_{1-x}Y_xMnO_3$ [HSP$^+$07] in comparison with that of the stoichiometric $RMnO_3$ series from [KIS$^+$03]. Indicated are the magnetic phases as well as the corresponding ferroelectric polarisation. It can be seen that a similarity between the magnetic phases of $RMnO_3$ ($R = Eu^{3+}$, Gd^{3+} and Tb^{3+} – indicated by the red box) and that of $Eu_{1-x}Y_xMnO_3$ ($0 \leq x \leq 0.5$) exists. Thus, it can be concluded that the doped $Eu_{1-x}Y_xMnO_3$ cover the magnetic phases from $EuMnO_3$ to $TbMnO_3$.

Naturally, a substitutional approach gives rise to the question of crystalline disorder. Investigations were carried by the means of measurements concerning the static lattice properties to exclude the occurrence of secondary phases [HSP$^+$07]. However, a systematic investigation, which also includes measurements of the lattice dynamics are not carried out yet. This point will be dealt with in chapter 6 of this thesis.

Chapter 4

Lattice vibrations and selection rules

In the two previous chapters the spectroscopical techniques as well as the static properties of crystal and magnetic lattice within the $RMnO_3$ system were discussed. Both discussions showed the importance of symmetry aspects. In this chapter these two topics will be brought together for an introduction into the lattice dynamics of $RMnO_3$. This discussion will be based on a group theoretical classification of the lattice vibrations and the resulting optical selection rules, which determine their observability either with Raman or Infrared–Spectroscopy.

4.1 Lattice vibrations and group theory

In section 2.1 it was already mentioned, that for a treatment of the Raman process, i.e. a scattering process generating a lattice vibration, a purely classical description is not sufficient. The essential of the classical approach is, that lattice vibrations can be written as a sum of harmonic oscillators with Eigenfrequencies Ω and the wave vectors $\mathbf{q}$. The Quantum–Mechanical treatment is in close analogy to that of photons [Gro09].
For this task, the quantisation of the vibrational energy has to be taken into account. The resulting discrete energy niveaus $E_n = (n + 1/2)\,\hbar\Omega$ of the one–dimensional harmonic oscillator are occupied according to an occupation number n describing the excitation state of normal vibrations. The wave–particle dualism allows to express a vibration as a quasi–particle with energy $E = \hbar\Omega$ and momentum $\mathbf{p} = \hbar\mathbf{q}$, the *phonon*. The particle picture is especially suitable for the description of interaction processes, e.g. phonon–phonon interaction or scattering processes (see section 2.1).
According to [Kuz98], the Hamiltonian of the lattice vibrations can be written in mass–weighted normal coordinates Q_k for the 3N oscillators

$$H = \frac{1}{2}\sum_{k=1}^{3N}\left(\dot{Q}_k^2 + \Omega_k^2 Q_k^2\right), \tag{4.1}$$

where Q_k are the normal coordinates and Ω_k the resonance frequencies of the normal oscillators of the system. The energy of this ensemble does not change, if a symmetry

Table 4.1: Character table of the Pnma space group. In this table the symmetry classes (first line) of the group, their irreducible representations (left column) and the resulting characters of the matrices are listed. Also shown in the column on the right are the corresponding basis functions. From [Hal69].

	E	$C_2(z)$	$C_2(y)$	$C_2(x)$	i	σ_{xy}	σ_{xz}	σ_{yz}	
A_g	1	1	1	1	1	1	1	1	x^2, y^2, z^2
B_{1g}	1	1	–1	–1	1	1	–1	–1	xy
B_{2g}	1	–1	1	–1	1	–1	1	–1	xz
B_{3g}	1	–1	–1	1	1	–1	–1	1	xy
A_u	1	1	1	1	–1	–1	–1	–1	
B_{1u}	1	1	–1	–1	–1	–1	1	1	z
B_{2u}	1	–1	1	–1	–1	1	–1	1	y
B_{3u}	1	–1	–1	1	–1	1	1	–1	x

action (see section 3.1) of the corresponding space group is applied. Thus, each normal coordinate Q_k must be transformed into itself or into $-Q_k$. The normal coordinates Q_k can therefore be regarded as a basis for one possible representation of the space group.
In general, this representation can be reduced to an irreducible representation of the corresponding space group. A representation is called irreducible, if it does not fix any proper non–trivial subgroup. This means, that their matrix elements are arranged in a way around the diagonals, that no further decomposition into submatrices (i.e. subgroups) is possible. All lattice vibrations can be classified into the irreducible representations of the group and, thus, are assigned with the particular Mulliken symbol of the representation. For an explanation of the systematics of the Mulliken symbols, the reader is referred to [Kuz98, HW03]. It should be noted, that in the case of the orthorhombic Pnma group all representations are one–dimensional.
For a classification of the vibrational normal modes, it is necessary to know the traces $\chi(R)$ of the representation matrices for each symmetry action R. A trace is the sum of the matrix entries on the main diagonal. A table, in which the characters for each class of symmetry actions are listed for each irreducible representation, is called character table. The character table for the space group of the $RMnO_3$ system – Pnma in international notation, D_{2h}^{16} in Schoenfliess notation – is shown in table 4.1.
The next step will be the derivation of the optical selection rules.

4.2 Selection rules for Spectroscopy

Selection rules are simple rules stating if the transition probability for a system changing from one quantum–mechanical state to another is vanishing or not [Kuz98]. This probability can be expressed as proportional to the square of the corresponding element of the

transition matrix from the quantum–mechanical state i to the state f

$$M_{fi} = \int \psi_f^* \mathbf{P} \psi_i dx, \tag{4.2}$$

where ψ_i denotes the wave function of the initial state and ψ_f the final state, respectively. $\mathbf{P}$ is the operator causing the transition. Since the Hamiltonian introduced in equation (4.1) and also the corresponding Schrödinger equation are invariant under all symmetry actions, the wave functions to a particular Eigenvalue of H form a basis, that can be classified according to the irreducible representations of the space group. The same holds for the operator $\mathbf{P}$ due to the transformation properties of its corresponding basis functions. Thus, we can consider equation (4.2) as a triple product of basis functions each representing their irreducible representation. Thus, for the integral in equation (4.2) to be non–vanishing, the triple product of the corresponding representations

$$\Gamma^{(\psi_f)} \times \Gamma^{(\mathbf{P})} \times \Gamma^{(\psi_i)} \tag{4.3}$$

has to contain the trivial representation (i.e. A_g for Pnma) [Kuz98]. In that case, the matrix element M_{fi} is non–vanishing and the transition from state i to state f is allowed. This can be used immediately to derive the selection rules for the infrared active phonons.

4.2.1 FT–IR Spectroscopy

The transition between two vibronic states, induced by the electric field of the infrared radiation, is between states of different symmetry with respect to a spatial inversion. This can be easily understood by regarding the quantum–mechanical wave functions of the harmonic oscillator (see for example [Hal69]). The operator $\mathbf{P}$, responsible for the transition, is a dipole moment $e \cdot \mathbf{x}$ and, therefore, transforms according to the coordinates x, y or z.
In the case of FT–IR Spectroscopy, we are exciting phonons at temperatures $T \leq 300K$ and, thus, assume the vibrational ground state (i.e. the vacuum state) as initial state ψ_i. This state is characterised by the full symmetry of the static lattice, which is equal to the trivial representation A_g. Now it is clear, that for equation (4.3) to contain A_g, the dipole operator $\mathbf{P}$ and the final state ψ_f must both belong to the same representation. Thus, the excited phonon state must also transform according to the coordinates x, y or z and, thus, belongs to the irreproducible representations B_{1u}, B_{2u} or B_{3u}.
These three phonon symmetry classes can be selectively studied by employing polarised light with its electric polarisation $\mathbf{E}$ parallel to the corresponding crystal axes (i.e. $\mathbf{E}||\mathbf{x}, \mathbf{y}$, or $\mathbf{z}$). For the Pnma space group, the x–, y– and z–coordinates in the character table 4.1 are equivalent to the c–, b–, and a–axis of the crystal, respectively [Smi99].
In table 4.2 the possible directions for polarised light are listed together with the resulting phonon symmetry. It should be mentioned, that there exist two possible notations for the orthorhombic $RMnO_3$ system in literature: the Pnma notation and the Pbnm notation. These two can be transformed into each other by a permutation of the crystal axes. To avoid confusion, both notations will be shown in Table 4.2, but within this thesis the

Table 4.2: Light polarisations and corresponding phonon symmetry for the infrared–active phonon modes.

phonon symmetry	light polarisation in Pnma	light polarisation in Pbnm
B_{1u}	**E**||**a**	**E**||**b**
B_{2u}	**E**||**b**	**E**||**c**
B_{3u}	**E**||**c**	**E**||**a**

Pnma notation will be employed. A good thumb rule to distinguish between these two notations is, that in Pnma the b–axis is the elongated axis of the orthorhombic unit cell and in Pbnm the c–axis, respectively.

These group theoretical considerations can be underscored by the simplest model of the infrared active phonon modes: The A.C. electric field of the photon excites a phonon directly by changing its electric dipole moment [Kuz98]. Therefore, these phonon modes are also called *polar modes*. It is clearly understandable, that these modes have to transform like a vector due to the vector nature of the electric dipole. One can further conclude that by changing the polarisation vector of the incident light from one crystalline axis to another, the phonon symmetry is also changed and, thus, phonon modes of different symmetry are excited.

The group theoretical considerations further give the number of phonon modes for each mode symmetry in the $RMnO_3$ system. In summary, we have 25 infrared–active phonon modes: 9 B_{1u}, 7 B_{2u} and 9 B_{3u} [IAL+98].

4.2.2 Raman Spectroscopy

In contrast to the direct excitation of a phonon in FT–IR Spectroscopy, Raman Spectroscopy is based on a scattering process and must, therefore, be described by a quantum–mechanical process of second order. For an equivalent discussion of the selection rules resulting from group theoretical considerations, it is most instructive to return to equation (2.12), where the scattering probability of the Raman process is shown in terms of electronic transitions and electron–lattice interaction.

In summary, three interaction processes are involved: (i) the excitation of an electron by an incident photon to an intermediate state, (ii) the interaction between the intermediate state and the crystalline lattice, i.e. the phonon generation, and (iii) the electron–hole recombination into the initial electronic state. In this picture the processes (i) and (iii) can be described as electronic transitions equivalent to the vibrational transition process described in section 4.2.1 with the exception, that the initial and final electronic state are not necessarily the ground state. Thus, in general, the representations of ψ_i and ψ_s are not the trivial representation. The phonon excitation occurs in step (ii), where the interaction is described by the Raman tensor $\underline{\mathbf{R}}$. Thus, the selection rules for Raman spectroscopy

Table 4.3: Scattering geometry in Porto's notation [YC01] for all configurations possible for the Pnma space group and the resulting phonon symmetry for the Raman–active phonon modes. An interchange of the polarisation vectors e_i and e_s leads to the same symmetry representation, thus it is only shown once.

$k_i\,(e_i, e_s)\,k_s$	$a\,(\ldots)\,\overline{a}$	$b\,(\ldots)\,\overline{b}$	$c\,(\ldots)\,\overline{c}$
$\ldots(a,a)\ldots$	–	A_g	A_g
$\ldots(b,b)\ldots$	A_g	–	A_g
$\ldots(c,c)\ldots$	A_g	A_g	–
$\ldots(a,b)\ldots$	–	–	B_{1g}
$\ldots(a,c)\ldots$	–	B_{2g}	–
$\ldots(b,c)\ldots$	B_{3g}	–	–

can be derived by regarding the possible representations of the Raman tensor.
As a first step, the consequence of an application of the dipole operator on the electronic wave function of the initial state is considered. Consequently, a transition described by the dipole operator changes the symmetry character of the electronic wave function in a crystal structure with inversion symmetry from a g–mode to an u–mode or vice versa. This is a natural consequence of the spherical harmonic functions of the atomic wave functions and the selection rule $\Delta L = \pm 1$ (see textbooks about atomic physics, e.g. [MK97]). Thus, for (i) and (iii) the symmetry of the wave functions is changed and returns to the initial value, either g or u.
The direct consequence for (ii) is, that the Raman tensor has to project from one intermediate state $|a\rangle$ of symmetry g or u to another intermediate state $|b\rangle$ of the same symmetry. Thus, the tensor itself has to conserve the inversion symmetry and therefore has to belong to a g–type representation, i.e. A_g, B_{1g}, B_{2g}, or B_{3g}. This is also reflected in the transformation properties of the g–type representations. All of these transform like tensors, i.e. like the product of coordinates (i.e. x^2, y^2, z^2, xy, xz, or yz), as shown in the character table 4.1.
In summary, 24 Raman–active phonon modes are obtained for the $RMnO_3$ system with Pnma structure: 7 A_g, 5 B_{1g}, 7 B_{2g}, and 5 B_{3g} modes [IAL+98]. It should be pointed out, that for the highly symmetric cubic Perovskite (space group $Pm\overline{3}m$, see section 3.1), no Raman–active phonon modes exist [IA01]. Thus, the Raman–active modes are especially sensitive to the orthorhombic distortion of the Perovskite crystal structure.
The discussion of Raman– and infrared–active phonons also shows a very important general aspect of symmetry: in crystals with inversion symmetry, Raman– and infrared–active phonon modes exclude each other.

For the Raman selection rules, one has to consider the matrix representations of each of the Raman–active representations of the Pnma space group. These can be obtained from literature, e.g. from [Kuz98]. For a systematic derivation of the Raman selection rules, it is most convenient to use Porto's notation, which was already introduced in equation

(2.6).
A multiplication of the electric polarisation vector with the Raman tensors should lead to a polarisation vector, which is observable within the chosen scattering geometry. This means, for example, if $\mathbf{k}_i$ (and of course also $\mathbf{k}_s$) is chosen parallel to the normal vector (e.g. a or $\overline{a}$) of a plane spanned by two of the three crystalline axes (in this case, the bc–plane), one can probe light polarisations $\mathbf{e}_i$ parallel to one of the two in–plane axes due to the transversal nature of the light wave. A multiplication of these possible polarisation vectors with all Raman tensors of the Pnma space group gives non–vanishing $\mathbf{e}_s$ for two cases: (i) the A_g representation, if $\mathbf{e}_i||\mathbf{e}_s$, that is possible for (b,b) and (c,c) in Porto's notation and (ii) the B_{1g} representation, if $\mathbf{e}_i \perp \mathbf{e}_s$, which can either be (b,c) or (c,b), respectively. This can be done systematically for all possible scattering configurations, i.e. different $\boldsymbol{k}_i$ directions, $\boldsymbol{k}_s = \overline{\boldsymbol{k}}_i$ and the resulting possible $\boldsymbol{e}_i$ and $\boldsymbol{e}_s$ directions. The result is table 4.3, which lists the selection rules for all possible backscattering geometries.

4.3 Mode patterns of the investigated Raman– and infrared–active Phonons

As pointed out before, the group theoretical considerations give numbers for the allowed lattice vibrations of each mode symmetry. These can be selectively studied by the application of the just discussed optical selection rules. However, they do not give any information about the phonon frequencies. For this task, one has to carry out lattice dynamical calculations. In principle, there exist two possible approaches for a quantitative calculation of the phonon frequencies: (i) an empirical approach or (ii) an ab–initio calculation.
In the case of (i), the phonon modes are modelled by giving the atomic positions and the ionic charges of the atoms incorporated in the unit cell as well the displacement vectors of the lattice vibrations as input parameters. The fitting procedure is carried out by adjusting the values of the ionic charges and by fitting an appropriate number of force constants to obtain quantitative phonon frequencies. This was carried out in literature for various $RMnO_3$ compounds (e.g. for $LaMnO_3$ [Smi99], or for $SmMnO_3$, $EuMnO_3$, and $GdMnO_3$ [CRC$^+$09]). However, the empirical nature of this approach can be seen by the fact, that the number and values of the fitting parameters are chosen almost arbitrarily to match the experimental values of the phonon frequencies. In the case of $RMnO_3$, this procedure does not lead to a perfect agreement due to the complicated bond structure of the orthorhombic unit cell with a basis of 20 atoms [IAL$^+$98]. Thus, the physical meaning of the derived results is limited apart from the possibility to obtain phonon frequencies, which agree more or less well with experiment.

The second possibility – approach (ii) – which was chosen for the lattice dynamical calculations within this thesis, is an ab–initio technique. This means, only the atomic positions and the chemical element of the basis atoms of the crystalline lattice are given as input parameters and the physical quantities, e.g. phonon frequencies, are computed within the frame of a Density Functional Theory (DFT) calculation. An appropriate ap-

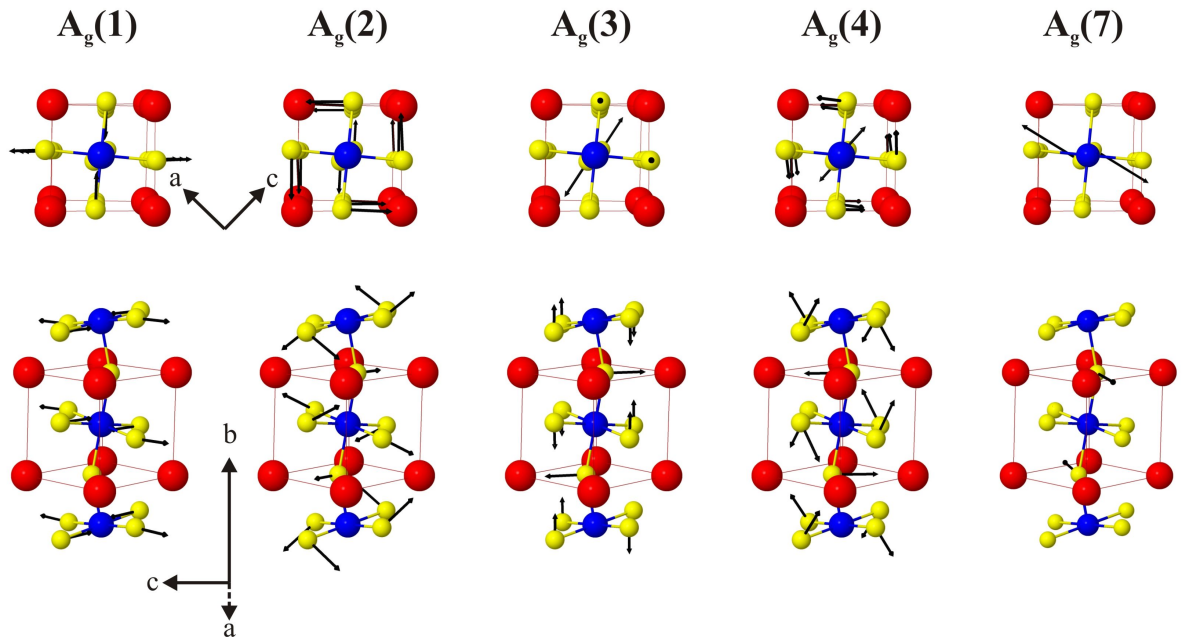

Figure 4.1: Main atomic displacement patterns of the experimentally observed Raman–active phonon modes with A_g symmetry. The mode patterns were calculated for $LaMnO_3$ within the frame of a Density Functional Theory (DFT) calculation with the ABINIT code [GRV+05, GAA+09].

proximation for the exchange correlation within this frame has to be chosen. In our case a Local Density Approximation (LDA) was employed. For detailed information about the DFT technique the reader is referred to Appendix E, where also the technical details of this calculation carried out for the $LaMnO_3$ system are explained.
Due to the physically more meaningful results and the availability of an open–source code for DFT–calculations (the ABINIT–code, see Appendix E), method (ii) is chosen, as stated before, and the phonon frequencies and their corresponding displacement patterns are calculated. It should be pointed out here that for a calculation with method (i), the symmetry of the phonon modes patterns would be an input parameter. For a DFT–calculation carried out with ABINIT on the other side, an algorithm is incorporated, that deduces the mode patterns from the symmetry properties of the given atomic positions within the unit cell according to the corresponding space group.

For the computation the system $LaMnO_3$ is chosen, because it is the most simple task for modelling a Perovskite $RMnO_3$ system due to its empty 4f–shells. The other elements with partially filled 4f–shells cannot be computed within a simple LDA–approach due to the small overlap of these orbitals and their resulting nearly localised electronic behaviour (see, for example, [DSGPS07] and references therein, especially [AZA91]). Thus, a system is chosen with space group Pnma leading to the phonon mode patterns equivalent to those of the $RMnO_3$ systems investigated within this thesis. The obtained theoretical phonon frequencies for $LaMnO_3$ are therefore of minor importance and will only be considered as determining the order of the IR–active phonon modes.

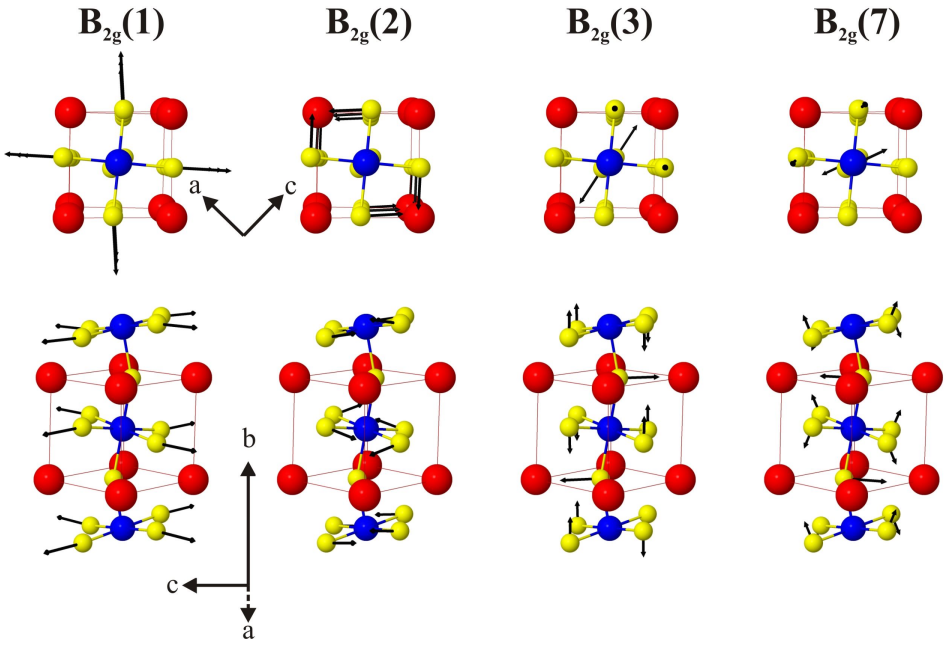

Figure 4.2: Main atomic displacement patterns of the experimentally observed Raman–active phonon modes with B_{2g} symmetry.

In the two figures 4.1 and 4.2, the mode patterns of the Raman–active phonons with A_g and B_{2g} symmetry are shown, respectively. For reasons of brevity only the patterns of those A_g and B_{2g} phonon modes are depicted, that have been experimentally observed within this thesis. The B_{1g} and B_{3g} modes are not shown due to the same reason. Comparison with published empirical calculations of [Smi99] and [IAL$^+$98] shows a good agreement concerning the mode patterns and phonon frequencies. The nomenclature of the phonon modes is adapted from [IAL$^+$98]. It can be seen, that all observed Raman–active phonon modes consist mainly of motions of the O^{2-} ions. It was pointed out before, that due to symmetry restrictions the Mn^{3+} ions cannot participate in g–modes. Further, as already demonstrated in [IAL$^+$98], the phonon modes with significant R^{3+} involvement are only very weakly Raman–active. This is attributed to the smaller polarisability of the longer R–O bonds in contrast to the shorter Mn–O bonds. The A_g and B_{2g} modes can further be classified into modes, that have their main movement within the MnO_2 (ac) plane or perpendicular to it.
The mode patterns of the experimentally observed IR–active phonon modes are shown in figure 4.3 for B_{1u} symmetry and in figure 4.4 for B_{3u} symmetry, respectively. In contrast to the literature–based nomenclature of the Raman–active modes, the IR–active modes are numbered according to the magnitude of their phonon frequency. It should be pointed out here, that some ambiguity remains in the numbering order of these modes due the small differences of their frequencies. Thus, no perfect agreement with the literature data of [Smi99] is achieved. Nevertheless, a classification of these modes into groups is possible. The criterion is the degree of participation of the various elements within the unit cell. For example, it is easily understandable, that the elements with the highest atomic

mass will be the main participants of the phonon modes with the lowest frequencies. A close inspection of the mode patterns shown in figure 4.3 and figure 4.4 shows, that the IR–active phonon modes can be classified in three main categories corresponding to a range for the phonon frequency:

1. Motions of R^{3+} and Mn^{3+}: 100 $cm^{-1} < \widetilde{\nu} <$ 300 cm^{-1}
2. Tilting, buckling and rotations of the MnO_6–octahedra: 300 $cm^{-1} < \widetilde{\nu} <$ 500 cm^{-1}
3. Stretching and internal modes of the MnO_6–octahedra: 500 $cm^{-1} < \widetilde{\nu} <$ 700 cm^{-1}

Summing up, the symmetry determined by group theoretical considerations can also be used for a selective study of the various lattice vibrations and their participating elements. Concretely, three main distinctions can be drawn: (i) According to their frequency and main participating ions, the IR–active phonons can be classified in the three groups introduced above. (ii) FT–IR and Raman Spectroscopy can be employed to discriminate phonon modes with (IR) and without (Raman) participation of the Mn^{3+}. (iii) Additionally, the mode patterns of the Raman–active phonon modes allow to distinguish between modes with their main movement within or perpendicular to the MnO_2 (ac) plane, respectively.

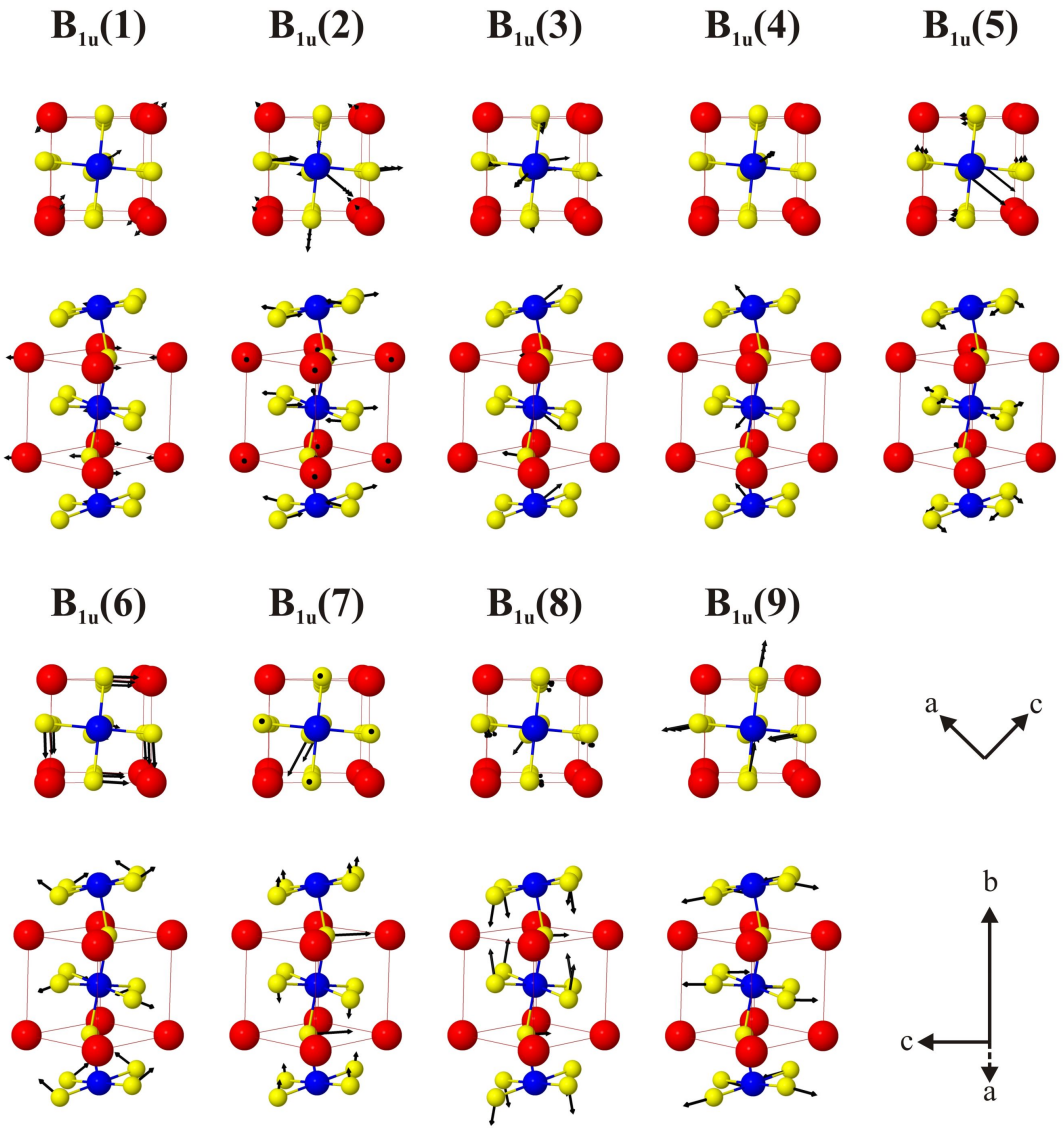

Figure 4.3: Main atomic displacement patterns of all IR–active phonon modes with B_{1u} symmetry.

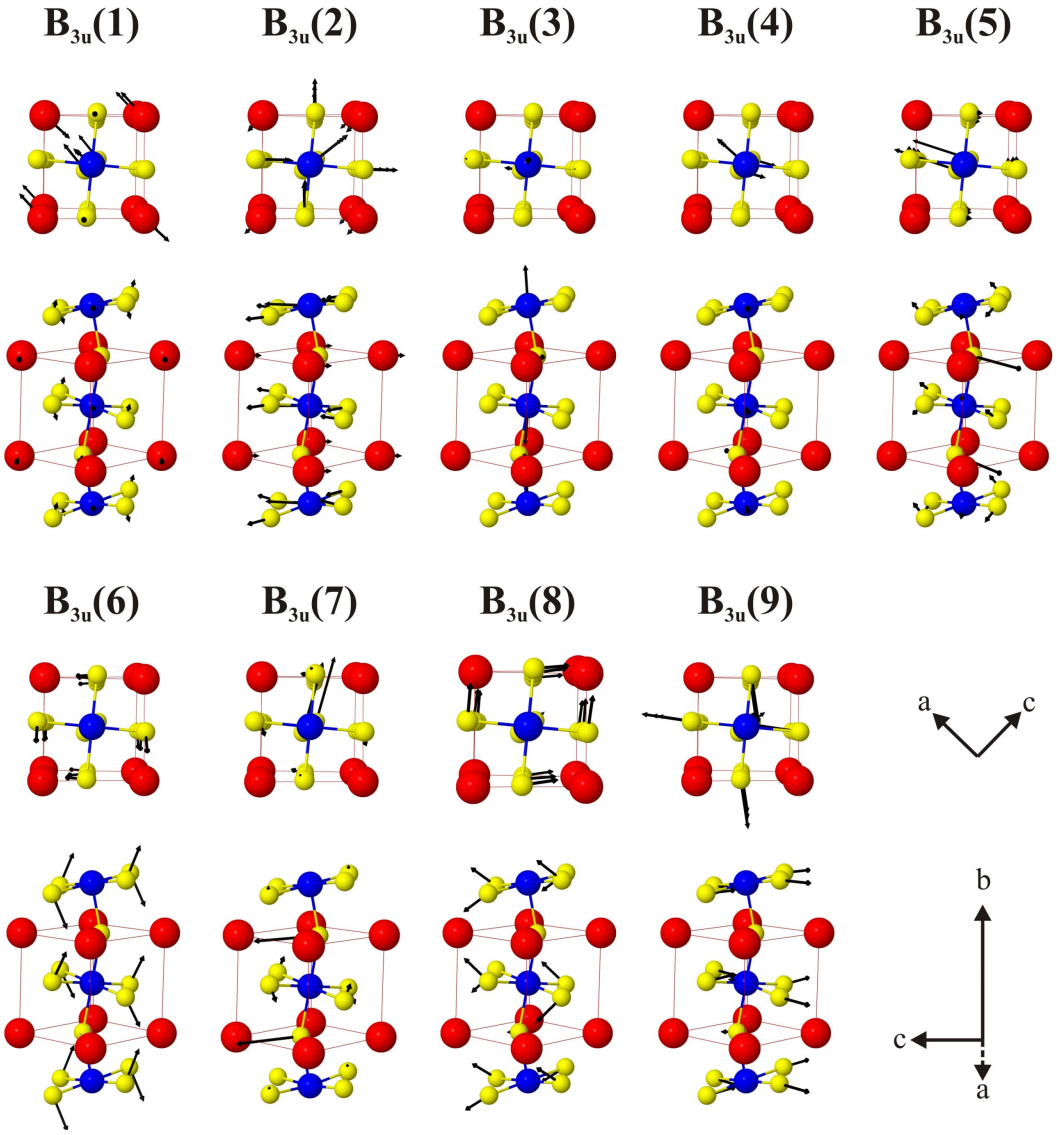

Figure 4.4: Main atomic displacement patterns of all IR–active phonon modes with B_{3u} symmetry.

Chapter 5

Coupling effects in $RMnO_3$

It was pointed out already in chapter 3, that in the $RMnO_3$ system an intimate coupling exists between lattice, orbital and spin degrees of freedom. This can be seen in various ground state properties, e.g. the magnetic structure, which can be tuned by size effects of the R–site cations (see sections 3.1 and 3.2), or the multiferroic properties determined by the interplay of lattice properties and magnetic frustration (see section 3.3).
Motivated by these coupled ground state properties, the main topic of this thesis is the study of dynamical coupling effects within the multiferroic $RMnO_3$ compounds. Concretely the coupling effects involving the interplay between lattice dynamics and the magnetic phases are investigated. Their main indication is a renormalisation of the phonon frequencies at entering the temperature region of the long range magnetic ordering. The experiments of this thesis will show that two main effects are responsible for this behaviour: Spin–Phonon Coupling (SPC) and Electromagnon–Phonon Coupling (EMPC). In the following two sections the theory of both effects will be introduced as far as they are already discussed in literature.

5.1 Superexchange and Spin–Phonon Coupling (SPC)

SPC relies on the interplay of the crystalline and the magnetic structure of the $RMnO_3$ system, but can be observed in various other crystalline systems with localised magnetic moments as well – see e.g. [RKM+07], [HCK+09] or [KMR+10].
The simplest model suitable for gaining a qualitative understanding of this effect is illustrated in figure 5.1. On the upper left, the situation for the paramagnetic phase is sketched, where the effective restoring force of a given lattice vibration mode is determined solely by the crystalline potential. In a classical picture, this can be understood as a spring constant D_{pot}. The situation changes at the onset of the long range magnetic ordering, where the spins of the Mn^{3+} begin to align. In the case of localised magnetic moments, whose exchange interaction is mediated by non–magnetic ions (see upper right part of figure 5.1), a lattice vibration can modulate the exchange interaction by displacements of the non–magnetic ions (in our case, the O^{2-} ions). Thus, the restoring force modelled by the spring constant D_{pot} is changed to $D_{pot} + D_{magn-ex}$ in the magnetically

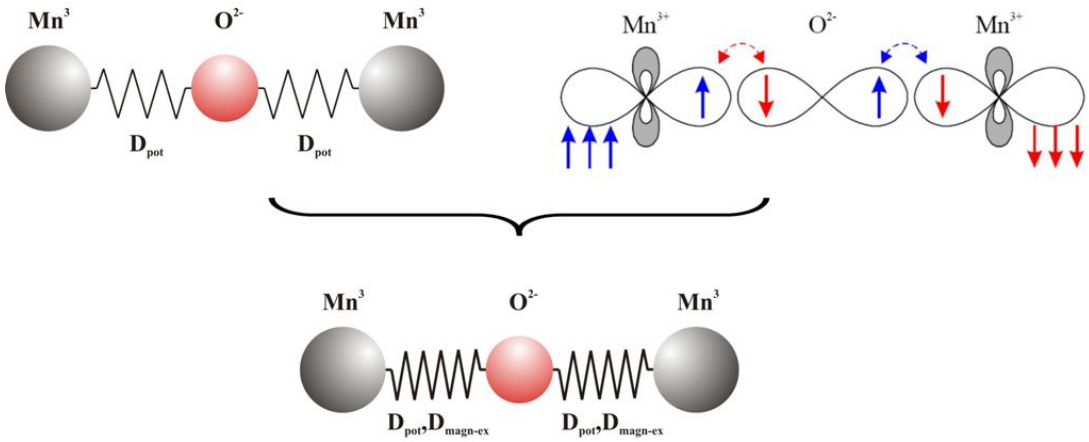

Figure 5.1: Simple model picture of SPC: (top left) a Raman–active phonon (e.g. the symmetric MnO_6 stretching mode $B_{2g}(1)$) modulates the Mn–O bonds within the MnO_2 (ac) plane. Lowering the temperature leads to the appearance of the ordered magnetic phase (top right) and, thus, to a modified restoring force due to the mediating role of the O^{2-} ion in the Superexchange interaction (lower part). Parts adapted from [Ope05].

ordered phases, as shown in the lower part of figure 5.1. This, in turn, also changes the energy of the corresponding lattice vibration, which can be observed as a frequency shift in this temperature range.

For a quantitative discussion of SPC, a more elaborated quantum–mechanical model relying on Superexchange is employed. It was introduced by Baltensperger et al. [BH68] for a description of EuO and adapted to $LaMnO_3$ by Granado et al. [GGS+99].
For this purpose, according to [GGS+99], the possible origins of a frequency change in magnetic materials need to be decomposed:

$$\omega_\alpha(T) - \omega_\alpha(T_0) \equiv \Delta\omega_\alpha(T) = (\Delta\omega_\alpha)_{latt} + (\Delta\omega_\alpha)_{anh} + (\Delta\omega_\alpha)_{ren} + (\Delta\omega_\alpha)_{SPC} \quad (5.1)$$

The term $(\Delta\omega_\alpha)_{latt}$ denotes contributions to the phonon frequencies due to a change of the ionic binding energies, because of an expansion or contraction of the crystalline lattice. $(\Delta\omega_\alpha)_{anh}$ is the frequency shift at constant volume caused by the anharmonicity of the vibrational potential. These two terms describe the temperature dependent phonon frequency shift without any coupling between lattice dynamics and magnetism. The resulting frequency shift can be modelled with a simple phonon–phonon decay model that will be described later in section 7.1. The expression $(\Delta\omega_\alpha)_{ren}$ accounts for the renormalisation of the phonon frequency, which can occur, if the electronic states of a system change near a spin–ordering temperature (for an example, see [ILL+99]). The last term $(\Delta\omega_\alpha)_{SPC}$ is the interesting part, whose origins are discussed in the following.

SPC in A–type $RMnO_3$

The starting point is the Hamiltonian of the $RMnO_3$ system, which can be decomposed into a lattice and a spin part, H_l and H_s, respectively. The first and second term on the right hand side of equation (5.1) are, thus, incorporated in H_l. H_s is based on localised Heisenberg spins, which couple via Superexchange. According to [GGS+99], in $LaMnO_3$, where the Mn^{3+} spins are ferromagnetically coupled within the MnO_2 (ac) plane, only nearest neighbour magnetic ions have to be considered. Effects of higher order (e.g. Dzyaloshinskii–Moriya interaction or magnetic anisotropies) can be neglected. H_s therefore reads as:

$$H_s = \sum_{i,j>i} J_{ij} \left\langle \boldsymbol{S}_i \cdot \boldsymbol{S}_j \right\rangle , \tag{5.2}$$

where J_{ij} is the Superexchange coupling constant between the Mn^{3+} ions i and j with $\boldsymbol{S}$ as their corresponding spin operator. The sum runs over the four nearest neighbours of the Mn^{3+} ion i avoiding double counting. $\langle \boldsymbol{S}_i \cdot \boldsymbol{S}_j \rangle$ is the scalar spin–spin correlation function.
Generally, in crystals with two atoms per unit cell, optical phonons at the Γ point are described by the relative displacement $\boldsymbol{u}(t)$ of the two sublattices from their equilibrium position [BH68]. H_l then becomes a linear oscillator for each mode with the inter–sublattice potential V^l and the reduced mass μ of the two sublattices:

$$V^l = \frac{1}{2} V_2^l u(t)^2 + anharmonic\, terms, \tag{5.3}$$

where $V_2^l = \mu\omega_0^2$ with ω_0 as the frequency of the optical phonon. This is of course only valid in a harmonic approximation.
In magnetic crystals, this picture needs to be expanded due to the possible perturbation of the lattice potential by the order dependent spin energy. This leads to another harmonic term describing the development of the spin energy with respect to the displacement $\boldsymbol{u}$:

$$V^m = \frac{1}{2} V_2^m u(t)^2, \tag{5.4}$$

This additional term modifies the total potential for the phonon to:

$$V = \frac{1}{2}\mu \left[(\omega_0 + \Delta_1\omega)^2 + \frac{1}{\mu} V_2^m \right] u(t)^2 + anharmonic\, terms, \tag{5.5}$$

where $\Delta_1\omega$ accounts for all phonon frequency shifts due to the first two terms on the right side of equation (5.1). Neglecting the anharmonic terms of equation (5.5) and the terms of order $(\Delta_1\omega/\omega_0)^2$, the total frequency shift becomes:

$$\frac{\Delta\omega}{\omega_0} = \frac{\Delta_1\omega}{\omega_0} + \frac{V_2^m}{2\mu\omega_0^2}. \tag{5.6}$$

As already pointed out, we are interested in the frequency shifts caused by the last term on the right side of equation (5.6). Thus, we will have to connect the quantity V_2^m with

the Hamiltonian H_s and equation (5.2). This can be achieved by remembering the naive picture, where SPC is described as a modulation of the magnetic exchange by the phonon mode. It can be modelled as a change ΔJ_{ij} of the Heisenberg energy J_{ij} due to the phonon α. According to [GGS+99], this can be done by a second order Taylor expansion with respect to the O^{2-} displacements associated with α:

$$\Delta J_{ij}^{\alpha}\left(\boldsymbol{u}_k^{\alpha}(t)\right) = \left[\boldsymbol{u}_k^{\alpha}(t)\cdot\boldsymbol{\nabla}_k\right] J_{ij} + \frac{1}{2}\left[\boldsymbol{u}_k^{\alpha}(t)\cdot\boldsymbol{\nabla}_k\right]^2 J_{ij}, \tag{5.7}$$

where $\boldsymbol{u}_k^{\alpha}(t)$ is the displacement vector of the kth O^{2-} ion located between the Mn^{3+} ions i and j. Applying equation (5.7) to equation (5.2) leads to a phonon–dependent part in the second derivative of the total potential energy within the $RMnO_3$ system. Taking into account the symmetry properties and considering only nearest neighbours, the summation of equation (5.2) can be carried out. Further, the magnetic exchange J_{ij} can be split into a J_{xz}–part located in the MnO_2 (ac) plane and a J_y–part perpendicular to this plane:

$$U_{spin}^{\alpha} = -4\left[\widehat{\boldsymbol{u}}_{O1}^{\alpha}(t)\cdot\boldsymbol{\nabla}_{O1}\right]^2 J_{xz}\left\langle\boldsymbol{S}_i\cdot\boldsymbol{S}_j\right\rangle_{xz} + 2\left[\widehat{\boldsymbol{u}}_{O2}^{\alpha}(t)\cdot\boldsymbol{\nabla}_{O2}\right]^2 J_y\left\langle\boldsymbol{S}_i\cdot\boldsymbol{S}_j\right\rangle_{y}, \tag{5.8}$$

with $\widehat{\boldsymbol{u}}_k^{\alpha}(t) = \boldsymbol{u}_k^{\alpha}(t)/\left|\boldsymbol{u}_k^{\alpha}(t)\right|$ as the unit vectors of the O^{2-} displacement for $k = O1, O2$, respectively. Due to the ferromagnetic coupling within the MnO_2 (ac) plane, the first term has a negative sign. For obtaining a frequency shift $\Delta\omega$ from equation (5.8), the total frequency shift derived in equation (5.6) is employed. The term V_2^m describing the frequency shift due to the magnetic contribution to the total potential is equivalent to the quantum mechanically obtained U_{spin}^{α}. Thus, it can be used to gain the following expression for $(\Delta\omega_{\alpha})_{SPC}$:

$$(\Delta\omega_{\alpha})_{SPC} = -\frac{2}{\mu_{\alpha}\omega_{\alpha}}\left[\widehat{\boldsymbol{u}}_{O1}^{\alpha}(t)\cdot\boldsymbol{\nabla}_{O1}\right]^2 J_{xz}\left\langle\boldsymbol{S}_i\cdot\boldsymbol{S}_j\right\rangle_{xz} + \frac{1}{\mu_{\alpha}\omega_{\alpha}}\left[\widehat{\boldsymbol{u}}_{O2}^{\alpha}(t)\cdot\boldsymbol{\nabla}_{O2}\right]^2 J_y\left\langle\boldsymbol{S}_i\cdot\boldsymbol{S}_j\right\rangle_{y}, \tag{5.9}$$

where μ_{α} is the reduced mass of the ions participating in phonon mode α with the corresponding mode frequency ω_{α}.
Of course the strength of SPC depends on the static crystalline properties, e.g. tilting of the MnO_6 octahedra and the mode symmetry. This point will be discussed in detail in chapter 7.
For a more quantitative modelling, the spin–spin correlation function $\langle\boldsymbol{S}_i\cdot\boldsymbol{S}_j\rangle$ has to be approximated. Considering the symmetric MnO_6 breathing mode $B_{2g}(1)$ (see figure 4.2), whose ionic motions are confined to the MnO_2 (ac) plane, equation (5.9) can be further simplified: (i) μ reduces to the mass m of O^{2-}, (ii) the second term on the right side of equation (5.9) can be neglected, reducing the second derivative of J_{ij} to $\partial^2 J_{xz}/\partial u_{xz}^2$, and (iii) in a molecular field approximation, we can write $\left\langle\boldsymbol{S}_i\cdot\boldsymbol{S}_j\right\rangle_{xz} \approx \left[M_{sublatt}(T)/4\mu_B\right]^2$, where $M_{sublatt}(T)$ is the ferromagnetic sublattice magnetisation per Mn^{3+}. These considerations reduce equation (5.9) to:

$$\Delta\omega_{B_{2g}(1)} \approx -\frac{2}{m\omega_{B_{2g}(1)}}\frac{\partial^2 J_{xz}}{\partial u_{B_{2g}(1)}^2}\left(\frac{M_{sublatt}(T)}{4\mu_B}\right)^2. \tag{5.10}$$

This expression enables us to derive a quantitative SPC coupling constant $\partial^2 J_{xz}/\partial u_{xz}^2$ for the $B_{2g}(1)$ mode, if the quantitative sublattice magnetisation $M_{sublatt}(T)$ is known. It can be extracted from measurements either by neutron diffraction or of the macroscopic magnetisation, which for A–type AFM is equivalent to the tilting of the Mn^{3+} spins out of the MnO_2 (ac) plane and, thus, allows the calculation of $M_{sublatt}(T)$ within the plane. Employing the results of the magnetisation experiments carried out in [HSL+97], Granado et al. [GGS+99] derived a coupling constant for $LaMnO_3$ of $\partial^2 J_{xz}/\partial u_{B_{2g}(1)}^2 \approx 16$ mRy/Å. As only the next nearest neighbours are considered until now, this model only accounts for the $RMnO_3$ systems with an A–type AFM structure. For a description of the $RMnO_3$ with incommensurate magnetic structures, e.g. $GdMnO_3$, $TbMnO_3$ or $Eu_{1-x}Y_xMnO_3$ ($x > 0.1$) this model needs to be extended as will be outlined below. It will be based on considerations carried out by Laverdière et al. [LJM+06].

SPC in magnetically incommensurate $RMnO_3$ systems

As already discussed in detail in section 3.2, a decrease of the ionic radius of the R^{3+} ions leads to an increasing structural orthorhombic distortion and, in turn, to a weakening of the A–type AFM. Latter is attributed to a compensation of the ferromagnetic nearest neighbour (NN) magnetic exchange J_1 by the antiferromagnetic next nearest neighbour (NNN) exchange J_2 and J_3 within the MnO_2 (ac) plane [KIS+03]. The direct consequence is the above mentioned weakening of the A–type AFM and, beginning at $EuMnO_3$, an incommensurate magnetic phase (sinusoidal or cycloidal, see phase diagrams in section 3.4) occurs. It is characterised by a propagation vector $\boldsymbol{Q}$ of the periodically modulated spin structure. For the $RMnO_3$ compounds with such a magnetic structure $\boldsymbol{Q} = (Q_x, 0, 0)$ [KIS+03, GKL+04].
To incorporate the magnetic exchange paths J_2 and J_3, the geometry depicted in figure 3.9 can be used to include these as additional terms in the sum of equation (5.2). Thus, the sum is extended from ferromagnetically coupled NN Mn^{3+} spins ($\boldsymbol{r} = \pm 0.5\boldsymbol{a} \pm 0.5\boldsymbol{c}$ with $J_{i,i+(\pm a \pm c)/2} = J_1 < 0$) to NNN Mn^{3+} spins. Latter can be distinguished in two species: along the spin spiral propagation $\boldsymbol{Q}$, i.e. $\boldsymbol{r} = \pm\boldsymbol{a}$, where the coupling is antiferromagnetic $J_{i,i\pm a} = J_2 > 0$, and perpendicular to $\boldsymbol{Q}$, i.e. $\boldsymbol{r} = \pm\boldsymbol{c}$ with a weak antiferromagnetic coupling $J_{i,i\pm c} = J_3 > 0$ [KIS+03].
Carrying out the procedure described for the A–type $RMnO_3$ again with the extended summation leads to the following expression for a phonon frequency shift of the $B_{2g}(1)$ mode:

$$\Delta\omega_{B_{2g}(1)} \approx \frac{1}{2m\omega_{B_{2g}(1)}} \sum_{j,\boldsymbol{r}} \frac{\partial^2 J_{ij}}{\partial u_{B_{2g}(1)}^2} \langle \boldsymbol{S}_i \cdot \boldsymbol{S}_{i+\boldsymbol{r}} \rangle \,, \tag{5.11}$$

where the summation now runs up to NNN Mn^{3+} spins, as discussed above. The spin–spin correlation function for the case of an incommensurate magnetic phase in $RMnO_3$ with $\boldsymbol{Q} = (Q_x, 0, 0)$ is:

$$\langle \boldsymbol{S}_i \cdot \boldsymbol{S}_{i+\boldsymbol{r}} \rangle = K(T) \cos(2\pi \boldsymbol{Q} \cdot \boldsymbol{r}) \,. \tag{5.12}$$

$K(T)$ is a temperature dependent prefactor, that is approximated by assumption (iii), i.e. $K(T) \propto M^2_{sublatt}(T)$. Carrying out the summation in equation (5.11), we get a phonon frequency shift of:

$$\Delta\omega_{B_{2g}(1)} = \frac{K(T)}{m\omega}\left[2D_1\cos(2\pi Q_x\frac{a}{2}) + D_2\cos(2\pi Q_x a) + D_3\right], \tag{5.13}$$

where the $D_j = \partial^2 J_j/\partial u^2_{B_{2g}(1)}$ $(j = 1, 2, 3)$ are the second derivatives of the exchange constants J_j with respect to the displacement pattern $u_{B_{2g}(1)}$ of the O^{2-} ions. In this equation the case of an A–type AFM ordering is included, as can be seen by setting $\boldsymbol{Q} = 0$ and $K(T) \propto M(T)^2_{sublatt}$. This leads to an expression equivalent to equation (5.10).
To connect this derived model with experimental data, one has to consider the measurable quantities in the equations (5.10) and (5.13). The phonon frequency softening $\Delta\omega$ can be obtained from temperature–dependent spectroscopic experiments, i.e. Raman spectroscopy in the case of the $B_{2g}(1)$ mode. For the calculation of a SPC constant, which is either the quantity $\partial^2 J_{xz}/\partial u^2_{B_{2g}(1)}$ in (5.10) or $D_{eff} = 2D_1\cos(\pi Q_x a) + D_2\cos(2\pi Q_x a) + D_3$ in (5.13), also the value of sublattice magnetisation $M_{sublatt}(T)$ within the MnO_2 (ac) plane has to be known.
Assuming that experimental data about $M_{sublatt}(T)$ are available, the just introduced model can be employed for the derivation of coupling constants allowing the comparison with literature data obtained for other $RMnO_3$ compounds. This will be one of the topics covered in section 7.

5.2 The Electromagnon and its Coupling to the polar Phonons

As already implied in section 3.3, the Magneto–Electric Coupling leads to the appearance of a new elementary excitation: the *Electromagnon* (EM). Experimentally it was first observed by Pimenov et al. [PMI+06] and attributed to a magnon, that causes oscillations of the electric polarisation via the Magneto–Electric Effect. Thus, it can be excited by an electric field, i.e. by photons with the matching frequency. The frequency range of the EM in the $RMnO_3$ compounds can be found in the THz–Regime and in the low FIR–regime (i.e. $10cm^{-1} < \widetilde{\nu} < 75cm^{-1}$) [SMP11].
The most interesting question arising from this finding is of course that of the microscopic mechanism responsible for the dipolar activity of a magnon. The first attempt was to model this as a dynamical analogue of the static Magneto–Electric Effect. An adequate model was introduced by Katsura et al. [KBN07]. However, quantitatively such a model would lead to a very weak dynamical response. This is due to the fact, that it is based on an inverse Dzyaloshinskii–Moriya interaction (DMI) (see section 3.3), which is a second–order correction to Superexchange. The experiments of [PMI+06] and the following spectroscopic results on various $RMnO_3$ compounds (e.g. $Eu_{1-x}Y_xMnO_3$ [PLM+08, TYK+09]) showed results contradicting the modelled weak response. Instead several EM with a strong dipolar activity were observed. An example illustrates this in

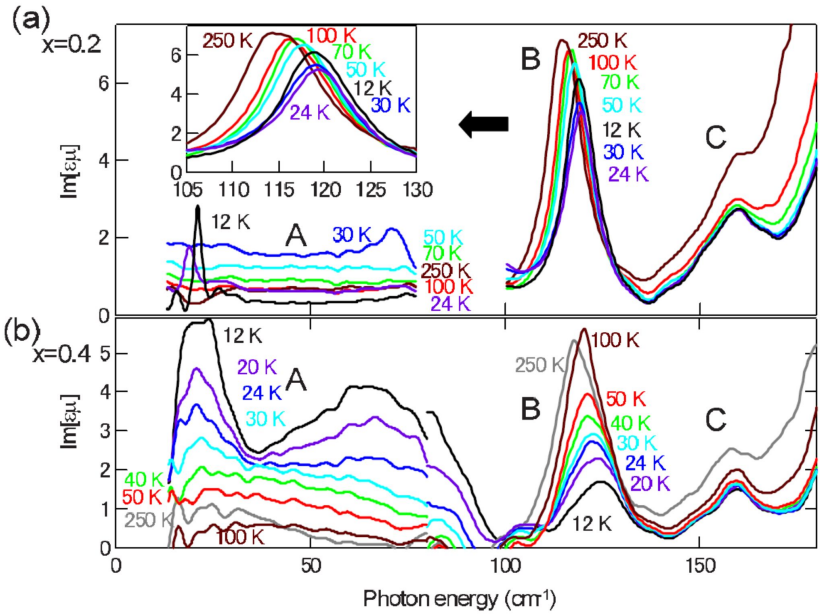

Figure 5.2: Imaginary part Im[ϵ], i.e. dielectric loss spectra, for $\boldsymbol{E}||\boldsymbol{c}$ of $Eu_{1-x}Y_xMnO_3$, (a) $x = 0.2$ and (b) $x = 0.4$, for various temperatures. For $T < 40K$, the emerging EM signature (A) can be seen together with the two phonon modes with the lowest frequencies denoted as (B) and (C), respectively. Taken from [TYK+09].

figure 5.2 that is taken from [TYK+09], where $Eu_{1-x}Y_xMnO_3$ ($x = 0.2$ and $x = 0.4$) was investigated.

These findings lead to the conclusion, that the mechanisms responsible for the static ferroelectric polarisation (i.e. the inverse DMI effect) and that for the dynamical response expressed by the dielectric function are not the same. Thus, a different modelling approach for the dipolar activity of the EM had to be developed. This was carried out by Valdés Aguilar et al. [VAMS+09] within the frame of a model based upon the so–called symmetric Heisenberg–Exchange coupling. It will now be discussed in more detail.

Origin of the dipolar activity of the Electromagnon

The starting point is the same as in the discussion of the SPC, i.e. a Hamiltonian incorporating the Superexchange interactions between Mn^{3+} spins:

$$H_{s-ex} = \frac{1}{2}\sum_{i,j} J_{ij}\boldsymbol{S}_i \cdot \boldsymbol{S}_j. \tag{5.14}$$

Magnetic anisotropies as well as the DMI are neglected in the following treatment. The Mn^{3+} are located at $\boldsymbol{R}_1 = (0, 0, 0.5)$, $\boldsymbol{R}_2 = (0.5, 0, 0)$, $\boldsymbol{R}_3 = (0, 0.5, 0.5)$, and $\boldsymbol{R}_4 = (0.5, 0.5, 0)$ (see table 3.2). The Mn^{3+} at $\boldsymbol{R}_1$ and $\boldsymbol{R}_2$ as well as the equatorial O_2^{2-} mediating the Superexchange within the MnO_2 (ac) plane are sketched in figure 5.3(b). As described in section 3.2, the spin spiral in the multiferroic phase results mainly

from the competition between nearest neighbour ferromagnetic exchange $J_{i,i+(\pm a \pm c)/2} < 0$ and the strong next nearest neighbour antiferromagnetic exchange $J_{i,i\pm a} > 0$ also within this plane. The resulting modulated magnetic structure is shown in figure 5.3(a) together with the corresponding vector of rotation $\boldsymbol{R} \propto \boldsymbol{S}_i \times \boldsymbol{S}_{i+1}$ and the propagation vector of

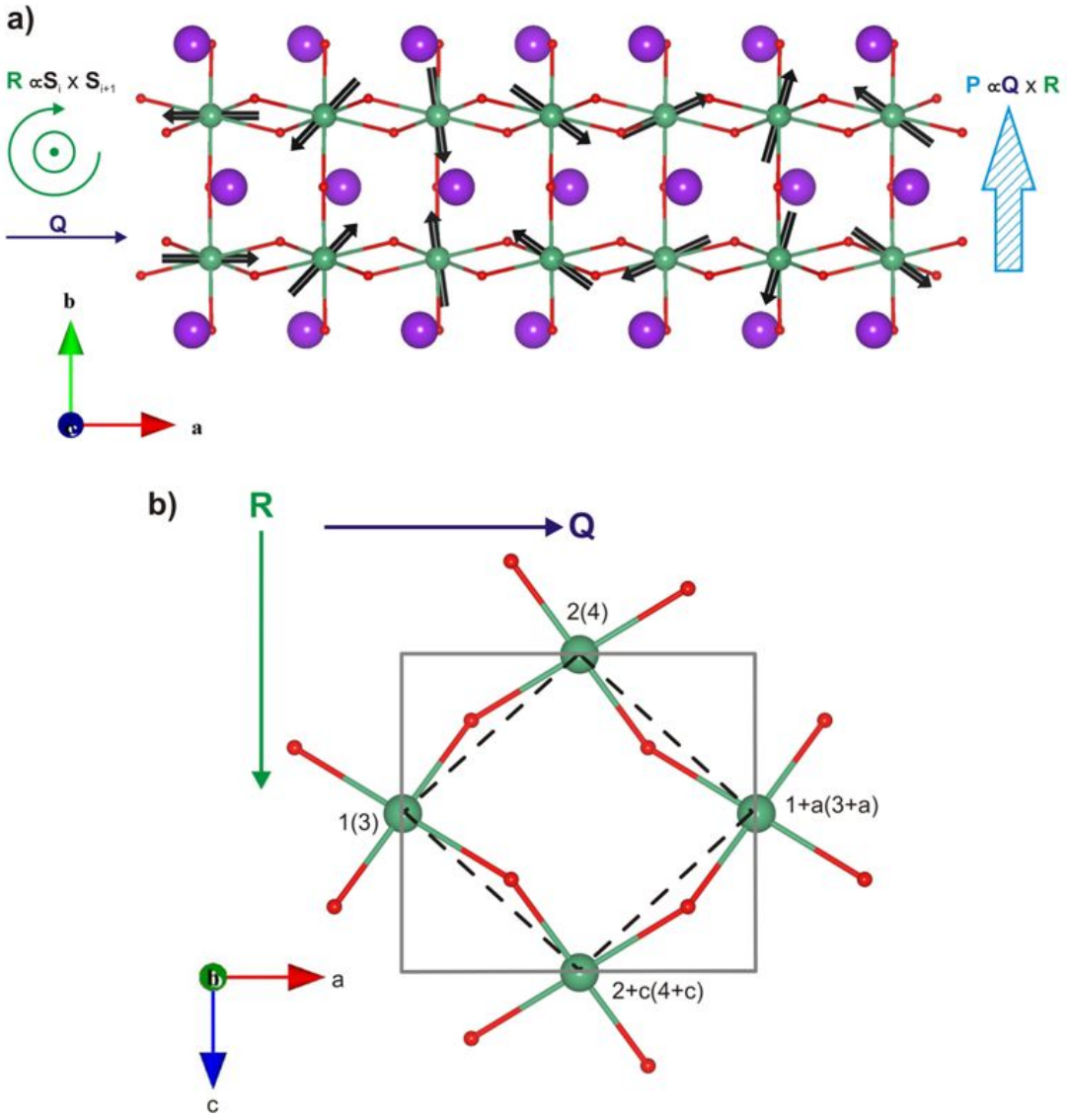

Figure 5.3: Sketch (a) of the orthorhombic $RMnO_3$ structure projected perpendicular to the c–axis and (b) of one MnO_2 (ac) layers of the Pnma unit cell. R^{3+} ions are shown as purple balls together with Mn^{3+} (green balls) and O^{2-}(red balls). Also indicated in (a) are the Mn^{3+} spins (black arrows) and in (a) and (b) the spin rotation axis $\boldsymbol{R} \propto \boldsymbol{S}_i \times \boldsymbol{S}_{i+1}$ as well as the propagation vector $\boldsymbol{Q}$ of the spin spiral. Partly adapted from [Kim07] and [VAMS+09].

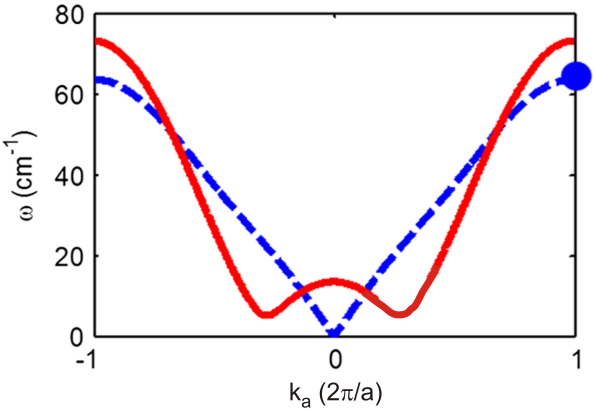

Figure 5.4: Typical magnon dispersion for a spin spiral confined within the (ab) plane of the $RMnO_3$ system (Pnma notation) along $\boldsymbol{k} = (k_a, 0, 0)$. The dashed blue line corresponds to the longitudinal magnon branch and the solid red line to the transversal branch (see explanation in the text). The solid blue circle indicates the position of the EM. Taken from [VAMS+09] and adapted to Pnma.

the spin spiral $\boldsymbol{Q}||\boldsymbol{a}$. In this sketch, one can also see, that the antiferromagnetic exchange along the b–axis with $J_{i,i+b/2} > 0$ leads to a "double spiral"with antiparallel spins in adjacent MnO_2 (ac) planes shifted by $\pm b/2$. This spin structure can be expressed as:

$$\langle \boldsymbol{S}_i \rangle = \pm \left(\boldsymbol{c} \cos\left(\boldsymbol{Q} \cdot \boldsymbol{r}_i\right) - \boldsymbol{b} \sin\left(\boldsymbol{Q} \cdot \boldsymbol{r}_i\right) \right), \tag{5.15}$$

where the positive (negative) sign on the right side corresponds to MnO_2 (ac) layers with integer or half–integer y/b ratio.
Until now, only static properties of the $RMnO_3$ system have been regarded. However, these have direct consequences for the spin dynamics. A sketch of the resulting magnon spectrum of a double spiral structure with its magnon propagation vector $\boldsymbol{k}$ along the a–axis is shown in figure 5.4. According to [VAMS+09], two branches in the magnon dispersion of a double spin spiral occur: a longitudinal branch (dashed blue line in figure 5.4) and a transversal branch (solid red line in figure 5.4). For the longitudinal branch, the oscillation of the order parameter $\boldsymbol{L} = \boldsymbol{S}_1 + \boldsymbol{S}_2 - \boldsymbol{S}_3 - \boldsymbol{S}_4$, where $\boldsymbol{S}_i$ is the spin associated with the Mn^{3+} ion located at $\boldsymbol{R}_i$, is confined within the (ab) plane of the spin spiral. This can be understood as a modulation of the tilting angle of the spins along the propagation of the spiral and, thus, as a phason mode. For the transversal branch of the magnon dispersion, $\boldsymbol{L}$ points out of this plane.

The crucial point for understanding the dipolar activity of the EM will now be illustrated. In agreement with the experimentally derived EM optical selection rules, a photon–induced electric field along the c–axis, $\boldsymbol{E}||\boldsymbol{c}$, has to be considered. An inspection of figure 5.3 (b) shows, that due to the static orthorhombic distortion of the $RMnO_3$ system, the O^{2-} ions between Mn^{3+} within the MnO_2 (ac) plane are shifted from the centre positions of the dashed lines, which indicate their high symmetry positions within the cubic $Pm\bar{3}m$ unit cell. An electric field now leads to an additional uniform displacement

of the O^{2-} along the c–axis and, due to the mediating role of the O^{2-} for the Superexchange interaction between adjacent Mn^{3+}, all magnetic exchange constants within the MnO_2 (ac) plane will be influenced by this uniform shift. Taking into account the Pnma symmetry of $RMnO_3$, these changes of the magnetic exchange constants can be written as follows:

$$\begin{aligned} J^*_{1,2} &= J_{1,2} + \Delta J, \\ J^*_{1+a,2} &= J_{1+a,2} - \Delta J, \\ J^*_{1,2+c} &= J_{1,2+c} + \Delta J, \\ J^*_{1+a,2+c} &= J_{1+a,2+c} - \Delta J, \end{aligned} \tag{5.16}$$

where ΔJ is the change of J_{ij} proportional to the external electric field. Thus, an applied uniform electric field along the c–axis is responsible for a modulation of the nearest neighbour magnetic exchange along the a–axis parallel to the propagation vector $\boldsymbol{Q}$ of the spin spiral. The resulting magnetic exchange in the presence of an electric field can be expressed as:

$$J \propto J_0 + \Delta J \cos\left(\boldsymbol{k_{EM}} \cdot \boldsymbol{r}\right) \tag{5.17}$$

with $\boldsymbol{k_{EM}} = (2\pi/a, 0, 0)$. An alternation with period $2\pi/a$ of the magnetic exchange along the a–axis, as described above, is equivalent to a longitudinal magnon at the Brillouin zone boundary, as indicated by the solid blue point in figure 5.4. Thus, a uniform electric field along the c–axis can excite a zone–edge longitudinal magnon with $\boldsymbol{k_{EM}} = (2\pi/a, 0, 0)$ within the $RMnO_3$ system. This excitation can be understood as a phason mode, i.e. a periodic modulation of the tilting angle between adjacent Mn^{3+} and, thus, of $\boldsymbol{S}_1$ and $\boldsymbol{S}_2$ in the (bc) plane, together with a simultaneous modulation of the tilting angle between $\boldsymbol{S}_3$ and $\boldsymbol{S}_4$ also in the (bc) plane, but shifted by $b/2$ [VAMS+09].
Similar interactions with $\boldsymbol{E}||\boldsymbol{a}$ or $\boldsymbol{E}||\boldsymbol{b}$ are also possible, but this would cause a modulation of the magnetic exchange, which is perpendicular to the propagation direction of the spin spiral, i.e. orthogonal to $\boldsymbol{Q}$. In these directions the Mn^{3+} spins order in a collinear way. Thus, a modulation of J does not lead to a change of the tilting angle between $\boldsymbol{S}_i$ and $\boldsymbol{S}_j$, as it is the case for $\boldsymbol{E}||\boldsymbol{c}$, and, therefore, not to the excitation of a magnon. This model explains the unique excitation condition of $\boldsymbol{E}||\boldsymbol{c}$, which is not connected to the relative orientation of the spin spiral in the (ab) plane. An application of an external magnetic field does not change this condition, as would be expected by a mechanism based on the dynamical analogue of the inverse DMI describing the static ferroelectric polarisation [SD06, KBN07]. Therefore, within the Heisenberg–Exchange model, the EM optical selection rules experimentally observed can be understood.
Having introduced the model describing the microscopic mechanism responsible for the dipolar activity of the EM, its coupling to the lattice dynamics, i.e. to the phonons, will now be discussed.

Coupling Effects of Electromagnons and Phonons

The coupling of EM and Phonons is of special importance, because the EM dipolar activity has to be transferred from the polar, i.e. infrared–active, phonons. This is due to the conservation of the spectral weight within absorption spectra.

Spectral weight in optical spectroscopy is defined as the area under the optical conductivity [SMP11]. It is directly connected to the total number of electrons within the sample and must, therefore, be conserved in all magnetic and dielectric phases. The appearance of an additional elementary excitation, i.e. the EM, at lower temperatures, therefore, goes along with a transfer of spectral weight to this excitation. Experimentally, it could be demonstrated, that the gain of spectral weight of the EM goes along with a loss of spectral weight on the side of the polar phonons, an example is shown in figure 5.5. This aspect of EMPC was subject of intensive investigative efforts and, thus, data concerning the shift of spectral weight are available for all multiferroic $RMnO_3$ compounds investigated within this thesis [PRM$^+$06, TYK$^+$09, SKR$^+$09]. These data showed, that mainly the phonons with B_{3u} symmetry and frequency $\widetilde{\nu} < 250 cm^{-1}$ (i.e. the $B_{3u}(1)$ to $B_{3u}(3)$ modes) loose spectral weight to the emerging EM. This could be verified in the FT–IR experiments carried out for this thesis (see section 8.1).

Another aspect of EMPC is a renormalisation of the phonon frequencies. In contrast to the detailed data about the shift of spectral weight, the shift of phonon frequency has been taken into account, but not systematically investigated for the whole $RMnO_3$ series. Only for $TbMnO_3$ the temperature dependence for all B_{3u} phonon modes was determined and discussed phenomenologically [SKR$^+$09].

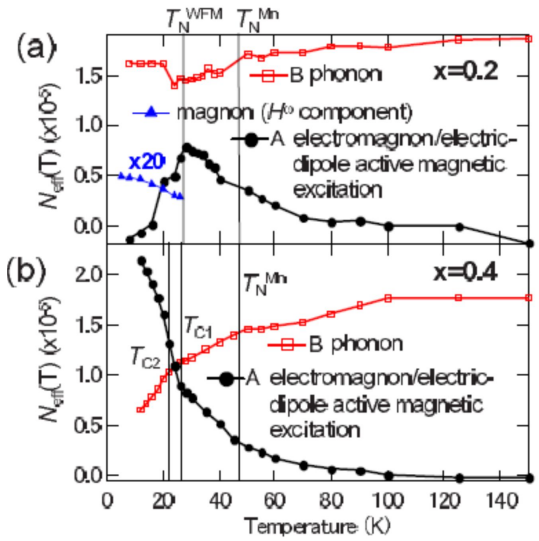

Figure 5.5: Spectral weight $N_{eff} = 2m_0V/\pi e^2 \int_{\omega_1}^{\omega_2} \omega' Im[\epsilon(\omega')]d\omega'$ of the EM and the B_{3u} phonon mode with the lowest frequency for $Eu_{1-x}Y_xMnO_3$ ($x = 0.2$ and $x = 0.4$) plotted with respect to temperature. m_0, e, and V are the electron mass, the charge, and the unit cell volume, respectively. Taken from [TYK$^+$09].

The renormalisation of phonon frequencies was already predicted within the above mentioned model of Katsura et al. [KBN07], who modelled the EM as excitations of the spin spiral. This model could be employed to obtain the right values for the phonon renormalisation in $GdMnO_3$ [PRM$^+$06], but it cannot reproduce the experimentally observed unique excitation condition $\boldsymbol{E}||\boldsymbol{c}$ as well as the spectral weight of the EM. It also fails to explain, that the onset of the phonon frequency shift is located at temperatures higher than the transition temperature of the ferroelectric phase. Thus, another model describing the shift of phonon frequencies due to EMPC has to be developed, which should be compatible with the Heisenberg–Exchange mechanism. A proposal for such a model will be presented in section 8.3 with the help of the insights the experimental results of this thesis provide.
As a last point, a rather subtle aspect will be pointed out to the reader: both discussions of the coupling effects (SPC and EMPC) start with a Heisenberg model of magnetic exchange. Further, the SPC as well as the dipolar activity of the EM base on the modulation of the magnetic exchange by a dynamical shifting of the O^{2-} ions mediating the Superexchange between adjacent Mn^{3+} ions. This fact again indicates the intimate coupling between lattice and spin degrees of freedom within the $RMnO_3$ system.
With the preparations of the last four chapters the fundamental theoretical concepts are introduced. Thus, we will now turn to the experimental results of Part II.

Part II

Results and discussion

Chapter 6

Lattice dynamics of stoichiometric $RMnO_3$ and doped $Eu_{1-x}Y_xMnO_3$

In this first chapter of part II the lattice dynamics of both investigated sample series will be discussed. This analysis will be the base for a following quantitative discussion of the coupling effects outlined in chapter 5. To exclude influences of the latter, the whole analysis presented in this chapter is based on measurements carried out at room temperature – far above the temperature regime of the magnetically ordered phases.
This chapter is organised as follows: The first section will be dedicated to phonon mode assignment using the $GdMnO_3$ compound. The experimentally obtained spectra are employed to connect the observed phonon frequencies to the mode patterns shown in section 4.3. Further, the Raman spectra will be used for a quantitative comparison with literature. Adding the information the reflectivity spectra provide concerning the IR–active phonon modes, a first time analysis of the complete lattice dynamics of $GdMnO_3$ can be presented.
In the second section, a systematic investigation of the impact of the R^{3+} substitution on the lattice dynamics of the stoichiometric $RMnO_3$ (R^{3+} = Eu^{3+}, Gd^{3+}, Tb^{3+}) and the doped $Eu_{1-x}Y_xMnO_3$ series ($0 \leq x \leq 0.5$) will be carried out. This section will give a complete analysis of these dynamics employing Raman and FT–IR Spectroscopy, thus considerably exceeding the published selective studies carried out on some of the discussed Manganite compounds. For that purpose, $RMnO_3$ will be discussed first, followed by a comparative analysis of $Eu_{1-x}Y_xMnO_3$. This approach will further give the opportunity to answer the upcoming question of disorder induced effects on the lattice dynamics of $Eu_{1-x}Y_xMnO_3$ potentially caused by the doping approach.

6.1 Mode assignment

As already discussed in the chapters 3 and 4, the lattice dynamics of the Multiferroic Manganites can be understood as resulting from the orthorhombic distortion of the cubic Perovskite structure. In this section, the Raman and reflectivity spectra obtained at room temperature will be analysed for the purpose of a mode assignment. The experimental

setups employed were the Raman spectrometer Renishaw 1000 equipped with a Leica Microscope type DM LM, the FT–IR spectrometer Bruker IFS 113v in Würzburg and the almost identical setup in Augsburg. A detailed description of these setups can be found in Appendix A.
For the mode assignment, we will use $GdMnO_3$ as model system for a *b–cut* sample, first due to its polished sample surface, which causes a rather low leakage of nominally symmetry forbidden phonon modes compared to unpolished samples, and second due to its stoichiometric composition minimising the potential effects of disorder, induced by the doping approach of $Eu_{1-x}Y_xMnO_3$. Both arguments will be illustrated in the following. The expression *b–cut* implies, that the crystal is cut as a flat platelet (thickness approximately 1 mm, lateral dimension $\approx 3 \times 3$ mm) in such a way, that the a– and c–axes are oriented parallel to the sample surface and, thus, the b–axis is perpendicular to this plane. This narrows the degrees of freedom for the selection rules in both spectroscopical techniques as discussed in section 4.2.1 for FT–IR and in section 4.2.2 for Raman Spectroscopy. For completeness, the only exception from the b–cut sample series, the a–cut $Eu_{0.9}Y_{0.1}MnO_3$, is discussed and also the consequences of this different orientation for the Raman- and reflectivity spectra.

6.1.1 Raman Spectroscopy

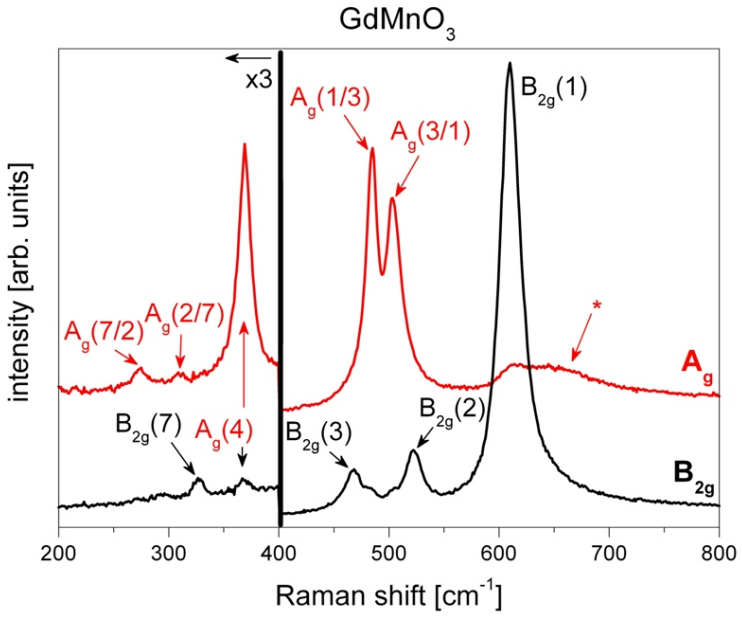

Figure 6.1: Polarised Raman spectra in $b\,(a,a)\,\bar{b}$ (red) and $b\,(a,c)\,\bar{b}$ (black) scattering geometry obtained from $GdMnO_3$. These geometries give access to the A_g and B_{2g} phonon modes, respectively. The spectra are vertically shifted for clarity and the low–energy parts ($\widetilde{\nu} < 400 cm^{-1}$) are multiplied by a factor of 3. The mode assignment is carried out according to [IAL+98].

Table 6.1: Main atomic motions and frequencies of the Raman–active phonon modes observed for $GdMnO_3$ compared to the data of [IAL$^+$06] obtained from polycrystalline $GdMnO_3$. The corresponding mode patterns obtained from own DFT calculations can be found in section 4.3.

Mode	Main atomic motions	Exp. Phonon frequency $[cm^{-1}]$	Phonon frequency of [IAL$^+$06] $[cm^{-1}]$
$A_g(7/2)$	O1(x) motion → in–phase MnO_6 y rotations	274.2	276.1
$A_g(2/7)$	in–phase MnO_6 y rotations → O1(x) motion	310.2	309.8
$A_g(4)$	out–of–phase MnO_6 x rotations	369.0	370.5
$A_g(1/3)$	O2 antistretching → MnO_6 bending	484.3	486.4
$A_g(3/1)$	MnO_6 bending → O2 antistretching	504.3	506.0
$B_{2g}(7)$	O1(z)	327.3*	329.2
$B_{2g}(3)$	out–of–phase MnO_6 bending	468.1	468.9
$B_{2g}(2)$	in–phase O2 "'scissorslike"'	522.6	525.0
$B_{2g}(1)$	in–plane O2 stretching (= "breathing"mode)	609.2	611.7

The polarised Raman spectra obtained for $GdMnO_3$ at room temperature are shown in figure 6.1. The spectra are recorded in $b\,(a,a)\,\overline{b}$ and $b\,(a,c)\,\overline{b}$ scattering geometry, giving access to the A_g (red) and B_{2g} (black) phonon modes, respectively. As already mentioned in the caption of table 4.3 (section 4.2.2), the above named scattering geometries are equivalent to $b\,(c,c)\,\overline{b}$ and $b\,(c,a)\,\overline{b}$, respectively.
The phonon modes are fitted with appropriate fit functions, i.e. Lorentz– and Fano–functions (the latter only for the $B_{2g}(1)$ mode). The fit parameters of these functions are the phonon frequency ω and the phonon linewidth Γ and – in the case of fitting a Fano line shape – the Fano–parameter q. Technical details about the fit functions and the argumentation for employing a different line shape for fitting the $B_{2g}(1)$ mode can be found in Appendix B.
Comparison with literature is carried out for the phonon frequencies of $GdMnO_3$ in table 6.1 yielding a good agreement. Good qualitative agreement can also be found for the general shape of the Raman spectra for the stoichiometric $RMnO_3$ (R^{3+} = Eu^{3+}, Gd^{3+}, Tb^{3+}) series presented in section 6.2.1 with polycrystalline $RMnO_3$ systems investigated in literature [IAL$^+$98, IAL$^+$06]. Therefore, the observed phonon modes are assigned as listed in table 6.1. The corresponding mode patterns can be found in section 4.3.

One characteristic feature of the Raman spectra is the very strong Raman–activity of the higher–frequency (phonon frequency $\omega > 300cm^{-1}$) Raman modes. Their main

participants are the O^{2-} ions, whose periodic motion modulates the Mn–O bonds. On the other hand, Raman modes with stronger involvement of the heavy Rare–Earth ions (e.g. $A_g(7/2)$, $A_g(2/7)$ or $B_{2g}(7)$) are rather weakly Raman–active. This behaviour is attributed to the smaller polarisability of the longer R–O bonds in contrast to the shorter Mn–O bonds. A further common feature of the Rare–Earth Manganites with orthorhombic Pnma structure is the broad structure centred around 650 cm^{-1} in the A_g spectra. It is attributed to a one–phonon mode from the Brillouin zone boundary [IHL+07]. The Raman activity originates from local disorder within the crystal and occurs for single crystalline as well as polycrystalline samples and – as can be seen in section 6.2 – for stoichiometric as well as doped Rare–Earth Manganite compounds.
An important point for the discussions in the following chapters is the influence of the quality of the crystalline surface on the fulfilment of the selection rules in the Raman spectra. This is especially relevant, as only three of the investigated samples ($GdMnO_3$, $Eu_{0.8}Y_{0.2}MnO_3$, and $Eu_{0.5}Y_{0.5}MnO_3$) are polished up to optical degree, while the other samples have different degrees of residual surface roughness. For an illustration of the consequences, the A_g and B_{2g} Raman spectra of a polished and an unpolished part of $Eu_{0.8}Y_{0.2}MnO_3$ are plotted in figure 6.2. For both phonon symmetries the selection rules are well fulfilled for the polished area, while strong symmetry forbidden peaks are observed in the rough area. The latter are marked by asterisks in figure 6.2 with the most prominent representative being the $B_{2g}(1)$ peak at $\approx 610 cm^{-1}$ in A_g symmetry.
It was mentioned before, that the only exception from the b–cut sample series is the a–cut $Eu_{0.9}Y_{0.1}MnO_3$. The consequences for the Raman spectra are modified possible scattering configurations, i.e. $a\,(b,b)\,\overline{a}$ and $a\,(b,c)\,\overline{a}$, leading to A_g and B_{3g} symmetry, respectively. Thus, the A_g spectra fit within the scheme of the b–cut sample series. The B_{3g} spectrum, however, showed no observable phonon modes due to the very weak Raman activity of the B_{3g} modes – a finding, which is in agreement with data of Iliev et al. obtained from $LaMnO_3$ and $YMnO_3$ with Pnma structure [IAL+98]. For this reason, the B_{3g} spectra are not regarded within this thesis. But, nevertheless, the unpolished sample surface of $Eu_{0.9}Y_{0.1}MnO_3$ allowed the observation and quantitative fitting of the strong $B_{2g}(1)$ mode due to the previously discussed leakage of symmetry forbidden phonon modes. This can be seen in the series of A_g spectra in figure 6.9 in section 6.2.

6.1.2 FT–IR Spectroscopy

As discussed in section 4.2.1, the different symmetries of the IR–active phonons can be distinguished by employing light polarised parallel to the individual crystal axes. Thus, according to table 4.2, for b–cut samples B_{1u} and B_{3u} symmetry are accessible, when applying the electric field of the polarised infrared radiation parallel to the a– and c–axis, respectively. For these two symmetries, the measured reflectivity spectra are shown in the upper row of figure 6.3 for $GdMnO_3$. The open circles hereby indicate the raw data, while the solid lines represent the reflectivity fit function. The latter is a model function, which has the appropriate number of phonon modes (chosen according to number of allowed modes determined by the IR selection rules). Its fitting parameters are transverse

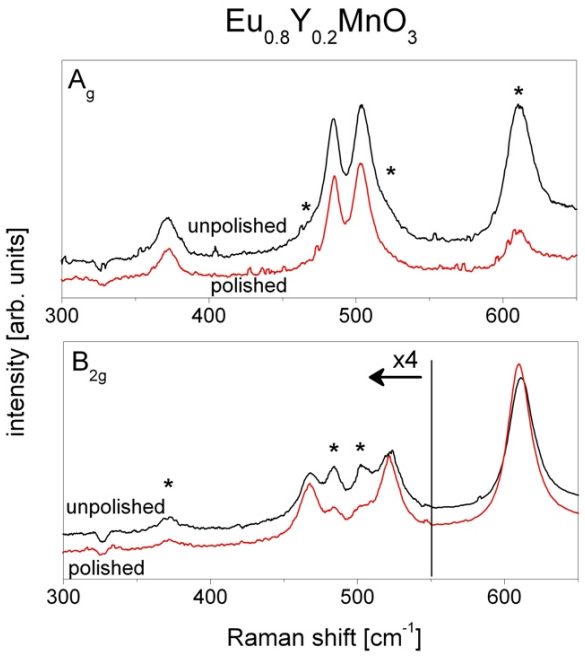

Figure 6.2: Polarised Raman spectra of a polished and an unpolished part of $Eu_{0.8}Y_{0.2}MnO_3$. The spectra were obtained under the same scattering configurations as that shown in figure 6.1. Nominally symmetry forbidden peaks are marked by asterisks.

optical frequency ω_T, ion plasma frequency ω_p and linewidth Γ for each phonon mode, respectively. The fitting procedure was carried out employing the fitting software RefFit [Kuz09]. More details of the fitting procedure can be found in Appendix B.

In the second row the imaginary part of the dielectric function, i.e. the dielectric loss, ϵ_2, is shown. For details about the fitting procedure and deriving ϵ_2 the reader is again referred to Appendix B.

In agreement with literature, see e.g. [SKR+09], the notation of the phonon modes is chosen as their symmetry character together with a number determined by the order of phonon frequencies. These numbers are indicated in the plots of ϵ_2 in figure 6.3.

In contrast to the other samples, the already mentioned a–cut $Eu_{0.9}Y_{0.1}MnO_3$ allows light polarised parallel to b– and c–axis and, therefore, the observation of phonons with B_{2u} and B_{3u} symmetry, respectively. Thus, for a comparison of $Eu_{0.9}Y_{0.1}MnO_3$ with the b–cut samples, only the B_{3u} spectrum can be considered. The measured reflectivity raw data, reflectivity fits and the derived ϵ_2 for both symmetries are shown in figure 6.4 – in the same arrangement as that employed in figure 6.3 for $GdMnO_3$. This sample is also a good example for the influence of an unpolished sample surface with moderate residual roughness on the reflectivity spectra. Especially the plots of ϵ_2 clearly show, that the phonon modes are stronger damped and less sharp than those obtained from a sample with a polished sample surface, e.g. from $GdMnO_3$.

As mentioned before, a quantitative comparison of the phonon frequencies with literature is not straightforward for the infrared–active phonon modes, because only in [PRM+06]

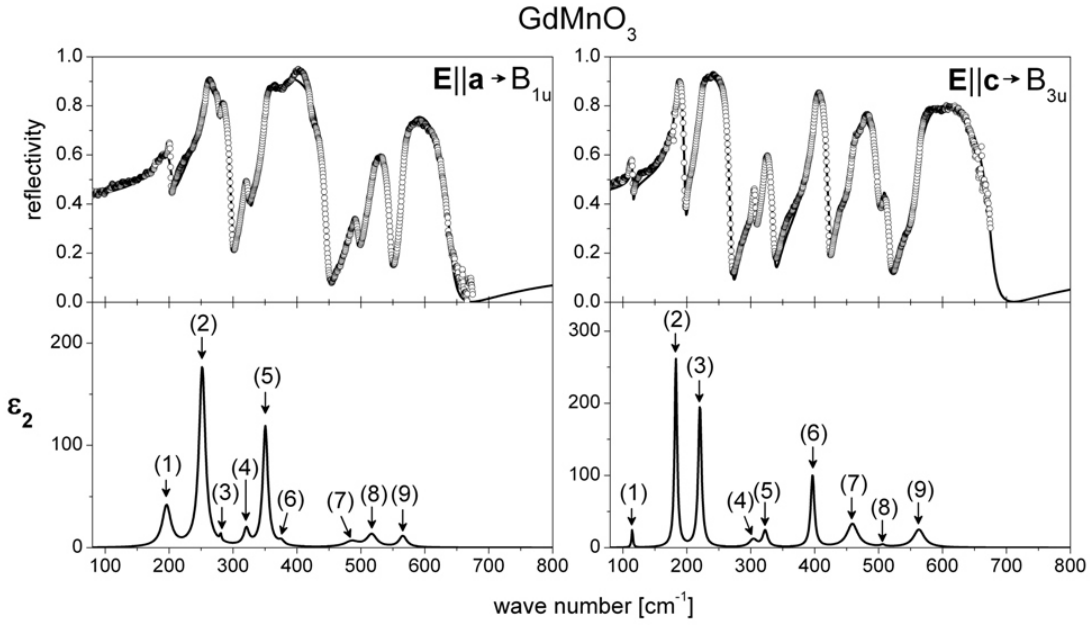

Figure 6.3: Polarised reflectivity spectra (upper row) and hence derived dielectric loss ϵ_2 (lower row) of $GdMnO_3$ in the FIR range. In the reflectivity spectra the open circles indicate the raw data, while the solid lines represent the reflectivity fit functions. The orientation of the electric field of the IR–radiation is indicated with respect to the crystalline axes together with the resulting phonon symmetry (B_{1u} or B_{3u} for a b–cut sample). The fitted phonon peaks are denoted within the ϵ_2 spectra.

polarised FT–IR spectra obtained from $GdMnO_3$ are shown. These were carried out on samples cut from the same macroscopic crystal than the $GdMnO_3$ sample employed for the measurements presented in this thesis. Also both spectroscopic experiments on $GdMnO_3$ were carried out on the same FT–IR spectrometer (Augsburg). Thus, a quantitative comparison of phonon frequencies is omitted here. However, polarised FT–IR spectra of another stoichiometric $RMnO_3$ compound, $TbMnO_3$, published in [SKR+09, SMSL10], show a good agreement of the spectral shape for the phonon modes with B_{3u} symmetry.

6.2 Impact of R^{3+} replacement on the lattice dynamics

Having assigned the phonon modes to their corresponding mode patterns employing the model system $GdMnO_3$, we will now turn to a first time complete analysis of the lattice dynamics of both samples series with respect to the incorporated R^{3+} ions.

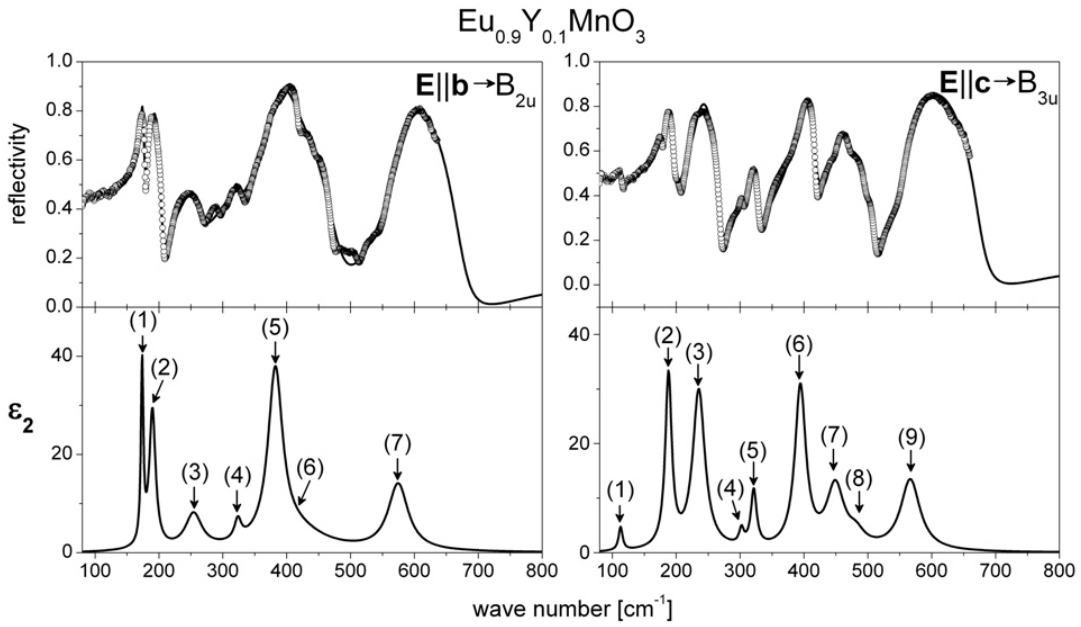

Figure 6.4: Polarised reflectivity spectra (upper row) and hence derived ϵ_2 (lower row) of the a–cut $Eu_{0.9}Y_{0.1}MnO_3$ for B_{1u} and B_{3u} symmetry, respectively. In the reflectivity spectra the open circles indicate the raw data, while the solid lines represent the reflectivity fit functions. Due to the a–cut sample surface, B_{2u} and B_{3u} phonon symmetries are accessible.

This section is organised as follows: First, in subsection 6.2.1, we will analyse the consequences of a complete replacement of the R^{3+} ion, i.e. the stoichiometric $RMnO_3$ (R^{3+} = Eu^{3+}, Gd^{3+}, Tb^{3+}) series. After that, a comparative analysis of the doped $Eu_{1-x}Y_xMnO_3$ ($0 \leq x \leq 0.5$) series will be carried out in subsection 6.2.2. In both sections, first the Raman spectra will be discussed followed by the reflectivity spectra obtained from FT–IR measurements.

6.2.1 Stoichiometric $RMnO_3$ (R^{3+} = Eu^{3+}, Gd^{3+}, Tb^{3+})

As already discussed in chapter 3, stable $RMnO_3$ compounds can be synthesised in the Pnma structure for the trivalent Rare–Earth ions R = La^{3+}, Pr^{3+}, Nd^{3+}, Sm^{3+}, Eu^{3+}, Gd^{3+}, Tb^{3+}, Dy^{3+}. For Ho^{3+} as well as for Y^{3+} (which is not a member of the Lanthanide series) the Pnma structure can be stabilised by applying pressure during the crystal growth [LWSC04]. This just described $RMnO_3$ series was investigated by Raman Spectroscopy on a mix of single crystalline and polycrystalline samples at room temperature [IAL+06]. The stoichiometric $RMnO_3$ series investigated within this thesis consists of single crystals with the trivalent Rare–Earth ions R^{3+} = Eu^{3+}, Gd^{3+} and Tb^{3+}. All samples are b–

cut with different degrees of surface polishing. While $GdMnO_3$ is polished up to optical degree, $EuMnO_3$ and $TbMnO_3$ have a rather high surface roughness and, thus, a more pronounced leakage of symmetry forbidden phonon modes can be expected in the Raman and reflectivity spectra. We will first discuss the Raman spectra of the stoichiometric $RMnO_3$ series.

Raman Spectroscopy

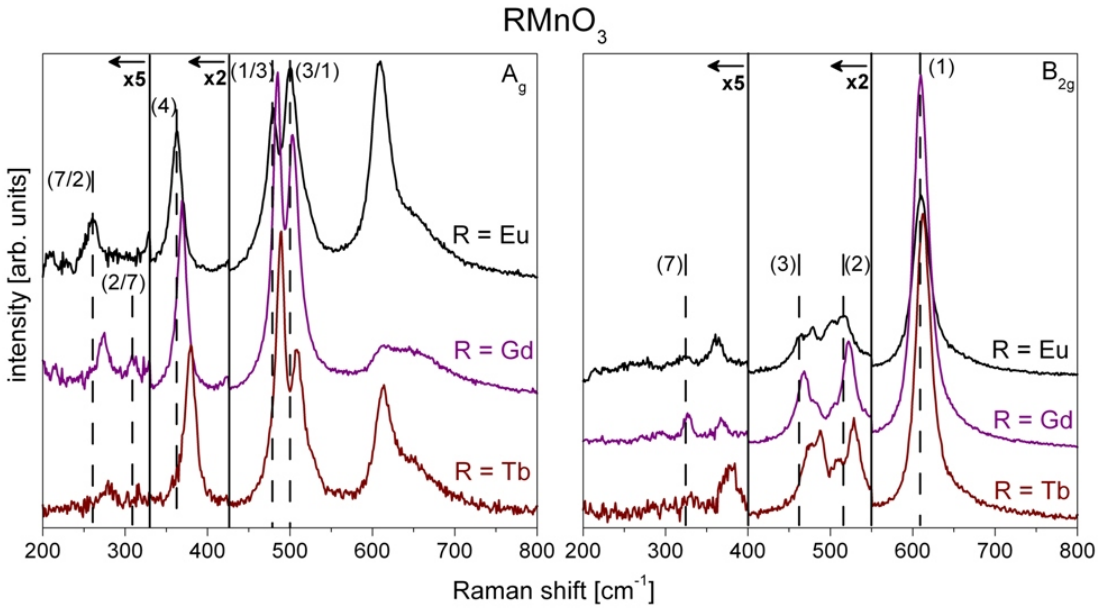

Figure 6.5: Polarised Raman spectra of the $RMnO_3$ series (R^{3+} = Eu^{3+}, Gd^{3+}, Tb^{3+}) in A_g (left panel) and B_{2g} (right panel) symmetry. For clarity, the spectra are vertically shifted and on their low frequency side the spectra are multiplied by the factors indicated on the left side of the vertical black bars.

The Raman spectra of the stoichiometric $RMnO_3$ series are shown in figure 6.5 for A_g (left panel) and B_{2g} symmetry (right panel), respectively. The spectra of all three samples show the characteristic shape of the Raman spectra obtained from $RMnO_3$ crystals with Pnma structure, as can be seen by comparison with [IAL+06].
A general trend observed in the Raman spectra is, that the phonon frequencies increase with decreasing R^{3+} ion radius. As almost all observed Raman active phonons are mainly displacements of the O^{2-}, the frequency shifts originate from an indirect effect: As pointed out in section 3.1, the tilting angle of the MnO_6 octahedra depends on the ionic radii of the R^{3+}. When these are decreased by replacing R^{3+} with another isovalent Rare–Earth ion with a smaller ionic radius, the Mn–O–Mn bond angle also further decreases, which is equivalent to an increase of the MnO_6 tilting. This implies a shift of the O^{2-} equilibrium position away from the Mn–Mn axis. This shift, in turn, influences the phonon frequencies of the Raman–active phonons. The amount of these frequency shifts depends on the

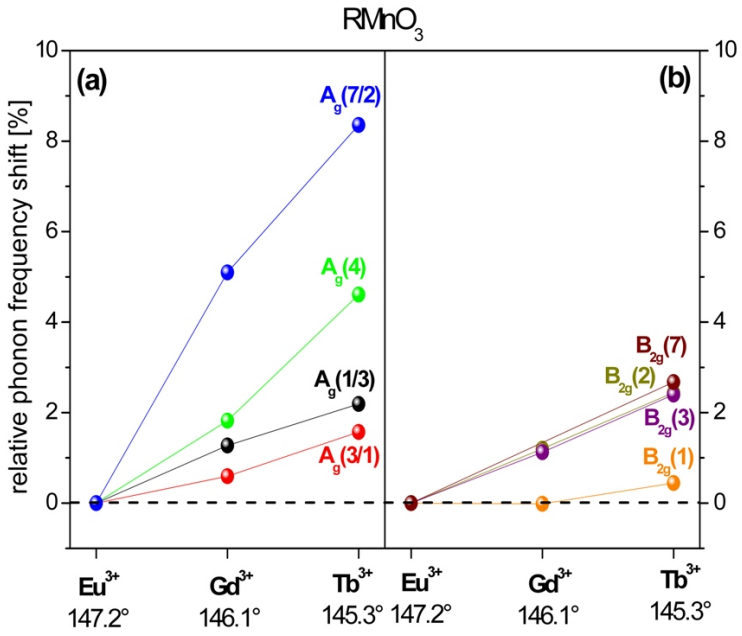

Figure 6.6: Relative shift of phonon frequencies for the $RMnO_3$ series with respect to $EuMnO_3$ as a function of the incorporated R^{3+} and the resulting Mn–O–Mn bond angle. (a) shows the phonons with A_g symmetry and (b) the phonons with B_{2g} symmetry, respectively. The quantitative values for the Mn–O–Mn bond angle are extracted from [GKL+04].

individual phonon modes.

For illustration, the mode–dependent relative frequency shifts with respect to the phonon frequencies of $EuMnO_3$ are plotted versus the incorporated R^{3+} ion in figure 6.6 for the A_g modes (left panel) as well as the B_{2g} modes (right panel), respectively. These data can also be found in table form in table B.1 (Appendix B). As the $A_g(2/7)$ mode cannot be observed in $EuMnO_3$, the relative R^{3+} dependence of this mode frequency is not shown in figure 6.6 due to the missing $EuMnO_3$ reference.

The strongest shifts among the Raman–active phonon modes are observed for the $A_g(7/2)$ ($\approx 8.4\%$) and $A_g(4)$ modes ($\approx 4.6\%$). This can be explained by the mode patterns of these phonons depicted in figure 4.1, i.e. a displacement of the apical O^{2-} of the MnO_6 octahedra along the orthorhombic a–axis and an out–of–phase rotation of the MnO_6 octahedra along the a–axis, respectively. It can easily be understood, that these Eigendisplacements are sensitive to a change of the Mn–O–Mn tilting angle along the b–axis. For the other mentioned phonon modes the shift is less pronounced ($\lesssim 2\%$).

A closer inspection of the two strong A_g modes at $\widetilde{\nu} \approx (480 - 500) cm^{-1}$ shows, that these strongly mix and an exchange of spectral weight occurs. This was also observed on polycrystalline $RMnO_3$ by Iliev et al. [IAL+06]. There it was shown, that for R^{3+} = Sm^{3+}, Eu^{3+}, Gd^{3+} and Tb^{3+} the $A_g(1)$ and $A_g(3)$ modes strongly mix, while for the other $RMnO_3$ compounds of the Lanthanide series they are separated. This mixing was attributed to the fact, that one of these modes – $A_g(3)$, which is a MnO_6 bending mode

– is rather sensitive to a change of the Mn–O–Mn tilting angle along the b–axis and, consequently, its Eigenfrequency increases with decreasing R^{3+} radius. This is in contrast to the other mode – $A_g(1)$, which is an antistretching mode of the O^{2-} in the MnO_2 (ac) plane of the MnO_6 octahedra and, therefore, independent of the R^{3+} ionic radius. In [IAL$^+$06] the frequencies of the pure modes would cross in the range of $SmMnO_3$ and $EuMnO_3$, i.e. an ionic radius of $R^{3+} \approx (1.12 - 1.13)$Å. In reality, a strong intermixing occurs, resulting in an anticrossing behaviour in the wide range from $PrMnO_3$ to $DyMnO_3$, i.e. ionic radii of 1.175Å $> R^{3+} >$ 1.09Å. The same intermixing behaviour can also be seen in our $RMnO_3$ spectra with the most noticeable aspect being the interchange of spectral weight reflected in the area of the phonon peaks. So, while for $EuMnO_3$ the $A_g(3/1)$ mode has a considerably higher area than $A_g(1/3)$, the situation is reversed in $TbMnO_3$. Because of the strong mode mixing, we do not denote these two modes with separate mode indices, but with $A_g(1/3)$ and $A_g(3/1)$. This nomenclature is also used for $A_g(7)$ and $A_g(2)$ according to [IAL$^+$06], though we do not observe signs of mode mixing in our Raman spectra.
From this intermixing behaviour it can further be concluded, that a moderate sensitivity of the phonon modes $A_g(1/3)$ and $A_g(3/1)$ with respect to a change of the Mn–O–Mn tilting angle caused by a R^{3+} replacement should be observable. The corresponding relative frequency shifts in figure 6.6 show exactly this expected behaviour.
In clear contrast to the other phonon modes, a negligible relative change of the phonon frequency ($\Delta\omega/\omega < 1\%$) is observed for the strongest phonon mode $B_{2g}(1)$ – the symmetric stretching (i.e. breathing) mode of the MnO_6 octahedra within the MnO_2 (ac) plane. This further confirms the picture of mode–dependent sensitivity, because in this case the displacement is confined within the MnO_2 (ac) plane, whose O^{2-} equilibrium positions are only slightly affected by a R^{3+} replacement.
In summary, the Raman spectra of the stoichiometric $RMnO_3$ series show the consequences of the R^{3+} replacement on the phonon modes with almost exclusive involvement of the O^{2-}. The induced frequency shifts are mode dependent and originate from the indirect mechanism of a change of the MnO_6 tilting caused by R^{3+} replacement within the orthorhombic unit cell.

FT–IR Spectroscopy

With the help of FT–IR spectroscopy, the reflectivity of the $RMnO_3$ ($R^{3+} = Eu^{3+}$, Gd^{3+}, Tb^{3+}) series and, thus, the IR–active phonon modes can be investigated. In contrast to the Raman–active phonons, the Mn^{3+} participate in these modes, as can be seen in the mode patterns of figure 4.3 and 4.4.
The reflectivity spectra as well as the hence derived ϵ_2 spectra obtained from $RMnO_3$ are shown in figure 6.7 in the same arrangement as in figure 6.3 for $GdMnO_3$. It can be seen in these spectra obtained from the whole investigated $RMnO_3$ series, that the number of phonon modes equals that expected by the group theoretical considerations in section 4.2.1. A list of the fit parameters ω_T, ω_p and Γ can be found in the tables B.2 and B.3 in Appendix B.

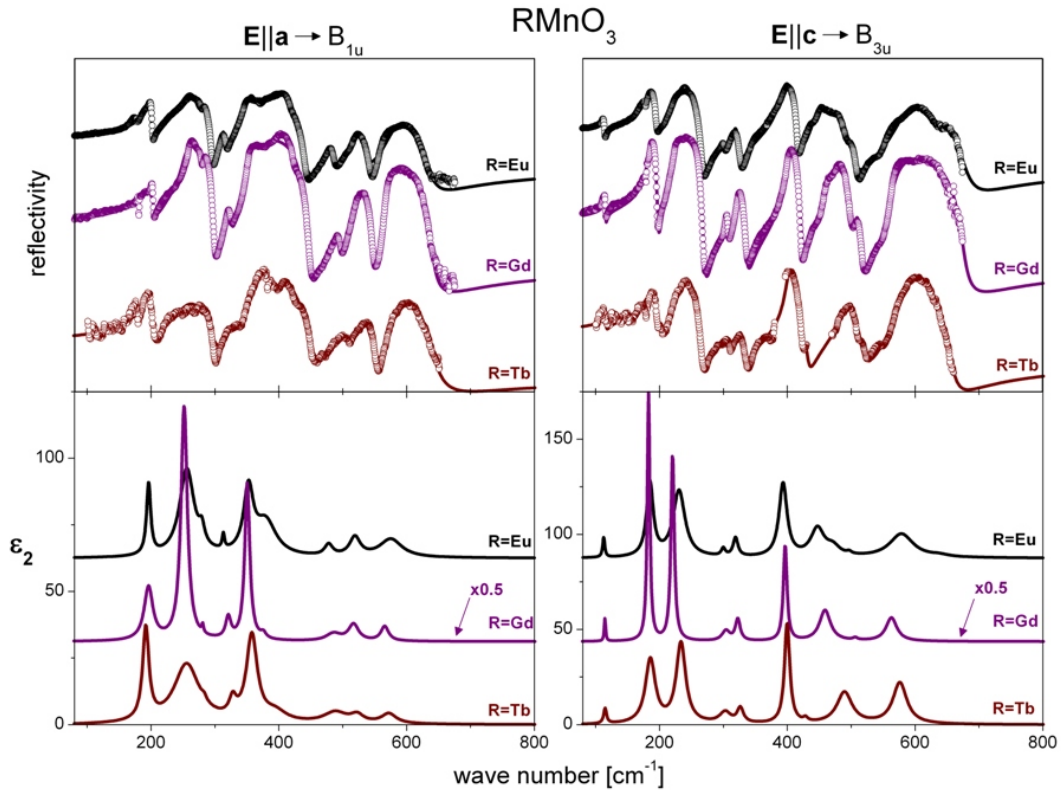

Figure 6.7: Polarised reflectivity spectra (upper row) and hence derived ϵ_2 for the $RMnO_3$ (R^{3+} = Eu^{3+}, Gd^{3+}, Tb^{3+}) series at room temperature in B_{1u} and B_{3u} symmetry, respectively. The open circles in the reflectivity spectra indicate the raw data, while the solid lines are the reflectivity fit functions. For clarity, the spectra are vertically shifted.

As in the case of the Raman spectra, the sample surface roughness leads to the appearance of nominally symmetry forbidden phonons and, additionally, to an overall reduced reflectivity. The reason is that for FT–IR measurements the reflectivity of the sample has to be obtained by comparing the measured reflectivity of the sample to that of a reference – in our case a gold mirror. Thus, the comparison of a rough sample surface to the polished mirror surface results in reduced reflectivity, which is especially pronounced for $EuMnO_3$ and $TbMnO_3$.

The relative shift of the phonon frequencies with respect to $EuMnO_3$ is drawn versus the incorporated R^{3+} in figure 6.8 for B_{1u} (upper row) and B_{3u} (lower row) symmetry, respectively. For better clarity, the phonons are arranged in panels according to the classification scheme presented in section 4.3. It can be seen, that the relative phonon frequency shifts of one class show mainly uniform trends. Thus, the following discussion will be based upon this classification scheme.

Comparing the relative frequency shifts leads to the conclusion, that for stoichiometric $RMnO_3$ (R^{3+} = Eu^{3+}, Gd^{3+}, Tb^{3+}) the strongest frequency shifts are observed for group 2 modes (i.e. tilting, buckling and rotation modes of the MnO_6 octahedra). These are in

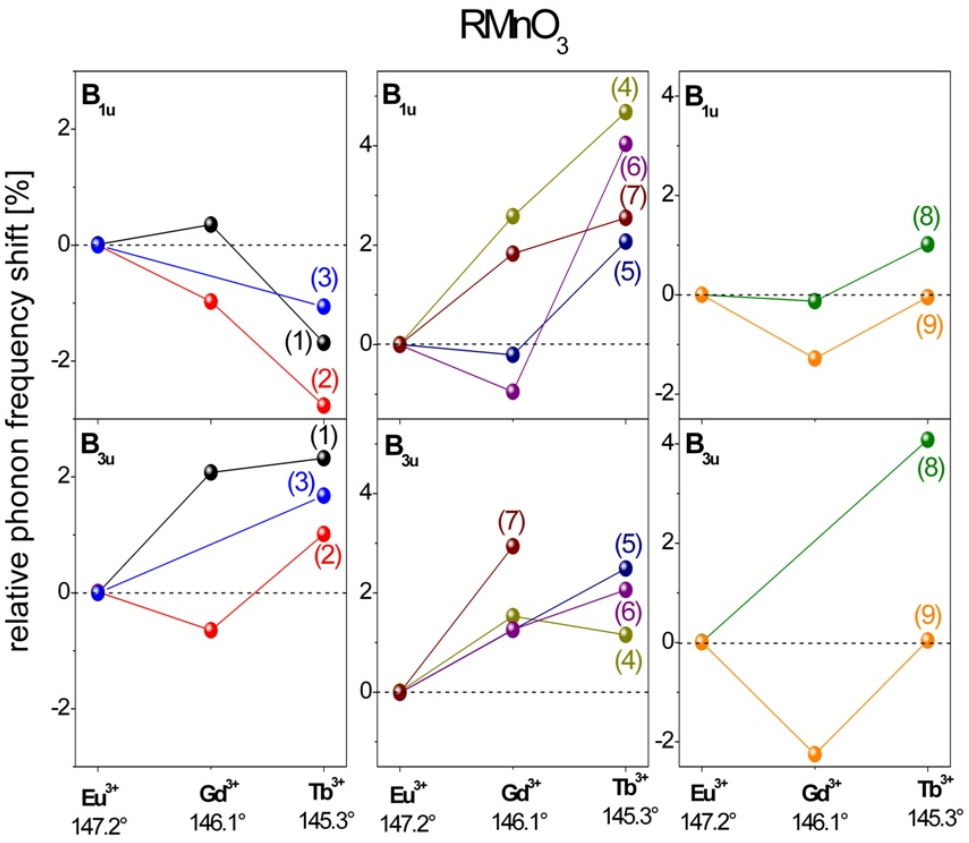

Figure 6.8: Relative shift of phonon frequencies for the $RMnO_3$ series versus the incorporated R^{3+} and the resulting Mn–O–Mn bond angle. The upper row shows the phonons with B_{1u} symmetry, the lower row phonons with B_{3u} symmetry, respectively. The phonons are arranged in panels reflecting the classification scheme outlined in section 4.3. The quantitative values for the Mn–O–Mn bond angle are extracted from [GKL+04].

an interval from 2 % to 4.5 % for B_{1u} and from 1.5 % to 3.5% for B_{3u} modes, respectively. In comparison, the phonon modes of group 3 (i.e. MnO_6 internal and stretching modes) show relatively moderate shifts (0 – 2 %) with the exception of $B_{3u}(8)$. This might be related to the fact, that this mode is rather difficult to fit due to its weak dipolar activity (the $B_{3u}(8)$ ion plasma frequency ω_p is in the range of $\approx 250cm^{-1}$ in $TbMnO_3$) and the simultaneous vicinity to the strong $B_{3u}(9)$ mode ($\omega_p \approx 600cm^{-1}$ in $TbMnO_3$). Thus, the fitting procedure can wrongly identify a symmetry forbidden phonon (e.g. $B_{1u}(7)$ or $B_{1u}(8)$) as $B_{3u}(8)$. The otherwise moderate shifts of the group 3 phonons are further evidence for the insensitivity of the MnO_6 stretching modes to a change of the incorporated R^{3+} in agreement to the shifting trend of the Raman–active symmetric stretching mode of the MnO_6 octahedra, i.e. $B_{2g}(1)$.

While the behaviour of the other classes is roughly identical for B_{1u} and B_{3u} symmetry, the group 1 modes (i.e. modes with strong R^{3+} and Mn^{3+} participation) show frequency shifts with different signs (-3 to -1% for B_{1u} symmetry and $+1$ to $+2.5$% for B_{3u} sym-

metry).
For an understanding of this behaviour, the different mechanisms, that determine the phonon frequency shift with respect to a R^{3+} replacement, need to be considered. These can be easily summarised within the picture of a harmonic oscillator, whose Eigenfrequency ω is obtained by

$$\omega = \sqrt{\frac{D}{\mu}}, \tag{6.1}$$

where D denotes the force constant of the corresponding bond modulated by a phonon mode. μ is the reduced mass of the ions involved in the displacement pattern of the same phonon mode. D is determined by the bond strength and the bond length, which can be influenced by a change of lattice constants. Thus, an increase or a decrease of a lattice constant should lead to a decrease or an increase of the phonon Eigenfrequency ω, respectively. On the other hand, a replacement of R^{3+} changes the reduced mass in the group 1 phonon modes. As we are substituting Eu^{3+} ($m_{Eu} \approx 152u$, u being the atomic mass unit) with heavier elements from the Lanthanide series, i.e. Gd^{3+} ($m_{Gd} \approx 157.25u$) and Tb^{3+} ($m_{Tb} \approx 159u$), the consequence is a moderate decrease of the phonon frequencies of the group 1 modes.

Concerning the first factor, it was already discussed in the previous section, that the increasing orthorhombic distortion leads to an enhancement of the inequivalence of a– and c–axis. A look at table 6.2, where the lattice constants of the investigated $RMnO_3$ series determined by XRD measurements are listed, shows a change of a from 5.8638 Å for $EuMnO_3$ to 5.8557 Å for $TbMnO_3$, which equals $\Delta a/a \approx -0.14\%$ and a change of c from 5.3451 Å for $EuMnO_3$ to 5.3019 Å for $TbMnO_3$, which equals $\Delta c/c \approx -0.81\%$. Thus, the relative reduction of the c–axis is almost a factor 6 larger than that of the a–axis.
Combining this with the factor of mass substitution ($(m_{Tb} - m_{Eu})/m_{Eu} \approx +4.6\%$) the symmetry dependent frequency shifts of the group 1 modes within $RMnO_3$ can be explained. The R^{3+} replacement results in only a minor change of the a–axis, thus for the group 1 B_{1u} modes, the mass substitution effect (i.e. an increase of the R^{3+} mass) is dominant and leads to an average decrease of the phonon frequencies of $\Delta\omega/\omega \approx -2\%$. On the other hand, the c–axis decrease is considerably larger and, thus, this effect overcomes

Table 6.2: Lattice constants (Pnma notation) of $RMnO_3$ (R = Eu, Gd, Tb) obtained from XRD literature data.

sample	$EuMnO_3$	$GdMnO_3$	$TbMnO_3$
a (Å)	5.8638[a]	5.8625[b]	5.8557[c]
b (Å)	7.4581[a]	7.4323[b]	7.4009[c]
c (Å)	5.3451[a]	5.3163[b]	5.3019[c]

[a] from [HSP+07], adapted to Pnma, [b] from [HLKvN+04], adapted to Pnma,
[c] from [BRG+00].

the mass substitution effect leading to an average increase of the phonon frequencies of $\Delta\omega/\omega \approx +1.75\%$ for the group 1 B_{3u} modes.
Summing up, the different features of the phonon spectra of the stoichiometric $RMnO_3$ ($R^{3+} = Eu^{3+}$, Gd^{3+}, Tb^{3+}) series can be explained as results of the R^{3+} substitution either directly or indirectly via a change of the orthorhombic distortion of the Pnma structure. This now enables us to carry out a comparative analysis of the doped $Eu_{1-x}Y_xMnO_3$ ($0 \leq x \leq 0.5$) series.

6.2.2 Doped $Eu_{1-x}Y_xMnO_3$ ($0 \leq x \leq 0.5$)

As already laid out in section 3.4, the doping approach to obtain Multiferroic Manganites via Y doping of $EuMnO_3$ has two major advantages over stoichiometric $RMnO_3$: (i) Doping gives the possibility for a quasi–continuous tuning of the average R^{3+} ionic radius and (ii) the magnetic properties of Y^{3+} and Eu^{3+} lead to magnetically ordered phases in $Eu_{1-x}Y_xMnO_3$, which are solely determined by the magnetism of the Mn^{3+}. This behaviour is due to the fact, that Y^{3+} is non–magnetic and Eu^{3+} has a total angular momentum of nominally $J = 0$ and, as is shown in the measurements of the magnetic susceptibility of [HSP+07], no ordered magnetic phases of the Eu^{3+} or Y^{3+} spins occur within this system. Doped $Eu_{1-x}Y_xMnO_3$ ($0 \leq x \leq 0.5$) is, therefore, of special importance for the investigative efforts concerning the nature of the multiferroic properties within the class of orthorhombic Manganites. The first time analysis of the lattice dynamics of the $Eu_{1-x}Y_xMnO_3$ series to be presented here is therefore another important part of a systematic investigation of the coupling effects between lattice dynamics and magnetism.
An open question of this doping approach is, whether the incorporation of isovalent Y^{3+} on the Eu^{3+}–sites leads to any kind of disorder induced effects due to its distinctly smaller ionic radius ($r_{Y^{3+}} \approx 1.075$Å compared to $r_{Eu^{3+}} \approx 1.12$Å). This has been discussed in [HSP+07], but not systematically studied by the means of a complete investigation of the lattice dynamics. This task will be carried out in the following. Similar to the last section, we will start with a discussion of the Raman spectra, followed by the reflectivity spectra obtained by FT–IR measurements.

Raman Spectroscopy

Figure 6.9 shows an overview of the Raman spectra of the $Eu_{1-x}Y_xMnO_3$ ($0 \leq x \leq 0.5$) sample series for A_g (left panel) and B_{2g} (right panel) symmetry, respectively. Comparison with the Raman spectra of the stoichiometric $RMnO_3$ series in figure 6.5 shows, that the characteristics of the spectra and the number of the observed phonon modes are the same for both series. Also clearly visible is the effect of sample surface roughness, as the samples with polished surfaces ($Eu_{0.8}Y_{0.2}MnO_3$ and $Eu_{0.5}Y_{0.5}MnO_3$) show only minor leakage of symmetry forbidden phonon modes.
In the same way as for the stoichiometric $RMnO_3$ series, the mode–dependent relative frequency shifts with respect to the phonon frequencies of $EuMnO_3$ are depicted in figure 6.10 as a function of the Y doping level x for the A_g modes (left panel) as well as the B_{2g}

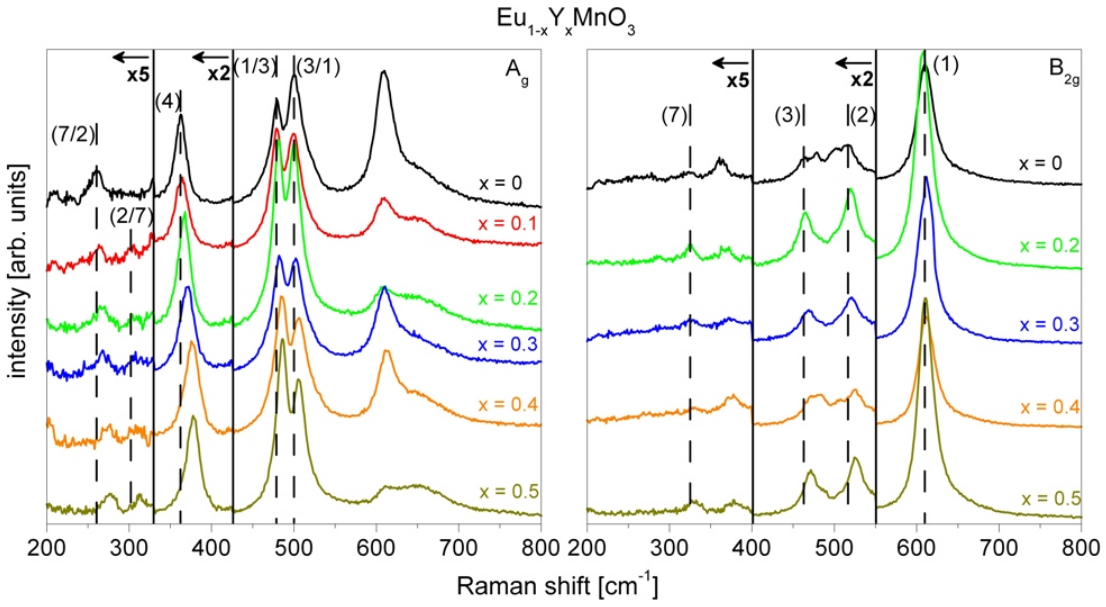

Figure 6.9: Polarised Raman spectra of the $Eu_{1-x}Y_xMnO_3$ ($0 \leq x \leq 0.5$) sample series in A_g (left panel) and B_{2g} (right panel) symmetry, respectively. For clarity, the spectra are vertically shifted and on their low frequency side the spectra are multiplied by the factors indicated on the left side of the vertical black bars.

modes (right panel). Due to the missing peak in the $EuMnO_3$ reference, the $A_g(2/7)$ mode is omitted as in the case of $RMnO_3$. Table B.1 in Appendix B lists the same information in tabular form.

Comparison of the relative phonon frequency shifts with that of the stoichiometric $RMnO_3$ series (see figure 6.6) shows a very similar behaviour for the doped $Eu_{1-x}Y_xMnO_3$ series: the strongest frequency shifts of $\Delta\omega/\omega \approx 6.4\%$ and $\approx 4.2\%$ are observed for the $A_g(7/2)$ and $A_g(4)$ mode, respectively. Further, the negligible shift for the $B_{2g}(1)$ mode ($\Delta\omega/\omega < 1\%$) does also occur in the doped series. This similar behaviour of the two sample series can be expected due to the almost pure O^{2-} displacement patterns of the observed Raman–active phonon modes. Therefore, for both series no disorder induced effects occur for the observed Raman–active phonon modes.

The mixing behaviour of $A_g(1)$ and $A_g(3)$ already discussed for $RMnO_3$ can also be demonstrated in the doped $Eu_{1-x}Y_xMnO_3$ series. This is illustrated in figure 6.11, where the left panel shows a comparison of the $A_g(1)$ and $A_g(3)$ phonon frequencies as a function of the R^{3+} ionic radius for the Lanthanide series of orthorhombic $RMnO_3$ (R^{3+} from La^{3+} to Ho^{3+}) taken from [IAL+06]) with the doped $Eu_{1-x}Y_xMnO_3$ ($0 \leq x \leq 0.5$) series investigated within this thesis. The same comparative depiction displays the relative phonon area of $A_g(1)$ and $A_g(3)$ for both series in the right panel normalised to the integral peak area of both modes, which is set to 100.

Especially the phonon frequencies show very clearly, that the intermixing behaviour of the $A_g(1)$ and $A_g(3)$ modes is almost identical in both systems, giving a further strong

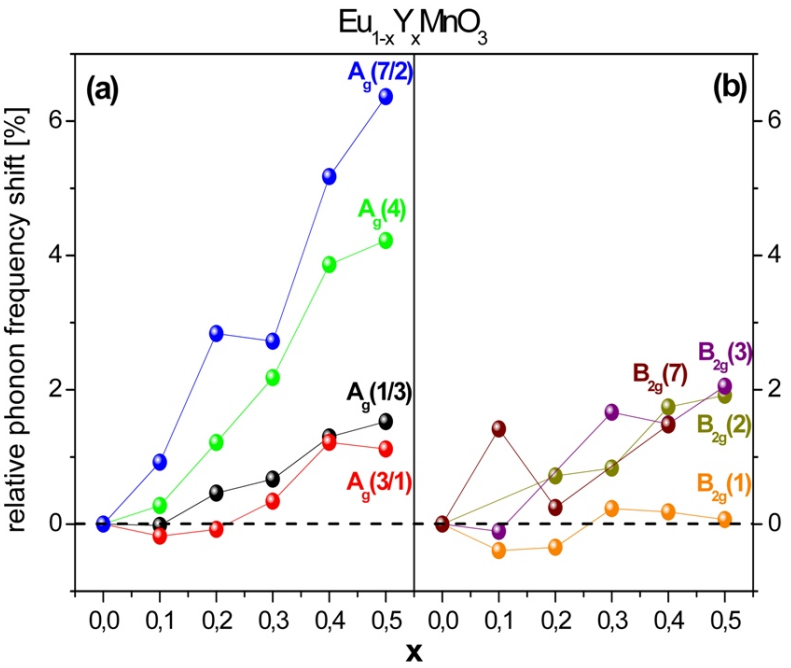

Figure 6.10: Relative shift of phonon frequency for the $Eu_{1-x}Y_xMnO_3$ series as a function of Y doping level x. (a) shows the phonons with A_g symmetry and (b) the phonons with B_{2g} symmetry.

indication, that the Raman–active phonon modes for the stoichiometric $RMnO_3$ series with R^{3+} =Eu^{3+}, Gd^{3+}, Tb^{3+} and the doped $Eu_{1-x}Y_xMnO_3$ ($0 \leq x \leq 0.5$) series can be regarded as equivalent.

The relative phonon area shown in the right panel of figure 6.11 also gives evidence of an interchange of spectral weight, i.e. $A_g(1)$ and $A_g(3)$ change their respective Raman activity through the whole Lanthanide series $RMnO_3$ with ranging R^{3+} from La^{3+} to Ho^{3+} [IAL+06]. Similar to the behaviour of the phonon frequencies, the phonon area shows, that the intermixing behaviour from $EuMnO_3$ to $TbMnO_3$ can also be found in the doped $Eu_{1-x}Y_xMnO_3$ series. The stronger deviations, that can be observed when comparing the phonon area of the measurements carried out within this thesis with that of [IAL+06], might originate from the different spectral resolution of the employed Raman setups. While Iliev et al. employ a Labram–800 single stage spectrometer with a spectral resolution of $\approx 0.5cm^{-1}$ [IAL+06, LJM+06], the Raman spectra at room temperature carried out within this thesis are recorded at a Renishaw 1000 single stage spectrometer with a spectral resolution of $\approx 4cm^{-1}$. Therefore, the relative phonon area of a phonon mode with a phonon linewidth in the range of the spectral resolution limit – $A_g(1/3)$ in this case – could be overestimated when comparing this mode to a mode with a higher linewidth – $A_g(3/1)$ in this case. Nevertheless, the qualitative mixing behaviour of an interchange of relative spectral weight can be demonstrated within $Eu_{1-x}Y_xMnO_3$.

Summing up the insights gained from the Raman measurements of the doped

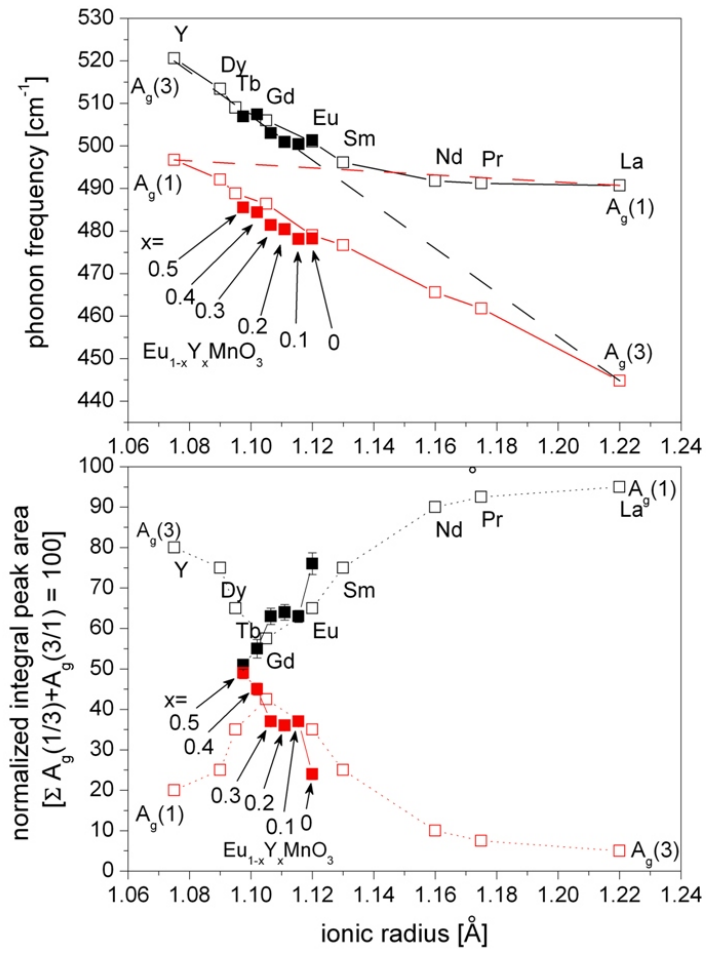

Figure 6.11: $A_g(1)$ and $A_g(3)$ phonon frequencies (upper panel) and relative phonon area (lower panel) as a function of the R^{3+} (average) ionic radius. In the upper panel the filled squares denote the $A_g(1)$ and $A_g(3)$ phonon frequencies of $Eu_{1-x}Y_xMnO_3$ shown in figure 6.9; open squares are data taken from [IAL$^+$06] and the dashed lines symbolise the hypothetical frequency shift of the two modes without intermixing effects. The lower panel shows the same arrangement for the integral peak area normalised to the sum of both modes. Values of the R^{3+} ionic radii are taken from [IAL$^+$06] for the stoichiometric $RMnO_3$ series, whereas the R^{3+} ionic radii of $Eu_{1-x}Y_xMnO_3$ are obtained by an arithmetic average of Eu^{3+} and Y^{3+} corresponding to the percentaged Y–content.

$Eu_{1-x}Y_xMnO_3$ series, we can conclude, that the Raman–active modes, i.e. the O^{2-} vibrations without involvement of Mn^{3+}, do not show disorder effects induced by Y^{3+} doping on the R^{3+} sites.

FT–IR Spectroscopy

The reflectivity and the hence derived ϵ_2 spectra of the $Eu_{1-x}Y_xMnO_3$ ($0 \leq x \leq 0.5$) series are depicted in figure 6.12 in the same arrangement as those of $RMnO_3$ in figure

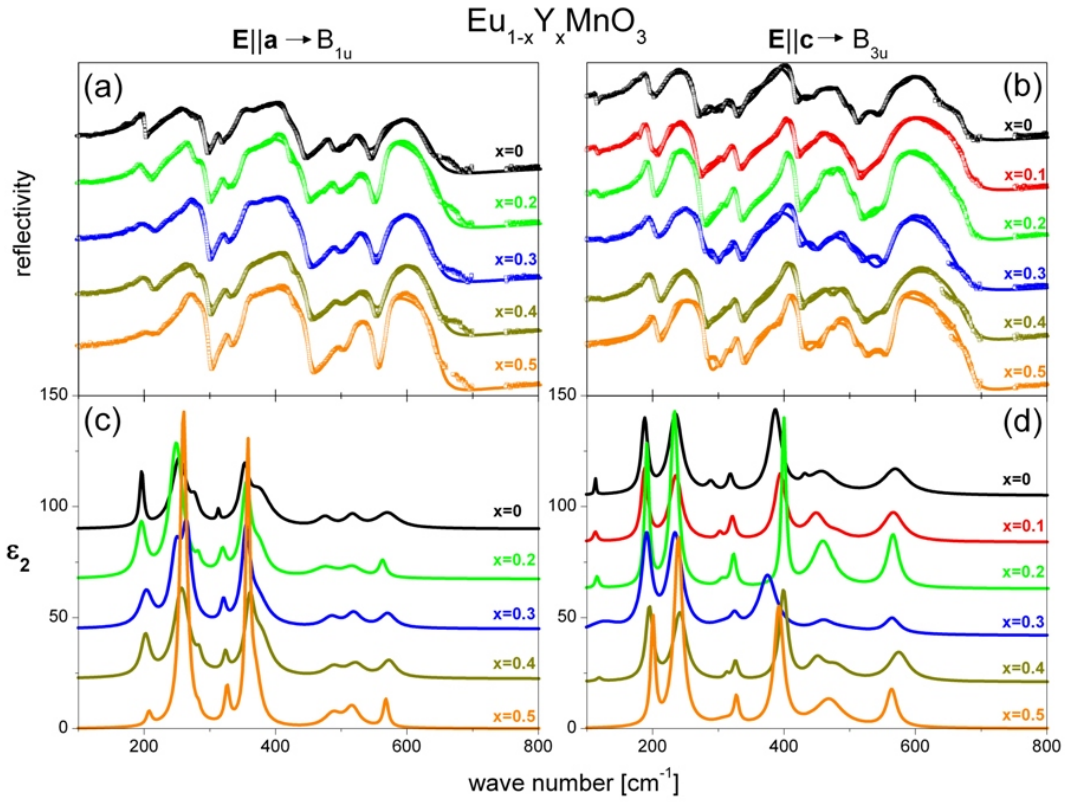

Figure 6.12: Polarised reflectivity spectra of the whole investigated $Eu_{1-x}Y_xMnO_3$ sample series ($0 \leq x \leq 0.5$) at room temperature in (a) B_{1u} and (c) B_{3u} symmetry, respectively. (b) and (d): hence derived ϵ_2.

6.7. It has to be pointed out, that due to the a–cut sample surface of $Eu_{0.9}Y_{0.1}MnO_3$ it is impossible to fulfil the excitation condition $\boldsymbol{E}||\boldsymbol{a}$ for observing phonon modes with B_{1u} symmetry for this sample. Thus, only its B_{3u} modes are shown.

At large, the shape of the reflectivity spectra of $Eu_{1-x}Y_xMnO_3$ resembles very close those of $RMnO_3$. Another similarity is the influence of the sample surface roughness. For $Eu_{0.8}Y_{0.2}MnO_3$ and $Eu_{0.5}Y_{0.5}MnO_3$, the polished sample surface leads to very sharp phonon modes, what can be seen especially clear in the ϵ_2 spectra. In comparison, the unpolished samples show broader phonon modes. This makes it difficult to quantitatively compare phonon properties determined by the phonon area or linewidth for the whole $Eu_{1-x}Y_xMnO_3$ series. Thus, we will concentrate on the phonon frequencies and the relative spectral weight of the phonon modes. First, the shift of phonon frequencies as a function of Y doping will be discussed.

Figure 6.13 shows the relative shifts of the phonon frequencies with respect to those of $EuMnO_3$ as a function of Y doping level x for B_{1u} (upper row) and B_{3u} symmetry (lower row), respectively. As in the case of $RMnO_3$, the quantitative shifts can be characterised according to the classification scheme introduced in section 4.3. For the phonon modes of group 2 (MnO_6 tilting, buckling and rotation modes) and group 3 (MnO_6 stretching

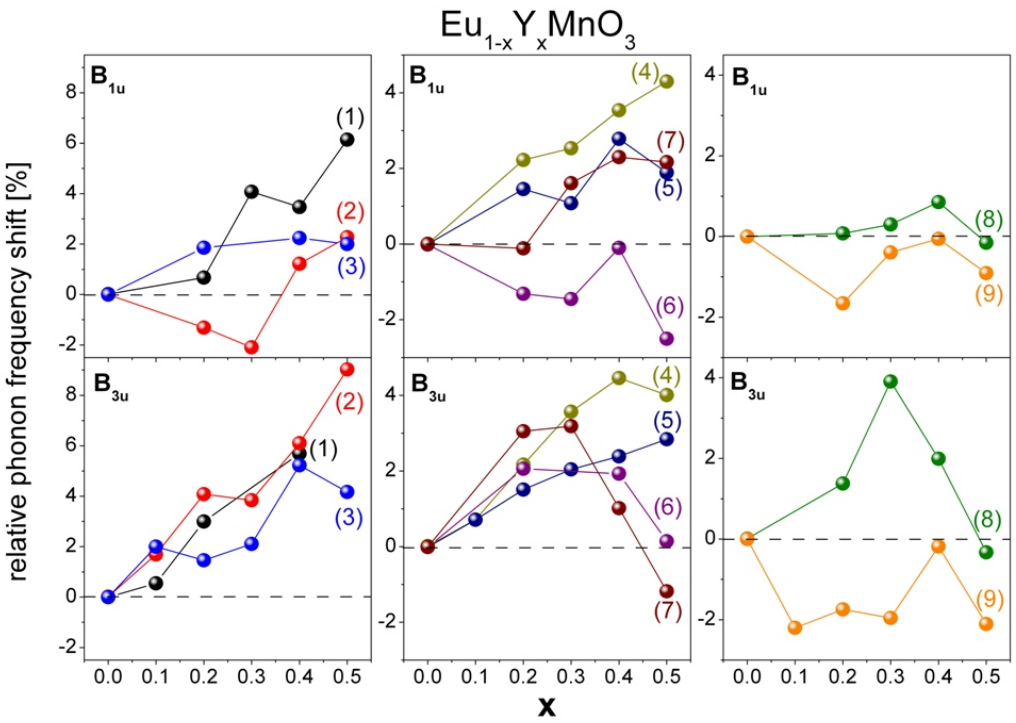

Figure 6.13: Relative shift of phonon frequency for the $Eu_{1-x}Y_xMnO_3$ series with respect to those of $EuMnO_3$ as a function of Y doping level x. The upper row shows the phonons with B_{1u} symmetry and the lower row the phonons with B_{3u} symmetry, respectively. The phonons are arranged in panels reflecting the classification according to their main participants and phonon frequency according to section 4.3.

and internal modes) a similar behaviour is observed for both sample series. The group 2 modes show a moderate increase of the phonon frequencies ($\Delta\omega/\omega \approx 0$ to $+4.5\%$) – with the exception of the $B_{1u}(6)$ and $B_{3u}(7)$ modes, whose shifts are slightly negative. For the group 3 modes, the trend of negligible frequency shifts found in the $RMnO_3$ is also confirmed for the doped $Eu_{1-x}Y_xMnO_3$ series. Both experimental findings are clear indications, that the Mn–O subsystem within the orthorhombic Pnma structure is almost unaffected by the doping approach of $Eu_{1-x}Y_xMnO_3$.
On the other hand, the group 1 modes (i.e. R^{3+} and Mn^{3+} displacements) show an entirely different behaviour for both sample series. While in $RMnO_3$ shifts in the range of $\Delta\omega/\omega \approx -3$ to -1% for the B_{1u} modes and $\Delta\omega/\omega \approx +1$ to $+2.5\%$ for the B_{3u} modes are observed, the frequency shifts in $Eu_{1-x}Y_xMnO_3$ are considerably stronger with $\Delta\omega/\omega \approx +2$ to $+6\%$ for the B_{1u} modes and $\Delta\omega/\omega \approx +4$ to $+8\%$ for the B_{3u} modes. As a matter of fact, these shifts are the strongest frequency shifts as a function of the incorporated R^{3+} ion observed. Further, it is found, that the shifts of the B_{1u} phonons are slightly weaker than those of the B_{3u} modes – an observation which is similar in both series.
This significant difference between both sample series can be understood within the simple

Table 6.3: Lattice constants (Pnma notation) of $Eu_{1-x}Y_xMnO_3$ ($0 \leq x \leq 0.5$ with the exception of $Eu_{0.6}Y_{0.4}MnO_3$) obtained from XRD measurements of Hemberger et al. [HSP+07].

sample	$EuMnO_3$	$Eu_{0.9}Y_{0.1}MnO_3$	$Eu_{0.8}Y_{0.2}MnO_3$	$Eu_{0.7}Y_{0.3}MnO_3$	$Eu_{0.5}Y_{0.5}MnO_3$
a (Å)	5.8638	5.8636	5.8681	5.8597	5.8556
b (Å)	7.4581	7.4469	7.4381	7.4276	7.4091
c (Å)	5.3451	5.3368	5.3306	5.3195	5.3042

harmonic oscillator picture introduced in the last section. This picture, which explains the dependence of the phonon frequencies on the force constant D and, thus, on the lattice constants, and the reduced mass μ of the participating ions can account for two aspects of the group 1 frequency shifts in $Eu_{1-x}Y_xMnO_3$: (i) the symmetry dependence of the group 1 frequency shifts within the $Eu_{1-x}Y_xMnO_3$ series. This can be understood in the same way as the observations for group 1 phonons within the $RMnO_3$ series. In both sample series, the change of lattice constants with decreasing R^{3+} ionic radius is more pronounced on the c–axis than on the a–axis. For $Eu_{1-x}Y_xMnO_3$ the lattice constants obtained from XRD measurements by Hemberger et al. [HSP+07] are listed in table 6.3. From these data it can be calculated, that the change of lattice constants for increasing the Y–content from 0% to 50% is $\Delta a/a \approx -0.14\%$ and $\Delta c/c \approx -0.77\%$, which is in close analogy to the change within the $RMnO_3$ series. Thus, it can be concluded, that the phonon frequency shifts of the group 1 modes with B_{3u} symmetry should be more pronounced than those with B_{1u} symmetry. (ii) The second aspect explainable within the harmonic oscillator picture is the aforementioned significant difference in the group 1 shifts between $RMnO_3$ and $Eu_{1-x}Y_xMnO_3$. The explanation relies on the second influencing factor – the reduced mass μ. While for $RMnO_3$ the R^{3+} ionic mass is changed only by a minor amount of $\approx +4.6\%$ from Eu^{3+} to Tb^{3+}, a 50% Y^{3+} doping of $EuMnO_3$ results in a change of $\approx -20\%$ for the average R^{3+} ionic mass. Thus, a more pronounced impact of the frequency increasing factor of changing the reduced mass μ can be concluded. This nicely explains the strong positive frequency shifts observed in $Eu_{1-x}Y_xMnO_3$ for the group 1 phonon modes.

In the following, a further aspect of the IR–active phonon modes will be discussed: their dipolar strength. This is a direct measure of the electric dipole moment associated with the corresponding phonon and its displacement pattern. Usually (see e.g. [RKM+07]) it is expressed in terms of the dipolar strength of mode j as:

$$\Delta\epsilon_j = \frac{\omega_{p,j}^2}{\omega_{T,j}^2}, \tag{6.2}$$

with $\omega_{T,j}$ as the transversal phonon frequency and $\omega_{p,j}$ as the ion plasma frequency defined in equation (2.22). Unfortunately, the different polishing degree of the sample surfaces of our two sample series make a direct quantitative comparison of ω_p impossible, due the ef-

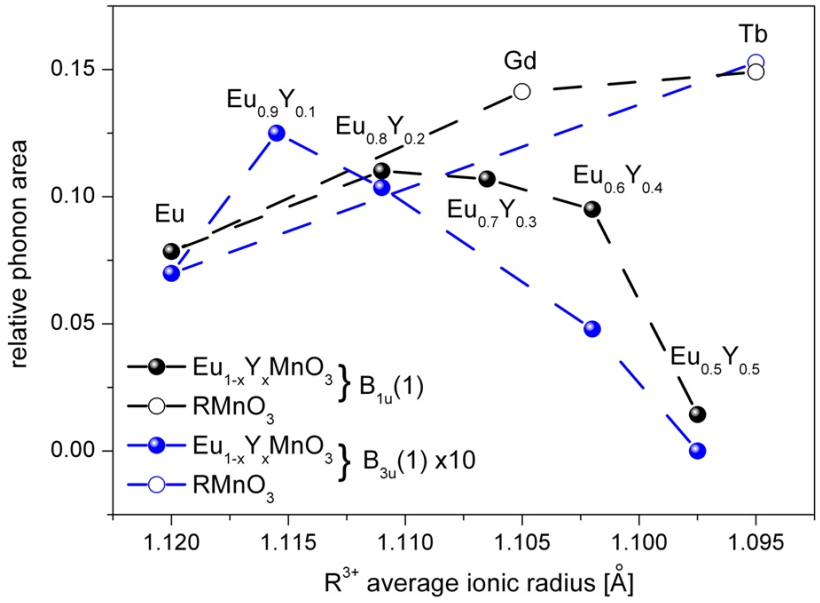

Figure 6.14: Relative peak area in the ϵ_2 spectra of $B_{1u}(1)$ (black), and $B_{3u}(1)$ (blue, multiplied by a factor 10) modes as a function of the (average) R^{3+} ionic radius. The open circles denote the peak area for the stoichiometric $RMnO_3$ series, while the closed circles show the relative peak area of the doped $Eu_{1-x}Y_xMnO_3$ series. The relative peak area is obtained by dividing the peak area of the corresponding phonon mode by the integrated peak area of all phonon modes in the ϵ_2 spectrum with B_{1u} or B_{3u} symmetry, respectively.

fects of the surface roughness on the reflectivity spectra already discussed in section 6.1.2. This problem can be avoided by considering the relative phonon area in the ϵ_2 spectra for two reasons: (i) Regarding the peak area takes into account the height and the linewidth of the phonon modes, thus compensating the effects of broader phonon modes observed for the unpolished samples and (ii) the differences in the reflectivity obtained with respect to the reference sample (i.e. a gold mirror) are avoided by considering the relative peak area within an ϵ_2 spectrum, i.e. the peak area of the corresponding phonon divided by the integrated peak area of all phonon modes with the same symmetry.

This analysis is carried out for those phonon modes, whose dipolar strength shows qualitative differences for both sample series (see figures 6.7 and 6.12). These modes are $B_{1u}(1)$ and $B_{3u}(1)$. The obtained relative phonon area of both modes is drawn as a function of the average R^{3+} ionic radius in figure 6.14. For the $RMnO_3$ series, R^{3+} is simply the ionic radius of Eu^{3+}, Gd^{3+} or Tb^{3+}, respectively, while for $Eu_{1-x}Y_xMnO_3$ it is obtained by the arithmetic average value of Eu^{3+} and Y^{3+} determined by the Y doping level x. For clarity, the relative phonon area of the weaker $B_{3u}(1)$ mode is multiplied by a factor 10. It can be clearly seen, that for the doped $Eu_{1-x}Y_xMnO_3$ series the relative phonon area and, thus, the dipolar strength is weakened for both modes with increasing Y doping level x. While for the stronger $B_{1u}(1)$ mode a small dipolar activity remains in $Eu_{0.5}Y_{0.5}MnO_3$, the $B_{3u}(1)$ mode could not even be fitted. Thus, the dipolar activity

of the latter can be regarded as approaching zero for a Y doping level of 50 %. In clear contrast, the relative phonon area for $B_{1u}(1)$ and $B_{3u}(1)$ increases slightly for decreasing R^{3+} ionic radius within the $RMnO_3$ series. Due to the very sharp and pronounced $B_{3u}(1)$ peak in the polished $GdMnO_3$, which eventually cannot be completely compensated by the approach of considering the relative phonon area in the ϵ_2 spectra, its relative phonon area would far overreach the chosen scale of the y–axis and is thus omitted in favour of observability of the average trend within both sample series. Nevertheless the trend of a stronger dipolar strength of the $B_{3u}(1)$ within the $RMnO_3$ series is confirmed also for this mode.
The different trend observed for the dipolar strength of $B_{1u}(1)$ and $B_{3u}(1)$ in both series obviously correlates with the different approaches employed to decrease the (average) R^{3+} ionic radius, either by complete replacement ($RMnO_3$) or by doping ($Eu_{1-x}Y_xMnO_3$). Both modes showing these opposite trends are assigned to mode patterns with a high degree of R^{3+} participation (see figures 4.3 and 4.4). Thus, one possible interpretation is local disorder on the R^{3+} sites due to Y doping. Another explanation is a splitting of the phonon modes $B_{1u}(1)$ and $B_{3u}(1)$ into two modes, respectively – one is characteristic for $EuMnO_3$ and one for $YMnO_3$. An increasing amount of Y^{3+} would mean a decrease of spectral weight of the $EuMnO_3$ mode and in turn an increase of the $YMnO_3$ mode. Although within this thesis, no $YMnO_3$–like $B_{1u}(1)$ and $B_{3u}(1)$ modes are observed neither at room temperature nor at lower temperatures, Takahashi et al. [TYK+09] report the appearance of a $YMnO_3$–like phonon mode with B_{3u} symmetry at $\approx 160 cm^{-1}$ in $Eu_{1-x}Y_xMnO_3$, thus confirming the assumption of mode splitting.
Another aspect of the reflectivity spectra giving insight in possible disorder effects are the linewidths Γ of the observed phonons. Again it has to be pointed out, that due to the different roughness degree of the sample surfaces a quantitative comparison of the whole $RMnO_3$ and $Eu_{1-x}Y_xMnO_3$ series cannot be carried out. What is possible, is a qualitative discussion regarding only the samples, that were polished up to optical degree, i.e. $GdMnO_3$, $Eu_{0.8}Y_{0.2}MnO_3$ and $Eu_{0.5}Y_{0.5}MnO_3$. The indications are visible in the general view of the reflectivity spectra in the figures 4.3 and 4.4. They can further be verified by regarding the quantitative phonon linewidths Γ of the polished samples listed in the tables B.2 and B.3 in Appendix B. From these, it can be concluded, that increasing Y doping does not induce mode broadening, because the Γ for all observed IR–active phonon modes are within the same range for $GdMnO_3$, $Eu_{0.8}Y_{0.2}MnO_3$ and $Eu_{0.5}Y_{0.5}MnO_3$. Otherwise a systematic increase of Γ for at least the group 1 phonon modes within the $Eu_{1-x}Y_xMnO_3$ series should be detectable with increasing Y–content. This is not the case. Furthermore, a qualitative inspection of the reflectivity and ϵ_2 spectra of the whole $Eu_{1-x}Y_xMnO_3$ series in figure 6.12 including the unpolished samples substantiates this observation, that Y incorporation does not lead to systematic mode broadening.

Implications concerning disorder induced effects in $Eu_{1-x}Y_xMnO_3$

Considering the collected data of IR– and Raman–active phonons, we will discuss the question of local disorder in the lattice of doped $Eu_{1-x}Y_xMnO_3$ series compared to the

stoichiometric $RMnO_3$.
The MnO_6 octahedra, which are the main participants of the phonon modes observed at higher frequencies (i.e. $\widetilde{\nu} > 300 cm^{-1}$), are almost undisturbed by Y incorporation apart from mode–dependent frequency shifts. These observed with both spectroscopical techniques show, that both approaches lead to the same behaviour with respect to a reduction of the (average) R^{3+} ionic radius. E.g. for the Raman–active phonon modes $A_g(1)$ and $A_g(3)$ mode mixing in both sample series occurs with almost identical frequency shifts and a transfer of spectral weight. The trend of mode–dependent frequency shifts can be verified for the IR–active phonon modes of group 2 and 3, i.e. phonons with mainly MnO_6 involvement. Further, the phonon linewidths Γ do not show mode broadening effects for the doped $Eu_{1-x}Y_xMnO_3$ series.
An effect of Y doping manifests itself as a reduction of the dipolar strength of the lowest–frequency IR–active phonon modes, which is – on the basis of [TYK+09] – attributed to a transfer of spectral weight from the $EuMnO_3$–like $B_{1u}(1)$ and $B_{3u}(1)$ modes to the corresponding $YMnO_3$–like phonons, respectively. For the group 1 IR–active phonon modes no systematic mode broadening could be found either.
All these findings are consistent with results obtained for the static lattice properties by XRD (lattice constants derived from these data are shown in the tables 6.2 and 6.3) in [HSP+07].
We can therefore conclude that both investigated sample series show good crystalline quality and low disorder. Also we can follow, that the doping approach in $Eu_{1-x}Y_xMnO_3$ can be regarded as a stochastic substitution of Eu^{3+} with Y^{3+} in $EuMnO_3$ without the formation of clusters.
After this systematic analysis, the coupling effects between lattice dynamics and magnetism can be studied in detail by temperature dependent Raman– and FT–IR Spectroscopy.

Chapter 7

Spin–Phonon Coupling (SPC)

After considering the consequences for both substitutional approaches, i.e. for stoichiometric $RMnO_3$ and for doped $Eu_{1-x}Y_xMnO_3$, on the lattice dynamics in the previous chapter, the Spin–Phonon Coupling (SPC) effects in both sample series will be discussed systematically now. For this purpose, we will employ the results of temperature dependent polarised Raman– and FT–IR measurements.
Figure 7.1 shows exemplarily the Raman spectra of $EuMnO_3$ for several temperatures in the range from room temperature to $T = 10K$. An inspection of the phonon frequencies reveals, that especially for the $B_{2g}(1)$ mode a strong frequency shift towards lower frequencies occurs in the temperature range $T < 50K$. This is in clear contrast to the temperature dependent behaviour expected for phonons without coupling effects between lattice dynamics and magnetism. In that case, an increase of the phonon frequency with decreasing temperature should be observable. This anomalous behaviour is interpreted as a manifestation of SPC, whose theoretical basis was presented in section 5.1.
In the following sections, we will systematically discuss the SPC effects and their dependencies on mode symmetry and the composition of the $RMnO_3$ system. First, in section 7.1, the dependence of SPC on the mode symmetry will be covered for the Raman– and IR–active phonons. This will be followed by an analysis of the compositional dependence of SPC for the stoichiometric $RMnO_3$ and doped $Eu_{1-x}Y_xMnO_3$ series in section 7.2. In the last section, 7.3, the observations of 7.1 and 7.2 will be summed up to a discussion about the physical origins of the observed dependencies of SPC. Further, quantitative coupling constants will be derived for the breathing mode $B_{2g}(1)$ in both sample series and compared to literature.

7.1 Mode dependence

The first dependence of SPC, that will be systematically discussed, is the mode dependence, i.e. the dependence of the strength of SPC on the symmetry properties of the mode patterns of the Raman– and IR–active phonon modes. This will be carried out by considering the phonon modes of $EuMnO_3$ due to the most pronounced occurrence of SPC for all investigated $RMnO_3$ compounds. We will start with the Raman–active

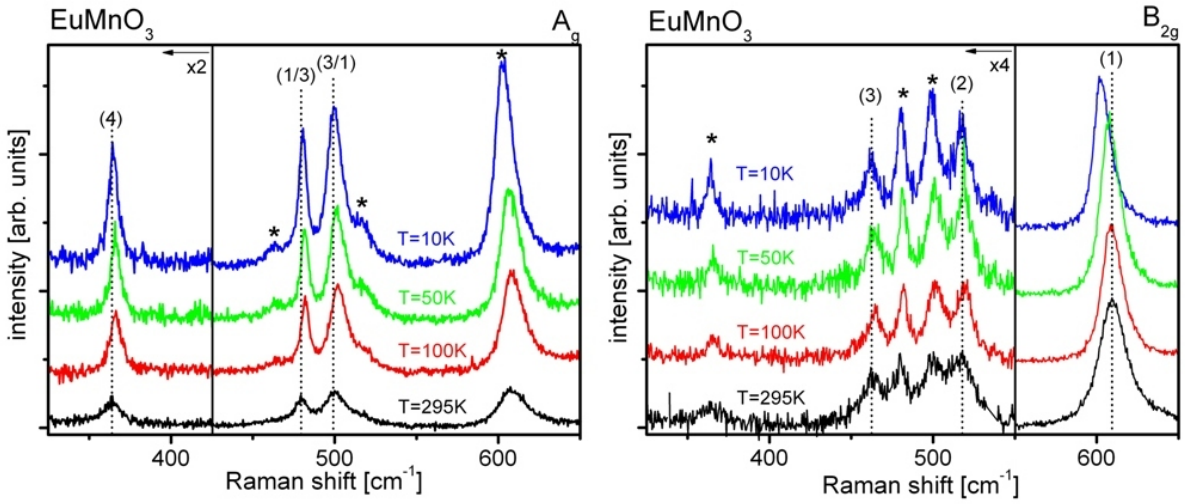

Figure 7.1: A_g (left panel) and B_{2g} (right panel) Raman spectra of $EuMnO_3$ for several temperatures ranging from room temperature to $T = 10K$. The spectra are vertically shifted for clarity and on the low–frequency site multiplied by the factor indicated beside the solid black lines. The room temperature frequencies of the phonon modes are marked by dotted black lines. Symmetry forbidden phonons are marked by asterisks.

phonon modes in section 7.1.1 followed by the IR–active phonon modes in section 7.1.2.

7.1.1 Raman–active phonon modes

To obtain a more quantitative picture of the temperature dependent phonon frequency shifts, the frequencies of all $EuMnO_3$ modes indicated in figure 7.1 are drawn versus a logarithmic temperature scale in figure 7.2. The solid red lines correspond to the modelling function

$$\omega\left(T\right) = \omega_0 - C\left(1 + \frac{2}{e^{\hbar\omega_0/kT} - 1}\right) \tag{7.1}$$

describing the expected temperature dependence of the phonon frequencies solely based on the decay of optical phonon modes into acoustic ones with phonon–phonon decay processes up to third order [BWH83]. This is equivalent to the simple Klemens model [Kle66]. For fitting this function to the experimental data, the parameters ω_0 and C are optimized for matching the data for $T \gg T_N$, where T_N is the onset temperature of the magnetically ordered phases, i.e. $T \approx 46K$ in $EuMnO_3$. It is indicated by the dotted black vertical lines in figure 7.2. The extrapolation of the fit function to $T = 0K$ shows the temperature behaviour expected without SPC.
Obviously, for the depicted temperature dependence of all phonon modes in the temperature region below $T \approx 100K$, a significant deviation from the behaviour predicted by equation (7.1) occurs. Instead a softening of the phonon frequencies is visible, whose value depends on the individual phonon mode.

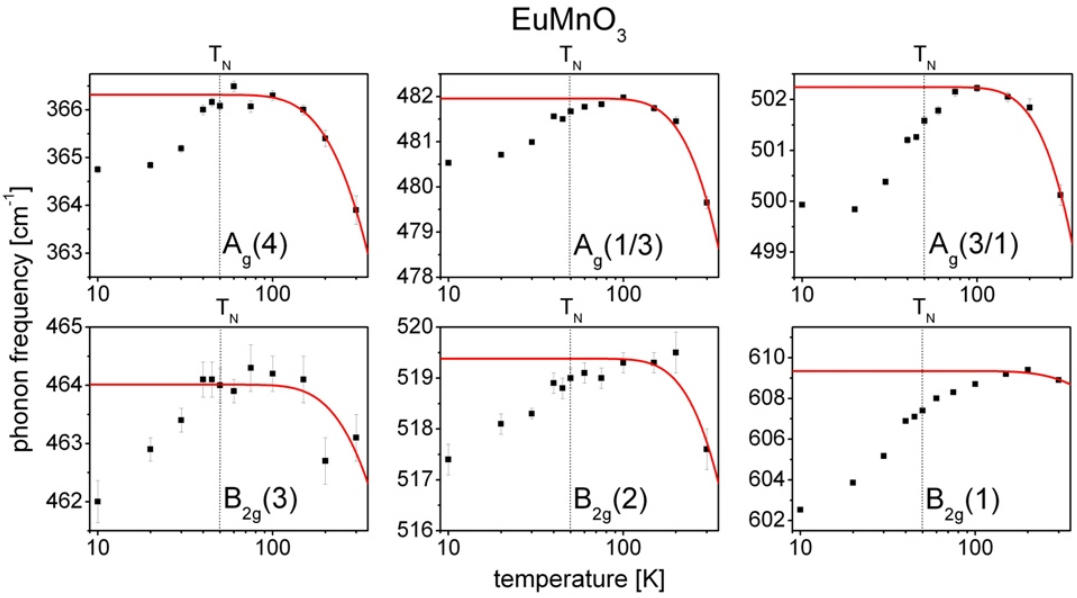

Figure 7.2: Temperature dependence of the phonon frequencies of all Raman–active phonon modes indicated in figure 7.1. The red lines are fits corresponding to equation (7.1) for $T \gg T_N$, the onset temperature of the magnetically ordered phases indicated by the dotted black vertical line.

In literature, similar softening was reported for several other $RMnO_3$ compounds, such as $LaMnO_3$ [GGS+99], $PrMnO_3$, $NdMnO_3$ and $SmMnO_3$ [LJM+06], but not for $EuMnO_3$. For the latter, a temperature dependent behaviour of the $A_g(1/3)$, $A_g(3/1)$ and $B_{2g}(1)$ modes according to equation (7.1) was observed. This discrepancy to the measurements carried out within this thesis, which show strong SPC effects for the Raman–active phonon modes, is attributed to the polycrystallinity of the $EuMnO_3$, $GdMnO_3$ and $TbMnO_3$ samples investigated in [LJM+06]. For the measurements shown in this thesis, only single crystalline samples are employed.

For a quantitative comparison of the observed phonon softenings, a plot of the relative shift of the phonon frequencies as a function of temperature is shown in figure 7.3. The relative shifts are obtained by calculating the deviation to the corresponding frequency at $T = 100K$. Among the observed phonon modes, the symmetric stretching mode $B_{2g}(1)$ shows the most pronounced frequency softening (i.e. an asymptotical value $\Delta\omega/\omega \approx -1.1\%$ extrapolated to $T = 0K$). The relative shifts of the other modes are about a factor 2–3 weaker. A list of the frequency softenings observed in $EuMnO_3$ can be found in table 7.1 (section 7.3).

An important aspect is the onset temperature of the frequency renormalisation. In figure 7.2 it is clearly visible, that already for temperatures $T \gtrsim T_N$ a deviation from the temperature behaviour described by equation (7.1) occurs. As in the case of the relative frequency shifts, the $B_{2g}(1)$ mode shows the strongest effect, i.e. an onset of frequency softening at $T \approx 150K$ with an inclination point at T_N. For the other phonon modes this onset is located at temperatures closer to T_N. The different onset of frequency renor-

malisation can be explained by considering spin fluctuations, that are already present in the paramagnetic phase above T_N. According to [LJM+06], the ith Mn^{3+} spin can be represented as

$$\boldsymbol{S}_i = \frac{\boldsymbol{M}}{4\mu_B} + \Delta\boldsymbol{S}_i, \tag{7.2}$$

where $\boldsymbol{M}$ is the average sublattice magnetisation of the MnO_2 (ac) plane per Mn^{3+} and $\Delta\boldsymbol{S}_i$ is the spin fluctuation due to quantum and thermal effects. As discussed in section 5.1, SPC is most pronounced for $RMnO_3$ systems with A–type antiferromagnetism, where the Mn^{3+} spins within the MnO_2 (ac) plane are ferromagnetically coupled. This further implies, that phonon modes with in–plane oxygen displacement should show a stronger SPC than those modes with out–of–plane or oxygen movement within the RO (ac) plane. Due to the aforementioned spin fluctuations within the MnO_2 (ac) plane, the onset of the frequency softening should be located at higher temperatures for modes with mainly in–plane O^{2-} displacement.

For testing this model, the temperature dependent behaviour of the $B_{2g}(1)$, $A_g(1/3)$, $A_g(3/1)$ and $A_g(4)$ modes is considered. A comparison of the corresponding mode patterns of the four Raman–active modes (see figures 4.1 and 4.2) leads to the expectance, that the $B_{2g}(1)$ and $A_g(1)$ phonon modes should have the most pronounced frequency shifts and should be very sensitive to spin fluctuations in the MnO_2 (ac) plane. For $B_{2g}(1)$ this is nicely verified by the observed behaviour in the figures 7.2 and 7.3, while $A_g(1)$ shows a behaviour similar to the $A_g(3)$ mode, which only weakly modulates the in–plane Mn–O

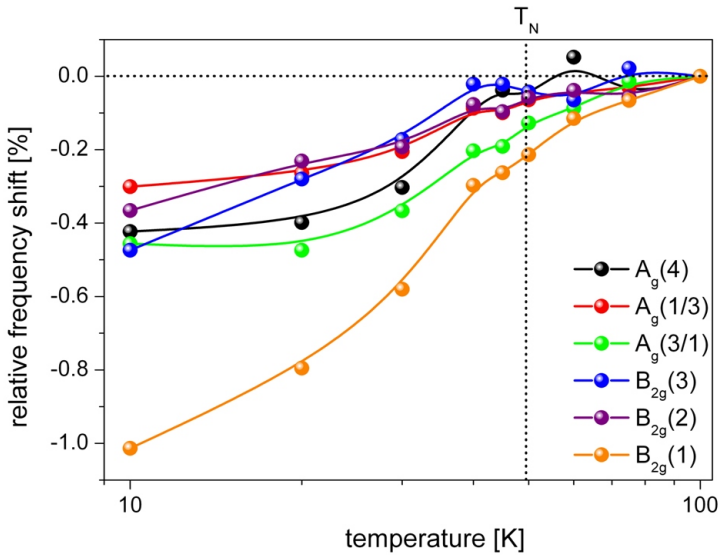

Figure 7.3: Relative frequency shift as a function of temperature for all $EuMnO_3$ phonon modes indicated in figure 7.1 with respect to the corresponding phonon frequency at T=100K. T_N symbolises the onset temperature of the magnetically ordered phases. The coloured lines act as a guide to the eye.

bonds. This can be understood by the mode–mixing effect of $A_g(1)$ and $A_g(3)$ already investigated in section 6.2 for both sample series. Thus, moderate frequency shifts and sensitivity to spin fluctuations within the MnO_2 (ac) plane can be expected for these two modes. Finally $A_g(4)$, which has mainly components perpendicular to the MnO_2 (ac) plane, has a small frequency shift and almost no fluctuation–induced renormalisation effects above T_N.
Summing up, for the Raman–active phonon modes in $EuMnO_3$ deviations of the temperature dependence of the phonon frequencies from the behaviour expected by the simple Klemens model are observed and interpreted as a manifestation of SPC. Its mode dependence can be traced back to the symmetry properties of the corresponding phonon mode patterns. So, the modes with mainly O^{2-} displacements within the ferromagnetically coupled MnO_2 (ac) plane show the strongest frequency softening and an onset of the frequency shift, that is located at temperatures significantly higher than the onset temperature of the magnetically ordered phases, T_N. The latter is attributed to spin fluctuations induced by quantum and thermal effects, which are already present in the paramagnetic phase and especially pronounced in the ferromagnetically coupled MnO_2 (ac) plane.

7.1.2 IR–active phonon modes

In contrast to the Raman–active modes discussed before, in the IR–active modes the Mn^{3+} can participate in the displacement pattern. For group 2 and 3 modes (i.e. MnO_6 tilting, buckling, rotations and MnO_6 stretching and internal modes, respectively) a relative displacement of Mn^{3+} and O^{2-} causes a modulation of the electric dipole moment of the IR–active lattice vibration, which due to the selection rules resulting from a b–cut sample surface has to be located either within the MnO_2 (ac), within the EuO (ac) plane or between both planes. Thus, a classification in modes with their main displacement pattern within the MnO_2 (ac) plane or out of this plane is not possible.
Further, it has to be pointed out, that only group 2 and 3 modes are expected to show SPC induced frequency shifts, because the SPC effect relies on the modulation of the Mn–O–Mn bonds. Thus, the IR–active modes of group 1 (i.e. mainly motions of Eu^{3+} and Mn^{3+}) are not considered here. A discussion about their temperature dependent frequency shifts will follow in chapter 8 in the context of Electromagnon–Phonon Coupling (EMPC).
On the other hand, the temperature dependent phonon frequencies of the IR–active phonon modes allow a selective study of the sensitivity of the IR–active group 2 and 3 phonon modes. Thus, the differences in SPC effects can be systematically analysed for bending, buckling and tilting modes, i.e. group 2 modes, and compared to the internal and stretching modes of the MnO_6 octahedra, i.e. group 3 modes.

In figure 7.4 the temperature dependent reflectivity and hence derived ϵ_2 spectra of $EuMnO_3$ are shown in B_{1u} and B_{3u} symmetry for several temperatures. As in the case of the Raman spectra, all phonon modes analysed within this section, i.e. $B_{1u}(4)$ to (9) and $B_{3u}(4)$ to (9) are marked by dotted black lines in the ϵ_2 spectra indicating the corre-

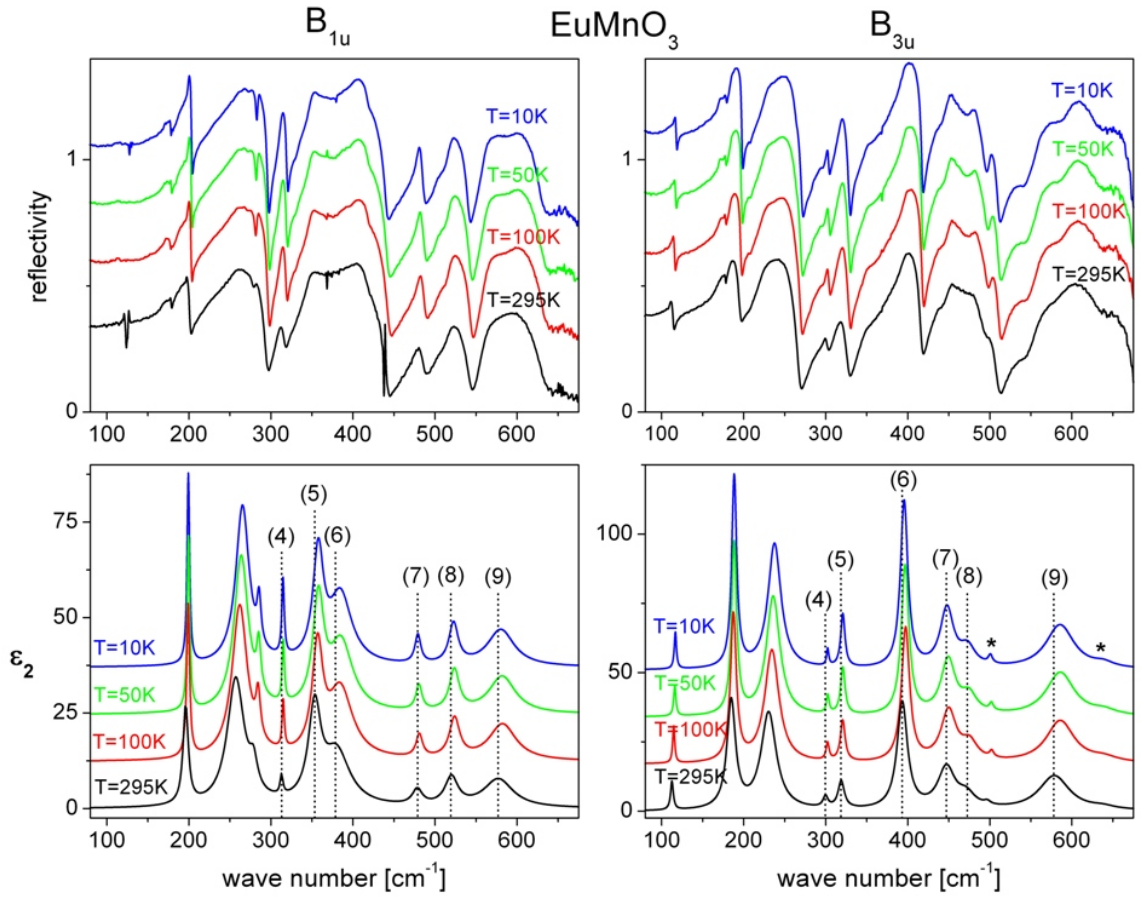

Figure 7.4: Reflectivity (upper row) and hence derived ϵ_2 (lower row) spectra of $EuMnO_3$ in B_{1u} (left column) and B_{3u} (right column) symmetry for several temperatures, respectively. The spectra are vertically shifted for clarity. Symmetry forbidden phonon peaks are marked by asterisks.

sponding phonon frequency at room temperature. An inspection of the phonon structure shows, that in the B_{1u} spectra the modes $B_{1u}(4)$ to (6) as well as $B_{1u}(7)$ to (9) can be nicely combined in two pairs of three modes, reflecting their classification in group 2 and 3 modes, respectively. In contrast, the situation is less clear in the B_{3u} spectra due to the frequencies of the relevant phonon modes. Most prominent is the case of the $B_{3u}(6)$ mode, which could also be classified as a group 3 mode due to its vicinity to the $B_{3u}(7)$ to (9) modes. This point will be important, when comparing the relative frequency softenings of the IR–active modes.

The phonon frequencies of all modes considered in this section are shown as a function of temperature in figure 7.5 on a semi logarithmic scale. As in the case of the Raman–active modes (see figure 7.2), the solid red lines are fit functions symbolising the temperature dependent behaviour expected without SPC. However, for the IR–active phonon modes phonon–phonon decay processes up to fourth order need to be considered to obtain a good quantitative agreement with experimental data for $T \gg T_N$. Thus, according to

[BWH83], equation (7.1) is expanded to

$$\omega(T) = \omega_0 - C\left(1 + \frac{2}{e^x - 1}\right) - D\left(1 + \frac{3}{e^y - 1} + \frac{3}{(e^y - 1)^2}\right), \tag{7.3}$$

where ω_0, C and D are fit parameters, $x = \hbar\omega_0/kT$ and $y = \hbar\omega_0/3kT$.
For temperatures $T \leq T_N$, a systematic deviation of the phonon frequencies from equation (7.3) is observed for most of the phonon modes plotted in figure 7.5. Thus, it can be immediately followed, that for Raman– as well as for IR–active phonon modes SPC effects occur. Another similarity is, that the onset of the frequency softening is located slightly above T_N though not so pronounced as for the $B_{2g}(1)$ mode.
To quantitatively compare the frequency shifts of the IR–active modes, their relative shifts with respect to the corresponding frequency value at $T = 100K$ are plotted as a function of temperature in figure 7.6. The data arrangement is chosen (i) according to the mode symmetry, i.e. the left panels show modes with B_{1u} symmetry, while the right panels those with B_{3u} symmetry, and (ii) according to the classification scheme of the IR–active phonons in group 2 and 3 modes. The comparison shows, that – in general – the group 3 phonon modes have a pronounced frequency softening, i.e. $\Delta\omega/\omega \approx -0.4\%$ to -0.25% for B_{1u} symmetry and $\Delta\omega/\omega \approx -0.5\%$ to -0.05% for B_{3u} symmetry, respectively. In contrast, the group 2 modes have slight negative to positive relative shifts with respect to their corresponding frequency at $T = 100K$ (i.e. $\Delta\omega/\omega \approx -0.05\%$ to $+0.25\%$ for B_{1u} symmetry and $\Delta\omega/\omega \approx +0.05\%$ for B_{3u} symmetry) with the exception of $B_{3u}(6)$.

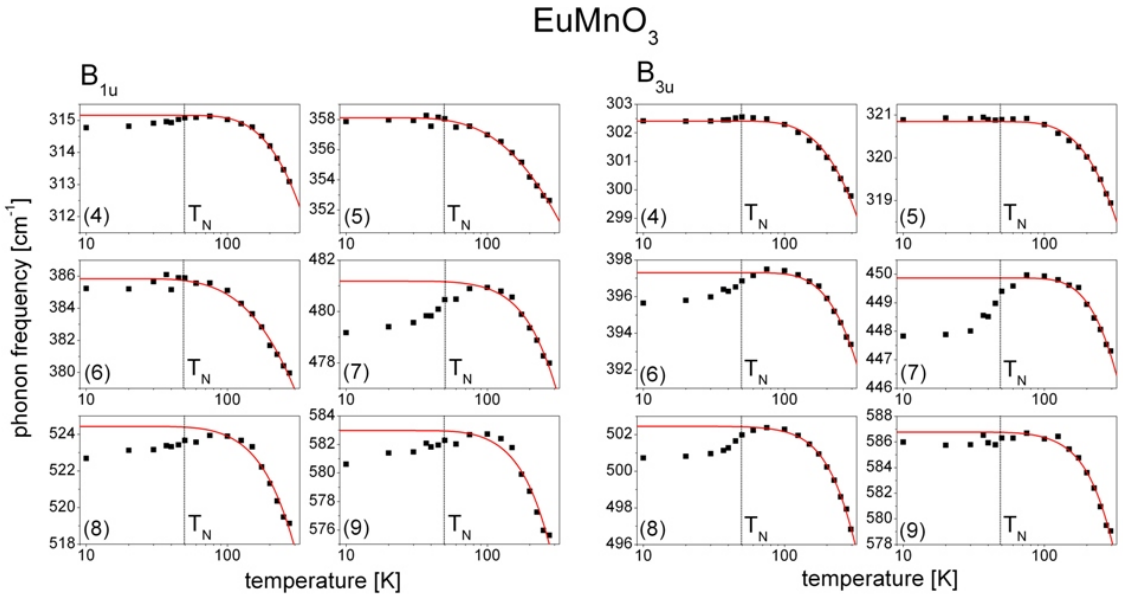

Figure 7.5: Temperature dependence of the IR–active phonon mode frequencies indicated in figure 7.4 for B_{1u} (left side) and B_{3u} (right side) symmetry, respectively. The red lines are fits optimised for $T \gg T_N$ (the onset temperature of the magnetically ordered phases) corresponding to equation (7.3).

The behaviour of this mode can be understood by an inspection of the reflectivity and ϵ_2 spectra in figure 7.4. As stated before, the classification in group 2 and 3 modes fails for the $B_{3u}(6)$ mode due to their vicinity to the $B_{3u}(7)$ to (9) modes. Thus, a more group 3 – like behaviour of this mode can be expected and is clearly visible as a pronounced relative phonon frequency shift of $\Delta\omega/\omega \approx -0.45\%$.
Summing up, a considerably higher sensitivity of the MnO_6 internal and stretching modes concerning SPC effects can be followed from the temperature dependent frequency shifts of the IR–active phonon modes compared to the MnO_6 tilting, buckling and rotational modes. It can also be concluded, that the participation of the Mn^{3+} in the IR–active modes has no impact on the observability of the SPC.
With this reasoning the analysis of the mode–dependence of SPC can be closed and the compositional dependence can be considered next.

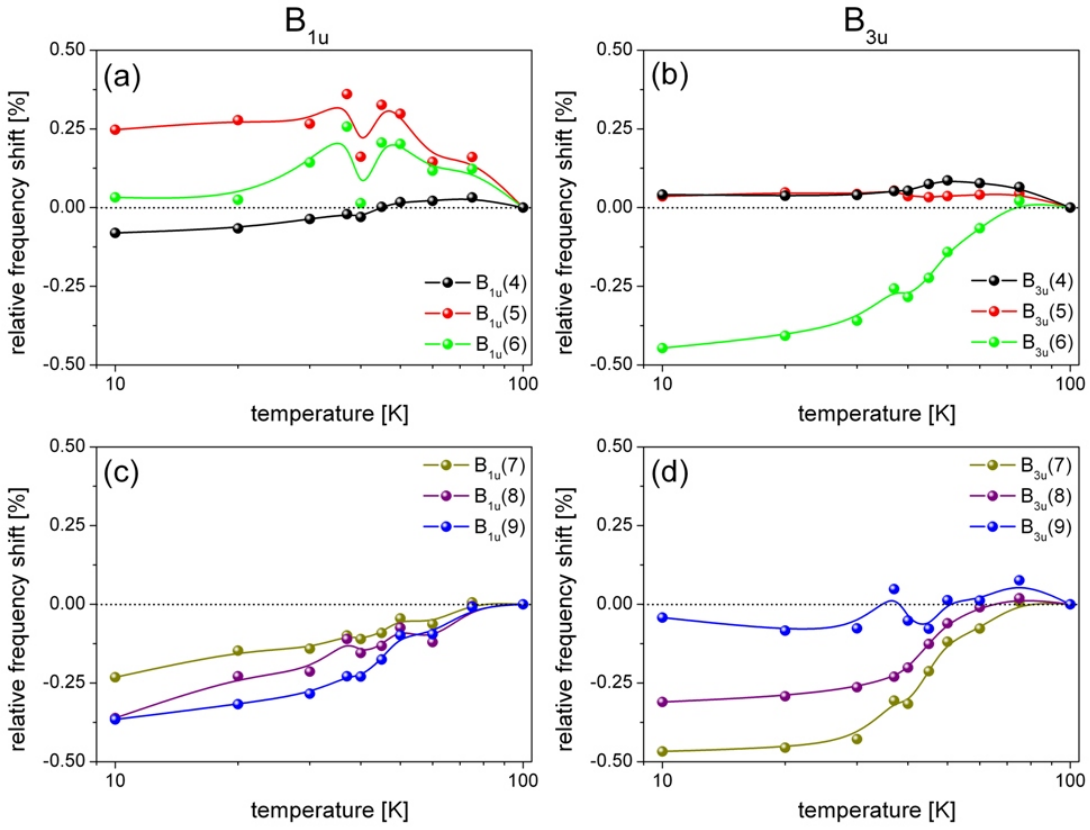

Figure 7.6: Relative frequency shifts as a function of temperature of the IR–active phonon modes indicated in figure 7.4 with respect to the corresponding phonon frequency at $T = 100K$ for B_{1u} – panels (a) and (c) – and B_{3u} symmetry – panels (b) and (d). While in (a) and (b) the group 2 modes are shown, (c) and (d) depict the group 3 modes, corresponding to the classification scheme introduced in section 4.3. The coloured lines act as a guide to the eyes.

7.2 Compositional dependence

In this section, the compositional dependence of the SPC will be discussed. For that purpose, the strength of the SPC effects will be analysed with respect to the R^{3+} ionic radius, which determines the orthorhombic distortion of the perovskite structure as already laid out in section 3.1. We will first consider the stoichiometric $RMnO_3$ ($R^{3+} = Eu^{3+}$, Gd^{3+}, Tb^{3+}) series followed by a comparative analysis of the doped $Eu_{1-x}Y_xMnO_3$ ($0 \leq x \leq 0.5$) series. A detailed discussion of the physical origins of the observed dependencies will be carried out in the last section of this chapter.

7.2.1 Stoichiometric $RMnO_3$ ($R^{3+} = Eu^{3+}$, Gd^{3+}, Tb^{3+})

First, the stoichiometric $RMnO_3$ series will be regarded. The reason for this approach is the possibility to put the SPC results obtained from $RMnO_3$ in context with literature. As mentioned before, temperature dependent Raman measurements were carried out on polycrystalline $RMnO_3$ ($R^{3+} = Eu^{3+}$, Gd^{3+}, Tb^{3+}, among others) in [LJM+06]. There, no SPC effects were observed for these compounds – an observation that could already be contradicted by the temperature dependent Raman and FT–IR measurements on single crystalline $EuMnO_3$ presented in section 7.1. We will now further elaborate this for the other compounds of the series.
One of the main findings discussed in section 7.1 was, that SPC effects occur for Raman– as well as for some group 2 and all group 3 IR–active phonons. The crucial factor for occurrence of SPC is the modulation of the Mn–O–Mn bonds. Thus, for a systematic discussion, Raman and reflectivity spectra need to be considered. First, the results of the temperature dependent Raman measurements will be presented.

Figure 7.7 shows the temperature dependence of the Raman–active $A_g(1/3)$, $A_g(3/1)$, $A_g(4)$ and $B_{2g}(1)$ modes arranged in panels for the whole $RMnO_3$ series, respectively. In contrast to the temperature dependence of the phonon frequencies obtained from $EuMnO_3$ in figure 7.2, figure 7.7 shows only the temperature region of the magnetically ordered phases, i.e. from $T = 100K$ towards lower temperatures. The dashed red lines are fits of the experimental data for $T \gg T_N$ corresponding to equation (7.1) and, therefore, model the expected temperature behaviour without SPC effects. The blue solid lines are parabola fits for $T \leq T_N$ acting as a guide to the eye for the temperature dependence of the SPC. This dependence is expressed by the temperature dependent prefactor $K(T)$ in equation (5.13) reflecting the temperature dependent magnetisation within the $RMnO_3$ system. It can be seen, that the parabola fits cross the high temperature fits corresponding to equation (7.1) in the temperature region of T_N. Thus, for temperatures above and below T_N model functions exist, which can give good approximations for the temperature dependence of the phonon modes either with or without SPC effects. The deviations from both fits within the intermediate region located at temperatures slightly above T_N are attributed to spin fluctuations persistent in the paramagnetic phase, whose mode dependencies were already discussed in section 7.1.1. These dependencies can be verified throughout the whole investigated $RMnO_3$ series. Utilising both fit functions, the

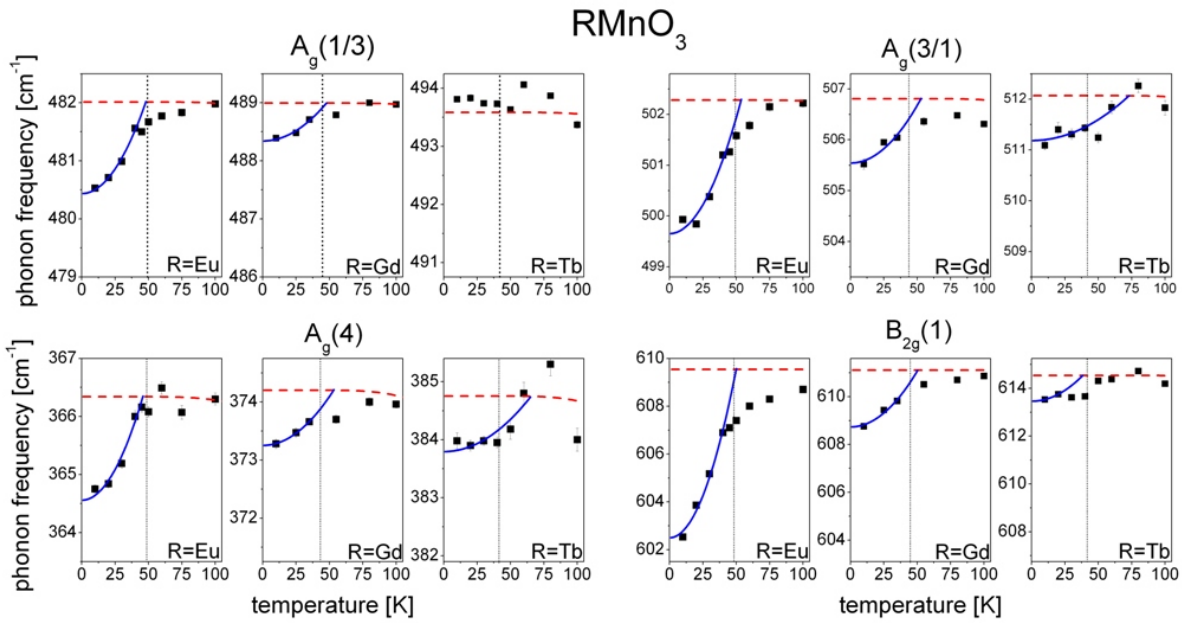

Figure 7.7: Temperature dependence of the Raman–active $A_g(1/3)$, $A_g(3/1)$, $A_g(4)$ and $B_{2g}(1)$ modes for the whole $RMnO_3$ series in the temperature region of the magnetically ordered phases. The dashed red lines refer to the fits for $T \gg T_N$ according to equation (7.1) describing the temperature dependence of the phonons without SPC. T_N is indicated by the vertical dotted line. The solid blue lines are parabola fits for $T \leq T_N$ acting as a guide to the eye.

quantitative phonon frequency softening $\Delta\omega$ can now be extracted by expanding both fits to $T = 0K$ and calculating the difference of the two obtained frequency values. This will be carried out on a systematic base in section 7.3.

Considering the compositional dependence of the SPC effects throughout the $RMnO_3$ series, all observed phonon modes show a monotonous weakening of the frequency softening with decreasing R^{3+} ionic radius, i.e. from $EuMnO_3$ to $TbMnO_3$. E.g. for the $B_{2g}(1)$ modes, where the phonon renormalisation effects are most pronounced in $EuMnO_3$ (see section 7.1.1), the relative phonon frequency shift is reduced from $\Delta\omega/\omega \approx -1.1\%$ in $EuMnO_3$ to $\Delta\omega/\omega \approx -0.2\%$ in $TbMnO_3$. These weakening effects originate from the increasing orthorhombic distortion caused by the replacement of Eu^{3+} by Gd^{3+} or Tb^{3+}. This distortion leads to a partial compensation of the NN Mn^{3+} ferromagnetic interaction responsible for the strong SPC effects within the MnO_2 (ac) plane by an increasing importance of the NNN Mn^{3+} antiferromagnetic exchange. A systematic discussion will follow in section 7.3 together with the results of the doped $Eu_{1-x}Y_xMnO_3$ series.
Nevertheless, SPC effects are observed for the $A_g(3/1)$, $A_g(4)$ and $B_{2g}(1)$ modes even in $TbMnO_3$, where no A–type AFM phase exists, but the spin spiral phases discussed in section 3.2. This observation is in clear contrast to the previous results of [LJM+06] on polycrystalline $RMnO_3$ (R^{3+} = Eu^{3+}, Gd^{3+}, Tb^{3+}). Thus, it is concluded, that SPC is not only observable in $RMnO_3$ compounds with A–type AFM.

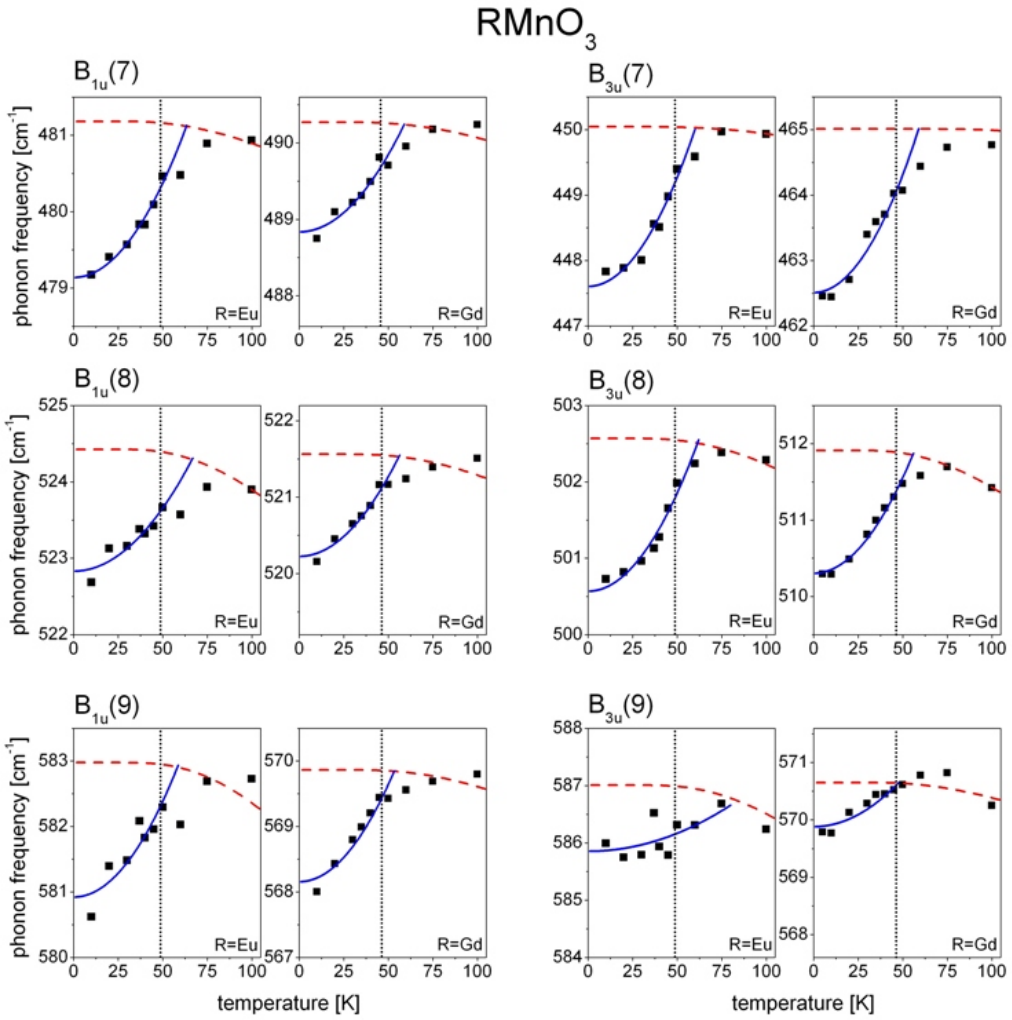

Figure 7.8: Temperature dependence of $B_{1u}(7)$ to (9) (left panels) and $B_{3u}(7)$ to (9) (right panels) for $EuMnO_3$ and $GdMnO_3$. The dashed red lines refer to the fits for $T \gg T_N$ (T_N is indicated by the vertical dotted line) according to equation (7.3) describing the temperature dependence of the phonons without SPC. The solid blue lines are parabola fits for $T \leq T_N$ acting as a guide to the eye. Temperature dependent reflectivity measurements of $TbMnO_3$ can be found in [SKR+09].

The second step in our analysis of the compositional dependence of SPC for the $RMnO_3$ series will be the consideration of the IR–active phonon modes. Thus, we will now turn to the temperature dependent reflectivity measurements. Due to brevity, only the IR–active modes of group 3, which all show considerable SPC in $EuMnO_3$ (see section 7.1.2), are shown in figure 7.8, i.e. $B_{1u}(7)$ to (9) and $B_{3u}(7)$ to (9), respectively. It has to be pointed out, that for the $RMnO_3$ series no temperature dependent reflectivity data of $TbMnO_3$ are needed, because in [SKR+09] these are already obtained from an a–cut $TbMnO_3$ sample – giving access to the B_{2u} and B_{3u} modes. This a–cut sample was cut from the same macroscopic crystal as that employed for the Raman and room temperature reflectivity

measurements carried out within this thesis.
For the IR–active phonon modes depicted in figure 7.8 with B_{1u} and B_{3u} symmetry the same general trend concerning the compositional dependence as for the Raman–active modes can be observed, i.e. a weakening of the phonon softening for decreasing R^{3+} ionic radius. This is likewise attributed to the increasing orthorhombic distortion and the simultaneously increasing importance of the NNN Mn^{3+} antiferromagnetic exchange (see the upcoming discussion in section 7.3).
It should be pointed out again, that a different fit function has to be employed for fitting the experimental data of figure 7.8 for $T \gg T_N$. In contrast to the Raman–active modes, where fit functions according to equation (7.1) are utilised, for the IR–active modes the Klemens model has to be expanded up to phonon decay processes of fourth order [BWH83] to gain reasonable agreement between experimental data and the fits. Thus, in figure 7.8 fit functions according to equation (7.3) are employed. The physical reason for this behaviour might be related to different relaxation channels for the Raman–active and IR–active optical phonons, which according to the Klemens model can decay in two or more acoustic phonons. A different relaxation behaviour of Raman– and IR–active modes would thus manifest itself in different temperature dependence of the phonon frequencies. Nevertheless, the SPC effects can be clearly separated, because both approaches employing the simple Klemens model cannot explain a frequency softening for decreasing temperature.
Summing up, the results presented in this subsection, SPC coupling effects are observable throughout the whole investigated stoichiometric $RMnO_3$ ($R^{3+} = Eu^{3+}$, Gd^{3+}, Tb^{3+}) series in A–type antiferromagnetic as well as incommensurate magnetic phases. For decreasing the R^{3+} ionic radius, the orthorhombic distortion increases and the NN Mn^{3+} ferromagnetic exchange is partially compensated by NNN Mn^{3+} antiferromagnetic exchange. This, in turn, causes a weakening of the SPC coupling effects, whose strength is determined by the magnetic exchange – and is strongest for ferromagnetic exchange within the MnO_2 (ac) plane.

7.2.2 Doped $Eu_{1-x}Y_xMnO_3$ ($0 \leq x \leq 0.5$)

Having carried out the analysis of stoichiometric $RMnO_3$ with the main result of clearly observable SPC effects throughout the whole sample series, a comparative investigation of the doped $Eu_{1-x}Y_xMnO_3$ series with Y–contents of $0 \leq x \leq 0.5$ will follow in this section. The most important question is: Does the doping approach pursued to quasi–continuously tune the R^{3+} ionic radius in $Eu_{1-x}Y_xMnO_3$ have any impact on the SPC?
It should also be mentioned here, that in contrast to the stoichiometric $RMnO_3$ system no temperature dependent Raman and only FT–IR measurements on selected samples (e.g. $TbMnO_3$, see [SKR+09]) carried out in the FIR spectral region are reported in literature. An identical approach to the discussion covering the $RMnO_3$ series in the previous section is followed here. Thus, first the Raman–active phonon modes are analysed, followed by the IR–active phonon modes of the groups 2 and 3.

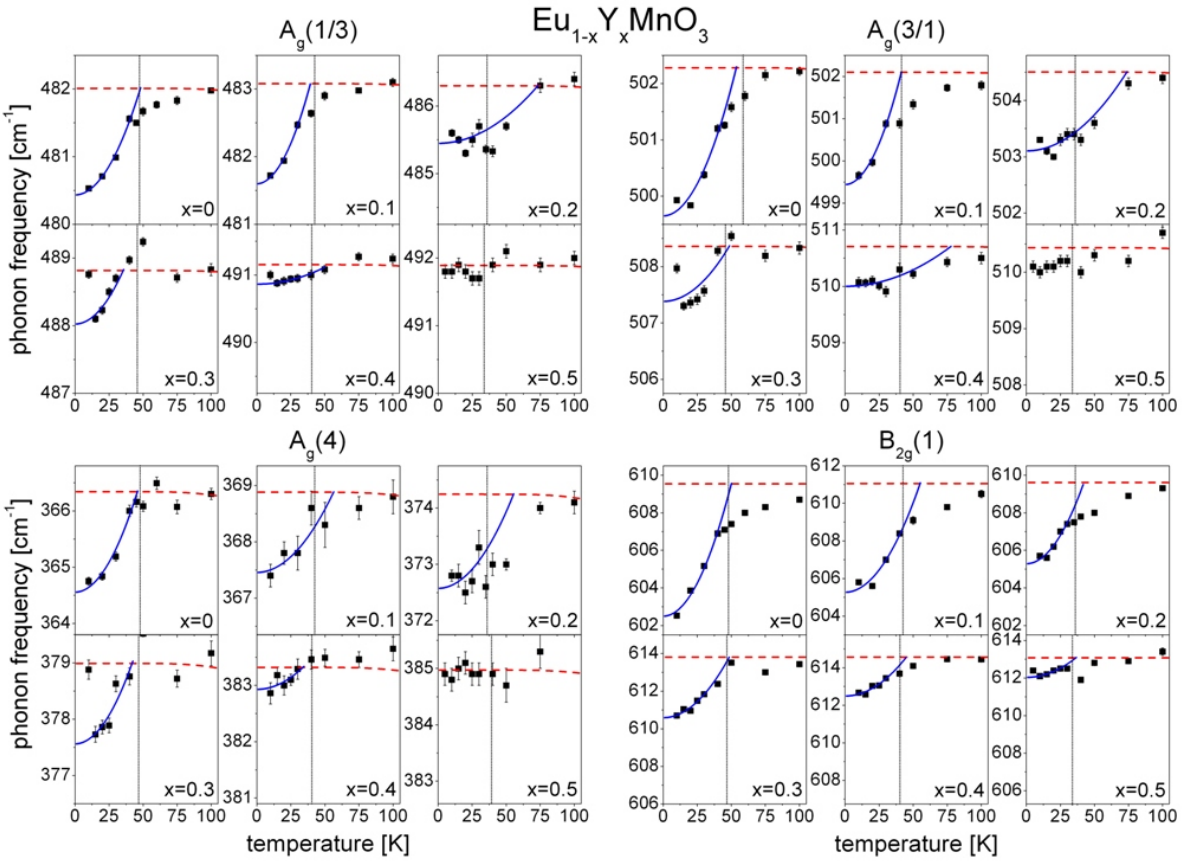

Figure 7.9: Temperature dependence of $A_g(1/3)$, $A_g(3/1)$, $A_g(4)$ and $B_{2g}(1)$ for the whole $Eu_{1-x}Y_xMnO_3$ series in the temperature region of the magnetically ordered phases. The data arrangement and the employed fit functions are the same as in figure 7.7 for the $RMnO_3$ series.

For the Raman spectra presented in the following, the whole $Eu_{1-x}Y_xMnO_3$ series was employed, yielding experimental data for samples with Y–contents of 0, 10, 20, 30, 40 and 50%. Figure 7.9 shows the temperature dependence of the Raman–active $A_g(1/3)$, $A_g(3/1)$, $A_g(4)$ and $B_{2g}(1)$ modes in the same arrangement and with the same fit functions as figure 7.7 for the $RMnO_3$ series.
It is immediately clear, that SPC effects are observable throughout the whole $Eu_{1-x}Y_xMnO_3$ series. An inspection of the strength of the phonon frequency softening throughout the series shows a general trend for all depicted phonon modes: a monotonous weakening of the frequency shifts with increasing Y doping and, thus, decreasing average $Eu_{1-x}Y_x$ ionic radius. This compositional dependence is equivalent to that observed in the stoichiometric $RMnO_3$ series. A natural interpretation of this behaviour is, that the doping induced possible disorder effects are restricted to the $Eu_{1-x}Y_x$ sites and do not affect the MnO_6 subsystem responsible for the SPC effects – as already concluded from the results of the room temperature measurements presented in section 6.2.2. As in the case of the $RMnO_3$ series, the employed parabola fits for the temperature dependent fre-

quencies including SPC cross those functions according to equation (7.3) in the vicinity of T_N. Again the reader is referred to section 7.3 for a more detailed discussion.
Another important aspect is the mode dependence of the SPC effects, that were systematically discussed in section 7.1.1 for $EuMnO_3$. It can be clearly observed, that the SPC strength ratio found in $EuMnO_3$ is valid throughout the whole investigated $Eu_{1-x}Y_xMnO_3$ series. Thus, the mode symmetry determining the SPC strength of the phonon modes is clearly conserved for doped $Eu_{1-x}Y_xMnO_3$. Further, the deviations from the temperature behaviour modelled by the above mentioned fit functions are visible with the same mode and temperature dependence as in the $RMnO_3$ series. This is a clear indication, that the magnetic fluctuations persistent in the paramagnetic phase are essentially the same for both sample series.
Now, the SPC effects of the IR–active phonon modes of the $Eu_{1-x}Y_xMnO_3$ series derived from temperature dependent reflectivity spectra will be considered. In contrast to the above discussed Raman spectra, only selected $Eu_{1-x}Y_xMnO_3$ samples could be measured due to the very different degree of surface quality with the $Eu_{1-x}Y_xMnO_3$ sample series. Thus, only the $Eu_{1-x}Y_xMnO_3$ samples with Y–contents of 0, 20 and 50 % are regarded in the following.
The temperature dependence of the group 3 IR–active phonon modes obtained from the above mentioned $Eu_{1-x}Y_xMnO_3$ samples are shown in figure 7.10 in the same arrangement as the IR–active group 3 modes obtained from $RMnO_3$ in figure 7.8. The fit functions employed for modelling the temperature dependent phonon frequencies are also the same.
As in the case of the Raman–active modes, the trend of weakened SPC effects for reduced average $Eu_{1-x}Y_x$ ionic radii is confirmed, although the weakening is less pronounced than observed for the Raman–active $B_{2g}(1)$ mode. This can be traced back to an effect of the fitting procedure: in contrast to the Raman spectra, the reflectivity spectra have to be fitted over the complete investigated frequency range. This is due to the fitting procedure when employing the Drude–Lorentz model for modelling the complex dielectric function $\epsilon(\omega)$, which can be easily understood when considering equation (2.25). Thus, especially for the IR–active phonons of group 3, that have a large linewidth Γ and frequencies ω_T very close to each other, a more intermixed behaviour concerning the SPC effects should be expected. An intermixed SPC behaviour for all IR–active modes of group 3 would mean, that for all phonon modes of this group an average SPC strength should be observable. This is obviously the case in comparison to the Raman–active modes, where strongly pronounced (e.g. $B_{2g}(1)$) as well as rather weak SPC effects (e.g. $A_g(4)$) occur.
Further, it should be noted, that the deviations in the temperature region slightly above T_N from the behaviour predicted by the two employed fit functions are less pronounced than those of the Raman–active modes, especially the $B_{2g}(1)$ mode. This could be a sign of a less pronounced sensitivity of the IR–active phonon modes to magnetic fluctuations within the paramagnetic phase and can be also interpreted as a sign for a more intermixed behaviour of these modes.
The experimental results presented in this subsection for the doped $Eu_{1-x}Y_xMnO_3$ ($0 \leq x \leq 0.5$) series clearly demonstrate, that SPC effects can be observed in this sample system, either. This is a clear indication, that SPC is an effect of the MnO_6 subsystem of

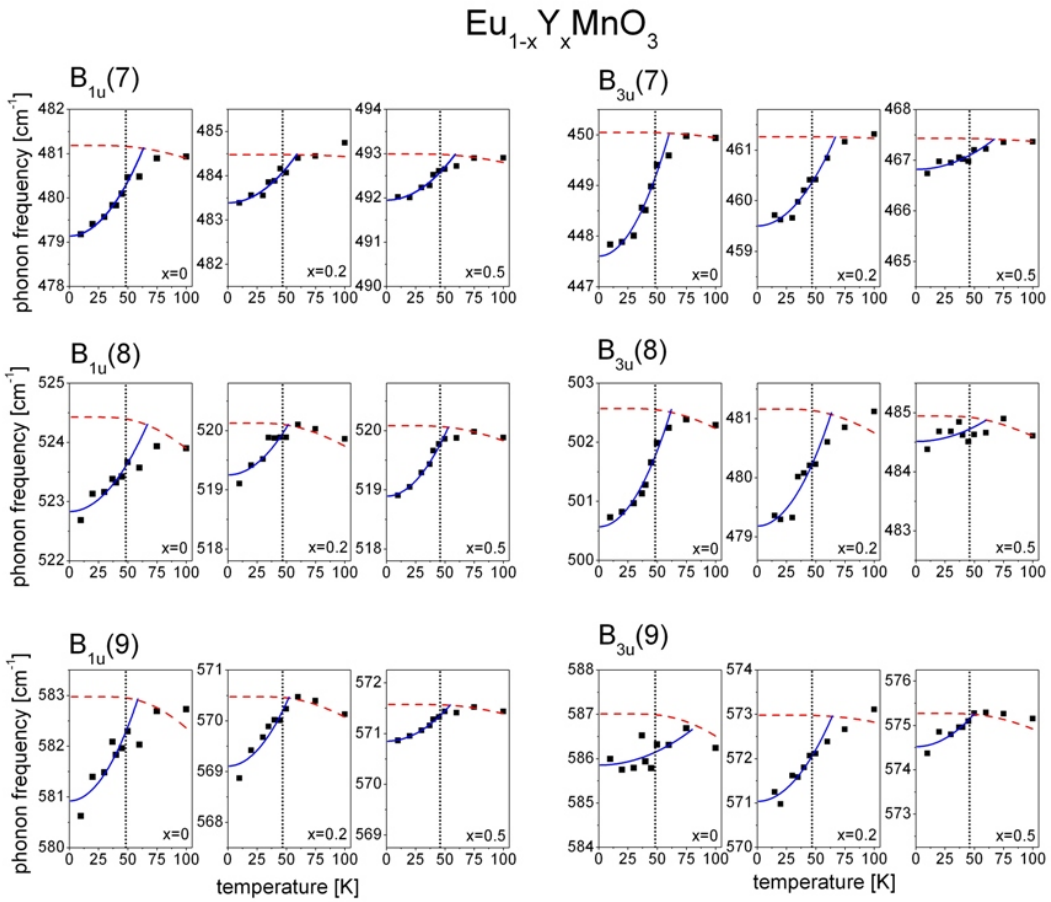

Figure 7.10: Temperature dependence of $B_{1u}(7)$ to (9) and $B_{3u}(7)$ to (9) for $EuMnO_3$, $Eu_{0.8}Y_{0.2}MnO_3$ and $Eu_{0.5}Y_{0.5}MnO_3$, respectively. The fit functions indicated are the same as in figure 7.7 for the temperature dependent Raman spectra.

the Pnma structure and, therefore, is not affected by the doping approach. A systematic discussion about the underlying physics responsible for the observed dependences will follow now in the next section taking into account the experimental results for both sample series.

7.3 Discussion

As stated before, the physical origins of the SPC effects and their dependency on the mode symmetry and the occupation of the R^{3+}–site will now be considered. The importance of this discussion is underscored by recently published temperature dependent Raman measurements of ceramic $Eu_{1-x}Y_xMnO_3$ [MAF+10] and a comparative study of SPC in ceramic $EuMnO_3$ and $GdMnO_3$ [FMA+09]. The experimental results of these studies lead to the conclusion of a correlation between SPC and the Electromagnons [MAF+10] and also to the finding, that SPC effects in $GdMnO_3$ should be more pronounced than those

Table 7.1: Relative phonon frequency softening $\Delta\omega/\omega$ in % extrapolated to $T = 0K$ with respect to the occupation of the R^{3+} site for all investigated Raman– and IR–active phonon modes. The softening values for the B_{3u} modes of $TbMnO_3$ are approximated from the temperature dependent phonon frequencies drawn in [Sch09].

Mode	Tb	Gd	Eu	$Eu_{0.8}Y_{0.2}$	$Eu_{0.5}Y_{0.5}$
$A_g(1/3)$	0	-0.13	-0.33	-0.18	0
$A_g(3/1)$	-0.17	-0.25	-0.52	-0.28	0
$A_g(4)$	-0.23	-0.25	-0.49	-0.44	0
$B_{2g}(1)$	-0.17	-0.39	-1.1	-0.71	-0.17
$B_{1u}(7)$	–	-0.29	-0.42	-0.22	-0.21
$B_{1u}(8)$	–	-0.26	-0.31	-0.17	-0.23
$B_{1u}(9)$	–	-0.30	-0.35	-0.24	-0.13
$B_{3u}(7)$	≈-0.3	-0.53	-0.54	-0.38	-0.13
$B_{3u}(8)$	≈-0.05	-0.31	-0.40	-0.41	-0.09
$B_{3u}(9)$	0	-0.13	-0.19	-0.34	-0.13

in $EuMnO_3$ [FMA+09]. Both deductions must be objected considering the experimental findings of this thesis, which are obtained from single crystalline sample series. Instead, an alternative consistent explanation of the SPC and its dependencies will be presented. For the purpose of a quantitative discussion, the relative phonon frequency softening $\Delta\omega/\omega$ is listed in table 7.1 for each investigated phonon mode (arranged in columns) and R^{3+} occupation (arranged in rows), respectively. The row arrangement, i.e. the R^{3+} occupation, is chosen such, that the "mother compound" $EuMnO_3$ is located in the centre row with the stoichiometric $RMnO_3$ series on the left and the doped $Eu_{1-x}Y_xMnO_3$ series on the right hand. Further, the Raman– and IR–active modes are grouped in blocks separated by horizontal lines. For all observed modes the general trend of a moderate weakening with decreasing R^{3+} ionic radius is confirmed for both series, thus immediately contradicting the observation of Ferreira et al. of stronger SPC effects in $GdMnO_3$ compared to those in $EuMnO_3$ [FMA+09]. Deviations from the general trend occur in two cases for the IR–active modes: (i) $B_{1u}(8)$ of $Eu_{0.8}Y_{0.2}MnO_3$ and $Eu_{0.5}Y_{0.5}MnO_3$ and (ii) $B_{3u}(8)$ of $EuMnO_3$ and $Eu_{0.8}Y_{0.2}MnO_3$, where a group of phonon modes has to be fitted in the reflectivity spectra. As already laid out in section 7.1.2, minor uncertainties in the fitting procedure can occur especially for the weak modes in a group of phonons with the same symmetry, that have frequencies very close to each other – e.g. the $B_{3u}(8)$ mode in the group of $B_{3u}(6)$ to (9). However, these uncertainties do not alter the general trend and are limited to the IR–active modes.

The most important finding in the two previous sections is, that SPC effects occur for stoichiometric $RMnO_3$ as well as for doped $Eu_{1-x}Y_xMnO_3$. Further in both series a moderate weakening of SPC with decreasing R^{3+} or average $Eu_{1-x}Y_x$ ionic radius is observed. Now the question arises, how the latter approach of Y doping in $EuMnO_3$ can lead to

almost the same results as a complete replacement of Eu^{3+} by Gd^{3+} or Tb^{3+}. From the previous discussions it was already concluded, that the SPC effects should depend on the respective R^{3+} ionic radius, which determines the orthorhombic distortion. For a consistent microscopic picture, in principle, two scenarios are possible:
(i) Phase separation in $Eu_{1-x}Y_xMnO_3$ for $x > 0$ and, thus, local canted A–type antiferromagnetic domains are assumed. These could still be possible though a macroscopic magnetic moment would not be detectable due to the random distribution of the domains. This scenario can be ruled out for two reasons: as shown in [HSP+07] the magnetisation measurements should show a weak ferromagnetic moment along the b–axis. In the case of domains, these should have been aligned in the B field, resulting in a finite value for the macroscopic magnetisation – which is not the case according to the results of [HSP+07]. Additionally a phase separation should lead to clustering of the incorporated Y^{3+} ions, thus causing $YMnO_3$–like domains in $EuMnO_3$. The Raman–active phonon modes, which are sensitive to a change in the Mn–O–Mn bending angle (e.g. the $A_g(4)$, $A_g(1/3)$, or the $B_{2g}(3)$ mode), should therefore show a two–mode behaviour, or at least an inhomogeneous broadening in this scenario. This is not observed in the Raman spectra for all investigated samples.
(ii) The second scenario is the base of the model introduced in section 5.1 for the $RMnO_3$ systems with an incommensurate magnetic (ICM) structure: even in an ICM phase there still is a significant SPC because the latter is an effect caused by locally correlated spins. Thus, it is persistent in the ICM phase although the macroscopic magnetic moment connected with the canted A–type AFM phase vanishes. The reduction in the strength of the phonon softening and, thus, the SPC is originating from the increased MnO_6 octahedra tilting and in turn the compensation of the ferromagnetic NN Mn^{3+} exchange with the antiferromagnetic NNN Mn^{3+} exchange. The finite remaining value is therefore not connected to the existence of an A–type AFM but to a local correlation of the Mn^{3+} spins.
However, the main difference between the stoichiometric and doped single crystals should be stressed here. Due to Y doping a random distribution of Y^{3+} ions is incorporated in $EuMnO_3$ leading to an inherent distribution of the lattice distortion of the MnO_6 octahedra, e.g. the Mn–O–Mn tilting angle. Though in the measurements presented in this thesis no effects on the Raman–active phonons (e.g. inhomogeneous broadening) are detected, one has to consider that for explaining the phonon softening a model is employed, which sums up not only NN Mn^{3+} spins, but also NNN. This leads to a correlation length of SPC, which is clearly larger than one single unit cell. Thus, phonons are a local probe for SPC, but on a correlation length scale larger than a single unit cell. This allows adopting an "effective medium approximation"on the scale of a few unit cells without having to average over the whole crystal. This is also in agreement with the theoretical model of SPC presented in section 5.1.
The next step in the analysis of the SPC dependencies and its origins is a comparison with literature data that were also obtained from single crystals. Thus, in the following the results of Granado et al. [GGS+99] from $LaMnO_3$ and those of Laverdière et al. [LJM+06] from single crystalline $PrMnO_3$, $NdMnO_3$ and $SmMnO_3$ will be considered. Equation (5.13) can be used to derive SPC coupling constants $D_{eff} = 2D_1 \cos(\pi Q_x a) +$

Table 7.2: : Quantitative phonon frequency softening $\Delta\omega$ extrapolated to $T = 0K$, the sublattice magnetisation $\mu_{unit\ cell}$ within the MnO_2 (ac) plane, as well as D_{eff} hence derived from equation (5.13). The values of both sample series are compared with literature. For $Eu_{1-x}Y_xMnO_3$ with $x > 0.2$ and $TbMnO_3$ no data of $\mu_{unit\ cell}$ could be obtained. Thus, only $\Delta\omega$ is shown.

sample	$\Delta\omega$ $[cm^{-1}]$	$\mu_{unit\ cell}$ $[\mu_B]$	D_{eff} [mRy/Å^2]
$LaMnO_3$	8.0[5]	3.65[1]	16[5]
$PrMnO_3$	6.5[2]	3.5[2]	15.5[2]
$NdMnO_3$	6.0[2]	3.22[3]	13.5[2]
$SmMnO_3$	5.5[2]	3.5[4]	12.9[2]
$EuMnO_3$	6.5	4[6]	13.4
$GdMnO_3$	2.3	4[7]	4.8
$TbMnO_3$	1.0	–	–
$Eu_{0.9}Y_{0.1}MnO_3$	5.6	4[6]	11.6
$Eu_{0.8}Y_{0.2}MnO_3$	4.2	4[6]	8.6
$Eu_{0.7}Y_{0.3}MnO_3$	3.2	–	–
$Eu_{0.6}Y_{0.4}MnO_3$	2.0	–	–
$Eu_{0.5}Y_{0.5}MnO_3$	1.2	–	–

[1] values taken from [HSL+97], [2] values taken from [LJM+06],
[3] values taken from [MAML+00], [4] values taken from [IMPB03],
[5] values taken from [GGS+99], [6] values taken from [HSP+07],
[7] values taken from [HLKvN+04].

$D_2 \cos(2\pi Q_x a) + D_3$ for the $B_{2g}(1)$ modes of all investigated compounds, where values of the sublattice magnetisation can be found, and be compared to literature either.
Unfortunately, values of the sublattice magnetisation needed for a quantitative derivation of these constants are available only for $RMnO_3$ systems – stoichiometric or doped – with A–type AFM ordering, i.e. $EuMnO_3$, $GdMnO_3$ and $Eu_{1-x}Y_xMnO_3$ with $x \leq 0.2$. These values can be extracted either from neutron diffraction or magnetisation measurements. Thus, only for the mentioned samples a quantitative D_{eff} can be calculated from the experimental data.
In table 7.2 the SPC coupling constant D_{eff} for $RMnO_3$ crystals from literature (R^{3+} = La^{3+}, Pr^{3+}, Nd^{3+} and Sm^{3+}) and both sample series investigated within this thesis are listed together. Also indicated is the value of the sublattice magnetisation $\mu_{unit\ cell}$, that was employed for the calculation of D_{eff}. In order to maintain comparability for the whole sample series experimentally investigated within this thesis, the absolute phonon softening $\Delta\omega$ is listed for all samples.
An inspection of table 7.2 shows a good agreement of the experimentally obtained phonon softening and hence derived D_{eff} with literature apart from a small step of $\approx 1cm^{-1}$ in $\Delta\omega$ from the literature data of $SmMnO_3$ to the experimentally obtained data of $EuMnO_3$.

Table 7.3: Comparison of the (average) ionic radii $Eu_{1-x}Y_x$ calculated from the ionic radii of Eu^{3+} and Y^{3+} to the stoichiometric ionic radii of Eu^{3+}, Gd^{3+}, Tb^{3+} and Y^{3+}. Values of the R^{3+} are taken from [Kor55]. Further, the orthorhombic parameters $\epsilon = \frac{a-c}{a+c}$ calculated from the lattice parameters listed in tables 6.2 and 6.3 are shown for the corresponding R^{3+} occupation.

R =	Eu	Gd	Tb	Y
R^{3+} [Å]	1.13	1.11	1.09	1.06
$\epsilon = \frac{a-c}{a+c}$	0.04628	0.04886	0.04963	–

$Eu_{1-x}Y_x$ =	Eu	$Eu_{0.9}Y_{0.1}$	$Eu_{0.8}Y_{0.2}$	$Eu_{0.7}Y_{0.3}$	$Eu_{0.5}Y_{0.5}$
(average) R^{3+} [Å]	1.13	1.123	1.116	1.109	1.095
$\epsilon = \frac{a-c}{a+c}$	0.04628	0.04703	0.04800	0.04832	0.04941

This can be attributed either to the different Raman setups or differences in the sample quality. However, the general trend is confirmed for literature as well as for experimental data. In particular, the results of this thesis fit better in the scheme expected by the discussion of the physical origins above than the results published for polycrystalline $RMnO_3$ ($R^{3+} = Eu^{3+}$, Gd^{3+}, Tb^{3+}) [LJM+06] or ceramic $EuMnO_3$, $GdMnO_3$ and $Eu_{1-x}Y_xMnO_3$ [FMA+09, MAF+10].

Now, we want to go even further and compare both investigated sample series with each other in the light of their compositional dependence. Naively, for comparing stoichiometric and doped sample series one would calculate an average R^{3+} ionic radius of $Eu_{1-x}Y_x$ and search for a stoichiometric $RMnO_3$ sample with corresponding R^{3+} ionic radius. The average $Eu_{1-x}Y_x$ ionic radii derived from the stoichiometric ionic radii of Eu^{3+} and Y^{3+} are listed in table 7.3 and compared to those of Eu^{3+}, Gd^{3+}, Tb^{3+} and Y^{3+}. All stoichiometric values are taken from [Kor55]. According to this tabled values, one would expect, that SPC effects in $GdMnO_3$ should be roughly comparable to $Eu_{0.7}Y_{0.3}MnO_3$ and the same should be true for the sample pair $TbMnO_3$ and $Eu_{0.5}Y_{0.5}MnO_3$. However, when comparing quantitative values of the phonon frequency softening $\Delta\omega$ shown in table 7.2 one has to note, that $\Delta\omega = 2.3cm^{-1}$ in $GdMnO_3$ is significantly smaller than $\Delta\omega = 3.2cm^{-1}$ in $Eu_{0.7}Y_{0.3}MnO_3$. The naive picture of an average $Eu_{1-x}Y_x$ ionic radius is therefore not sufficient for a quantitative comparison of SPC in both sample series.

Another possibility would be considering the similarity of the magnetic phases by employing the magnetic phase diagrams of figure 3.14 in section 3.4. This approach would resemble the picture of a direct correlation of SPC and the Electromagnons and, thus, its link to the existence of specific magnetic phases. It would lead to the expectance, that $GdMnO_3$ should be comparable to $Eu_{0.8}Y_{0.2}MnO_3$, because in both compounds A–type AFM is observable at temperatures $T \lesssim 25K$. For $Eu_{0.7}Y_{0.3}MnO_3$ no A–type AFM exists but an incommensurate magnetic structure. Consequently, when considering the similarity in the magnetic structure as the crucial factor for a comparison of $RMnO_3$

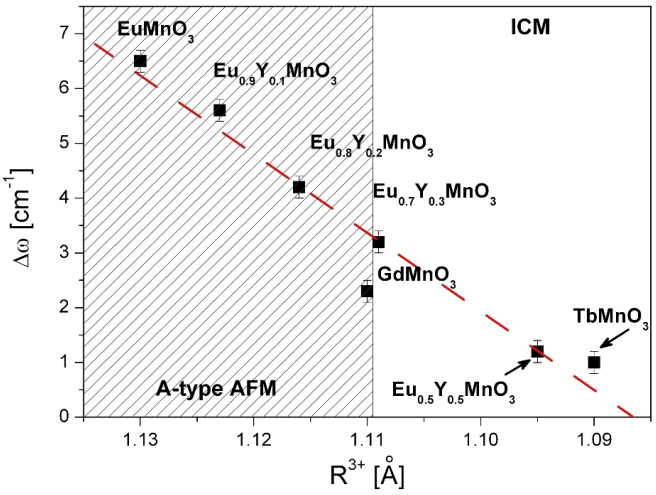

Figure 7.11: Phonon frequency softening $\Delta\omega$ of the $B_{2g}(1)$ mode as a function of the R^{3+} or average $Eu_{1-x}Y_x$ ionic radius, respectively. $\Delta\omega$ is extracted from the Raman measurements by extrapolating both fit functions to T = 0K. The dashed red line is a guide to the eye indicating a linear dependence.

and $Eu_{1-x}Y_xMnO_3$, the sample pairs $GdMnO_3$ and $Eu_{0.8}Y_{0.2}MnO_3$ as well as $TbMnO_3$ and $Eu_{0.5}Y_{0.5}MnO_3$ would have to be chosen. However, in this case, the difference in SPC strength between the sample pair $GdMnO_3$ ($\Delta\omega = 2.3cm^{-1}$) and $Eu_{0.8}Y_{0.2}MnO_3$ ($\Delta\omega = 4.2cm^{-1}$) is almost a factor 2 and therefore even larger than in the naive picture of averaged $Eu_{1-x}Y_x$ radii.

Both approaches and the corresponding dependencies are also visualised in figure 7.11, where the phonon frequency softening $\Delta\omega$ is plotted as a function of the (average) R^{3+} ionic radius in Å. The second approach of similar magnetic phases is indicated by the shaded area, which marks $RMnO_3$ or $Eu_{1-x}Y_xMnO_3$ with A–type AFM. The shortcomings of both pictures can be clearly seen by the deviation of the $GdMnO_3$ phonon softening from the general trend indicated by linear fit (dashed red line) and to a lesser amount by the deviation between the second sample pair $TbMnO_3$ and $Eu_{0.5}Y_{0.5}MnO_3$.

To overcome this complication, a third approach will be introduced now. It is based on the direct consideration of the MnO_6 octahedra tilting, which is reflected in the lattice properties of the orthorhombic unit cell. For an in–depth evaluation in terms of the MnO_6 tilting, the orthorhombic distortions of the doped and the corresponding stoichiometric samples have to be compared in detail. The XRD–derived lattice constants for all investigated samples are listed in the table 6.2 for $RMnO_3$ and in table 6.3 for $Eu_{1-x}Y_xMnO_3$. From these data the parameter for the orthorhombic distortion ϵ is calculated and shown below the R^{3+} and average $Eu_{1-x}Y_x$ ionic radius in table 7.3. It is defined as follows: $\epsilon \equiv (c-a)/(c+a)$ and reflects the inequality of a– and c–axis in the orthorhombic Pnma perovskite structure and, thus, the tilting of the MnO_6 octahedra within the MnO_2 (ac) plane [HSP+07].

The dependence of the phonon softening $\Delta\omega$ on the orthorhombic distortion ϵ is shown

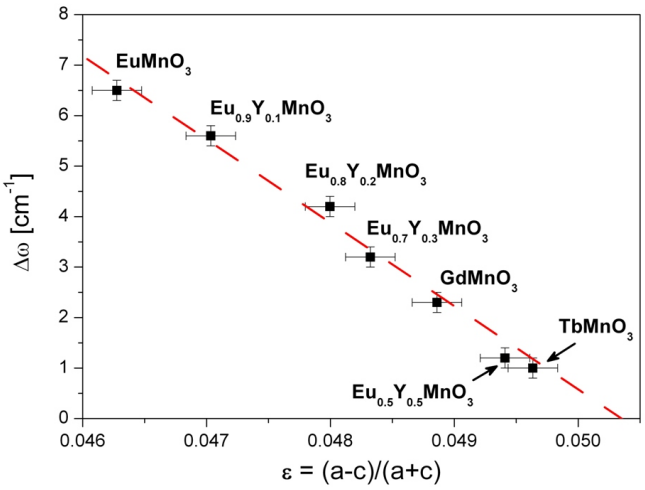

Figure 7.12: Phonon frequency softening $\Delta\omega$ of the $B_{2g}(1)$ mode as a function of the orthorhombic distortion ϵ. $\Delta\omega$ is extracted from the Raman measurements by extrapolating the fit functions to T = 0K. ϵ is calculated from the XRD–derived lattice constants listed in the tables 6.2 and 6.3. The dashed red line is a guide to the eye reflecting a linear dependence between $\Delta\omega$ and ϵ.

graphically in figure 7.12. The distortion-dependence of the phonon softening shows a linear decrease of SPC with increasing ϵ. In contrast to the previously introduced models, here all investigated compounds fit excellently within the linear trend indicated by the dashed red line within figure 7.12. Thus, an intimate connection between orthorhombic distortion ϵ and the SPC strength expressed by the phonon frequency softening $\Delta\omega$ can be concluded. It can further be followed, that the SPC of $GdMnO_3$ ($\Delta\omega = 2.3cm^{-1}$) should be best comparable to $Eu_{0.6}Y_{0.4}MnO_3$ ($\Delta\omega = 2.0cm^{-1}$), whose lattice parameters and, thus, ϵ are not known unfortunately. Nevertheless the value of the parameter ϵ of $Eu_{0.6}Y_{0.4}MnO_3$ should be in the region between $Eu_{0.7}Y_{0.3}MnO_3$ and $Eu_{0.5}Y_{0.5}MnO_3$, which would be in excellent agreement with $GdMnO_3$.

Summing up, one can deduce, that the difference in ϵ determines the difference in the strength of phonon softening. This result is explained consistently by the consideration, that the observed SPC is primarily related with the tilting of adjacent MnO_6 octahedra due to the orthorhombic lattice distortion (reflected in the parameter ϵ) and, thus, the local magnetic correlations, rather than relating it to specific macroscopic magnetic phases. Thus, the conclusions of [FMA+09] and [MAF+10] have to be objected, as they draw a picture of a correlation between SPC and the Electromagnons.

However, the concept of an intimate coupling between phonons and Electromangnons should not be abandoned completely. Instead a closer look at the symmetry properties and the possible coupling mechanisms leads to a more detailed understanding, which phonon modes can couple directly to the Electromagnons. The theoretical ground was already laid out in section 5.2 and in the next chapter experimental results concerning the Electromagnon–Phonon Coupling (EMPC) will be regarded.

Chapter 8

Electromagnon-Phonon Coupling (EMPC)

For an understanding of possible coupling effects in the dynamical response of the Multiferroic Manganites it is crucial to take symmetry aspects into account. As it was already discussed for SPC, the Raman– and IR–active phonon modes can couple to the magnetic order via the modulation of the magnetic exchange. SPC effects manifest themselves as phonon frequency shifts of those Raman– and those IR–active phonon modes, that mainly involve O^{2-} displacements, i.e. tilting, buckling and rotations of the MnO_6–octahedra, termed group 2 modes in section 4.3, as well as stretching and internal modes of the MnO_6–octahedra, termed group 3 modes. In this chapter, the IR–active phonon modes of group 1 shall be considered, i.e. the polar phonon modes with mainly R^{3+} and Mn^{3+} displacements. The discussion of the systematics of SPC clearly showed that for the group 1 modes no SPC effects are expected. However, a possible coupling of these modes with the elementary excitations of the Magneto–Electric Coupling, i.e. the Electromagnons (EM), is expected, due to the magnon–phonon hybrid nature of the latter.
Concerning the coupling effects of phonons and EM – in the following termed Electromagnon–Phonon Coupling (EMPC) – several studies have been carried out on Rare–Earth Manganites (e.g. $GdMnO_3$ [PRM$^+$06], $TbMnO_3$ [SKR$^+$09] and doped $Eu_{1-x}Y_xMnO_3$ [TYK$^+$09]), whose main observation was the transfer of spectral weight between these two elementary excitations. According to Shuvaev et al. [SMP11], this aspect can be generally understood as a consequence of the conservation of the total number of electrons within the sample. It will be discussed in detail later in this chapter.
However, the transfer of spectral weight is only one of the possible EMPC manifestations. Other aspects, e.g. the shift of resonance frequencies, are mentioned in literature, but not systematically studied or understood with the help of a microscopic model, which is explicitly based on the "Heisenberg–Exchange model"[VAMS$^+$09] (see also section 5.2). Only this model can consistently explain both the strong dipolar activity of the high–frequency EM and its optical selection rules [SMP11]. Thus, with the help of the experimental data obtained from temperature–dependent polarised reflectivity measurements presented in the following, a microscopic model will be introduced, which can cover these EMPC ef-

fects. Special attention will be paid to the frequency shifts observed for the low–frequency phonon modes, due to the clearness of the experimental data concerning this parameter.

For the following discussion covering the observed EMPC effects, the stoichiometric $RMnO_3$ (R = Eu, Gd and Tb) series will be considered in detail. The doped $Eu_{1-x}Y_xMnO_3$ series will be discussed at the end of the chapter for completeness. This chapter will be organised as follows: First, in 8.1, the transfer of spectral weight between phonons and EMs will be covered. The main purpose of this section is comparison with literature data, where this aspect was extensively studied in the recent years. Second, in 8.2, one of the main findings of this thesis will be presented: phonon frequency shifts attributed to hybridisation effects of phonons and EMs. This aspect has been presented in literature for selected compounds (e.g. in [LKY+09] for $Gd_{1-x}Tb_xMnO_3$ (x = 0.3 and 0.5) or in [SKR+09] for $TbMnO_3$), but not systematically discussed in terms of introducing a model, that explains these frequency shifts on a microscopic scale. Therefore, in 8.3 a microscopic model will be developed, that is based on considerations in close analogy to the previously discussed SPC effects, i.e. the dynamical modulation of magnetic exchange by lattice vibrations. Finally, in the last section of this chapter, the experimental data

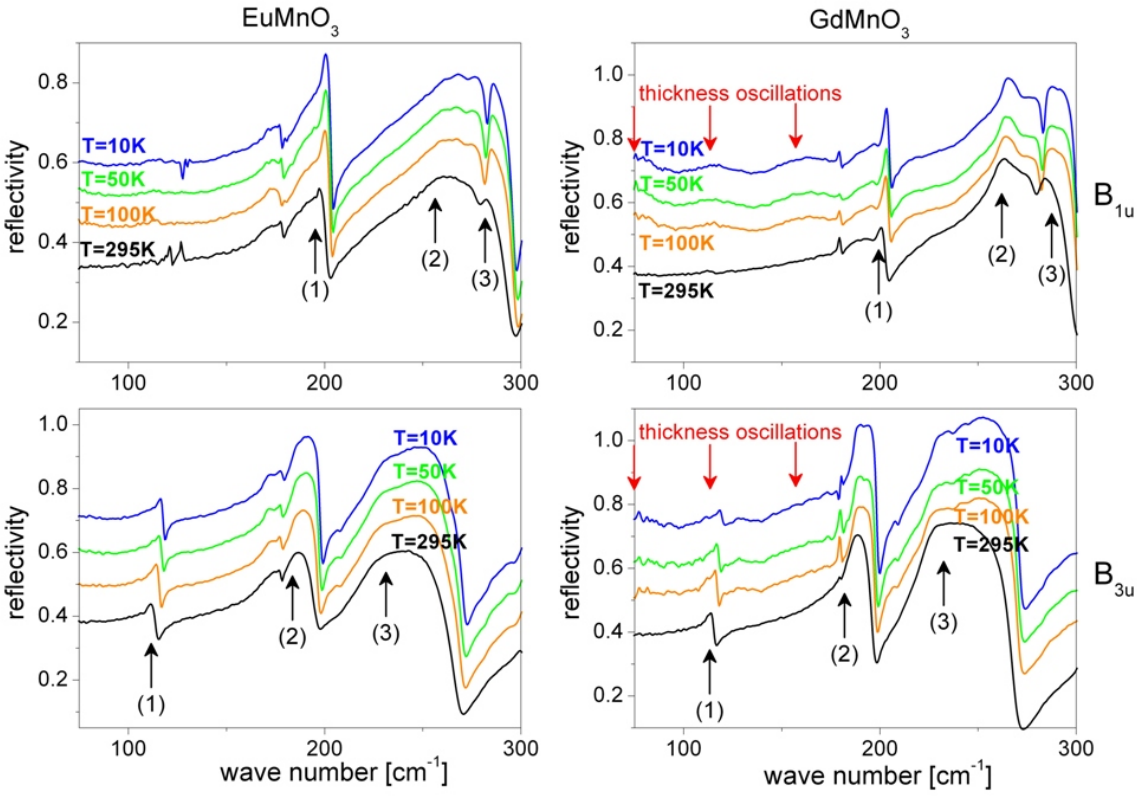

Figure 8.1: Reflectivity spectra in the range from 75 to 300 cm^{-1} obtained from $EuMnO_3$ and $GdMnO_3$ in B_{1u} (upper row) and B_{3u} (lower row) for several temperatures. The spectra are vertically shifted for clarity. The thickness oscillations caused by the cryostat window are indicated by the red arrows within the $GdMnO_3$ spectra.

of the doped $Eu_{1-x}Y_xMnO_3$ will be covered in the light of the previous observations and conclusions.
Thus, for a first qualitative overview, we consider the temperature dependent polarised reflectivity spectra of the $RMnO_3$ sample series shown in figure 8.1 for selected temperatures. These give access to the B_{1u} (upper row) and B_{3u} (lower row) phonon modes, respectively. As already discussed in section 7.2.1, temperature dependent reflectivity measurements on $TbMnO_3$ were already presented in [SKR+09], thus, only $EuMnO_3$ and $GdMnO_3$ need to be investigated to obtain a complete picture of the stoichiometric $RMnO_3$ sample series. For clarity, the reflectivity spectra are plotted in the range of $75cm^{-1} \leq \widetilde{\nu} \leq 300cm^{-1}$, thus showing the group 1 IR–active phonon modes according to the classification introduced in section 4.3. As will be argued in the following, only for these modes a significant EMPC can be expected.
It can be seen in figure 8.1, that for the reflectivity spectra of $GdMnO_3$ in B_{1u} and also in B_{3u} symmetry interference fringes with three maxima and a spacing of $\Delta\widetilde{\nu} \approx 50cm^{-1}$ occur for $\widetilde{\nu} < 200cm^{-1}$ at $T \leq 100K$. These patterns in both spectra of $GdMnO_3$ can be identified as thickness oscillations caused by the cryostat window. A spacing between interference maxima of $\Delta\widetilde{\nu} \approx 50cm^{-1}$ corresponds to a layer thickness in the range of $\approx 600\mu m$, which equals the thickness of the PE windows of the cryostat. Depending on the sample position within the cryostat, which must be optimised for each investigated sample and temperature, these can appear for certain samples and temperature regions and cause problems by obscuring possible resonance signatures of low–frequency phonons or EMs. For $GdMnO_3$, all phonon modes can be unambiguously identified in agreement with the room temperature reflectivity spectra shown in chapter 6. However, a possible observation of weaker EM signatures is not possible in these spectra. Further, this point should be kept in mind, especially when comparing dipolar strengths of the low–frequency phonon modes (i.e. $\widetilde{\nu} < 200cm^{-1}$) with literature as will be done in the following section.
Having considered these experimental aspects, we now move on to the discussion of the EMPC effects outlined above. The first point in the discussion will be the transfer of spectral weight between phonons and EMs.

8.1 Transfer of spectral weight

One of the main aspects of EMPC already intensively investigated in literature is the transfer of spectral weight between low–frequency IR–active phonons and EMs. According to Shuvaev et al. [SMP11], phonons need to be included in a systematic description of EMs. This can be understood by the conservation of spectral weight in the absorption or reflectivity spectra, respectively. Spectral weight in optical spectroscopy is defined as the area under the real part of the conductivity curve $\sigma_1(\omega)$, which can also be expressed by the imaginary part of the dielectric function, $\epsilon_2(\omega)$, as:

$$S = \int_0^\infty \sigma_1(\omega)\, d\omega = \epsilon_0 \int_0^\infty \epsilon_2(\omega)\, \omega d\omega \tag{8.1}$$

with ϵ_0 as the dielectric constant of vacuum. The spectral weight is further proportional to the number of electrons in the sample and, thus, must be conserved for all temperatures and magnetic phases. Therefore, if the EM gains spectral weight, a transfer from other elementary excitations must take place. Due to the hybrid nature of the EM – which is of mixed magnon and phonon character – it is obvious to identify phonon modes as the transfer partners. This effect has been investigated for stoichiometric $RMnO_3$ systems, e.g. for $GdMnO_3$ by Pimenov et al. [PRM+06] and for $TbMnO_3$ by Schmidt et al. [SKR+09] as well as for doped $Eu_{1-x}Y_xMnO_3$ by Takahashi et al. [TYK+09]. Within this thesis we will concentrate on manifestations of the coupling effects observable for the phonon frequencies and on developing a model describing the microscopic mechanism, but nevertheless the spectral weight transfer will be regarded by the means of comparing our results with literature.

Due to the previously mentioned differences concerning the polishing degree of the sample surface (see section 6.2), a quantitative comparison of dipolar strengths of the IR–active phonon modes of $EuMnO_3$ and $GdMnO_3$ with literature is not straightforward. Additionally, the above mentioned potential thickness oscillations in the low–temperature reflectivity spectra of $GdMnO_3$ do further complicate this task. Thus, to compensate these influences, the relative phonon areas in the ϵ_2 spectra are considered, as was already done in section 6.2, when regarding the room temperature reflectivity. Figure 8.2 shows the relative peak area of the $B_{3u}(1)$ modes obtained from $EuMnO_3$ and $GdMnO_3$ as a function of temperature as solid blue and red balls, respectively, and compares them to the corresponding $B_{3u}(5)$ modes (blue and red empty circles, respectively) as examples

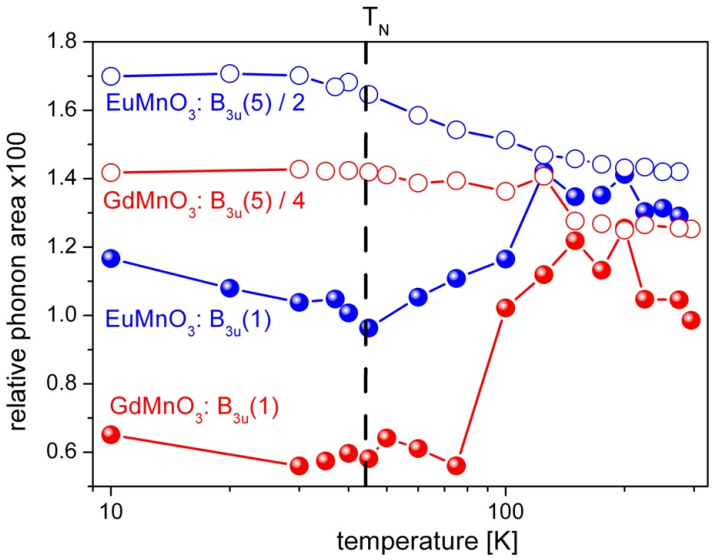

Figure 8.2: Relative peak area in the ϵ_2 spectra of the $B_{3u}(1)$ modes of $EuMnO_3$ (solid red balls) and $GdMnO_3$ (solid blue balls) as well as the $B_{3u}(5)$ modes of $EuMnO_3$ (empty blue circles) and $GdMnO_3$ (empty red circles), respectively. For reasons of clarity, the latter are divided by the factors indicated in the legend.

for IR–active modes without EMPC or SPC effects (see also figure 7.5). For $T < 100K$ a clear decrease of relative peak area of $B_{3u}(1)$ is observable in both compounds. It is especially pronounced in $GdMnO_3$, where the relative peak area is reduced almost by a factor of 2. Comparison with data of [SKR+09] obtained from a–cut $TbMnO_3$ shows, that the dipolar contribution $\Delta\epsilon = \omega_P^2/\omega_T^2$ of the $B_{3u}(1)$ mode to the dielectric function is also reduced by a factor of ≈ 2, which is in good qualitative agreement with the behaviour of the relative peak area of $B_{3u}(1)$ in $GdMnO_3$. These findings do also match published results of Pimenov et al. [PRM+06] obtained from $GdMnO_3$, where the suppression of the EM was reached via the application of an external magnetic field: the dielectric contribution of the $B_{3u}(1)$ mode in $GdMnO_3$ is $\Delta\epsilon \approx 0.2$ at $T \approx 15K$ in zero magnetic field. From the reflectivity measurements presented in this thesis a dielectric contribution of $\Delta\epsilon \approx 0.15$ of $B_{3u}(1)$ at $T = 15K$ in $GdMnO_3$ can be extracted from experiment, i.e. from the fit parameters ω_p and ω_T.

Considering the onset temperature of the reduction of the $B_{3u}(1)$ spectral weight in $GdMnO_3$ (see figure 8.2), one can see, that it is located at $T \approx 75 - 100K$ and, thus, above T_N indicated by the dashed black line. For comparison, data of M. Schmidt [Sch09] for $\Delta\epsilon$ as a function of temperature of the $B_{3u}(1)$, (2) and (5) modes in $TbMnO_3$ are plotted in figure 8.3 and show, that the decrease of $\Delta\epsilon$ of $B_{3u}(1)$ sets in very close to $T_N = 42K$. Thus, the temperature dependencies of the $B_{3u}(1)$ modes in $GdMnO_3$ and $TbMnO_3$ show clear differences. However, when considering the $B_{3u}(2)$ mode (see also figure 8.3) a very similar temperature dependence compared to the relative phonon area in ϵ_2 of $B_{3u}(1)$ in $GdMnO_3$, presented in this thesis, can be extracted. Thus, a qualitative similarity of the temperature dependence can be concluded. On the other hand, modes with higher phonon frequency, e.g. $B_{3u}(4)$, show a temperature dependent behaviour concerning $\Delta\epsilon$, that closely resembles that of the relative peak area in the ϵ_2 spectra observed for the $B_{3u}(5)$ modes of $EuMnO_3$ and $GdMnO_3$ (see figure 8.2).
Another possible comparison could be drawn with the data of Lee et al. [LKY+09], whose data of the mixed system $Gd_{1-x}Tb_xMnO_3$ show the same qualitative trends concerning the shift of spectral weight. Unfortunately, only relative shifts with respect to the spectral weight obtained at a reference temperature of $T = 50K$ are shown. Thus, a quantitative

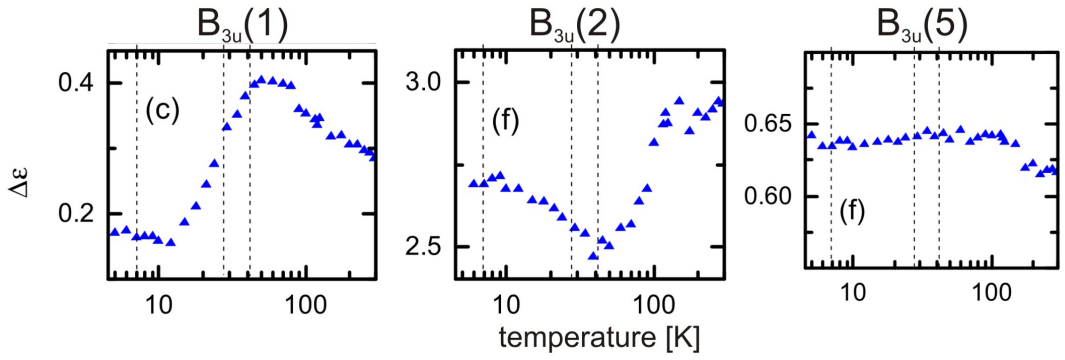

Figure 8.3: Dielectric contribution $\Delta\epsilon$ of $B_{3u}(1)$, (2) and (5) modes obtained from temperature dependent reflectivity measurements of a–cut $TbMnO_3$ extracted from [Sch09].

comparison cannot be carried out.
Surprisingly, no investigations concerning the transfer of spectral weight between phonons and EMs have been carried out on the "mother compound" $EuMnO_3$. This could have been a very important check for potential spectral weight transfer effects already present in the non–multiferroic $EuMnO_3$. The relative peak area of the $B_{3u}(1)$ mode in $EuMnO_3$ plotted in figure 8.2 demonstrates, that a reduction of the relative phonon area in the range of $\approx 20\%$ is observed upon lowering the temperature to $T < 100K$. Comparison with the $B_{3u}(5)$ mode of $EuMnO_3$, for which neither SPC nor EMPC effects are observed (see figure 7.5 in section 7.1.2), shows that this reduction of spectral weight is not present for other modes with higher mode frequency. One possible explanation could be magneto–electric fluctuations already present in the non–multiferroic compound $EuMnO_3$. An additional evidence for this assumption is the observation of EM signatures already present in the non–multiferroic $Eu_{0.9}Y_{0.1}MnO_3$ compound [PLM+08, TYK+09].
Summing up, a qualitative agreement between the measurements carried out within this thesis and literature data can be concluded concerning the reduction of spectral weight of the low–frequency phonons, when lowering the temperature and approaching the multiferroic phases. However, no quantitative comparison could be carried out, due to different degrees of surface polishing and – in the case of $GdMnO_3$ – thickness oscillations of the cryostat window.
The next point in the systematic discussion of EMPC are the phonon frequency shifts of the low–frequency IR–active modes. In contrast to the transfer of spectral weight, this aspect is not systematically investigated in literature. It is even more relevant in our case, because the frequency determination cannot be hampered by thickness oscillations, as long as they are clearly observable. Thus, in the next section frequency shifts observed for the group 1 IR–active phonon modes of the stoichiometric $RMnO_3$ series will be systematically considered.

8.2 Hybridisation–caused frequency shifts

In contrast to the previously discussed transfer of spectral weight, which relies on the ion plasma frequency ω_p and the transverse optical resonance frequency ω_T, the frequency shifts can be determined directly from the fit parameter ω_T. Thus, the frequency shifts are not sensitive to the degree of surface polishing or the appearance of thickness oscillations, as long as the corresponding phonon signatures can be clearly observed in the reflectivity spectra. For $EuMnO_3$ and $GdMnO_3$ this is clearly the case (see figure 8.1). Further, as already discussed before, the temperature dependent B_{3u} phonon frequencies of $TbMnO_3$ are available from [SKR+09].
Figure 8.4 shows an overview of the temperature dependence of the phonon frequencies for the group 1 IR–active modes within the stoichiometric $RMnO_3$ series. The upper row shows the temperature dependencies of the $B_{1u}(1)$ to (3) modes obtained from $EuMnO_3$ and $GdMnO_3$ and the lower row those of $B_{3u}(1)$ to (3) obtained from $EuMnO_3$, $GdMnO_3$ and $TbMnO_3$. It can be immediately seen, that only for $B_{3u}(1)$ obtained from $GdMnO_3$

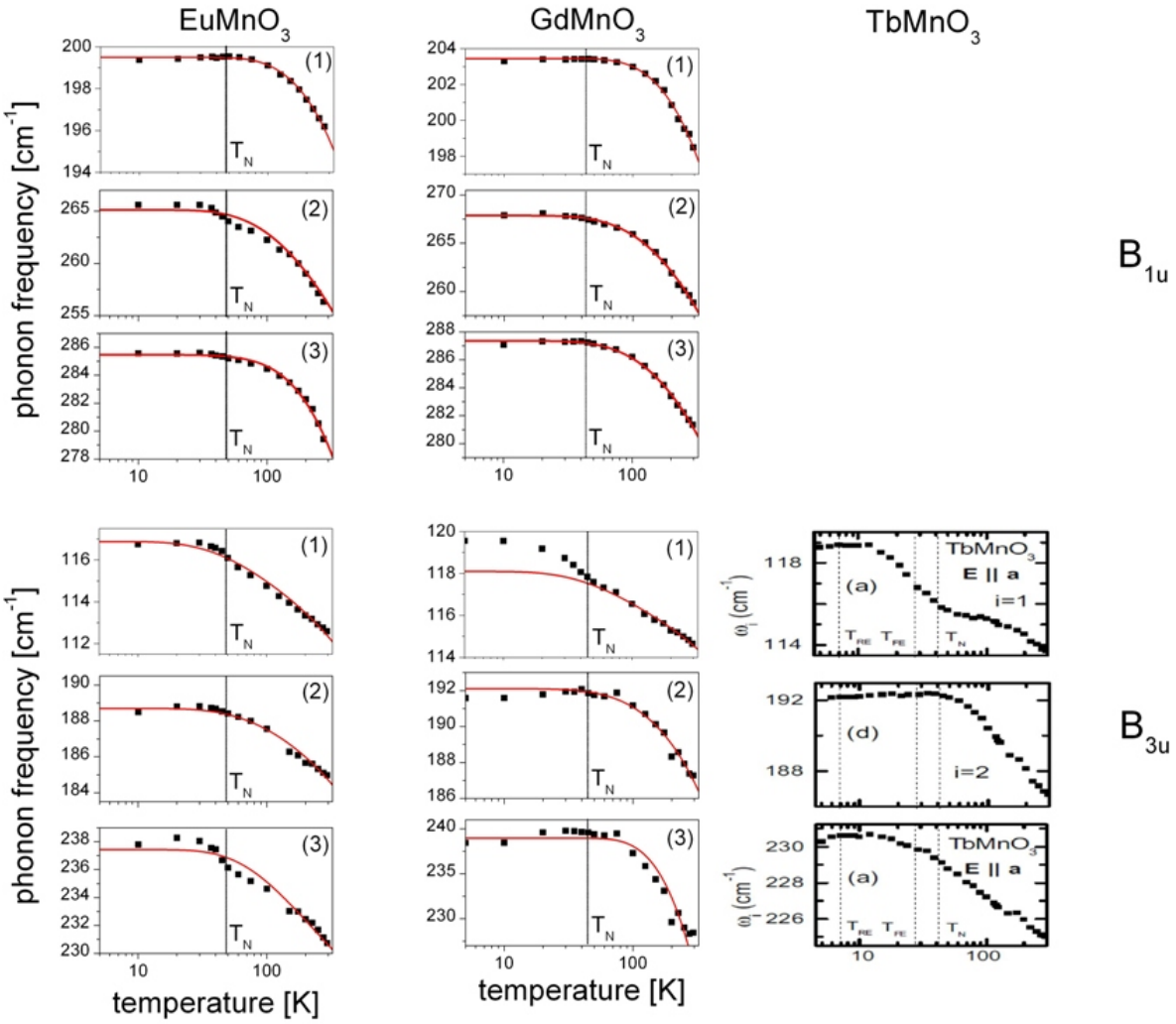

Figure 8.4: Temperature dependence of the $B_{1u}(1)$ to (3) (upper row) and $B_{3u}(1)$ to (3) (lower row) phonon modes obtained from $EuMnO_3$ and $GdMnO_3$. Also displayed (in the right column) are the temperature dependent B_{3u} phonon frequencies of Schmidt et al. [SKR+09] obtained from a–cut $TbMnO_3$. The red lines are fits according to equation (7.3) for $T > T_N$ reflecting the temperature dependence of the phonon frequencies without EMPC.

and $TbMnO_3$ significant deviations from the fit functions according to equation (7.3) do occur. In contrast to the previously investigated phonon frequency shifts of the Raman–active modes as well as those of the group 2 and 3 IR–active modes, for the $B_{3u}(1)$ modes of both compounds a pronounced shift to higher frequencies is observed. The relative difference between the expected phonon frequency of the $B_{3u}(1)$ mode according to equation (7.3) extrapolated to $T = 5K$ and the actually observed phonon frequency at this temperature is $\Delta\omega \approx +1.2\%$ in $GdMnO_3$ and $\Delta\omega \approx +2.6\%$ in $TbMnO_3$.
The opposite sign of the frequency shifts of the $B_{3u}(1)$ modes in $GdMnO_3$ and $TbMnO_3$ compared to the sign of the shifts observed for the Raman– and group 2 and 3 IR–active

modes lead to the conclusion, that these should originate from another coupling effect and not from SPC. Also, in the discussion of the systematics of the SPC mechanism (see section 7.1.2), it could already be reasoned, that for group 1 IR–active modes, which mainly consist of Mn^{3+} and R^{3+} displacements, no SPC effects should be observable. Additionally, the compositional dependence of the observed $B_{3u}(1)$ shifts is exactly opposite to that of the shifts explained by SPC, i.e. a phonon frequency shift of $\Delta\omega = 0$ for $EuMnO_3$ with a monotonous increase towards $TbMnO_3$, where $\Delta\omega = +2.6cm^{-1}$. This increase of $\Delta\omega$ appears simultaneously with the onset of multiferroicity (i.e. magneto–electric behaviour in our case) and, thus, is interpreted as a coupling effect of the low–frequency polar phonons and the EMs as the elementary excitations of magneto–electrically coupled systems. Strictly speaking, $EuMnO_3$ is non–magneto–electric, $GdMnO_3$ is on the border of magneto–electric behaviour [SML+11], because its ferroelectric moment can only be stabilised by the application of external magnetic fields ($B > 0.1T$ at temperatures $T < 20K$) and, finally $TbMnO_3$ is clearly magneto–electric with the appearance of a ferroelectric polarisation for temperatures $T < 28K$ [PMI+06]. This trend is nicely reflected in the phonon frequency shifts of the $B_{3u}(1)$ mode. Similar positive frequency shifts are also observed in mixed multiferroic $Gd_{1-x}Tb_xMnO_3$ ($x = 0.3$ and 0.5) compounds for the low–frequency modes with B_{3u} symmetry upon entering the temperature region of the magnetically ordered phases [LKY+09]. It can therefore be assumed, that these shifts to higher frequencies are intimately connected to the occurrence of the EM. These, in turn, are tied to the existence of Magneto–Electric Coupling in these compounds.

Another important aspect are the onset temperatures of the frequency shifts of $B_{3u}(1)$ in $GdMnO_3$ and $TbMnO_3$. For both compounds, these are located in the close vicinity of the onset temperature of the magnetic phases, T_N, as can be seen in figure 8.4. This is seemingly contradicting the conclusion of an intimate coupling between the frequency shifts of the $B_{3u}(1)$ modes and the magneto–electric behaviour connected with the EMs, that is not present in $GdMnO_3$ at zero field cooling at all [SML+11] and has its onset not until $T = 28K$ in $TbMnO_3$ [SKR+09]. However, as is evident especially from the transmittance measurements of $GdMnO_3$ published by Shuvaev et al. [SML+11], the high–frequency EM persists at temperatures clearly above the phase transition into the paraelectric phase (i.e. up to $T \approx 75K$). This was attributed to magneto–electric fluctuations persistent in the paraelectric phase. Thus, it can consistently be reasoned, that the positive phonon frequency shifts of the $B_{3u}(1)$ modes are directly connected to the high–frequency EM.

The next logical step will be developing an understanding, how both elementary excitations can couple. Thus, the Heisenberg–Exchange model employed by Valdés Aguilar et al. [VAMS+09] to explain the dipolar activity of the high–frequency EM will be considered with the additional inclusion of the low–frequency polar phonon mode $B_{3u}(1)$.

8.3 EMPC – origin and manifestations

As already laid out in section 5.2, the Heisenberg–Exchange model can explain the origin of the dipolar activity of a zone–edge magnon and the experimentally observed selection rules of the EM consistently. This model is based on the modulation of the magnetic exchange by the electric field of incoming radiation. Due to the crystalline properties of the Pnma structure, a polarised light wave with $\boldsymbol{E}||\boldsymbol{c}$ can cause a modulation of the magnetic exchange $J \propto J_0 + \Delta J \cos(\boldsymbol{k_0} \cdot \boldsymbol{r})$ along the a–axis and, in turn, a modulation of the angle between adjacent Mn^{3+} spins along the spin spiral with $\boldsymbol{Q}||\boldsymbol{a}$. This is equivalent to a zone edge magnon because of $\boldsymbol{k_0} = (2\pi/a, 0, 0)$.

For incorporating an explanation of the coupling effect between phonons and EM this model provides the base considerations concerning the EM. On the other side, a close inspection of the mode patterns of the lowest–frequency IR–active phonon modes with B_{1u} and B_{3u} symmetry, i.e. $B_{1u}(1)$ and $B_{3u}(1)$ is necessary. From experimental results and literature it is clear, that coupling effects only occur between $B_{3u}(1)$ and EM, while for $B_{1u}(1)$ no EMPC is observable and, therefore, should be excluded by symmetry reasons. The displacement pattern of the $B_{1u}(1)$ mode can be found in figure 4.3 and that of the $B_{3u}(1)$ mode in figure 4.4 and figure 8.5(a). For this discussion considering EMPC only the MnO_2 (ac) plane has to be considered, as the EM excitation is confined within this plane. Thus, in figure 8.5(b) the projection of the $B_{3u}(1)$ displacement pattern on this plane is drawn. The main displacement associated with $B_{3u}(1)$ is an anti–phase Mn^{3+} displacement parallel to the a–axis (indicated by the black arrows) with a small in–phase component parallel to the c–axis (green arrows). This small component is responsible for the modulation of the electric dipole within the MnO_2 (ac) plane and is in anti–phase with an equivalent displacement pattern of the R^{3+} ions within the RO (ac) plane. The mode patterns are obtained by DFT–calculations on $LaMnO_3$ with Pnma structure, as already discussed in section 4.3 – and can be verified by comparison with the patterns of Smirnova et al. [Smi99] employed for empirical shell model calculations of the same compound and also with those of Kovaleva et al. [KBC+09] employed for empirical shell model calculations of $YTiO_3$, which also crystallises in the Pnma structure.

The displacement pattern of $B_{1u}(1)$ is not plotted here, but from figure 4.3 it can easily be seen, that it is equivalent to that of $B_{3u}(1)$ but rotated by 90°, thus having the anti–phase modulation of the Mn^{3+} parallel to the c–axis and the small in–phase component parallel to the a–axis.

It is therefore obvious, to identify the in–phase modulation of the Mn^{3+} as the key component responsible for EMPC. Due to the positive charge of the Mn ions, it is exactly anti–phase to the O^{2-} displacement causing the excitation of the EM (indicated by the red arrows in figure 8.5(b)). These two displacements parallel to the c–axis lead to a modulation of the Mn–O–Mn bond angle along the a–axis with a corresponding $\boldsymbol{k_0} = (2\pi/a, 0, 0)$. This in turn causes a modulation of the magnetic exchange with the same $\boldsymbol{k_0}$. Thus, a hybridisation of high–frequency EM and $B_{3u}(1)$ can be concluded, because the in–phase component of Mn^{3+} or O^{2-} displacement in the mode patterns for both excitations are equivalent on a microscopic scale.

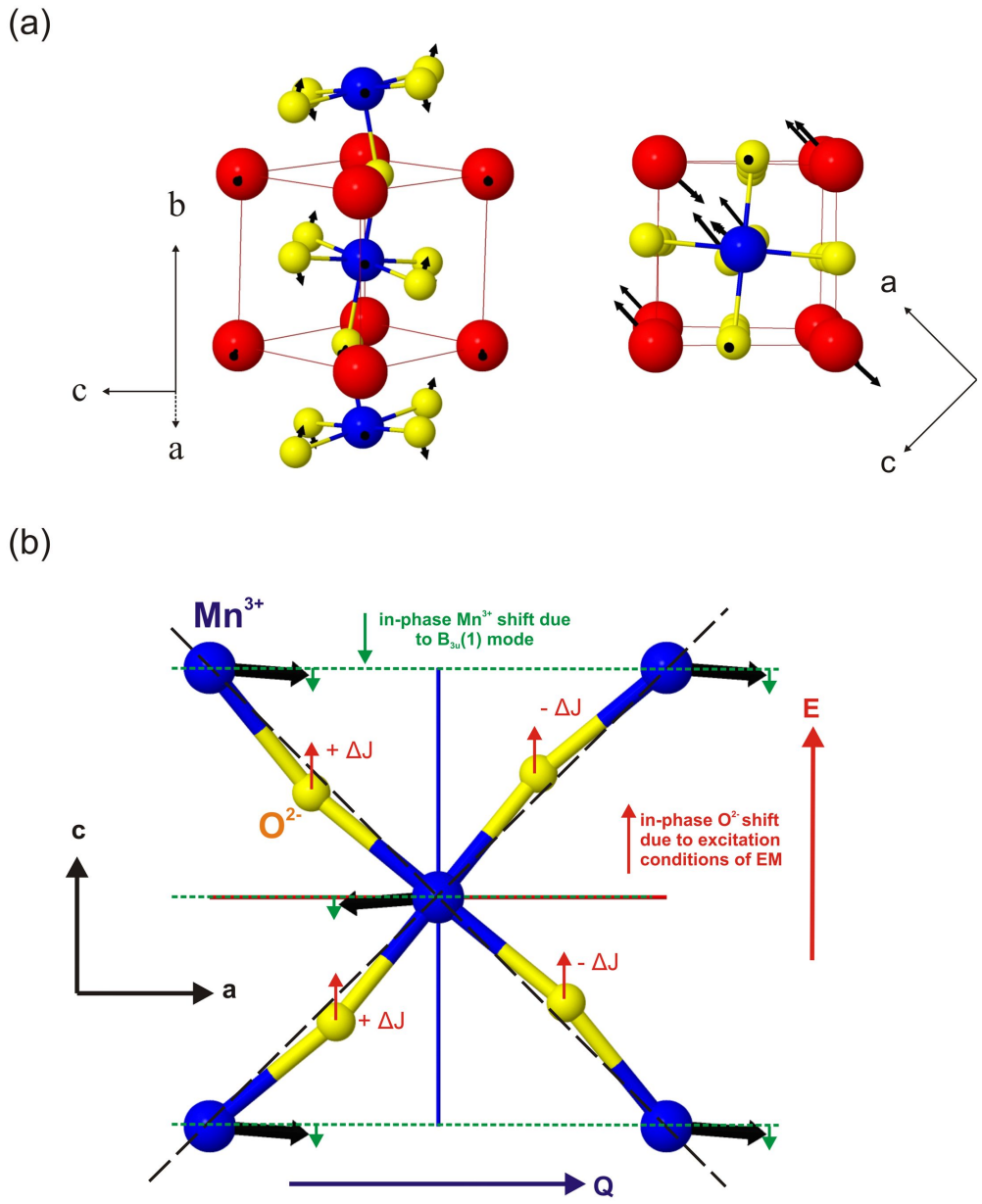

Figure 8.5: Proposed microscopic coupling mechanism for EMPC. (a) Displacement pattern of the $B_{3u}(1)$ mode (see also figure 4.4). The blue balls indicate the Mn^{3+}, the yellow balls the O^{2-} and the red balls the R^{3+}, respectively. (b) Projection of this displacement pattern on the MnO_2 (ac) plane. The red arrows indicate the uniform O^{2-} shift parallel to the c–axis responsible for the excitation of the high–frequency EM, according to [VAMS+09]. The green arrows indicate the uniform Mn^{3+} shift in the opposite direction due to the displacement pattern of the $B_{3u}(1)$ mode. Both shifts lead to a modulation of the magnetic exchange $\Delta J \cos(\boldsymbol{k_0} \cdot \boldsymbol{r})$ parallel to the a–axis.

On the other side, the $B_{1u}(1)$ mode cannot couple to the EM, because the small in–phase component is parallel to the c–axis and, therefore, the modulation of the magnetic ex-

change ΔJ parallel to the a–axis. A hybridisation would require, that both in–phase displacements are parallel, which is not the case for $B_{1u}(1)$.
Having established a microscopic explanation for EMPC, now its manifestations can be considered and explained in the light of this picture:

1. Transfer of spectral weight:
   This effect can be understood as already outlined by Shuvaev et al. [SMP11] (see section 8.1): Due to charge conservation the sum of spectral weight of all excitations remains constant for all temperatures and phases. Thus, the appearance of the EM leads to the reduction of the spectral weight of other excitations. With the help of the microscopic picture just introduced it can be immediately understood, that the low–frequency IR–active phonon mode with B_{3u} symmetry can transfer spectral weight, as the dipole moment associated with the in–phase displacement patterns of the Mn^{3+} for the $B_{3u}(1)$ phonon and the O^{2-} for the EM, respectively, can easily shift from one excitation to the other. A suppression of the EM by increasing temperature or applying external magnetic fields (as was done in [PRM+06]) shifts spectral weight back to the $B_{3u}(1)$ phonon. The microscopic picture therefore delivers an explanation for the strong transfer of spectral weight between EM and $B_{3u}(1)$ and its symmetry dependence.

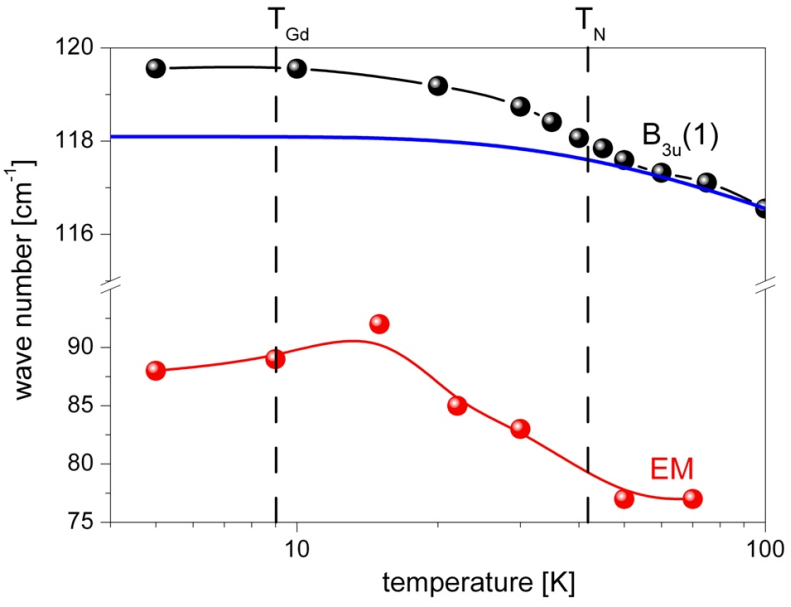

Figure 8.6: Temperature dependent frequency of the $B_{3u}(1)$ mode also plotted in figure 8.4 and that of the high–frequency EM extracted from [SML+11]. The blue line is the fit function to $B_{3u}(1)$ according to equation (7.3) reflecting the temperature dependence of this mode without EMPC. The red line is a guide to the eye.

2. Temperature dependent frequency shifts:
   Concerning the temperature dependent positive frequency shifts of the $B_{3u}(1)$ mode obtained from $GdMnO_3$, a comparison to those of the high–frequency EM taken from [SML+11] is shown in figure 8.7. For both excitations a frequency hardening with the same qualitative temperature dependence is observed. This manifestation of EMPC can be understood in the following way: the hybridisation of EM and $B_{3u}(1)$ leads to admixture of EM–characteristics to $B_{3u}(1)$ and vice versa. Thus, one can expect that also the temperature dependence of the frequency of the corresponding excitation is included in this hybridisation. The appearance of the EM at $\approx T_N$ and its frequency hardening with decreasing temperature would lead to an additional energy term for $B_{3u}(1)$ and, thus, beginning at the onset temperature a shift of the phonon frequency to higher values should be observable. Figure 8.6 shows exactly this expected behaviour. For the $B_{1u}(1)$ mode frequency shifts are not expected, what is nicely verified for the data plotted in figure 8.4. Thus, the temperature dependence of $B_{3u}(1)$ can be explained consistently as a manifestation of EMPC.
   However, it should be stressed here, that due to the overdamped nature of the EM (according to [SML+11], the linewidth is $\Gamma \approx 125 \pm 5cm^{-1}$) this trend can only be very qualitatively and not further quantified, because of the resulting high error in determining the EM frequency.

3. Signatures of EMPC on the spectral line shape of $B_{3u}(1)$:
   Generally speaking, the imaginary part ϵ_2 (or ϵ_{im}) – also called dielectric loss – of the complex dielectric function $\epsilon(\omega)$ accounts for the absorption associated with an excitation. An inspection of equation (2.24) describing the real and imaginary part of $\epsilon(\omega)$ shows, that in contrast to ϵ_1 (or ϵ_r) in ϵ_2 excitation processes only contribute in the corresponding frequency range. Usually these are fitted by a sum of Lorentz functions, as was done before in this thesis on several occasions (see e.g. section 6.2.2).
   The transmittance data of Shuvaev et al. [SML+11] obtained from a very thin $GdMnO_3$ (thickness $\approx 220\mu m$) single crystal are shown in figure 8.7 in the range of $7cm^{-1} \leq \widetilde{\nu} \leq 150cm^{-1}$ and also the dielectric function of $GdMnO_3$ derived from transmittance, reflectivity and THz measurements, respectively. A close inspection of the spectral shape of the $B_{3u}(1)$ mode reveals an asymmetric line shape for $T < 300K$. The most prominent feature, i.e. a characteristic increase of transmittance and a characteristic decrease of ϵ_2 on the high–energy side of $B_{3u}(1)$, respectively, are marked by black arrows in the corresponding spectra. In the light of the just discussed EMPC effects, this can be interpreted as a characteristic effect of a coupling between the $B_{3u}(1)$ mode and the high–frequency EM.
   Including coupling effects between different excitations – in our case between phonons and EM – leads to characteristic spectral line shapes, e.g. in the ϵ_2 spectrum. These can be described as Fano resonance, where the coupling of a very broad excitation (here the high–frequency EM with $\omega \approx 80cm^{-1}$ and $\Gamma \approx 125 \pm 5cm^{-1}$ [SML+11])

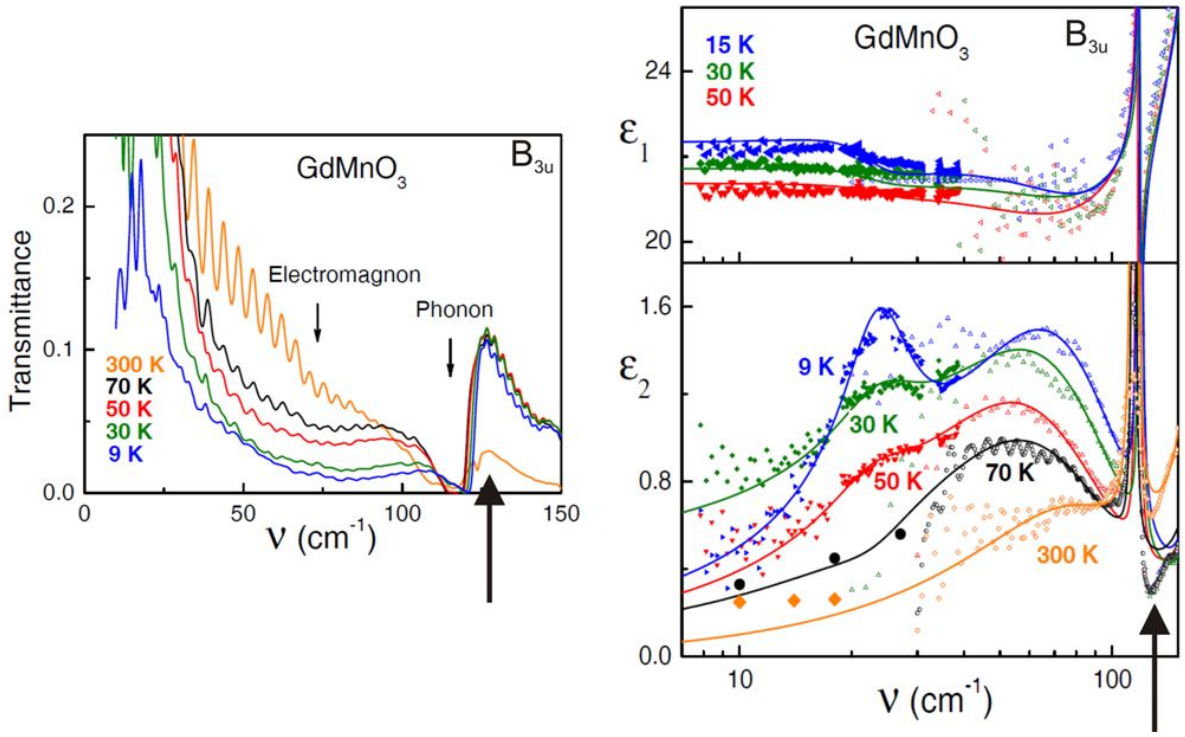

Figure 8.7: Transmittance spectra (left panel) as well as real (ϵ_1) and imaginary (ϵ_2) part of the dielectric function (right panels) for selected temperatures derived from transmittance, reflectivity and THz measurements of $GdMnO_3$ [SML+11]. The solid lines indicate the corresponding model function based on a sum of Drude–Lorentz oscillators. The black arrows mark the spectral region, where the appearance of an anti–resonance of a Fano line shape [Fan61] is clearly observable for $T < 300K$.

and a sharp excitation (here the $B_{3u}(1)$ mode with $\omega_T \approx 119cm^{-1}$ and $\Gamma \approx 4cm^{-1}$ – see table B.3) located on the shoulder of the broad one, causes a characteristic asymmetric line shape of the latter. This asymmetric shape is a very general phenomenon in optical and also Raman Spectroscopy. It was described by U. Fano [Fan61] in the 1960s. Qualitatively this line shape can be easily understood: While the phase of the broad excitation remains constant, that of the sharp excitation changes sign, when crossing its resonance frequency. Thus, for one shoulder of the sharp excitation constructive interference with the broad excitation and for the other shoulder destructive interference must occur. This is reflected in the line shape of the sharp resonance by asymmetry. The corresponding line shape in ϵ_2 can be modelled by the Fano–function:

$$\epsilon_2(\omega) = A\frac{[1 + q(\omega - \omega_T)/\Gamma]^2}{1 + [(\omega - \omega_T)/\Gamma]^2} + y_0, \tag{8.2}$$

where A, ω_T, Γ are a scaling factor, the resonance frequency, the line width of the sharp resonance and y_0 is an offset term, respectively. The asymmetry of the Fano function is expressed by the so–called *Fano parameter* q. The observed spectral

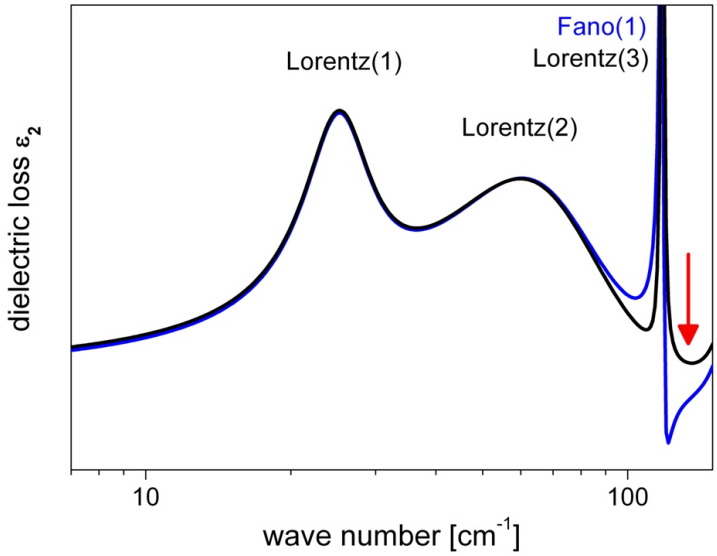

Figure 8.8: Theoretical curves for ϵ_2 modelling the dielectric loss for $\widetilde{\nu} < 150cm^{-1}$ of $GdMnO_3$ in B_{3u} symmetry. These curves are obtained by summing up the dielectric loss associated with the three indicated excitations. The first two peaks located at $25cm^{-1}$ and $80cm^{-1}$, respectively, are the EM structures observed in [SML+11]. The third peak at $118cm^{-1}$ is modelled by a Fano–function (with the Fano parameter $q = -2$) for the blue line and by a Lorentz–function for the black line. The red arrow marks the region of interest, where the two curves differ most significantly.

shape of ϵ_2 in the range of $7cm^{-1} \leq \widetilde{\nu} \leq 150cm^{-1}$ of Shuvaev et al. [SML+11] plotted in figure 8.7 is modelled by theoretical curves in figure 8.8, where a sum of Lorentzian peaks is employed for modelling the EMs and a Lorentz (black line) or a Fano (blue line) line shape for the $B_{3u}(1)$ mode. Comparison with the ϵ_2 spectra of figure 8.7 shows, that for $T < 300K$ the blue curve incorporating the Fano function for $B_{3u}(1)$ (with an arbitrarily chosen Fano parameter $q = -2$) agrees well with the experimentally obtained ϵ_2 – especially in the spectral region of $120cm^{-1} \leq \widetilde{\nu} \leq 150cm^{-1}$ marked by the red arrow, where the anti–resonance between both excitations is visible. On the other side, the black curve (i.e. the model curve without EMPC) gives a good description of the room temperature ϵ_2. From these findings, it can be concluded, that the spectral asymmetry appears simultaneously with the other manifestations of EMPC, i.e. transfer of spectral weight and shift of phonon frequencies, and can be interpreted as another sign of the intimate coupling between the high–frequency EM and $B_{3u}(1)$.

These three points illustrate manifestations of the coupling between the high–frequency EM and the $B_{3u}(1)$ mode. They could be obtained by own measurements of the $RMnO_3$ (R = Eu, Gd) series together with literature data of [SKR+09] obtained from $TbMnO_3$. Specifically, these manifestations are transfer of spectral weight and positive shift of phonon frequencies. Further, literature data of transmittance and THz measurements

of the same systems are inspected and an additional feature – the asymmetric line shape of the $B_3u(1)$ mode in $GdMnO_3$ – was found and interpreted as an EMPC effect.
All these observations are consistent with the proposed microscopic coupling mechanism responsible for the EMPC, thus providing a complete picture of the coupling mechanism and its manifestations in the Multiferroic Manganites. The next and final step of the discussion of EMPC will be the consideration of the doped $Eu_{1-x}Y_xMnO_3$ series, which will be presented in the next section.

8.4 EMPC in the doped $Eu_{1-x}Y_xMnO_3$ series

To complete the EMPC analysis carried out on the stoichiometric $RMnO_3$ series and the SPC investigations on $Eu_{1-x}Y_xMnO_3$ carried out in chapter 7, here the group 1 IR–active modes of $Eu_{1-x}Y_xMnO_3$ will be considered. As already discussed in section 6.2, the lowest–frequency IR–active phonons are affected by the doping approach, due to the strong participation of the Rare–Earth ions. In the $Eu_{1-x}Y_xMnO_3$ series the Eu^{3+} ions are partially substituted by Y^{3+} causing a decrease of the dipolar activity of the $B_{1u}(1)$ and $B_{3u}(1)$ modes with increasing Y doping level x (see figure 6.14). Thus, for increasing Y–content the corresponding resonance structures in the reflectivity spectra tend to be weakened.
This trend can be inspected in the polarised reflectivity spectra of in $Eu_{1-x}Y_xMnO_3$ (x = 0, 0.2 and 0.5) for selected temperatures drawn in figure 8.9. The phonon structures

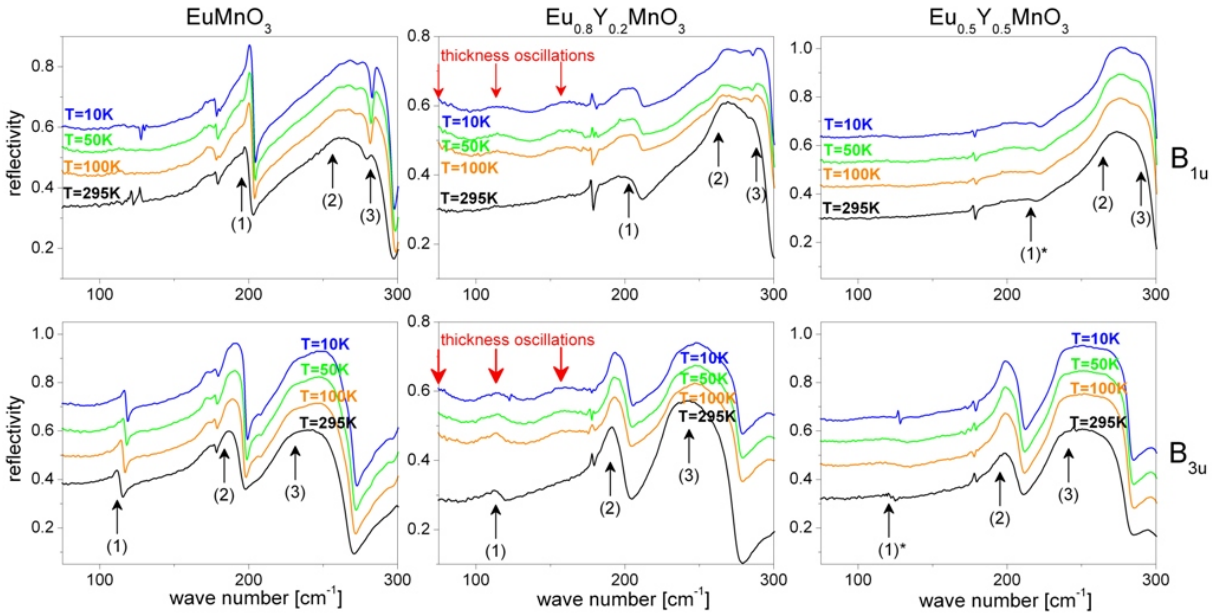

Figure 8.9: Reflectivity spectra from 75 to 300 cm^{-1} obtained from $EuMnO_3$, $Eu_{0.8}Y_{0.2}MnO_3$ and $Eu_{0.5}Y_{0.5}MnO_3$ in B_{1u} and B_{3u} symmetry for several temperatures. The thickness oscillations are indicated within the $Eu_{0.8}Y_{0.2}MnO_3$ spectra. In B_{3u} symmetry they obscure the $B_{3u}(1)$ phonon mode for $T < 100K$.

are marked by arrows and the number corresponding to the phonon notation. The room temperature reflectivity (black line) already verifies the trend of a reduction of the dipolar strength nicely. The phonon signatures of $B_{1u}(1)$ and $B_{3u}(1)$ (marked by asterisks) in $Eu_{0.5}Y_{0.5}MnO_3$ are so weak, that a quantitative fitting procedure does not lead to reliable results.
Additionally, the experimental difficulties already mentioned for the stoichiometric $RMnO_3$ series (see begin of chapter 8) – i.e. the thickness oscillations caused by the cryostat window – are also present in the reflectivity spectra of $Eu_{0.8}Y_{0.2}MnO_3$ for $T < 295K$. In contrast to the relatively strong dipolar contribution $\Delta\epsilon$ of $B_{3u}(1)$ in $GdMnO_3$, $\Delta\epsilon$ of the same mode in $Eu_{0.8}Y_{0.2}MnO_3$ is less pronounced. Therefore, the detection of this mode is seriously hampered by the thickness oscillations, as can be seen in the middle panels of figure 8.9 (marked by the red arrows). Thus, a quantitative fitting of this mode for $T < 295K$ is not possible. Therefore, for the $Eu_{1-x}Y_xMnO_3$ series investigated within this thesis reliable fitting data of $B_{3u}(1)$ for $x > 0$ cannot be extracted, due to the just discussed reasons. On the other side, when considering the B_{1u} reflectivity spectra, the stronger $\Delta\epsilon$ of $B_{1u}(1)$ compared to $B_{3u}(1)$ allows a quantitative fit of this mode for all temperatures.
It should be pointed out here, that these difficulties do not obscure other modes. Thus, a systematic investigation of the stronger group 1 IR–active modes is still possible and is carried out in the following for completing the EMPC investigations of this thesis.

Figure 8.10 shows the temperature dependence of all observable group 1 IR–active phonon modes of the $Eu_{1-x}Y_xMnO_3$ (x = 0, 0.2 and 0.5) series. The arrangement is chosen equivalent to that of figure 8.4 for the stoichiometric $RMnO_3$ series. The red lines are fits to the experimental data optimised for $T \gg T_N$, according to equation (7.3), thus referring to the temperature dependence expected without EMPC. It can be immediately seen, that for all displayed group 1 IR–active phonon modes a behaviour in accordance with equation (7.3) occurs. Thus, it can be followed, that these phonon modes, i.e. all group 1 phonon modes with the exception of $B_{1u}(1)$ in $Eu_{0.5}Y_{0.5}MnO_3$ and $B_{3u}(1)$ in $Eu_{0.8}Y_{0.2}MnO_3$ and $Eu_{0.5}Y_{0.5}MnO_3$, do not show EMPC. This observation is actually expected with the knowledge of the conclusions of the previous sections, where phonon frequency shifts only occurred for the $B_{3u}(1)$ mode, due to its close coupling to the high–frequency EM.
On the other hand, EMPC effects concerning the transfer of spectral weight or the shift of phonon frequencies could not be confirmed within own reflectivity measurements, due to the aforementioned experimental difficulties obscuring the unambiguous investigation of the $B_{3u}(1)$ mode. However, there is strong evidence, that these should be observable given that the experimental difficulties could be overcome. The main evidence is – as in the case of EMPC manifestations for the $RMnO_3$ series – a close inspection of literature data. In the case of $Eu_{1-x}Y_xMnO_3$, Takahashi et al. [TYK+09] have published a systematic investigation of the low–frequency IR–active phonons and EMs of this series with x = 0.1, 0.2, 0.3, 0.4 and 0.45 in the FIR and THz regime – i.e. for $\widetilde{\nu} < 200cm^{-1}$. Their data show a strong coupling between the $B_{3u}(1)$ mode and the high–frequency EM manifesting itself as a transfer of spectral weight (see figure 5.5). For $Eu_{0.6}Y_{0.4}MnO_3$ a decrease of the

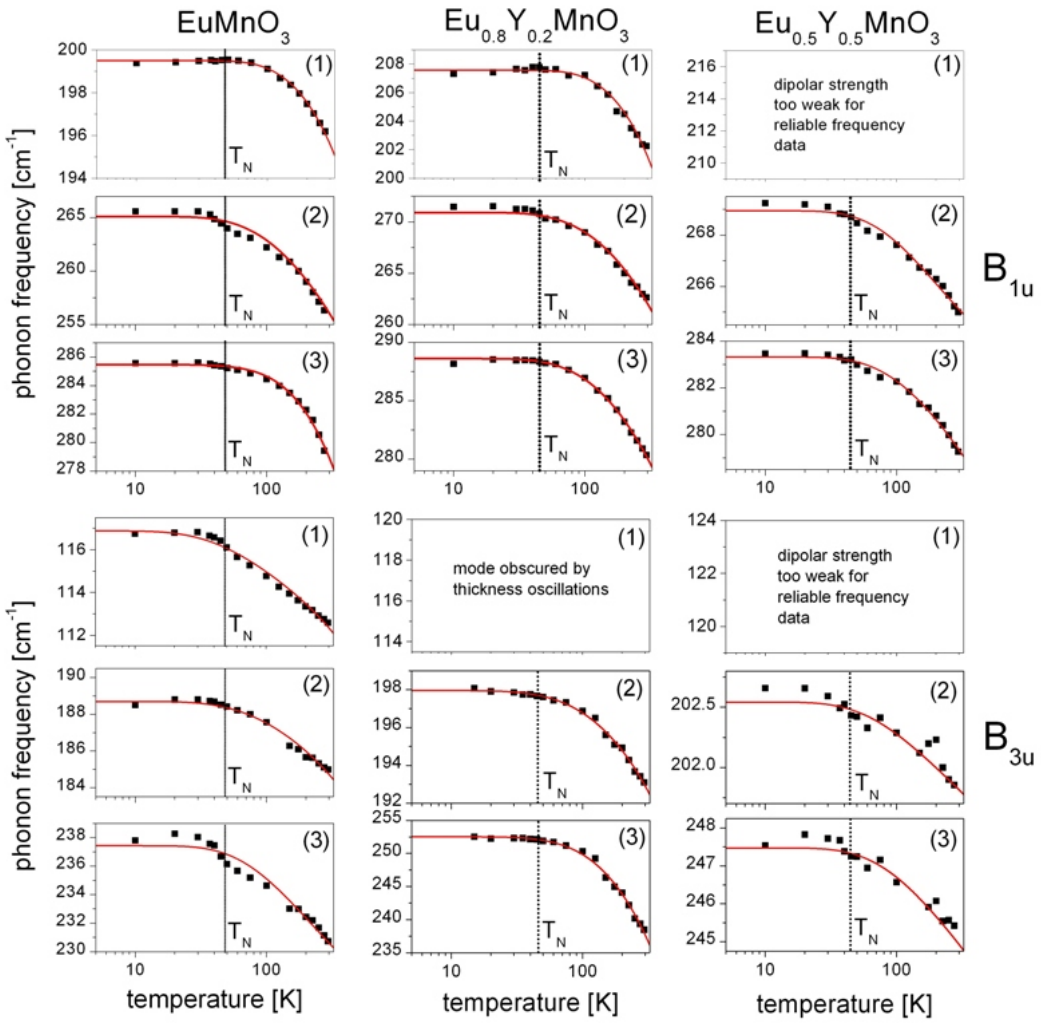

Figure 8.10: Temperature dependence of the $B_{1u}(1)$ to (3) and $B_{3u}(1)$ to (3) phonon modes obtained from $EuMnO_3$, $Eu_{0.8}Y_{0.2}MnO_3$ and $Eu_{0.5}Y_{0.5}MnO_3$. The red lines are fits according to equation (7.3) optimised for $T \gg T_N$ (indicated by the vertical line).

spectral weight by a factor of ≈ 2 occurs with its onset temperature located well above T_N, which is in close similarity to the data concerning the transfer of spectral weight of $RMnO_3$ presented in section 8.1. In contrast to the systematic investigation of this transfer, the phonon frequencies have not been analysed further. Thus, a confirmation of the expected EMPC induced frequency shifts cannot be given by inspection of the literature data published in [TYK+09].

Summing up, the polarised temperature dependent reflectivity measurements of doped $Eu_{1-x}Y_xMnO_3$ give a complete picture of the phonon frequencies as a function of temperature with the exception of the $B_{3u}(1)$ mode. For all other modes, the expected temperature dependence, i.e. no observable EMPC effects, could be verified. Inspection of literature data of $Eu_{1-x}Y_xMnO_3$ published in [TYK+09] gives strong evidence for the existence of EMPC between the high–frequency EM and the $B_{3u}(1)$ mode manifesting it-

self as a transfer of spectral weight. Further evidence, e.g. frequency shifts upon entering the magnetically ordered phases could not be extracted from the data of Takahashi et al. Nevertheless, EMPC effects in the doped $Eu_{1-x}Y_xMnO_3$ series are tentatively assigned employing own measurements in combination with the close inspection of literature data.

Chapter 9

Summary

In this thesis a systematic analysis of the correlation effects between lattice dynamics and magnetism in the Multiferroic Manganites $RMnO_3$ with Pnma structure was conducted. For this task, Raman and FT–IR Spectroscopy were employed for an investigation of all optically accessible lattice vibrations, i.e. phonons. To study the correlation effects as well as their specific connections to symmetry and compositional properties of the Multiferroic Manganites, the polarisation and temperature dependence of the phonons were considered explicitly. In combination with lattice dynamical calculations based on Density Functional Theory, two coupling effects – Spin–Phonon Coupling and Electromagnon–Phonon Coupling – were systematically analysed. In the following, the results obtained by the described efforts will be summarised.

Lattice dynamics of stoichiometric and doped Rare–Earth Manganites (Chapter 6)

As a base for a further analysis, the lattice dynamics of both studied sample series, i.e. stoichiometric $RMnO_3$ (R = Eu, Gd, Tb) and doped $Eu_{1-x}Y_xMnO_3$ ($0 \leq x \leq 0.5$), were investigated. In order to exclude possibly interfering correlation effects, these Raman and FT–IR measurements were carried out at room temperature – far above the temperature regime of the magnetically ordered phases.
As a preliminary step, ab–initio calculations of the lattice dynamics of the $LaMnO_3$ system based on Density Functional Theory (DFT) were carried out. These yielded the mode displacement patterns of the corresponding phonon mode, which were employed for a detailed analysis of the coupling effects later on.
The first step of this analysis was a mode assignment for all experimentally observed Raman– and IR–active phonon modes. For this purpose, the $GdMnO_3$ system was employed, due to its polished b–cut sample surface leading to a good fulfilment of the optical selection rules and – at least for the Raman spectra – the possibility to compare with literature data published by Iliev et al. [IAL$^+$06]. A very good agreement between these data and those obtained experimentally within this thesis was confirmed by comparing frequencies and polarisation dependencies of the Raman modes.

In contrast to the Raman–active modes, the IR–active phonon modes of the stoichiometric $RMnO_3$ (R = Eu, Gd, Tb) had not been systematically studied at room temperature until now. As in the case of the Raman spectra, in this thesis a mode assignment was carried out by employing reflectivity spectra obtained from the b–cut $GdMnO_3$ giving access to B_{1u} and B_{3u} symmetries. The phonon numbers expected from group theory could be well reproduced. Further, the obtained phonon frequencies, linewidths and ionic plasma frequencies were qualitatively compared to measurements of Schmidt et al. [SKR+09] carried out on $TbMnO_3$. Thus, the FT–IR measurements in combination with the Raman data carried out on both sample series give a complete first time analysis of the lattice dynamics of this system.
Having carried out this systematic mode assignment, in the next step the influence of (i) the complete replacement of the R^{3+} ion in the stoichiometric $RMnO_3$ (R = Eu, Gd, Tb) series and (ii) the doping approach of partially substituting Eu^{3+} by Y^{3+} in $Eu_{1-x}Y_xMnO_3$ ($0 \leq x \leq 0.5$) was investigated. This was done in the form of a comparative analysis of the changes in the Raman and reflectivity spectra obtained from both series.
Considering the Raman–active phonon modes of $RMnO_3$ a clear trend was observed: Phonon modes, that mainly comprise O^{2-} displacements perpendicular to the MnO_2 (ac) plane, show significant frequency shifts towards higher values, when reducing the R^{3+} ionic radii. This was attributed to the simultaneous reduction of the Mn–O–Mn tilting angle. On the other side, the breathing mode of the MnO_6 octahedra with its displacement pattern located within the MnO_2 (ac) plane, as a prominent example, is almost completely insensitive to a change of this angle. This mode and composition dependent sensitivity could be systematically explained by considering the calculated mode displacement patterns. Further, mode mixing effects of $A_g(1)$ and $A_g(3)$ modes were observed in excellent agreement with literature [IAL+06].
Turning to the reflectivity spectra and, thus, the IR–active phonon modes, a classification according to the mode displacement patterns and the phonon frequencies of the polar phonon modes was employed to explain the trends observed with respect to R^{3+} replacement. It was found, that in the case of the IR–active modes, their compositional dependence can be explained by a simple model picture of a harmonic oscillator. In this picture, the two factors determining the frequency shifts are (i) the reduced mass of the participating ions and (ii) the force constants of the bonds modulated by the corresponding phonon. Considering quantitative literature values for the lattice constants with respect to the incorporated R^{3+} as well as the corresponding ion masses, all observed trends could be explained consistently.
The doped $Eu_{1-x}Y_xMnO_3$ series revealed very similar results. Concerning the Raman–active modes, an identical behaviour with respect to Y doping, i.e. mode–dependent frequency shifts and mode mixing effects, was found. The IR–active modes showed differences concerning the frequency shifts of phonons with strong involvement of the Rare–Earth ions. This was also explained within the picture of a simple harmonic oscillator. Further, the dipolar activity of the IR–active modes with the lowest frequency was reduced by Y doping. However, as this reduction is restricted to the lowest frequency polar phonon mode, the doped $Eu_{1-x}Y_xMnO_3$ system is considered equally suitable for an investigation

of the correlation effects between lattice dynamics and magnetism as the stoichiometric $RMnO_3$. These effects were analysed in the following.

Spin–Phonon Coupling (Chapter 7)

The first correlation effect to be investigated systematically was Spin–Phonon Coupling (SPC). It manifests itself as a renormalisation of the phonon frequencies when approaching the temperature region of the magnetically ordered phases. The origin of SPC is the modulation of the magnetic exchange interaction by the corresponding phonon modes. Thus, the resulting phonon frequency renormalisation is correlated with the increasing strength of the magnetic exchange with decreasing temperature. Observed on $RMnO_3$ with relatively large R^{3+} ionic radius ($R^{3+} = La^{3+} \ldots Sm^{3+}$) by Raman spectroscopy [GGS+99, LJM+06] and on $TbMnO_3$ by FT–IR spectroscopy [SKR+09], until now, no systematic investigation of the SPC effect was carried out in the Multiferroic Manganites. An analysis of the mode dependence of the strength and onset temperature of these renormalisation effects revealed, that it is mainly determined by the magnetic exchange within the MnO_2 (ac) plane. This could be demonstrated by considering the mode symmetry, where for the Raman–active phonon modes it was clearly visible, that modes with a main displacement pattern within this plane show stronger renormalisation effects and higher onset temperatures than those with displacement patterns perpendicular to this plane or within the RO (ac) plane, respectively. The investigation of the IR–active phonon modes, in turn, led to the conclusion, that SPC is primarily observed for phonon modes with a rather strong modulation of the Mn–O–Mn bonds. Phonon modes with strong R^{3+} involvement showed no SPC. Additionally, the minor impact of Mn^{3+} participation for the occurrence of SPC could be demonstrated, as for both Raman– and IR–active phonons renormalisation effects were observed.
Considering the compositional dependence of SPC, i.e. the strength and onset of SPC with respect to the incorporated R^{3+} ion, the two sample series were analysed comparatively. (i) For the stoichiometric $RMnO_3$ series a decrease of the strength of the renormalisation effects with decreasing R^{3+} ionic radius from Eu^{3+} to Gd^{3+} and Tb^{3+} was demonstrated. This could be traced back to the weakening of the ferromagnetic exchange within the MnO_2 (ac) plane by an increased octahedra tilting caused by the R^{3+} replacement and the resulting increasing importance of the next nearest neighbour antiferromagnetic exchange. (ii) The doped $Eu_{1-x}Y_xMnO_3$ series showed the same trend of a reduced SPC strength with increasing Y^{3+} doping, which reduced the average R^{3+} ionic radius similar to the complete replacement in $RMnO_3$. Thus, it could be concluded, that the doping approach followed in $Eu_{1-x}Y_xMnO_3$ to quasi–continuously tune the average R^{3+} radius had no impact on SPC – another clear sign, that disorder induced effects are negligible in this system. (iii) A quantitative comparison of the two sample series revealed the clear correlation between the orthorhombic lattice distortion, i.e. the inequivalence of the short a– and c–axis in the Pnma structure, expressed by the distortion parameter ϵ and the SPC induced phonon renormalisation. It could therefore be shown that SPC is not explicitly coupled to the existence of certain magnetic phases, but to the magnetic exchange

between Mn^{3+} ions within the MnO_2 (ac) plane. Further, it is observable for Raman– as well as for IR–active phonon modes modulating the Mn–O bonds within the MnO_2 (ac) plane. Thus, conclusions published in literature on ceramic Multiferroic Manganites [FMA$^+$09, MAF$^+$10], that related SPC to the multiferroic properties of the Manganites, could be disproven.
A correlation effect between lattice dynamics and magnetism in the Manganites that is explicitly linked to the existence of multiferroic phases was likewise regarded in this thesis and its results will be summarised in the following.

Electromagnon–Phonon Coupling (Chapter 8)

The second correlation effect between lattice dynamics and magnetism investigated in this thesis was Electromagnon–Phonon Coupling (EMPC). One of its manifestations – the shift of spectral weight from the IR–active phonon modes with low frequency ($\widetilde{\nu} < 300 cm^{-1}$) to the emerging EM upon entering the temperature region of the multiferroic phases – was extensively studied in literature [PRM$^+$06, TYK$^+$09, SKR$^+$09]. However, for other manifestations, as phonon frequency renormalisation upon entering the temperature region of the magnetically ordered phases, no systematic analysis was carried out. Further, a detailed explanation of its microscopic origin was still missing. To correct this vacancy, the low frequency IR–active phonon modes were selectively studied with special attention to their optical selection rules and displacement patterns.
Temperature dependent reflectivity measurements on $RMnO_3$ (R = Eu, Gd) together with the results of Schmidt et al. [SKR$^+$09] obtained from $TbMnO_3$ showed a clear transfer of spectral weight from the lowest frequency polar phonon mode with B_{3u} symmetry, i.e. $B_{3u}(1)$, to the emerging EM in the stoichiometric $RMnO_3$ series, as expected. Further, a compositional dependence of the strength of spectral transfer was proven. It increased monotonically from $EuMnO_3$ to $TbMnO_3$, which was interpreted as increasing strength of EMPC. Thus, this manifestation of EMPC could be verified with own measurements. In addition to this verification, positive frequency shifts of the polar $B_{3u}(1)$ phonon upon entering the magnetically ordered phases were observed in $EuMnO_3$ and $GdMnO_3$. These were in good agreement with the data of [SKR$^+$09] obtained from $TbMnO_3$. Again the trend of increasing EMPC strength upon approaching those $RMnO_3$ systems with multiferroic phases was demonstrated. These data clearly showed, that the $B_{3u}(1)$ renormalisation can not originate from SPC, due to the positive sign of the frequency shift and the strong R^{3+} involvement in this mode.
Having collected the main experimental findings, a microscopic explanation for the exclusive coupling between EM and $B_{3u}(1)$ was given. It is based on the close inspection of the mechanism responsible for the dipolar activity of the high–frequency EM – the Heisenberg–Exchange Model of Valdés Aguilar [VAMS$^+$09] – as well as the mode displacement patterns of the $B_{3u}(1)$ mode obtained from own DFT calculations. Considering both aspects, a uniform Mn^{3+} displacement parallel to the c–axis characteristic to the $B_{3u}(1)$ mode was identified as being responsible for this coupling. Thus, also in the case of EMPC, a dynamic modulation of the magnetic exchange by a phonon mode with

suitable displacement pattern causes the correlation effect.
In the light of this microscopic model, the observed manifestations of EMPC were discussed and an additional manifestation was found by a close inspection of the $GdMnO_3$ data of Shuveav et al. [SML$^+$11]. The three discussed manifestations are: (i) the transfer of spectral weight, (ii) the temperature dependent frequency shifts of $B_{3u}(1)$, whose shift was shown to be explicitly linked to the temperature dependent EM frequency, and (iii) an asymmetric line shape of the $B_{3u}(1)$ mode observable in the transmission spectra obtained from literature measurements of $GdMnO_3$ [SML$^+$11]. The asymmetric spectral shape could be well reproduced by employing a Fano–type spectral function for modelling the ϵ_2 spectrum.
Further, these results were compared to experimental data obtained from the doped $Eu_{1-x}Y_xMnO_3$ series. The obtained reflectivity spectra showed the decreasing dipolar activity of $B_{1u}(1)$ and $B_{3u}(1)$ caused by the doping approach, as expected from the reflectivity spectra obtained at room temperature, and, due to additional experimental difficulties in the case of $Eu_{0.8}Y_{0.2}MnO_3$, no reliable frequency shifts of $B_{3u}(1)$ could be detected for $x > 0$. However, all other IR–active phonon modes showed the behaviour expected within the microscopic model picture introduced before. Additional literature data [TYK$^+$09] covering the transfer of spectral weight further confirmed the expected EMPC trends. Thus, based on the combination of own data and literature, the similar occurrence of EMPC effects in the doped $Eu_{1-x}Y_xMnO_3$ series was concluded.

Conclusion

The systematic investigation of the temperature dependent lattice dynamics of the Multiferroic Manganites showed two prominent coupling effects with the magnetic properties of these systems: SPC and EMPC. The various dependencies of both were explained based on model pictures that rely on the dynamic modulation of the magnetic exchange by the phonons. Both effects could be well separated by employing explicitly the mode displacement patterns, the optical selection rules and the phonon frequencies. This thesis therefore provides systematic evidence for the intimate correlation of lattice dynamics and magnetism in the Multiferroic Manganites on a microscopic scale.

Appendix A

Experimental setups

The employed spectroscopical setups will now be introduced briefly. Among the four utilised setups, there are two Raman and two FT–IR setups.
First, both Raman setups will be discussed. The main components of the experimental Raman setups are (i) a Laser as light source, (ii) optical components to guide the light to the sample, (iii) a dispersive spectrometer (single or triple stage in our case) and (iv) a multichannel detector, i.e. a CCD. Additionally, both employed Raman setups are micro–Raman setups. Thus, the Laser light is coupled into an optical microscope via a beam splitter, where the beam is focused onto the sample. This way, a spatial resolution in the range of a few microns and a drastic increase of the beam power density can be achieved. In the following, the Renishaw 1000 setup employed for the Raman measurements at room temperature (presented in chapter 6) will be discussed, followed by the Dilor XY 120 setup, that was used for the temperature dependent Raman experiments of chapter 7:

- Renishaw RM 1000 Setup
  The Renishaw RM 1000 Raman setup equipped with a Leica DM LM microscope was used for the room temperature Raman measurements presented in chapter 6. Figure A.1 shows a front sight of the system with open cover. It offers two possible Laser excitation lines, i.e. $\lambda = 514.5nm$ of an Argon ion Laser or $\lambda = 632.8nm$ of a Helium–Neon Laser. Only the latter was used for the Raman experiments carried out within this thesis. The light is guided from the laser to the beam splitter. The latter couples the light into the optical axis of the Leica microscope. There, the Laser beam is focused by a 50x ULWD (ultra large working distance) objective onto the sample. The backscattered light is then collected by the same objective, guided back to the beam splitter and then transmitted to the notch filter, where the elastically scattered Laser light is suppressed. The single–stage monochromator decomposes the scattered light into its spectral components that are finally analysed by a Peltier–cooled CCD detector.
  The whole setup is optimised for maximum light throughput and high sensitivity due to the usage of a single monochromator. On the other side, this limits the spectral resolution to $\approx 4cm^{-1}$ and the detectability to Raman signals with an

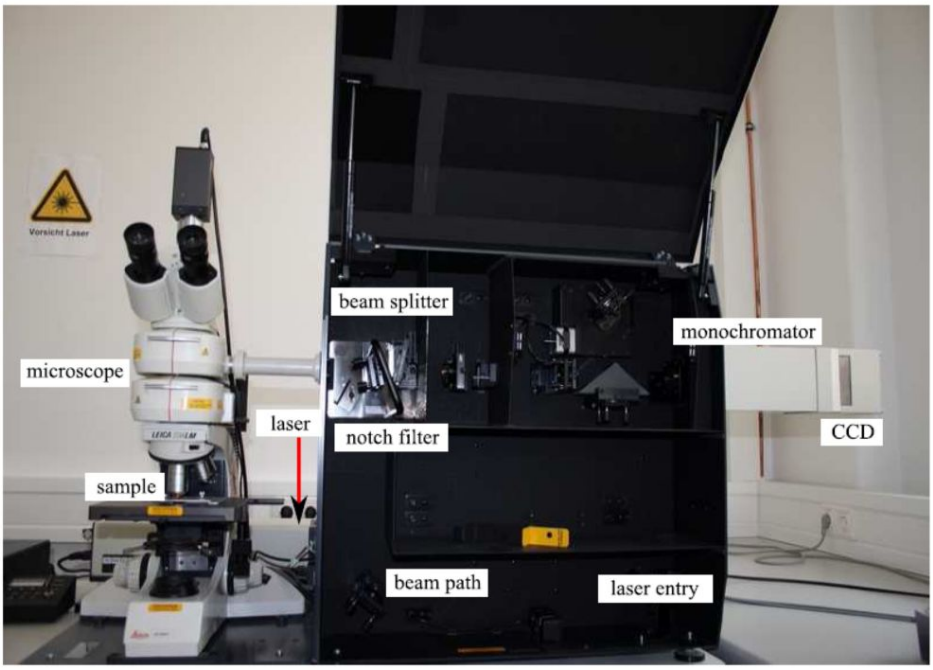

Figure A.1: Renishaw RM 1000 Raman setup with Leica Microscope DM LM. Taken from [Sch08]

energy of $\widetilde{\nu} \geq 200cm^{-1}$. Further, a low temperature option, i.e. the integration of a cryostat in this setup, is not possible. Thus, the temperature dependent Raman measurements are carried out on the second Raman setup, the Dilor XY 120 setup.

- Dilor XY 120 Setup
  In contrast to the compact Renishaw RM 1000 setup, the Dilor XY 120 setup consists of separated components, i.e. Laser, optical components for guiding the beam to the microscope and for manipulating the polarisation of the Laser light, microscope (Olympus BHT equipped with 10x, 50x ULWD, 80x ULWD and 100x objectives) and a triple stage monochromator (Dilor XY 120) in multichannel mode, where the split up scattered light is detected by a liquid–nitrogen cooled CCD detector. In contrast to the Renishaw setup introduced before, the Dilor setup is designed for maximum variability and spectral resolution. The latter is $\approx 1cm^{-1}$ in the low dispersion mode employed for all Raman measurements carried out for this thesis. Additionally, this setup allows the incorporation of a continuous–flow liquid–helium cryostat (CryoVac) in the microscope. This way, the sample can be cooled down from room temperature to $T = 10K$. A clear disadvantage of the triple stage Dilor setup is its reduced throughput compared to the single stage Renishaw setup. Thus, longer integration times had to be chosen to obtain a comparable signal–to–noise ratio.
  For the experiments carried out at the Dilor setup, the 632.8 nm line of a Helium–

Neon Laser with $P = 17mW$ was used. To keep the irradiance power density low and to avoid strong local heating at the Laser spot, a 50x ULWD objective was used, thus yielding a Laser power density of $\approx 2mW/\mu m^2$.
A schematic sketch of the optical beam path is depicted in figure A.2. This picture shows, that the basic principle of both Raman setups, i.e. employing a beam splitter to couple the Laser light in the microscope and guiding the scattered light to the spectrometer entrance, is essentially the same.

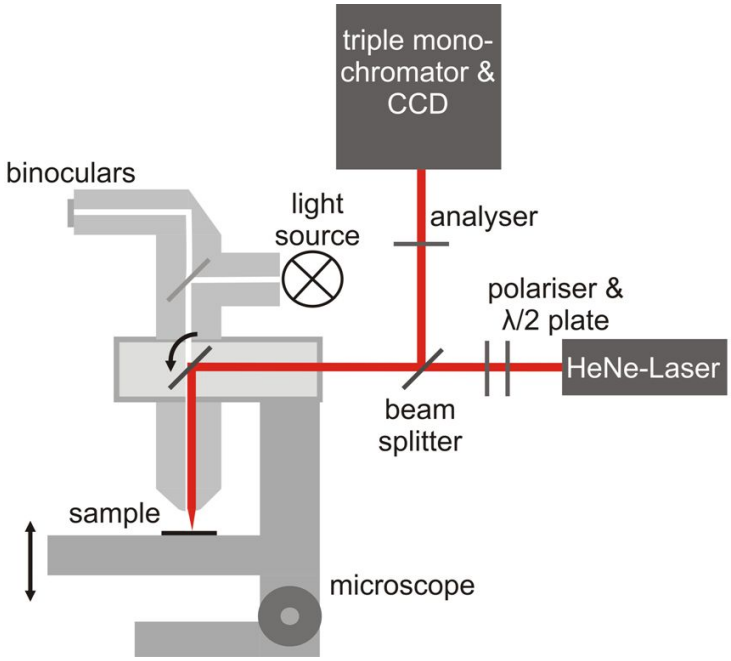

Figure A.2: Schematics of the Dilor XY 120 setup

Having covered the Raman setups, the FT–IR setups employed for obtaining the reflectivity spectra presented in this thesis will be briefly discussed now. Both setups are Bruker IFS113v FT–IR spectrometer optimised for a wide frequency range from FIR to NIR. However, for the reflectivity measurements carried out in this thesis almost exclusively the FIR regime was considered. Only for the room temperature measurements also MIR data were included in the reflectivity. An important difference between Raman and FT–IR setups is that the spectral resolution in the Raman setup is mainly determined by the grating of the spectrometer, while the same in a FT–IR setup is set by the movement length of the mobile mirror. The employed Bruker IFS113v setups can achieve spectral resolutions up to $0.3cm^{-1}$, however, due to comparability of Raman and reflectivity spectra, a resolution of $1cm^{-1}$ was chosen. Further, both FT–IR setups could be evacuated to low vacuum to suppress spectroscopic signals of the ambient atmosphere.
In the following, the Augsburg setup, employed for the temperature dependent reflectivity measurements presented in the chapters 7 and 8, will be discussed. Then the Würzburg setup, where the room temperature results of chapter 6 were obtained, will be covered briefly to explain the main differences.

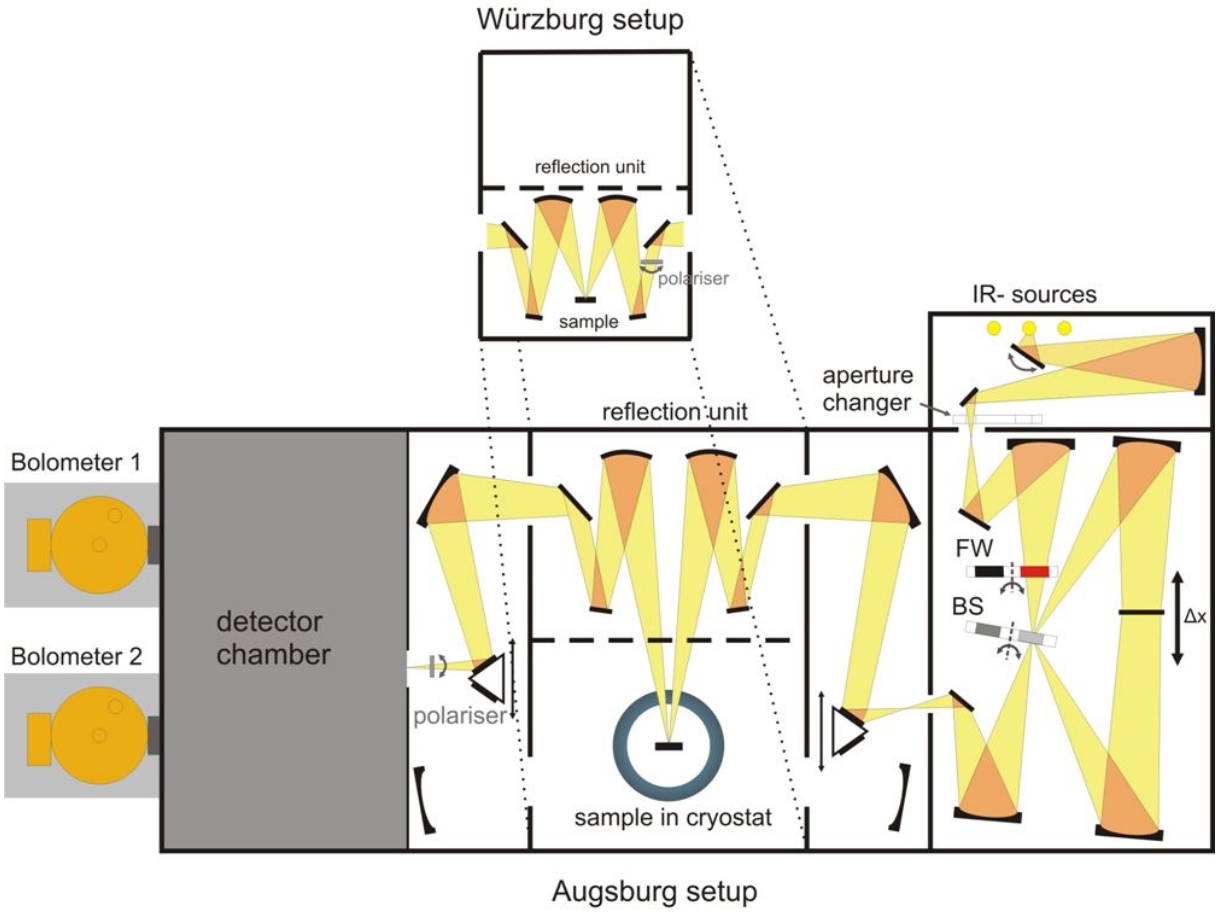

Figure A.3: Schematic sketch of the Bruker IFS113v setup in Augsburg. FW denotes the filter wheel and BS the automatically interchangeable beam splitters. The inset above shows the sample chamber in the Würzburg setup. The other parts of both spectrometers are mainly identical. The Augsburg part is adapted from [May02].

- Bruker IFS113v Setup in Augsburg
  The basic layout of the Bruker setup in Augsburg is drawn in figure A.3. It shows the typical construction of a Michelson interferometer in Genzel geometry. The IR–radiation sources (for FIR a Hg lamp, for MIR a globar and for NIR a tungsten lamp can be chosen) are guided through an aperture wheel to the interferometer chamber, where the beam – after passing a filter wheel (FW) – is focused via mirrors on the automatically interchangeable beam splitters (BS). The light is then split into two parts, that are further guided to a mobile mirror (maximum shift is $2\Delta x$), where both partial beams are reflected back to the beam splitter. There one part of the two beams is reflected (or transmitted) and then directed into the sample chamber. There a reflection unit focuses the beam onto the sample that is mounted into a continuous–flow cryostat (CryoVac), and collects the reflected radiation. The latter is then passed through a polariser – thus giving the possibility for polarised FT–IR Spectroscopy – and then into the detector chamber (not plotted in detail). The

detector chamber contains a total of six detectors. For the reflectivity measurements carried out in this thesis, only the 4.2 K Bolometer (Bolometer 1) optimised for FIR measurements, i.e. for $50cm^{-1} \leq \widetilde{\nu} \leq 650cm^{-1}$ was used.

- Bruker IFS113v Setup in Würzburg
  As already mentioned before, the Bruker FT–IR setup in Würzburg was employed for the room temperature measurements presented in chapter 6. The inset in figure A.3 shows the different sample chamber, which also explains the better suitability of the Augsburg setup for temperature dependent reflectivity measurements: in the Würzburg setup, the reflection unit is in the same part chamber as the sample itself. Thus, very little space for adjusting the optical path would be left, when introducing a cryostat into this setup. Another difference is the design of the detector chamber, which incorporates five detectors in Würzburg. For the room temperature measurements carried out in the FIR regime also a 4.2 K Bolometer was employed and for those carried out in the MIR regime (i.e. $600cm^{-1} \leq \widetilde{\nu} \leq 4000cm^{-1}$) a MCT (mercury–cadmium–telluride) detector. Otherwise both setups are identical.

Appendix B

Fitting procedure and fitting parameters

In this Appendix, the procedure of fitting appropriate functions to the raw data of the Raman and reflectivity spectra is described in more detail. It is applied for obtaining parameters as phonon frequencies, linewidths etc. of the corresponding phonon modes. This Appendix is organised as follows: first the fitting procedure of the Raman spectra will be discussed, followed by the reflectivity spectra obtained by FT–IR measurements.

Raman spectra

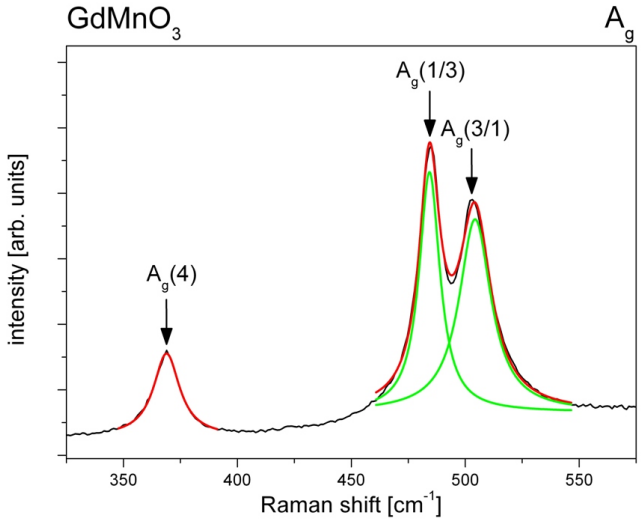

Figure B.1: Illustration of single (red) and multi-peak (red line composed of the green lines) fits of the A_g spectrum obtained from $GdMnO_3$ with the Lorentz–function. The black arrows mark the fitted phonon peak structures, here $A_g(4)$ at $369.0cm^{-1}$ and the double peak structure of $A_g(1/3)$ and $A_g(3/1)$ at $484.3cm^{-1}$ and $504.3cm^{-1}$, respectively.

The Raman spectra obtained either at the Renishaw or Dilor setup (see Appendix A) are analysed with the help of the fitting software Origin. Within this software various fit functions are available for fitting the raw data. From these, two functions are chosen: Lorentz– and Fano–functions. The first function is usually used for fitting phonon modes observed in Raman spectra. Its spectral shape is modelled by the Lorentz–function $I_L(\omega)$:

$$I_L(\omega) = \frac{2A}{\pi} \frac{\Gamma}{4(\omega - \omega_0)^2 + \Gamma^2} + y_0, \tag{B.1}$$

where A is a scaling factor, ω_0 the centre and Γ the FWHM (full width at half maximum and, thus, the linewidth) of the fitted curve. Additionally y_0 is used as offset to subtract a uniform background. The resulting fit functions are plotted with the raw data, e.g. in figure B.1 for the A_g spectrum obtained from $GdMnO_3$ at room temperature. This figure also shows the treatment of two or more phonon modes, which are very close to each other. This can be done by a so–called *Multi-Peak Lorentzian fit*. There two or more Lorentz–functions can be used to model a multi–peak structure with very close frequencies, as is illustrated in figure B.1 in the range of $460cm^{-1} < \widetilde{\nu} < 540cm^{-1}$.

All phonon modes observed in the Raman spectra are fitted with Lorentz–functions (either single or multi–peak), except the $B_{2g}(1)$ mode. Figure B.2(a) shows the fit of a Lorentz function to this mode. Obviously the Lorentz fit does not account the asymmetric shape, which is most clearly visible at the flanks. Instead a Fano–function $I_F(\omega)$ is

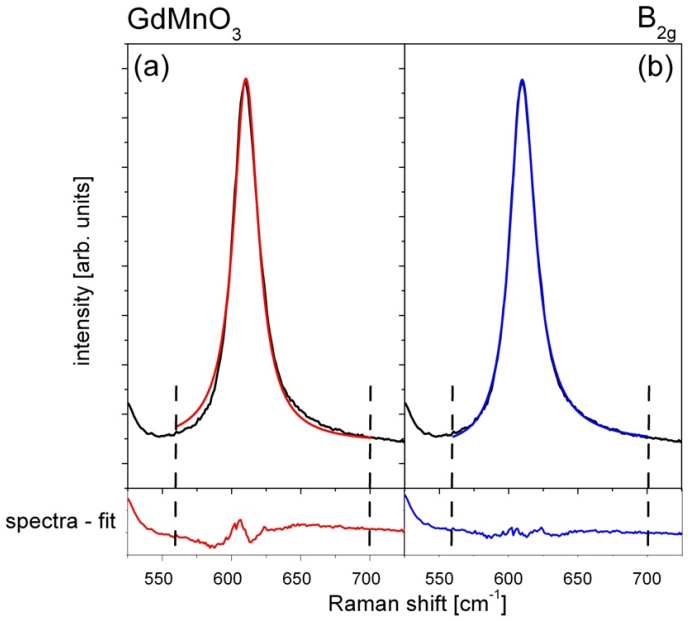

Figure B.2: Fits of the $B_{2g}(1)$ phonon of $GdMnO_3$ with a Lorentz (a) and Fano (b) function. The insets below the spectra show the difference between raw data and the fit functions.

employed. It reads as:

$$I_F(\omega) = A\frac{\left[1 + q(\omega - \omega_0)/\Gamma\right]^2}{1 + \left[(\omega - \omega_0)/\Gamma\right]^2} + y_0, \tag{B.2}$$

with identical nomenclature as for the Lorentz–function and, additionally, the Fano parameter q as a measure of the asymmetry of the phonon mode. A fit of the $B_{2g}(1)$ mode with a Fano–function is shown in figure B.2(b). It is clearly visible, that the fitting of the experimental data is improved by employing a Fano fit. Thus, it is used to model all observed $B_{2g}(1)$ modes.
The Fano parameter q is composition and temperature independent for all Raman measurements carried out within this thesis. Its value is in the range of ≈ 1.5. Thus, it is assigned as inherent to the $B_{2g}(1)$ mode in a Pnma crystal structure. One possible origin might be, that for the high– and low–frequency side of the $B_{2g}(1)$ mode the phonon density of states is rather different. One indication is the broad structure centred at $\approx 650cm^{-1}$ in the A_g spectra observed for all samples. Being assigned to a disorder–induced one–phonon mode from the Brillouin zone boundary [IHL+07], it can also be interpreted as a rather high phonon density of states, thus increasing the decay probability on the high–frequency site of $B_{2g}(1)$ in comparison to the low–frequency site. This effect was also observed for other materials, e.g. ZnO, where the E_2^{high} mode at $438cm^{-1}$ exhibits a similar behaviour with a very prominent low–frequency tail [CALIn+07]. There, this asymmetry was attributed to a resonant interaction of the E_2^{high} mode with a phonon density band of second–order contributions (so–called Fermi resonance). However, a systematic investigation is beyond the scope of this thesis and, thus, will not be regarded further.
For a systematic analysis of the Raman spectra, the fit parameters with physical meaning, i.e. phonon frequency ω and linewidth Γ, are extracted for all observed phonon modes. These parameters are listed in table B.1. As discussed in chapter 6, the residual roughness of the sample surface has a distinct influence on the phonon linewidth Γ. Thus, for reasons of comparability, only the phonon linewidths obtained from samples with a surface polished up to optical degree (i.e. $GdMnO_3$, $Eu_{0.8}Y_{0.2}MnO_3$ and $Eu_{0.5}Y_{0.5}MnO_3$) are included in this table.

Reflectivity spectra

The reflectivity spectra were obtained by FT–IR measurements that were carried out at the Bruker IFS 113v setups in Würzburg and Augsburg. Both are described in Appendix A. The obtained reflectivity data were analysed with the fitting software RefFIT [Kuz09]. In our case, the reflectivity data are measured only in a very limited frequency range, i.e. in FIR ($80cm^{-1} \leq \widetilde{\nu} \leq 800cm^{-1}$). For the room temperature measurements, these data could be supported by additional measurements in the MIR range, i.e. $\widetilde{\nu} \leq 4000cm^{-1}$. A fitting of these data relies therefore strongly on approximations of the reflectivity in the low– and high–frequency limit.

Table B.1: Phonon frequencies ω and linewidths Γ of the Raman–active phonons assigned in the figures 6.5 and 6.9 for the $RMnO_3$ and the $Eu_{1-x}Y_xMnO_3$ series, respectively. Asterisks mark very weak phonon signals. Because of the different degree of sample surface roughness only the phonon linewidths of the polished (and thus comparable) samples are shown.

ω $[cm^{-1}]$ $RMnO_3$									
R	$A_g(7/2)$	$A_g(2/7)$	$A_g(4)$	$A_g(1/3)$	$A_g(3/1)$	$B_{2g}(7)$	$B_{2g}(3)$	$B_{2g}(2)$	$B_{2g}(1)$
Eu	260.9	—	362.4	478.2	501.3	325.1	462.9	516.4	609.3
Gd	274.2	310.2*	369.0	484.3	504.3	327.3*	468.1	522.6	609.2
Tb	282.7	—	379.1	488.7	509.2	333.8	474.0	529.0	612.0
ω $[cm^{-1}]$ $Eu_{1-x}Y_xMnO_3$									
x	$A_g(7/2)$	$A_g(2/7)$	$A_g(4)$	$A_g(1/3)$	$A_g(3/1)$	$B_{2g}(7)$	$B_{2g}(3)$	$B_{2g}(2)$	$B_{2g}(1)$
0	260.9	—	362.4	478.2	501.3	325.1	462.9	516.4	609.3
0.1	263.3	303.6	363.4	478.1	500.4	329.7	462.4	517.9*	606.9
0.2	268.3	307.6*	366.8	480.4	500.9	325.9	466.0*	520.1	607.2
0.3	268.0	309.5*	370.3	481.4	503.0	326.2*	470.6	520.7	610.7
0.4	274.4	307.9*	376.4	484.4	507.4	329.9	469.8	525.4	610.4
0.5	277.5	314.8	377.7	485.5	506.9	331.0*	472.4	526.3	609.7
Γ $[cm^{-1}]$ $RMnO_3$									
R	$A_g(7/2)$	$A_g(2/7)$	$A_g(4)$	$A_g(1/3)$	$A_g(3/1)$	$B_{2g}(7)$	$B_{2g}(3)$	$B_{2g}(2)$	$B_{2g}(1)$
Gd	16.5	33.0*	14.0	11.0	17.0	16.2*	20.5	16.7	22.3
Γ $[cm^{-1}]$ $Eu_{1-x}Y_xMnO_3$									
x	$A_g(7/2)$	$A_g(2/7)$	$A_g(4)$	$A_g(1/3)$	$A_g(3/1)$	$B_{2g}(7)$	$B_{2g}(3)$	$B_{2g}(2)$	$B_{2g}(1)$
0.2	21.6	33.5*	18.8	22.1	13.6	14.4	26.5*	18.6	23.5
0.5	24.9	21.3	20.0	19.2	14.5	32.5*	27.4	19.3	22.3

In RefFIT the issue of fitting can be carried out in several ways. For the measurements carried out in this thesis, the approach of employing a so–called *formula–defined dielectric function* is chosen as the most convenient way. As described in detail in the manual of RefFIT [Kuz09], this approach is based on the Drude–Lorentz (DL) model, where the frequency dependent dielectric function $\epsilon(\omega)$ is written as:

$$\epsilon(\omega) = \epsilon_\infty + \sum_i \frac{\omega_{p,i}^2}{\omega_{T,i}^2 - \omega^2 - i\Gamma_i\omega}, \tag{B.3}$$

where ϵ_∞ describes the high–frequency response of the material, i.e. the contribution of all oscillators i at frequencies far above the investigated frequency range. $\omega_{T,i}$, $\omega_{p,i}$ and

Γ_i are the fit parameters for each oscillator i representing the transverse (i.e. resonance) frequency, the ion plasma frequency and the linewidth, respectively. This model describes the optical response of harmonic oscillators equivalent to equation (2.22).
With equation (B.3) the reflectivity R can be fitted within the DL model according to the Fresnel formula:

$$R = \left| \frac{1 - \sqrt{\epsilon}}{1 + \sqrt{\epsilon}} \right|^2 . \tag{B.4}$$

Choosing an appropriate number of oscillators (in our case the number of phonon modes expected by group theory) gives a reflectivity fit function with fit parameters $\omega_{T,i}$, $\omega_{p,i}$ and Γ_i for each phonon mode i. Due to the fact that an appropriate dielectric function is already chosen, the Kramers–Kronig–Transformation (KKR) can be carried out immediately – as it is already known.
The obtained parameters by fitting the reflectivity within the DL model are listed for all samples in table B.2 for B_{1u} and in table B.3 for B_{3u} symmetry, respectively. As already discussed in chapter 6, the polishing degree of the sample surfaces has direct influence on the reflectivity spectra and, thus, on ω_p and Γ. Therefore, ω_p and Γ are only listed for comparable samples, whose surface was polished up to optical degree.

Table B.2: Phonon frequencies ω_T, ion plasma frequencies ω_p and linewidths Γ of the infrared–active phonons with B_{1u} symmetry assigned in the figures 6.7 and 6.12 for the $RMnO_3$ and the $Eu_{1-x}Y_xMnO_3$ series, respectively. Asterisks mark phonon signals that are not comparable to the other samples because of too strong influence from phonons with forbidden symmetry (see explanation in the text). Due to the different degree of sample surface roughness the ion plasma frequencies and linewidths are listed only for the polished (and thus comparable) samples (i.e. $GdMnO_3$, $Eu_{0.8}Y_{0.2}MnO_3$ and $Eu_{0.5}Y_{0.5}MnO_3$).

ω_T $[cm^{-1}]$ $RMnO_3$									
R	$B_{1u}(1)$	$B_{1u}(2)$	$B_{1u}(3)$	$B_{1u}(4)$	$B_{1u}(5)$	$B_{1u}(6)$	$B_{1u}(7)$	$B_{1u}(8)$	$B_{1u}(9)$
Eu	195.5	254.3	277.4	312.8	351.3	379.3	477.2	517.7	573.1
Gd	196.2	251.8	280.7*	320.9	350.6	375.7	485.9	517.0	565.7
Tb	192.2	247.3	274.5	327.4	358.6	394.6	489.4	523.0	572.8
ω_T $[cm^{-1}]$ $Eu_{1-x}Y_xMnO_3$									
x	$B_{1u}(1)$	$B_{1u}(2)$	$B_{1u}(3)$	$B_{1u}(4)$	$B_{1u}(5)$	$B_{1u}(6)$	$B_{1u}(7)$	$B_{1u}(8)$	$B_{1u}(9)$
0	195.5	254.3	277.4	312.8	351.3	379.3	477.2	517.7	573.1
0.2	196.8	251.0	282.5	319.8	356.4	374.3	476.7	518.1	563.6
0.3	203.5	249.0	265.1*	320.7	355.1	373.8	484.9	519.2	570.8
0.4	202.3	257.4	283.6	323.9	361.1	378.9	488.2	522.1	572.8
0.5	207.5	260.1	282.9	326.2	357.9	369.8	487.6	516.9	567.9
ω_p $[cm^{-1}]$ $RMnO_3$									
R	$B_{1u}(1)$	$B_{1u}(2)$	$B_{1u}(3)$	$B_{1u}(4)$	$B_{1u}(5)$	$B_{1u}(6)$	$B_{1u}(7)$	$B_{1u}(8)$	$B_{1u}(9)$
Gd	357.6	723.8	74.6*	226.3	620.7	125.5	273.5	347.5	299.4
ω_p $[cm^{-1}]$ $Eu_{1-x}Y_xMnO_3$									
x	$B_{1u}(1)$	$B_{1u}(2)$	$B_{1u}(3)$	$B_{1u}(4)$	$B_{1u}(5)$	$B_{1u}(6)$	$B_{1u}(7)$	$B_{1u}(8)$	$B_{1u}(9)$
0.2	255.0	611.0	118.9	188.7	469.6	426.4	317.3	304.2	254.9
0.5	107.7	671.0	78.8	215.5	567.1	397.4	301.2	347.3	256.2
Γ $[cm^{-1}]$ $RMnO_3$									
R	$B_{1u}(1)$	$B_{1u}(2)$	$B_{1u}(3)$	$B_{1u}(4)$	$B_{1u}(5)$	$B_{1u}(6)$	$B_{1u}(7)$	$B_{1u}(8)$	$B_{1u}(9)$
Gd	16.3	11.8	3.2*	9.9	9.3	10.3	27.7	18.9	14.5
Γ $[cm^{-1}]$ $Eu_{1-x}Y_xMnO_3$									
x	$B_{1u}(1)$	$B_{1u}(2)$	$B_{1u}(3)$	$B_{1u}(4)$	$B_{1u}(5)$	$B_{1u}(6)$	$B_{1u}(7)$	$B_{1u}(8)$	$B_{1u}(9)$
0.2	14.8	22.6	9.2	11.5	14.6	29.3	42.9	33.1	12.7
0.5	9.2	12.1	7.1	8.9	7.3	20.4	31.3	26.3	9.2

Table B.3: Phonon frequencies ω_T, ion plasma frequencies ω_p and linewidths Γ of the infrared–active phonons with B_{3u} symmetry assigned in the figures 6.7 and 6.12 for the $RMnO_3$ and the $Eu_{1-x}Y_xMnO_3$ series, respectively. Asterisks mark phonon signals that are not comparable to the other samples because of too strong influence from phonons with forbidden symmetry (see explanation in the text). Due to the different degree of sample surface roughness the ion plasma frequencies and linewidths are listed only for the polished (and thus comparable) samples (i.e. $GdMnO_3$, $Eu_{0.8}Y_{0.2}MnO_3$ and $Eu_{0.5}Y_{0.5}MnO_3$).

ω_T $[cm^{-1}]$ $RMnO_3$									
R	$B_{3u}(1)$	$B_{3u}(2)$	$B_{3u}(3)$	$B_{3u}(4)$	$B_{3u}(5)$	$B_{3u}(6)$	$B_{3u}(7)$	$B_{3u}(8)$	$B_{3u}(9)$
Eu	112,2	184,0	229,8	299,4	318,5	391,7	446,0	470,5	576,0
Gd	114,5	182,8	220,4*	304,0	322,5	396,6	459,1	506,3*	563,0
Tb	114,8	185,9	233,7	302,9	326,4	399,8	428,4*	489,7	576,2
ω_T $[cm^{-1}]$ $Eu_{1-x}Y_xMnO_3$									
x	$B_{3u}(1)$	$B_{3u}(2)$	$B_{3u}(3)$	$B_{3u}(4)$	$B_{3u}(5)$	$B_{3u}(6)$	$B_{3u}(7)$	$B_{3u}(8)$	$B_{3u}(9)$
0	112.2	184.0	229.8	299.4	318.5	391.7	446.0	470.5	576.0
0.1	112.8	187.1	234.4	301.5	320.8	377.9*	396.1*	449.9*	563.3
0.2	115.6	191.5	233.2	305.9	323.3	399.8	459.6	477.0*	566.0
0.3	128.4*	191.1	234.6	310.1	325.0	375.3*	460.2	488.9	564.7
0.4	118.6	195.2	241.8	312.8	326.1	399.3	450.5	479.9	575.0
0.5	–	200.6	239.4	311.4*	327.5	392.3	440.7*	468.9	563.9
ω_p $[cm^{-1}]$ $RMnO_3$									
R	$B_{3u}(1)$	$B_{3u}(2)$	$B_{3u}(3)$	$B_{3u}(4)$	$B_{3u}(5)$	$B_{3u}(6)$	$B_{3u}(7)$	$B_{3u}(8)$	$B_{3u}(9)$
Gd	357.6	723.8	74.6*	226.3	620.7	125.5	273.5	347.5*	299.4
ω_p $[cm^{-1}]$ $Eu_{1-x}Y_xMnO_3$									
x	$B_{3u}(1)$	$B_{3u}(2)$	$B_{3u}(3)$	$B_{3u}(4)$	$B_{3u}(5)$	$B_{3u}(6)$	$B_{3u}(7)$	$B_{3u}(8)$	$B_{3u}(9)$
0.2	62.8	309.8	510.4	110.8	212.1	488.8	612.3	36.4*	531.7
0.5	–	276.3	568.8	185.0*	178.5	601.0	21.2*	541.5	420.8
Γ $[cm^{-1}]$ $RMnO_3$									
R	$B_{3u}(1)$	$B_{3u}(2)$	$B_{3u}(3)$	$B_{3u}(4)$	$B_{3u}(5)$	$B_{3u}(6)$	$B_{3u}(7)$	$B_{3u}(8)$	$B_{3u}(9)$
Gd	16.3	11.8	3.2*	9.9	9.3	10.3	27.7	18.9*	14.5
Γ $[cm^{-1}]$ $Eu_{1-x}Y_xMnO_3$									
x	$B_{3u}(1)$	$B_{3u}(2)$	$B_{3u}(3)$	$B_{3u}(4)$	$B_{3u}(5)$	$B_{3u}(6)$	$B_{3u}(7)$	$B_{3u}(8)$	$B_{3u}(9)$
0.2	6.5	7.9	14.0	14.4	9.7	8.0	39.0	2.4*	21.1
0.5	–	7.9	15.9	39.5*	8.3	17.1	5.2*	50.0	18.6

Appendix C

Sample synthetisation

The sample synthetisation and the principles of the underlying technique, i.e. the floating zone method with radiation heating, will be described in very brief form in this Appendix. For further information about Perovskites and possible synthetisation techniques, the reader is referred to literature (e.g. [JL06, BGR00] and references therein).

The two sample series investigated within this thesis are single crystalline stoichiometric or mixed manganite compounds $RMnO_3$ (R = $Eu_{1-x}Y_x$, Gd, Tb) crystallising in the orthorhombic Perovskite structure (space group Pnma). The crystalline properties of these compounds could be verified by various investigations, e.g. with X–Ray diffraction (XRD) [HSP$^+$07], magnetic and dielectric susceptibility [HSP$^+$07, HLKvN$^+$04] or

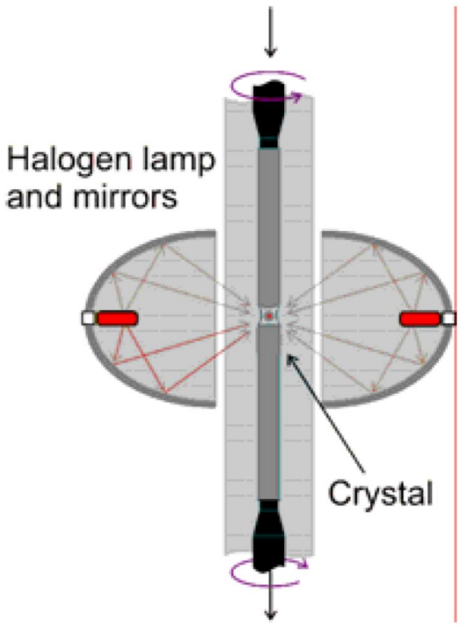

Figure C.1: Schematic sketch of a floating zone mirror furnace, where the single crystal is grown by moving polycrystalline powder rods through an optically heated zone. Taken from [JL06].

Terahertz Spectroscopy [PMI$^+$06, PLM$^+$08]. Additionally, the fulfilment of the optical selection rules derived in chapter 4 for Raman and FT–IR Spectroscopy also confirmed the single crystallinity very clearly.
All crystals were synthesised with the same floating zone method mentioned above. The first step is the preparation of polycrystalline samples from a solid state reaction, where oxides acting as precursors are thoroughly mixed and heated at temperatures of $\approx 600-1000K$ for periods up to ten hours [BGR00]. The obtained polycrystalline samples are then put into a mirror furnace, whose basic principle is illustrated in figure C.1. In this furnace strong local heating is achieved via focusing the light of halogen lamps on a small spot. Further, the oxygen content can be carefully controlled. Within this furnace, a zone melting procedure of the polycrystalline samples is performed, thus leading to the growth of large single crystals ($> 10cm$ long, according to [JL06]), that can be cut into thin plates oriented along the specific crystallographic axes.
A common problem, when synthesising $RMnO_3$ single crystals should also be mentioned: the so–called twinning of crystalline axes. When twinning occurs, the single crystallinity is lifted and the short a– and c–axes within the Pnma structure are mixed on a mesoscopic scale and cannot be distinguished anymore. This problem is especially pronounced for $RMnO_3$ compounds with large R^{3+} ionic radii, e.g. $LaMnO_3$, due to the close similarity of the lattice constants of a– and c–axis. However, as can be seen in the optical spectra as well as in the literature data twinning does not occur for $RMnO_3$ compounds with smaller R^{3+} ionic radii as Eu^{3+}, Gd^{3+} or Tb^{3+}, respectively. This is attributed to the more pronounced orthorhombic distortion and the resulting increased difference between the lattice constants of a– and c–axis (for quantitative lattice constants of $RMnO_3$ or $Eu_{1-x}Y_xMnO_3$, see tables 6.2 and 6.3, respectively).

Appendix D

Superexchange and Dzyaloshinskii–Moriya interaction

In this Appendix a theoretical motivation of the anisotropic corrections to the Superexchange – the Dzyaloshinskii–Moriya interaction – will be given. The Hamiltonian for this interaction favouring a canted spin alignment is of the form shown in equation (3.4). A short but instructive derivation according to [Mor60] starts from the localized electron orbitals considered for Superexchange (in our case the e_g orbitals of the Mn^{3+} ions). The unperturbed situation would thus be that of Superexchange without considering spin–orbit interaction. The unperturbed ground states of the ions i and j are denoted as n_i and n_j, respectively, while the virtual excited states are m_i and m_j, respectively. The energy corrections are obtained by perturbation theory in second order with respect to the spin–orbit coupling and the exchange interaction by

$$\begin{aligned} E_{i,j} = \sum_{m_i} \Bigg\{ & \frac{\langle n_i | \, \lambda \boldsymbol{l}_i \boldsymbol{S}_i \, | m_i \rangle \, 2 J_{i,j} \boldsymbol{S}_i \cdot \boldsymbol{S}_j}{\epsilon_{n_i} - \epsilon_{m_i}} \\ & + \frac{2 J_{i,j} \boldsymbol{S}_i \cdot \boldsymbol{S}_j \, \langle m_i | \, \lambda \boldsymbol{l}_i \boldsymbol{S}_i \, | n_i \rangle}{\epsilon_{n_i} - \epsilon_{m_i}} \Bigg\} \\ & + \ldots , \end{aligned} \tag{D.1}$$

where $J_{i,j}$ is the coupling constant for the Superexchange between ion i and j, λ the spin–orbit coupling constant, and $\boldsymbol{l_i}$ the angular momentum of ion i. The dots on the right side indicate that a term similar to the first one on the right side has to be added corresponding to a summation over m_j. In the case of a non–degeneracy of the orbital states, the matrix elements of $\boldsymbol{l}$ are purely imaginary and (D.1) can be rewritten as

$$E_{i,j} = 2\lambda \sum_{m_i} \frac{J_{i,j}}{\epsilon_{n_i} - \epsilon_{m_i}} \langle n_i | \, \boldsymbol{l}_i \, | m_i \rangle \, [\boldsymbol{S}_i, (\boldsymbol{S}_i \cdot \boldsymbol{S}_j)] + \ldots , \tag{D.2}$$

where the square brackets denote the anti–commutator of $\boldsymbol{S}_i$ and $\boldsymbol{S}_i \cdot \boldsymbol{S}_j$. With the relation $[\boldsymbol{S}_i, (\boldsymbol{S}_i \cdot \boldsymbol{S}_j)] = i \boldsymbol{S}_i \times \boldsymbol{S}_j$ this leads to

$$E_{i,j} = 2i\lambda \left(\sum_{m_i} \frac{J_{i,j} \, \langle n_i | \, \boldsymbol{l}_i \, | m_i \rangle}{\epsilon_{n_i} - \epsilon_{m_i}} + \cdots \right) (\boldsymbol{S}_i \times \boldsymbol{S}_j) \, . \tag{D.3}$$

This equation includes the vector product of the spins $\boldsymbol{S}_1$ and $\boldsymbol{S}_2$. The other terms on the right side can be combined to the Dzyaloshinskii–vector $\boldsymbol{D}$ specified in equation (3.4). Thus, we have formally deduced, how an inclusion of spin–orbit interaction in the Superexchange mechanism can lead to an energy term which favours non–collinear alignment of the magnetic moments. This effect leads to a canted antiferromagnetic arrangement where the resulting weak ferromagnetism can be experimentally verified e.g. by measurements of the macroscopic magnetic moment [HLKvN$^+$04].

Appendix E

DFT–Calculations of the $LaMnO_3$ lattice dynamics

For the derivation of the displacement patterns associated with the corresponding phonon modes ab–initio calculations based on *Density Functional Theory* (DFT) in the *Local Density Approximation* (LDA) were employed. For the calculation of the linear response, *Density Functional Perturbation Theory* (DFPT) was used, thus yielding phonon frequencies and mode patterns calculated from first principles. The numerical calculations were carried out employing the open–source code ABINIT [GRV$^+$05, GAA$^+$09]. In the following, the underlying theoretical background will be motivated very briefly for understanding the advantages and the limits of the DFT–approach. The hence derived results are presented graphically as mode displacement patterns in section 4.3. It should be stressed, that the main purpose of these calculations was not to obtain quantitative phonon frequencies that could be compared to experiment, but displacement patterns from first principle calculations. Obtaining such mode patterns ab–initio is very important, as all results for the phonon mode patterns of Pnma Perovskite systems published in literature are based on the empirical shell model [Smi99, KBC$^+$09].
This Appendix is organised as follows: First, the basic principle of DFT and DFPT will be explained in compact form. Second, the ABINIT code employed for the DFT calculations will be described and, third, the technical details, i.e. the input files, of the calculations will be given. Especially for the first section, we will rely mostly on [BdGDCG01] and [Wag03].

DFT and DFPT – Basics

DFT is a quantum–mechanical modelling method commonly used in solid state physics to investigate the electronic structure of many–body systems. With the help of DFT, the properties of a many–electron system can be theoretically studied by calculating the spatially dependent electron density within a functional approach. It is based on the two theorems of Hohenberg and Kohn from 1964 [HK64], where it was shown, that the ground state wave functions of a complex self–interacting many–body system, such as a crystalline

solid, can be bijectively described by its electronic ground state density. Precisely, the first Hohenberg–Kohn theorem states, that every ground state wave function Ψ of a system with N electrons (and, thus, 3N coordinates) can be bijectively mapped onto a functional of the electron density n (with only 3 coordinates). Thus, every ground state wave function $|\psi_0\rangle$ can be written as a functional of the ground state electron density n_0:

$$|\psi_0\rangle = |\psi_0\left[n_0\right]\rangle . \tag{E.1}$$

Every quantum–mechanical expectation value of the electronic ground state can now be expressed via this functional approach. An example is the single–particle potential $v_0(\boldsymbol{r})$, which can be derived from the external potential $\widehat{V}$ and written as a functional of the corresponding ground state electron density n_0:

$$v_0\left[n_0\right] = \langle\psi_0\left[n_0\right]|\,\widehat{V}\,|\psi_0\left[n_0\right]\rangle = \int v_0(\boldsymbol{r})n_0(\boldsymbol{r})d^3r. \tag{E.2}$$

Thus, taking into account the other energy terms in the time–dependent Schrödinger equation, for a single–particle potential the energy functional $E_{v_0}[n_0]$ can be written as:

$$E_{v_0}[n_0] = \langle\psi_0\left[n_0\right]|\,\widehat{T} + \widehat{W}\,|\psi_0\left[n_0\right]\rangle + \int v_0(\boldsymbol{r})n_0(\boldsymbol{r})d^3r, \tag{E.3}$$

with $\widehat{T}$ and $\widehat{W}$ being the kinetic energy and the electron–electron Coulomb interaction, respectively. This expression describes the energy via its ground state electron density n_0. The second Hohenberg–Kohn theorem now states, that minimising the energy with a variational approach, gives the ground state density n_0 and with it all other ground state expectation values. These can be expressed similar to the expression of the external potential $\widehat{V}$ in equation (E.2).
The Hohenberg–Kohn theorems, however, do not give any possibility to obtain results from real systems, e.g. the electronic ground state of crystalline solids. This is done by the Kohn–Sham formalism [KS65], which will be introduced in the following:
The basic idea of this formalism is to describe a many–particle system by a set of single–particle Schrödinger equations within an effective potential v_s^{eff}:

$$\left(-\frac{\hbar^2}{2m}\nabla^2 + v_s^{eff}(\boldsymbol{r})\right)\varphi_j(\boldsymbol{r}) = \epsilon_j\varphi_j(\boldsymbol{r}), \tag{E.4}$$

where $\varphi_j(\boldsymbol{r})$ are the single–particle wave functions solving these Schrödinger equations. The electronic ground state density is then obtained by:

$$n_0(\boldsymbol{r}) = \sum_{i=1}^{N} \left|\varphi_i(\boldsymbol{r})\right|^2 , \tag{E.5}$$

with the sum running over the first N Eigenenergies ϵ_j. A variational approach of minimising the energy functional $E[n_0]$ with respect to $n_0(\boldsymbol{r})$ as outlined above for the second

Hohenberg–Kohn theorem gives the effective potential:

$$v_s^{eff}(\boldsymbol{r}) = v_0(\boldsymbol{r}) + e^2 \int d^3r' \, \frac{1}{4\pi\epsilon_0} \frac{n_0(\boldsymbol{r'})}{|\boldsymbol{r} - \boldsymbol{r'}|} + \frac{\delta E_{XC}[n_0]}{\delta n_0(\boldsymbol{r'})}, \tag{E.6}$$

where $v(\boldsymbol{r})$ is the external potential, $\frac{1}{4\pi\epsilon_0}\frac{n_0(\boldsymbol{r'})}{|\boldsymbol{r}-\boldsymbol{r'}|}$ the Coulomb interaction between electrons and $E_{XC}[n_0]$ is the Exchange–Correlation potential. The latter is introduced to describe all quantum–mechanical effects due to exchange or correlation effects of the many–body system. It is the only unknown variable within this formalism and has to be approximated.
v_s^{eff} depends on $n_0(\boldsymbol{r})$ (see equation (E.6)) and $n_0(\boldsymbol{r})$, in turn, is determined by v_s^{eff} via the solution of the Schrödinger equations (E.4). Thus, the solutions need to be computed iteratively to find self consistent $n_0(\boldsymbol{r})$ and v_s^{eff}.
The Kohn–Sham formalism gives a good calculational starting point, if a reasonable approximation for the Exchange–Correlation potential $E_{XC}[n_0]$ can be found. In our case, the *Local Density Approximation* (LDA) is employed. The basic idea of the LDA is to approximate the charge density of an inhomogeneous system with that of a uniform electron gas with the same charge density. Thus, the Exchange–Correlation potential $E_{XC}[n_0]$ can be rewritten as a functional depending solely on the electron density:

$$E_{XC}[n_0] = \int d\boldsymbol{r} \; n_0(\boldsymbol{r}) \epsilon_{XC}(n_0)|_{n_0 = n_0(\boldsymbol{r})}, \tag{E.7}$$

with ϵ_{XC} being the Exchange–Correlation potential of the homogeneous electron gas. Various approximate forms – some even in analytical form – of ϵ_{XC} are known (see e.g. [PZ81]). Thus, with the LDA, the Kohn–Sham Formalism can be employed to calculate ground state electronic properties of solid state systems. For the most common systems studied in solid state physics DFT calculations employing the LDA approximation lead to a remarkably good agreement between ab–initio calculations and experiment [JG89]. Major drawbacks of the LDA are a large overestimate ($\approx 20\%$) of the crystal binding energies, the systematic underestimation of the optical gap in insulators and the inability to describe strongly correlated systems such as transition–metal oxides. However, due to its relatively moderate need of computational resources and the still qualitatively correct results, it can nevertheless be applied for calculations of ground state properties even of correlated systems.
The previous treatment explains the procedure to obtain ground state properties of a many–body system within the frame of DFT. The next step would be the consideration of a linear response of such systems to a perturbation, which can be expressed as a derivative of the total energy. In our case, we will deal with the perturbation of atomic displacements causing lattice vibrations. According to [Gon08], the total energy of a periodic crystal with small deviations of atomic positions from its equilibrium can be written as:

$$E_{tot}\left(\Delta\boldsymbol{R}\right) = E_{tot}^{(0)} + \sum_{ak\alpha} \sum_{a'k'\alpha'} \frac{1}{2} \left(\frac{\partial^2 E_{tot}}{\partial R_{k\alpha}^{a} \partial R_{k'\alpha'}^{a'}} \right) \Delta R_{k\alpha}^{a} \Delta R_{k'\alpha'}^{a'}, \tag{E.8}$$

where $\Delta R^a_{k\alpha}$ is the displacement of the atom k in the unit cell α from its equilibrium position along direction a. The matrix of the interatomic force constants is now defined as:

$$C_{k\alpha,k'\alpha'}(a,a') = \frac{\partial^2 E_{tot}}{\partial R^a_{k\alpha} \partial R^{a'}_{k'\alpha'}}. \tag{E.9}$$

The Fourier transform of this matrix is called the dynamical matrix and incorporates the phonon frequencies and the mode displacement patters as a solution of an Eigenvalue problem. Thus, one has to compute the dynamical matrix for obtaining quantitative results about the lattice dynamics. This procedure is referred as *Density Functional Perturbation Theory* (DFPT) and relies on the connection of the linear response of the electron density of a system to the above introduced matrix of the interatomic force constants.
The crucial point of DFPT is therefore to obtain the derivatives of the total energy with respect to atomic displacements. Without going into details, one can state, that by the use of the Hellmann–Feynman theorem these derivatives can be calculated. This theorem states, that the first derivative of the Eigenvalues $\partial E_\lambda / \partial \lambda$ of a Hamiltonian H_λ depending on the parameter λ is given by the expectation value of the derivative of H_λ:

$$\frac{\partial E_\lambda}{\partial \lambda} = \langle \psi_\lambda | \frac{\partial H_\lambda}{\partial \lambda} | \psi_\lambda \rangle , \tag{E.10}$$

where ψ_λ is the unperturbed wave function corresponding to $H_\lambda \psi_\lambda = E_\lambda \psi_\lambda$. For the calculation of phonon energies, the first and second derivatives of H_λ with respect to atomic displacements as parameter λ need to be computed as well as the first derivative of the wave function. Having obtained these, the dynamical matrix can be calculated by a Fourier transformation of the matrix of the interatomic force constants.
It should further be mentioned, that due to the polar nature of the studied crystal also the linear response to a homogeneous electric field needs to be computed and incorporated in the phonon dynamical matrix. This can be also carried out in the frame of DFPT by calculating the first derivative with respect to such an electric field.
Having covered the general procedure of obtaining phonon frequencies and the corresponding displacement patterns from first principles, in the next section the employed ABINIT code will be introduced.

The ABINIT code

ABINIT is an open–source software package for the ab–initio study of material properties [GRV+05]. The free availability of ABINIT under the GNU General Public License [GNU] led to a large developer and user group compared to other scientific or commercial software packages. Thus, the capability of ABINIT is very rich and covers a wide spectrum of computationally available material properties. The most interesting in our case are (i) the computation of ground state equilibrium cell parameters and atomic positions and

(ii) the vibrational properties, i.e. phonon frequencies and mode patterns.
The underlying theoretical framework of ABINIT are the previously discussed DFT and DFPT approaches. The implementation is based on a plane wave expansion of the electronic wave functions with periodic boundary conditions, which is therefore ideal for studies of crystalline solids. To reach acceptable computational resource consumption, pseudopotentials for the atoms incorporated in the unit cell to be studied allow avoiding an explicit treatment of the fast oscillating wave functions of the core electrons. ABINIT is able to incorporate a large number of different pseudopotential schemes for the whole periodic table.
The most important ground state aspect for the DFT calculations within this thesis is the atomic geometry. For a given geometry, the software is able to calculate analytically the forces on the atoms within the unit cell. Minimising these forces allows therefore the optimisation of atomic positions and unit cell parameters. The typical accuracy of such geometry parameters compared to experiment is a few percent. Further, the symmetries of the corresponding crystal can be used to reduce the computational effort, e.g. when calculating the forces on the atoms within the unit cell. The symmetries are incorporated as a database including all 230 space and all 1191 magnetic groups.
It should also be mentioned, that the electronic properties are subject to the well known shortcomings of DFT. Thus, a prediction of the band structure especially of materials with strong electronic correlations is questionable within the LDA frame and will not be pursued in this thesis.
Concerning the properties of the excited states, the DFPT outlined before enables ABINIT to compute the linear response to three types of perturbations: electric fields, internal atomic displacements and strain. In the case of phonons in a partially polar material, as the $RMnO_3$ system with Pnma structure, the first and the second perturbation are needed. Thus, as outlined before, the derivatives of the electronic density with respect to these two perturbations are computed within the DFPT frame and listed in a density derivative database (DDB). This DDB can be post processed to obtain the phonon frequencies, the displacement patterns and symmetries of the corresponding phonon modes.
An additional feature of ABINIT is its implementation of parallel computing via the Message Passing Interface (MPI), which enables a significant speed up of the computational procedure by dividing the calculation task over several processors. This aspect is very important, as the orthorhombic Perovskite systems with Pnma structure have 20 atoms within a single unit cell. Without parallel computing, this would cause inacceptable long calculation times. Nevertheless, such parallel computing requires the usage of a computational cluster with a significant number of cpus. Thus, for the calculations presented within this thesis, the parallel version of ABINIT was used on the supercomputer HLRB–II of the Leibniz-Rechenzentrum in Garching (project h0142, see [Iss]).
Having covered the general introduction of the ABINIT software package and its capabilities, the technical details of the calculation of the lattice dynamics will be presented.

Input files for the calculation of the $LaMnO_3$ lattice dynamics

As already discussed in section 4.3, the system $LaMnO_3$ was chosen for the computation of phonon mode patterns in a Pnma system due to its empty 4f–orbitals. This minimises the impact of electronic correlations on the stability of the lattice parameters, which are crucial for the computation of reliable phonon frequencies and mode patterns. Trial calculations with those $RMnO_3$ systems studied experimentally within this thesis did not lead to stable results for the crystalline geometry and, thus, were not further considered. The technical details will be presented in the order, they were needed to obtain first the ground state and then the linear response of the $LaMnO_3$ system. Thus, the first ABINIT input file covers the computation of the ground state properties. The main purpose of this file is the computation of the ground state electronic density and the resulting lattice constants and atomic positions within the unit cell. To gain information about the reliability of the ground state properties, the following procedure is suited most appropriate: (i) The interatomic forces are minimised within the unit cell by relaxing the lattice parameters and the relative atomic positions and (ii) then the hence calculated lattice parameters are compared with the experimental ones. In the following, this input file and the resulting output of ABINIT will be presented. Explaining comments have a leading asterisk.

** LaMnO3: cell optimization to minimise static interatomic forces in the ground state*

ecut 70
**cut–off energy for the plane waves in Hartree (= 2 · 13.6 eV)*

ngkpt 4 4 4
kptopt 1
nshiftk 1
shiftk 0.5 0.5 0.5
**k–point grid used for the Fourier Transformation of the plane waves*

acell 1.0394627523E+01 1.4691486786E+01 1.0440736841E+01 Bohr
**lattice constants in Bohr*

rprim
1 0 0
0 1 0
0 0 1
**vectors spanning the primitive cell*

spgroup 62
spgaxor 1

spgorig 1
brvltt 1
**definition of the space group 62 = Pnma*

natrd 4
ntypat 3
znucl 57 25 8
natom 20
typat 1 2 3 3
xred
0.5246 0.2500 0.0093
0.0000 0.0000 0.0000
-0.0057 0.2500 -0.0621
0.2787 0.0349 0.2292
**type, number and reduced coordinates of atoms on non–equivalent Wyckoff–sites within the unit cell*

nband 70
**number of bands to be computed*

toldff 1.0d-5
nstep 50
**stop criteria for the self–consistent calculation loop*
diemac 1
**start value of the dielectric constant*

**optimization of lattice parameters:*

optcell 1
ionmov 3
ntime 20
dilatmx 1.20
ecutsm 0.5
tolmxf 1.0d-3
nline 12
nnsclo 3
**parameters for the optimisation of the unit cell to minimise the interatomic forces*

ixc 1
** chosen parameterisation for the Exchange–Correlation Potential, here: LDA HGH parameterisation*

For details about specific meanings of input parameters, the reader is referred to the

documentation on the ABINIT website [ABI]. It should also be mentioned, that the employed pseudopotentials are declared in a separate file (not shown here). These were pseudopotentials of Troullier–Martins type [TM91] and can be downloaded from [ABI]. The obtained optimised lattice parameters are part of a very long output file. Due to brevity, only the optimised lattice constants are listed in the following:

———outvars: echo values of variables after computation ———
acell 1.1282524240E+01 1.5946416110E+01 1.1332572161E+01 Bohr

---

These lattice constants can be compared to the experimental ones (which are actually identical to the input lattice constants) and show a difference of $\approx +7.5\%$. This is a rather bad agreement and, therefore, the phonon frequencies obtained via the DFPT calculation in the following should not be taken as benchmark values for theoretically obtained phonon frequencies. Employing different types of pseudopotentials (e.g. pseudopotentials according to [HGH98]) improved this agreement, but caused even more serious problems in the DFPT part of the calculations, precisely in the symmetry properties of the displacement patterns of the phonon modes. As we are mainly interested in the mode patterns, the shortcomings of the Troullier–Martins type pseudopotentials can be tolerated in our case. The next step is the computation of the density derivative database (DDB) with these optimised lattice parameters. The corresponding input file is shown in the following:

** Crystalline LaMnO3: computation of the response to homogeneous electric field and atomic displacements, at the Gamma point q=0*

ndtset 3
**3 step calculation*

** Ground state calculation*
kptopt1 1
** Automatic generation of k points, taking into account the symmetry*

tolvrs1 1.0d-8
** SCF stopping criterion*
iscf1 7
** Self-consistent calculation, using algorithm 7*
nstep1 100

** Response Function calculation: d/dk*
rfelfd2 2
** Activate the calculation of the d/dk perturbation*
rfdir2 1 1 1
** Need to consider the perturbation in all directions (orthorhombic crystal)*
nqpt2 1

qpt2 0.0 0.0 0.0
** This is a calculation at the Gamma point*

getwfk2 -1
** Uses as input the output wave functions of the previous dataset*

kptopt2 2
** Automatic generation of k points, using only the time–reversal symmetry to decrease the size of the k point set.*

iscf2 -3
** The d/dk perturbation must be treated in a non-self-consistent way*

tolwfr2 1.0d-3
** Must use tolwfr for non-self-consistent calculations. Here, the value of tolwfr is very low.*
nstep2 100

** Response Function calculation: phonons*

rfphon3 1
** Activate the calculation of the atomic displacement perturbations*
rfatpol3 1 20
** All the atoms will be displaced*
rfdir3 1 1 1
Need to calculate perturbations in all directions (orthorhombic lattice)
nqpt3 1
qpt3 0.0 0.0 0.0
** This is a calculation at the Gamma point*

getwfk3 -2
** Uses as input wfs the output wfs of the dataset 1*
getddk3 -1
** Uses as input ddk wfs the output of the dataset 2*

kptopt3 2
** Automatic generation of k points, using only the time-reversal symmetry to decrease the size of the k point set.*
tolvrs3 1.0d-2
iscf3 7
nstep3 75

**Common input variables same as in the case of cell optimization*

These calculations led to the computation of the DDB incorporating the first derivative with respect to an electric field and the first and second derivative with respect to atomic displacements within the unit cell. This database needs to be analysed to obtain the phonon frequencies and the Eigendisplacements. This is done subsequently with the corresponding ABINIT subroutine, which is called *anaddb*. The input file reads as:

**Input file for the anaddb code. Analysis of the LaMnO3 DDB (pseudopotential: Troullier–Martins type)*

**Wavevector grid number 1 (coarse grid, from DDB)*
ngqpt 4 4 4
nqshft 1
** number of q-points in repeated basic q-cell*
*q1shft 3*0.5*

**Wave vector at gamma point:*
nph1l 1
qph1l 0.000 0.000 0.000 1.0

**Output of phonon eigenvectors and Eigen displacements:*
eivec 1

** This line added when defaults were changed (v5.3) to keep the previous, old behaviour*
symdynmat 0

With these input files the mode patterns of section 4.3 can be easily reproduced.

Bibliography

[ABI] ABINIT–website. http://www.abinit.org.

[ADGF+92] M. Abbate, F. M. F. De Groot, J. C. Fuggle, A. Fujimori, O. Strebel, F. Lopez, M. Domke, G. Kaindl, G. A. Sawatzky, M. Takano, Y. Takeda, H. Eisaki, and S. Uchida. Controlled–Valence Properties of $La_{1-X}Sr_xFeO_3$ and $La_{1-X}Sr_xMnO_3$ studied by soft X–Ray Absorption Spectroscopy. *Phys. Rev. B*, 46(8):4511–4519, 1992.

[Ast60] D.N. Astov. The magnetoelectric effect in antiferromagnets. *Sov. Phys. JETP*, 11:708, 1960.

[AZA91] V. I. Anisimov, J. Zaanen, and O. K. Andersen. Band theory and Mott insulators: Hubbard U instead of Stoner I. *Phys. Rev. B*, 44(3):943–954, 1991.

[BdGDCG01] Stefano Baroni, Stefano de Gironcoli, Andrea Dal Corso, and Paolo Giannozzi. Phonons and related crystal properties from density-functional perturbation theory. *Rev. Mod. Phys.*, 73(2):515–562, 2001.

[BGR00] A. S. Bhalla, R. Guo, and R. Roy. The perovskite structure - a review of its role in ceramic science and technology. *Mat. Res. Innovat.*, 4:3–26, 2000.

[BH68] W. Baltensperger and J. S. Helman. Influence of Magnetic Order in Insulators on the Optical Phonon Frequency. *Helv. Phys. Acta*, 41:668, 1968.

[Blu03] S. Blundell. *Magnetism in Condensed Matter*. Oxford University Press, Oxford, 2003.

[BRG+00] J. Blasco, C. Ritter, J. García, J. M. de Teresa, J. Pérez-Cacho, and M. R. Ibarra. Structural and magnetic study of $Tb_{1-x}Ca_xMnO_3$ perovskites. *Phys. Rev. B*, 62(9):5609–5618, 2000.

[BWH83] M. Balkanski, R. F. Wallis, and E. Haro. Anharmonic effects in light scattering due to optical phonons in silicon. *Phys. Rev. B*, 28(4):1928–1934, Aug 1983.

[CALIn+07] Ramon Cuscó, Esther Alarcón-Lladó, Jordi Ibáñez, Luis Artús, Juan Jiménez, Buguo Wang, and Michael J. Callahan. Temperature dependence of Raman scattering in ZnO. *Phys. Rev. B*, 75(16):165202, 2007.

[CBL+04] K. J. Choi, M. Biegalski, Y. L. Li, A. Sharan, J. Schubert, R. Uecker, P. Reiche, Y. B. Chen, X. Q. Pan, V. Gopalan, L. Q. Chen, D. G. Schlom, and C. B. Eom. Enhancement of ferroelectricity in strained $BaTiO_3$ thin films. *Science*, 306(5698):1005–1009, 2004.

[CM07] S. W. Cheong and M. Mostovoy. Multiferroics: a magnetic twist for ferroelectricity. *Nat. Mater.*, 6(1):13–20, 2007.

[CRC+09] R. Choithrani, M. N. Rao, S. L. Chaplot, N. K. Gaur, and R. K. Singh. Lattice dynamics of manganites $RMnO_3$ (R = Sm, Eu or Gd): Instabilities and Coexistence of orthorhombic and hexagonal Phases. *New J. Phys.*, 11(7):073041, 2009.

[Cur94] P. Curie. no title. *Physique*, 3, 1894.

[DSGPS07] J. L. F. Da Silva, M. V. Ganduglia-Pirovano, and J. Sauer. Formation of the cerium orthovanadate $CeVO_4$: $DFT + U$ study. *Phys. Rev. B*, 76(12):125117, 2007.

[Fan61] U. Fano. Effects of Configuration Interaction on Intensities and Phase Shifts. *Phys. Rev.*, 124(6):1866–1878, 1961.

[Fie05] M. Fiebig. Revival of the magnetoelectric effect. *J. Phys. D: Appl. Phys.*, 38(8):R123–R152, 2005.

[FLF+02] M. Fiebig, T. Lottermoser, D. Froehlich, A.V. Goltsev, and R.V. Pisarev. Observation of coupled magnetic and electric domains. *Nature*, 419:818–820, 2002.

[FMA+09] W. S. Ferreira, J. A. Moreira, A. Almeida, M. R. Chaves, J. P. Araújo, J. B. Oliveira, J. M. Machado Da Silva, M. A. Sa, T. M. Mendonca, P. Simeao Carvalho, J. Kreisel, J. L. Ribeiro, L. G. Vieira, P. B. Tavares, and S. Mendonca. Spin-Phonon Coupling and Magnetoelectric Properties: $EuMnO_3$ versus $GdMnO_3$. *Phys. Rev. B*, 79(5):054303, 2009.

[FS75] A. J. Freeman and H. Schmid, editors. *Magnetoelectric Interaction Phenomena in Crystals*. Gordon & Breach, London, 1975.

[GAA+09] X. Gonze, B. Amadon, P. M. Anglade, J. M. Beuken, F. Bottin, P. Boulanger, F. Bruneval, D. Caliste, R. Caracas, M. Cote, T. Deutsch, L. Genovese, Ph. Ghosez, M. Giantomassi, S. Goedecker, D. R. Hamann, P. Hermet, F. Jollet, G. Jomard, S. Leroux, M. Mancini, S. Mazevet, M. J. T. Oliveira, G. Onida, Y. Pouillon, T. Rangel, G. M. Rignanese, D. Sangalli, R. Shaltaf, M. Torrent, M. J. Verstraete, G. Zerah, and J. W. Zwanziger. ABINIT: First–principles approach to material and nanosystem properties. *Comput. Phys. Commun.*, 180(12):2582–2615, 2009.

[GGS+99] E. Granado, A. García, J. A. Sanjurjo, C. Rettori, I. Torriani, F. Prado, R. D. Sánchez, A. Caneiro, and S. B. Oseroff. Magnetic ordering effects in the Raman spectra of $La_{1-x}Mn_{1-x}O_3$. *Phys. Rev. B*, 60(17):11879–11882, 1999.

[GKL+04] T. Goto, T. Kimura, G. Lawes, A. P. Ramirez, and Y. Tokura. Ferroelectricity and Giant Magnetocapacitance in Perovskite Rare-Earth Manganites. *Phys. Rev. Lett.*, 92(25):257201, 2004.

[GNU] GNU–GPL. http://www.gnu.org/copyleft/gpl.txt.

[Gol25] V. Goldschmidt. *Geochemische Verteilungsgesetze der Elemente*. Kristiania : Ja. Dybwad, Oslo, 1925.

[Gon08] X. Gonze. Density Functional Perturbation Theory: Atomic Displacements and Homogeneous Electric Field. http://qro.cinvestav.mx/∼abinit/DFPT_v2.pdf, 2008.

[Goo55] J. B. Goodenough. Theory of the Role of Covalence in the Perovskite–type Manganites [La, M(II)]MnO_3. *Phys. Rev.*, 100(2):564–573, 1955.

[Goo63] J. B. Goodenough. *Magnetism and the Chemical Bond*. Interscience Publishers, New York, 1963.

[Gro09] R. Gross. Festkörperphysik, Vorlesungskript zur Vorlesung im WS 2004/2005. http://www.wmi.badw.de/teaching/Lecturenotes/index.html, 2009.

[GRV+05] X. Gonze, G. M. Rignanese, M. Verstraete, J. M. Beuken, Y. Pouillon, R. Caracas, F. Jollet, M. Torrent, G. Zerah, M. Mikami, Ph. Ghosez, M. Veithen, J. Y. Raty, V. Olevano, F. Bruneval, L. Reining, R. Godby, G. Onida, D. R. Hamann, and D. C. Allan. A brief introduction to the ABINIT software package. *Z. Kristallogr.*, 220(5–6):558–562, 2005.

[Hal69] L. H. Hall. *Group Theory and Symmetry in Chemistry*. McGraw–Hill Inc., New York, 1969.

[HCK+09] H. C. Hsu, F. C. Chou, K. Koyama, K. Watanabe, and H. L. Liu. Spin-Phonon Coupling in antiferromagnetic $Bi_2Sr_2CoO_{6+\delta}$: An infrared reflectance study. *Phys. Rev. B*, 79(15):155109, 2009.

[HGH98] C. Hartwigsen, S. Goedecker, and J. Hutter. Relativistic separable dual-space Gaussian pseudopotentials from H to Rn. *Phys. Rev. B*, 58(7):3641–3662, 1998.

[Hil00] Nicola A. Hill. Why are there so few Magnetic Ferroelectrics? *J. Phys. Chem. B*, 104(29):6694–6709, 2000.

[HK64] P. Hohenberg and W. Kohn. Inhomogeneous Electron Gas. *Phys. Rev.*, 136(3B):B864–B871, 1964.

[HLKvN+04] J. Hemberger, S. Lobina, H.-A. Krug von Nidda, N. Tristan, V. Yu. Ivanov, A. A. Mukhin, A. M. Balbashov, and A. Loidl. Complex interplay of $3d$ and $4f$ magnetism in $La_{1-x}Gd_xMnO_3$. *Phys. Rev. B*, 70(2):024414, 2004.

[HSL+97] Q. Huang, A. Santoro, J. W. Lynn, R. W. Erwin, J. A. Borchers, J. L. Peng, and R. L. Greene. Structure and magnetic order in undoped lanthanum manganite. *Phys. Rev. B*, 55(22):14987–14999, 1997.

[HSP+07] J. Hemberger, F. Schrettle, A. Pimenov, P. Lunkenheimer, V. Yu. Ivanov, A. A. Mukhin, A. M. Balbashov, and A. Loidl. Multiferroic phases of $Eu_{1-x}Y_xMnO_3$. *Phys. Rev. B*, 75(3):035118, 2007.

[Hub63] J. Hubbard. Electron Correlations in Narrow Energy Bands. *Proc. R. Soc. Lond. A*, 276(1365):238–257, 1963.

[HW03] H. Haken and H.C. Wolf. *Molekülphysik und Quantenchemie*. Springer Verlag, 4th edition, 2003.

[IA01] M. N. Iliev and M. V. Abrashev. Raman phonons and Raman Jahn-Teller bands in perovskite-like manganites. *J. Raman Spectrosc.*, 32(10):805–811, 2001.

[IAL+98] M. N. Iliev, M. V. Abrashev, H.-G. Lee, V. N. Popov, Y. Y. Sun, C. Thomsen, R. L. Meng, and C. W. Chu. Raman spectroscopy of orthorhombic perovskitelike $YMnO_3$ and $LaMnO_3$. *Phys. Rev. B*, 57(5):2872–2877, 1998.

[IAL+06] M. N. Iliev, M. V. Abrashev, J. Laverdiere, S. Jandl, M. M. Gospodinov, Y.-Q. Wang, and Y.-Y. Sun. Distortion–dependent Raman spectra and mode mixing in $RMnO_3$ perovskites (R = La, Pr, Nd, Sm, Eu, Gd, Tb, Dy, Ho, Y). *Phys. Rev. B*, 73(6):064302, 2006.

[IHL+07] M. N. Iliev, V. G. Hadjiev, A. P. Litvinchuk, F. Yen, Y.-Q. Wang, Y. Y. Sun, S. Jandl, J. Laverdiere, V. N. Popov, and M. M. Gospodinov. Multiple–order Raman scattering from rare–earth manganites: Oxygen isotope and rare–earth substitution effects. *Phys. Rev. B*, 75(6):064303, 2007.

[ILL+99] M. N. Iliev, A. P. Litvinchuk, H.-G. Lee, C. L. Chen, M. L. Dezaneti, C. W. Chu, V. G. Ivanov, M. V. Abrashev, and V. N. Popov. Raman spectroscopy of $SrRuO_3$ near the paramagnetic-to-ferromagnetic phase transition. *Phys. Rev. B*, 59(1):364–368, 1999.

[IMPB03] V. Yu. Ivanov, A. A. Mukhin, A. S. Prokhorov, and A. M. Balbashov. Phase transitions in $Sm_{1-x}Sr_xMnO_3$ single crystals ($0 \leq x \leq 0.8$). *Phys. Status Solidi B*, 236(2):445–449, 2003.

[IMT+06] V. Y. Ivanov, A. A. Mukhin, V. D. Travkin, A. S. Prokhorov, Yu. F. Popov, A. M. Kadomtseva, G. P. Vorob'ev, K. I. Kamilov, and A. M. Balbashov. New orthorhombic multiferroics $R_{1-x}Y_xMnO_3$ (R = Eu, Gd). *Phys. Status Solidi B*, 243(1):107–111, 2006.

[IPI+10a] S. Issing, A. Pimenov, V. Yu. Ivanov, A. A. Mukhin, and J. Geurts. Composition-dependent Spin-Phonon Coupling in mixed crystals of the multiferroic Manganite $Eu_{1-x}Y_xMnO_3$ ($0 \leq x \leq 0.5$) studied by Raman spectroscopy. *Phys. Rev. B*, 81(2):024304, 2010.

[IPI+10b] S. Issing, A. Pimenov, Y. Vu. Ivanov, A. A. Mukhin, and J. Geurts. Spin-phonon coupling in multiferroic manganites $RMnO_3$: comparison of pure (R = Eu, Gd, Tb) and substituted ($R = Eu_{1-x}Y_x$) compounds. *Eur. Phys. J. B*, 78:367–372, 2010.

[Iss] S. Issing. DFT calculation of lattice dynamics in multiferroic rare-earth manganites. http://www.lrz.de/projekte/hlrb-projects/0000000000F4289A.html.

[JG89] R. O. Jones and O. Gunnarsson. The density functional formalism, its applications and prospects. *Rev. Mod. Phys.*, 61(3):689–746, 1989.

[JL06] M. Johnsson and P. Lemmens. Crystallography and Chemistry of Perovskites. In H. Kronmüller and S. Parkin, editors, *Handbook of Magnetism and Advanced Magnetic Materials*. John Wiley & Sons Ltd. Chichester, UK, 2006.

[JT37] H. A. Jahn and E. Teller. Stability of Polyatomic Molecules in Degenerate Electronic States. I. Orbital Degeneracy. *Proc. R. Soc. Lond. A*, 161(905):220–235, 1937.

[KBC+09] N. N. Kovaleva, A. V. Boris, L. Capogna, J. L. Gavartin, P. Popovich, P. Yordanov, A. Maljuk, A. M. Stoneham, and B. Keimer. Dipole-active optical phonons in $YTiO_3$: Ellipsometry study and lattice-dynamics calculations. *Phys. Rev. B*, 79(4):045114, 2009.

[KBN07] H. Katsura, A. V. Balatsky, and N. Nagaosa. Dynamical Magnetoelectric Coupling in Helical Magnets. *Phys. Rev. Lett.*, 98(2):027203, 2007.

[KDG10] V. V. Kruglyak, S. O. Demokritov, and D. Grundler. Magnonics. *J. Phys. D*, 43(26):264001, 2010.

[KGS+03] T. Kimura, T. Goto, H. Shintani, K. Ishizaka, T. Arima, and Y. Tokura. Magnetic control of ferroelectric polarisation. *Nature*, 426:55–58, 2003.

[KHJ+05] M. Kenzelmann, A. B. Harris, S. Jonas, C. Broholm, J. Schefer, S. B. Kim, C. L. Zhang, S. W. Cheong, O. P. Vajk, and J. W. Lynn. Magnetic inversion symmetry breaking and ferroelectricity in $TbMnO_3$. *Phys. Rev. Lett.*, 95(8), 2005.

[Kim07] T. Kimura. Spiral magnets as magnetoelectrics. *Annual Review of Materials Research*, 37(1):387–413, 2007.

[KIS+03] T. Kimura, S. Ishihara, H. Shintani, T. Arima, K. T. Takahashi, K. Ishizaka, and Y. Tokura. Distorted perovskite with e_g^1 configuration as a frustrated spin system. *Phys. Rev. B*, 68(6):060403, 2003.

[Kit02] C. Kittel. *Einführung in die Festkörperphysik*. Oldenbourg Verlag, 13th edition, 2002.

[Kle66] P. G. Klemens. Anharmonic Decay of Optical Phonons. *Phys. Rev.*, 148(2):845–848, 1966.

[KLG+05] T. Kimura, G. Lawes, T. Goto, Y. Tokura, and A. P. Ramirez. Magnetoelectric phase diagrams of orthorhombic $RMnO_3$ (R=Gd, Tb, and Dy). *Phys. Rev. B*, 71(22), 2005.

[KMR+10] Ch. Kant, F. Mayr, T. Rudolf, M. Schmidt, F. Schrettle, J. Deisenhofer, and A. Loidl. Spin–phonon coupling in highly correlated transition-metal monoxides. *Eur. Phys. J. Special Topics*, 180:43–59, 2010.

[Kor55] S. Koritnig. *Landolt-Börnstein: Numerical Data and Functional Relationsships in Science and Technology*, volume I, Part 4. Springer Verlag, Berlin, 6th edition, 1955.

[KS65] W. Kohn and L. J. Sham. Self-Consistent Equations Including Exchange and Correlation Effects. *Phys. Rev.*, 140(4A):A1133–A1138, 1965.

[KSN+04] R. Krüger, B. Schulz, S. Naler, R. Rauer, D. Budelmann, J. Backstrom, K. H. Kim, S. W. Cheong, V. Perebeinos, and M. Rübhausen. Orbital ordering in $LaMnO_3$ investigated by resonance Raman spectroscopy. *Phys. Rev. Lett.*, 92(9), 2004.

[Kuz98] H. Kuzmany. *Solid-State Spectrocopy – An Introduction*. Springer Verlag, Berlin, 1998.

[Kuz09] A. Kuzmenko. Reffit. http://optics.unige.ch/alexey/reffit.html, 2009.

[LHK+05] G. Lawes, A. B. Harris, T. Kimura, N. Rogado, R. J. Cava, A. Aharony, O. Entin-Wohlman, T. Yildirim, M. Kenzelmann, C. Broholm, and A. P. Ramirez. Magnetically Driven Ferroelectric Order in $Ni_3V_2O_8$. *Phys. Rev. Lett.*, 95(8):087205, 2005.

[LJM+06] J. Laverdière, S. Jandl, A. A. Mukhin, V. Yu. Ivanov, V. G. Ivanov, and M. N. Iliev. Spin-Phonon Coupling in orthorhombic $RMnO_3$ (R = Pr, Nd, Sm, Eu, Gd, Tb, Dy, Ho, Y): A Raman study. *Phys. Rev. B*, 73(21):214301, 2006.

[LKY+09] J. S. Lee, N. Kida, Y. Yamasaki, R. Shimano, and Y. Tokura. Lattice dynamics in the *ab*– and *bc*–spiral spin-ordered states of perovskite manganites. *Phys. Rev. B*, 80(13):134409, 2009.

[LWSC04] B. Lorenz, Y. Q. Wang, Y. Y. Sun, and C. W. Chu. Large magnetodielectric effects in orthorhombic $HoMnO_3$ and $YMnO_3$. *Phys. Rev. B*, 70(21), 2004.

[MAF+10] J. Agostinho Moreira, A. Almeida, W. S. Ferreira, J. E. Araújo, A. M. Pereira, M. R. Chaves, J. Kreisel, S. M. F. Vilela, and P. B. Tavares. Coupling between phonons and magnetic excitations in orthorhombic $Eu_{1-x}Y_xMnO_3$. *Phys. Rev. B*, 81(5):054447, 2010.

[MAML+00] A. Munoz, J. A. Alonso, M. J. Martinez-Lope, J. L. Garcia-Munoz, and M. T. Fernandez-Diaz. Magnetic structure evolution of $NdMnO_3$ derived from neutron diffraction data. *J. Phys.: Condens. Matter*, 12(7):1361–1376, 2000.

[May02] F. Mayr. *Breitbandige optische Spektroskopie an Manganaten mit Perowskit–Struktur*. PhD thesis, Universität Augsburg, 2002.

[MF09] M. Mochizuki and N. Furukawa. Microscopic model and phase diagrams of the multiferroic perovskite manganites. *Phys. Rev. B*, 80(13):134416, 2009.

[MK97] T. Mayer-Kuckuk. *Atomphysik: Eine Einführung*. Teubner Verlag, Stuttgart, 5th edition, 1997.

[Mom08] Momma, K. and Izumi, F. *VESTA*: a three-dimensional visualization system for electronic and structural analysis. *J. Appl. Cryst.*, 41(3):653–658, 2008.

[Mor60] T. Moriya. Anisotropic Superexchange Interaction and Weak Ferromagnetism. *Phys. Rev.*, 120(1):91–98, 1960.

[Mos06] M. Mostovoy. Ferroelectricity in Spiral Magnets. *Phys. Rev. Lett.*, 96(6):067601, 2006.

[Mot37] N. F. Mott. Discussion of the paper by de Boer and Verwey. *Proc. Phys. Soc. London A*, 49:72, 1937.

[Nal05] S. Naler. *Optical studies of ordering phenomena in manganese oxides*. Cuvillier Verlag, Göttingen, 2005.

[O'D70] T. H. O'Dell. *The Electrodynamics of Magneto-Electric Media*. North-Holland Pub. Co, Amsterdam, 1970.

[Ope05] M. Opel. Magnetismus – Vorlesungsskript der TU München. http://www.wmi.badw.de/E23/lehre/skript/index.html, 2005.

[PLM+08] A. Pimenov, A. Loidl, A. A. Mukhin, V. D. Travkin, V. Yu. Ivanov, and A. M. Balbahov. Terahertz spectroscopy of Electromagnons in $Eu_{1-x}Y_xMnO_3$. *Phys. Rev. B*, 77(1):014438, 2008.

[PMI+06] A. Pimenov, A.A. Mukhin, V. Yu. Ivanov, V. D. Travkin, A. M. Balbashov, and A. Loidl. Possible evidence for Electromagnons in multiferroic manganites. *Nature Physics*, 2:97–100, 2006.

[PRM+06] A. Pimenov, T. Rudolf, F. Mayr, A. Loidl, A. A. Mukhin, and A. M. Balbashov. Coupling of phonons and electromagnons in $GdMnO_3$. *Phys. Rev. B*, 74(10):100403, 2006.

[PZ81] J. P. Perdew and Alex Zunger. Self-interaction correction to density-functional approximations for many-electron systems. *Phys. Rev. B*, 23(10):5048–5079, 1981.

[QTRM+77] S. Quezel, F. Tcheou, J. Rossat-Mignod, G. Quezel, and E. Roudaut. Magnetic structure of the perovskite-like compound $TbMnO_3$. *Physica B*, 86-88:916–918, 1977.

[Ram08] T. V. Ramakrishnan. Strongly correlated electrons in solids. *Current Science*, 95(9):1284–1309, 2008.

[RCG+10] P. Rovillain, M. Cazayous, Y. Gallais, A. Sacuto, M-A. Measson, and H. Sakata. Magnetoelectric excitations in multiferroic $TbMnO_3$ by Raman scattering. *Phys. Rev. B*, 81(5):054428, 2010.

[RdSG+10] P. Rovillain, R. de Sousa, Y. Gallais, A. Sacuto, M. A. Measson, D. Colson, A. Forget, M. Bibes, A. Barthelemy, and M. Cazayous. Electric–field control of spin waves at room temperature in multiferroic $BiFeO_3$. *Nat. Mater.*, 9(12):975–979, 2010.

[RKM+07] T. Rudolf, Ch. Kant, F. Mayr, J. Hemberger, V. Tsurkan, and A. Loidl. Polar phonons and spin-phonon coupling in $HgCr_2S_4$ and $CdCr_2S_4$ studied with far-infrared spectroscopy. *Phys. Rev. B*, 76(17):174307, 2007.

[Sch94] H. Schmid. Multi-ferroic magnetoelectrics. *Ferroelectrics*, 162:317, 1994.

[Sch08] M. Schumm. *ZnO–based semiconductors studied by Raman spectroscopy: semimagnetic alloying, doping, and nanostructures.* PhD thesis, Julius-Maximilians-Universität Würzburg, 2008.

[Sch09] M. Schmidt. Optische Anregungen im Multiferroikum Terbiummanganat. Master's thesis, Universität Augsburg, 2009.

[SD06] I. A. Sergienko and E. Dagotto. Role of the Dzyaloshinskii-Moriya interaction in multiferroic perovskites. *Phys. Rev. B*, 73(9):094434, 2006.

[SF05] Nicola A. Spaldin and M. Fiebig. The renaissance of magnetoelectric multiferroics. *Science*, 309(5733):391–392, 2005.

[SHV+08] J. R. Simpson, A. R. Hight Walker, R. Valdés Aguilar, A. B. Sushkov, H. D. Drew, S. Park, Y. J. Choi, C. Zhang, and S.-W. Cheong. Raman spectroscopy of multiferroic $TbMnO_3$. http://meetings.aps.org/Meeting/MAR08/Event/77518, 2008. APS March Meeting Abstracts.

[SKR+09] M. Schmidt, Ch. Kant, T. Rudolf, F. Mayr, A. A. Mukhin, A. M. Balbashov, J. Deisenhofer, and A. Loidl. Far-infrared optical excitations in multiferroic $TbMnO_3$. *Eur. Phys. J. B*, 71:411–418, 2009.

[Smi99] I. S. Smirnova. Normal modes of the $LaMnO_3$ Pnma phase: comparison with La_2CuO_4 Cmca phase. *Physica B: Condensed Matter*, 262(3–4):247–261, 1999.

[SML+11] A. M. Shuvaev, F. Mayr, A. Loidl, A. A. Mukhin, and A. Pimenov. High-frequency electromagnon in $GdMnO_3$. *Eur. Phys. J. B*, 80:351–354, 2011.

[SMP11] A. M. Shuvaev, A. A. Mukhin, and A. Pimenov. Magnetic and magnetoelectric excitations in multiferroic manganites. *J. Phys.: Condens. Matter*, 23(11):113201, 2011.

[SMSL10] R. Schleck, R. L. Moreira, H. Sakata, and R. P. S. M. Lobo. Infrared reflectivity of the phonon spectra in multiferroic $TbMnO_3$. *Phys. Rev. B*, 82(14):144309, 2010.

[SPacVac96] S. Satpathy, Zoran S. Popović, and Filip R. Vukajlović. Electronic Structure of the Perovskite Oxides: $La_{1-x}Ca_xMnO_3$. *Phys. Rev. Lett.*, 76(6):960–963, 1996.

[TM91] N. Troullier and J. L. Martins. Efficient pseudopotentials for plane–wave calculations. *Phys. Rev. B*, 43(3):1993–2006, 1991.

[TT99] Y. Tokura and Y. Tomioka. Colossal magnetoresistive manganites. *J. Magn. Magn. Mater.*, 200(1–3):1–23, 1999.

[TYK+09] Y. Takahashi, Y. Yamasaki, N. Kida, Y. Kaneko, T. Arima, R. Shimano, and Y. Tokura. Far-infrared optical study of Electromagnons and their coupling to optical phonons in $Eu_{1-x}Y_xMnO_3$ (x = 0.1, 0.2, 0.3, 0.4, and 0.45). *Phys. Rev. B*, 79(21):214431, 2009.

[VAMS+09] R. Valdés Aguilar, M. Mostovoy, A. B. Sushkov, C. L. Zhang, Y. J. Choi, S-W. Cheong, and H. D. Drew. Origin of Electromagnon Excitations in Multiferroic $RMnO_3$. *Phys. Rev. Lett.*, 102(4):047203, 2009.

[WA74] V. E. Wood and A. E. Austin. Possible applications for magnetoelectric materials. *Int. J. Magnetism*, 5, 1974.

[WAB+01] S. A. Wolf, D. D. Awschalom, R. A. Buhrman, J. M. Daughton, S. von Molnr, M. L. Roukes, A. Y. Chtchelkanova, and D. M. Treger. Spintronics: A Spin-Based Electronics Vision for the Future. *Science*, 294(5546):1488–1495, 2001.

[Wag03] J. Wagner. *Optische Charakterisierung von II–VI Halbleiter Oberflächen in Kombination mit 1st Principles Rechnungen.* PhD thesis, Julius-Maximilians-Universität Würzburg, 2003.

[Wyc64] R. Wyckoff. Inorganic compounds RX_n, R_nMX_2, R_nMX_3. In *Crystal structures*, volume 2. John Wiley & Sons Ltd. Chichester, UK, 2nd edition, 1964.

[YC01] P. Yu and M. Cardona. *Fundamentals of Semiconductors*. Springer Verlag, New York, 3rd edition, 2001.

[YMG+07] Y. Yamasaki, S. Miyasaka, T. Goto, H. Sagayama, T. Arima, and Y. Tokura. Ferroelectric phase transitions of $3d$–spin origin in $Eu_{1-x}Y_xMnO_3$. *Phys. Rev. B*, 76(18):184418, 2007.

Publications and Conference Contributions

Parts of this thesis have already been published:

- S. Issing, F. Fuchs, C. Ziereis, E. Batke, A. Pimenov, Y. Vu. Ivanov, A. A. Mukhin, and J. Geurts, *Lattice dynamics of $Eu_{1-x}Y_xMnO_3$ ($0 \leq x \leq 0.5$) studied by Raman and infrared spectroscopy*, Eur. Phys. J. B **73**, 353–360 (2010)

- S. Issing, A. Pimenov, V. Yu. Ivanov, A. A. Mukhin, and J. Geurts, *Composition–dependent spin–phonon coupling in mixed crystals of the multiferroic manganite $Eu_{1-x}Y_xMnO_3$ ($0 \leq x \leq 0.5$) studied by Raman spectroscopy*, Phys. Rev. B **81**, 024304 (2010)

- S. Issing, A. Pimenov, Y. Vu. Ivanov, A. A. Mukhin, and J. Geurts, *Spin–phonon coupling in multiferroic manganites $RMnO_3$: comparison of pure (R = Eu, Gd, Tb) and substituted ($R = Eu_{1-x}Y_x$) compounds*, Eur. Phys. J. B **78**, 367–372 (2010)

Other parts have been presented at conferences:

- S. Issing, A. Pimenov, A. A. Mukhin, and J. Geurts, *Raman spectroscopy of the multiferroic manganite $Eu_{1-x}Y_xMnO_3$*, DPG Spring Meeting of the Condensed Matter Section, Dresden (2009)

- S. Issing, F.Fuchs, C. Ziereis, E. Batke, A. Pimenov, Y. Vu. Ivanov, A. A. Mukhin, and J. Geurts, *Influence of doping on the lattice dynamics: stoichiometric and mixed orthorhombic manganites $RMnO_3$ (R=Gd, Tb, Eu:Y)*, DPG Spring Meeting of the Condensed Matter Section, Regensburg (2010)

- S. Issing, A. Pimenov, Y. Vu. Ivanov, A. A. Mukhin, and J. Geurts, *Spin-phonon coupling in multiferroic stoichiometric and mixed $RMnO_3$ compounds (R = Gd, Tb, Eu:Y) studied by Raman spectroscopy*, DPG Spring Meeting of the Condensed Matter Section, Regensburg (2010)

- S. Issing, A. Pimenov, Y. Vu. Ivanov, A. A. Mukhin, and J. Geurts, *Spin-phonon coupling in multiferroic stoichiometric and mixed $RMnO_3$ compounds (R = Gd, Tb, Eu:Y) studied by Raman spectroscopy*, 13th International Conference on Phonon Scattering in Condensed Matter, Taipei (2010)

- S. Issing, M. Schmidt, F. Mayr, J. Deisenhofer, A. Pimenov, A. A. Mukhin, A. Loidl, and J. Geurts, *Coupling Effects between Lattice dynamics and Magnetism in $GdMnO_3$ studied by optical spectroscopy in the FIR-regime*, DPG Spring Meeting of the Condensed Matter Section, Dresden (2011)

Danksagung

Viele Personen haben in direkter oder indirekter Weise zum Entstehen dieser Dissertation beigetragen. Daher möchte ich mich hier in nicht wertender Reihenfolge und in höchstwahrscheinlich nicht vollständiger Erwähnung folgenden Personen danken:

- Meinem Doktorvater, Prof. Dr. Jean Geurts, für die Möglichkeit der Promotion in der angenehmen und kollegialen Arbeitsatmosphäre seiner Gruppe und natürlich auch für die zahllosen Hintergrundgespräche zur Erweiterung meines physikalischen Horizonts

- Dem Lehrstuhlinhaber, Prof. Dr. Laurens W. Molenkamp, für die Arbeitsmöglichkeit am Lehrstuhl Experimentelle Physik III

- Der gesamten AG Geurts, insbesondere Christian Kehl, Utz Bass, Franziska Fricke, Franziska Fuchs, Sina Zapf, Christian Ziereis, Dr. Michael Leufgen und Dr. Michael Lentze für die gute Zusammenarbeit und die zahllosen Hilfen physikalischer und nicht physikalischer Natur

- Prof. Dr. Andrei Pimonev und Alexey Shuvaev für die Vermittlung der Proben sowie die stetige Diskussions– und Hilfsbereitschaft in allen Fragen betreffend das Thema "Multiferroika"

- Prof. Dr. Alois Loidl, Dr. Joachim Deisenhofer, Dr. Franz Mayr sowie Michael Schmidt vom Lehrstuhl Experimentelle Physik V der Universität Augsburg für die Möglichkeit, kurzfristig an ihrem sensationellen FT–IR Setup meine temperaturabhängigen IR Messungen durchzuführen

- Prof. Dr. Edwin Batke für die Bereitstellung des Raumtemperatur FT–IR Setups

- Dr. Alexander A. Mukhin für die exzellenten einkristallinen Proben

- Auch den restlichen Mitarbeitern des Lehrstuhls Experimentelle Physik III, hier insbesondere Prof. Dr. Karl Brunner, Dr. Claus Schumacher, Petra Fries, Prof. Dr. Wolgang Ossau, Dr. Tobias Kiessling und vielen anderen die mir in meiner Zeit in Würzburg unterstützend zur Seite gestanden haben

- Den Mitarbeitern der Mechanik– sowie der Elektronik–Werkstatt und insbesondere Roland Ebert für Hilfestellungen in allen Fragen der Probenbefestigung, elektrischer Kontaktierung und der Tieftemperaturphysik
- Den Sekretärinnen des Lehrstuhls Anja Brück–Poirer und Angelika Berger
- Der Studienstiftung des Deutschen Volkes e.V. für die Gewährung des Promotionsstipendiums
- natürlich meinen Eltern und meiner im wahrsten Sinne des Wortes besseren Hälfte...

Ehrenwörtliche Erklärung

gemäß§ 5 Abs. 1 Ziff. 2, 3 und 5
der Promotionsordnung der
Fakultät für Physik und Astronomie
der Universität Würzburg

Hiermit erkläre ich ehrenwörtlich, dass ich die Dissertation selbständig und ohne Hilfe eines kommerziellen Promotionsberaters angefertigt und keine anderen als die angegebenen Quellen und Hilfsmittel benutzt habe. Die Dissertation wurde bisher weder in gleicher noch in anderer Form in einem anderen Prüfungsfach vorgelegt.
Am 14. Dezember 2006 wurde mir von der Julius-Maximilians-Universität Würzburg der akademische Grad *Diplom Ingenieur (Univ.)* verliehen. Weitere akademische Grade habe ich weder erworben noch versucht zu erwerben.

Würzburg, den 22. August 2011

(Sven Issing)